TU Delft

Delft University of Technology

Transport and Morphodynamics in a Fine Sediment Estuary
From Conceptual Understanding to Numerical Modeling

Mathew, R.

DOI
10.4233/uuid:67cefd79-5a66-46ff-982c-1d0885bf8d2c

Publication date
2021

Document Version
Final published version

Citation (APA)
Mathew, R. (2021). *Transport and Morphodynamics in a Fine Sediment Estuary: From Conceptual Understanding to Numerical Modeling*. [Dissertation (TU Delft), Delft University of Technology]. https://doi.org/10.4233/uuid:67cefd79-5a66-46ff-982c-1d0885bf8d2c

Important note
To cite this publication, please use the final published version (if applicable).
Please check the document version above.

Copyright
Other than for strictly personal use, it is not permitted to download, forward or distribute the text or part of it, without the consent of the author(s) and/or copyright holder(s), unless the work is under an open content license such as Creative Commons.

Takedown policy
Please contact us and provide details if you believe this document breaches copyrights.
We will remove access to the work immediately and investigate your claim.

This work is downloaded from Delft University of Technology.
For technical reasons the number of authors shown on this cover page is limited to a maximum of 10.

Transport and Morphodynamics in a Fine Sediment Estuary

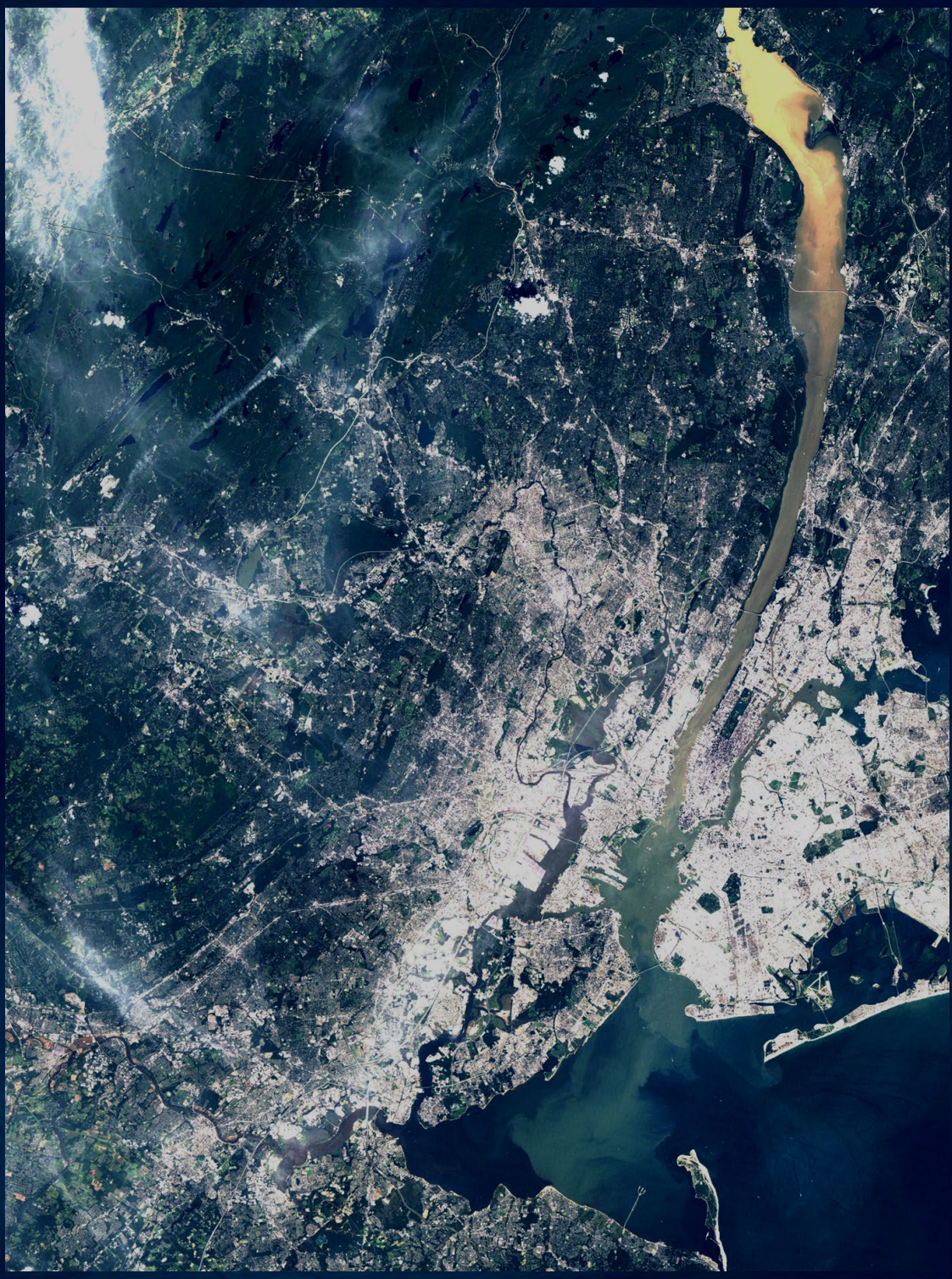

Rooni Mathew

TRANSPORT AND MORPHODYNAMICS IN A FINE SEDIMENT ESTUARY

FROM CONCEPTUAL UNDERSTANDING TO NUMERICAL MODELING

TRANSPORT AND MORPHODYNAMICS IN A FINE SEDIMENT ESTUARY

FROM CONCEPTUAL UNDERSTANDING TO NUMERICAL MODELING

Dissertation

for the purpose of obtaining the degree of doctor
at Delft University of Technology,
by the authority of the Rector Magnificus prof.dr.ir. T.H.J.J. van der Hagen,
chair of the Board for Doctorates,
to be defended publicly on
Wednesday 22 September 2021 at 15:00 o'clock

by

Rooni MATHEW

Master of Science in Civil and Environmental Engineering, Duke University, USA,
born in Kerala, India

This dissertation has been approved by the promotors.

Composition of the doctoral committee:

Rector Magnificus	chairperson
Prof.dr.ir. J.C. Winterwerp	Delft University of Technology, promotor
Independent members:	
Prof.dr.ir. Z.B. Wang	Delft University of Technology
Prof.dr.ir. A.J.H.M. Reniers	Delft University of Technology
Prof.dr.ir. J.A. Roelvink	IHE Delft
Prof.dr.ir. A.J.F. Hoitink	Wageningen University
Prof.dr. L.P. Sanford	University of Maryland, USA
Prof.dr. D.S. van Maren	East China Normal University, China

Keywords: Fluff layer, erodibility, transport regimes, morphodynamics, MORFAC, morphological upscaling

Printed by: Book1One, Rochester, NY, USA

Cover: Satellite photo showing transport of sediment plume from erosion in the Hudson River (the Lower Passaic River is visible to the west) during a Regime III event in August 2011 (Hurricane Irene).

Copyright © 2021 by Rooni Mathew

ISBN 978-0-578-97186-5

An electronic version of this dissertation is available at
http://repository.tudelft.nl/.

Any system obvious enough for an observer to possess the whole truth about it is not a system interesting enough to be worth modelling.

John D. Salt

J. D. Salt, *The seven habits of highly defective simulation projects*, J Simul **2**, 155–161 (2008)

CONTENTS

SUMMARY

This dissertation presents a study of fine sediment transport and morphodynamics in estuarine settings using data from the Lower Passaic River (LPR), located in New Jersey, USA. Originally a relatively shallow system, it has been dredged and deepened for navigation purposes from the late-1800s onwards, along with other modifications such as wetland reclamation, shoreline armoring, construction of bridges, etc. The last such dredging occurred several decades ago, and although the subsequent long-term morphological trend has been one of infilling, morphological trends over the short term (inter-annual durations) are more variable, with some years experiencing erosion and others experiencing infilling. Therefore, this dissertation seeks to understand the processes driving the long- and short-term morphological trends and the processes controlling the long-term morphodynamic equilibrium of the estuary. The dissertation approaches this problem by first assessing the small-scale (spatial and temporal) transport processes responsible for morphological evolution over the short term. Subsequently, it assesses the large-scale system dynamics from a morphodynamic perspective and the processes driving the variations thereof. Finally, the information gained from the small- and large-scale assessments is used to support the development and application of a morphodynamic model.

Sediment transport, and consequently morphodynamics, in starved-bed or erosion-limited fine sediment systems is a non-equilibrium process related to the availability of mobile sediment. This defines one time-scale of transport in such systems, that of the tidal period. During such conditions, transport is associated with the dynamics of a thin layer (2-4 mm thick in the LPR) of easily-erodible surficial sediments termed the fluff layer. Based on variations in suspended sediment concentrations that follow the oscillatory tidal currents, an analytical method referred to as the entrainment flux method for quantifying fluff layer erodibility (specifically, the critical shear stress for erosion and the erosion rate coefficient) was formulated and applied. The results of the entrainment flux method are analogous to the erosion data used to formulate the well-known standard linear erosion formulation; the inferred erosion properties are also comparable to direct measurements of erodibility on sediment samples using a Gust Microcosm. The favorable comparison with the direct measurements suggests that the entrainment flux method can be used to quantify the erodibility of the fluff layer in such systems.

Further to the various time-scales of transport in fine sediment systems, another time-scale is that spanning episodic scouring events. In the LPR, such scouring conditions are primarily associated with high river-flow events occurring every few years. During such conditions, depending on river flow-rate, erosion can extend beyond the fluff layer and up to tens of centimeters in the bed; consequently, sediment dynamics during such conditions is dependent on the fluvial forcing. However, during non-event conditions, sediment dynamics are controlled by barotropic and baroclinic circulation. In order to understand and quantify the dynamic impact of the various forcings on transport,

an extensive dataset consisting of suspended sediment fluxes, inter-annual morphological change, sediment erodibility, and a numerical hydrodynamic model was analyzed. The former two datasets were used to develop an understanding of sediment dynamics over the full range of hydrologic conditions, and the latter two datasets were used to interpret the system behavior. Subsequently, a conceptual picture was developed, one that classifies the instantaneous morphological status of the system into three regimes dependent on river flow — under Regime I the system imports sediments, under Regime II the system exports sediments by flushing the fluff layer, and under Regime III the system exports sediments by scouring the less-erodible strata underneath the fluff layer. Regime III is relevant for the long-term morphodynamic equilibrium of the estuary by providing a mechanism that scours and exports sediment accumulated under Regime I conditions. Limited information from the literature suggests that such a conceptualization of sediment dynamics may be common to estuaries characterized by starved-bed transport. These regimes also imply that transport in such systems also depends on the time-history of river flow and the long-term morphological progression of the system, i.e., the system develops a memory (represented by the availability of mobile sediment) that influences subsequent morphological response.

The conceptual and quantitative information on transport and sediment dynamics in the LPR was used as the basis for the development of a process-based morphodynamic model. Key processes of relevance in fine sediment settings were formulated and parameterized in the model. Specifically, these include sediment mobility considerations that lead to erosion-limited transport, either due to armoring effects or decreasing sediment erodibility with depth in the bed. The model framework also includes morphological upscaling using the Morfac approach, with specific formulations and considerations relevant for morphodynamics in fine sediment settings. Model performance was assessed against various metrics including suspended sediment concentrations and fluxes, and short- and long-term morphological change. Although the model does not capture measured morphological response at local scales over the short term, it predicts the large-scale spatial and temporal (river flow-dependent) short- and long-term morphological trends of the system. The model was subsequently applied to assess the long-term morphodynamic evolution of the estuary in response to changes in various forcings, with results that are conceptually and theoretically explainable. The results support the application of the morphodynamic model using Morfac for studying the long-term morphodynamic evolution of such fine sediment systems.

The overall conceptual findings, and the analytical and numerical methods developed in this dissertation are generally applicable to fine sediment systems characterized by starved-bed conditions. For instance, features such the presence of a fluff layer and its relatively high erodibility, and transport dynamics modulated by river flow have been observed in other systems as well. Similarly, concepts of sediment mobility and erosion-limited transport are also well known in the literature. This dissertation seeks to add to the body of knowledge for such systems by formulating a new method for quantifying the erodibility of the fluff layer, by presenting a conceptualization of sediment dynamics over the full range of hydrological conditions, by presenting a morphodynamic model framework that accounts for sediment mobility and erosion-limited transport, and by extending the applicability of the Morfac approach to fine sediment settings.

SAMENVATTING

Dit proefschrift presenteert een studie van fijn-sediment transport en morfodynamica in estuariumomgevingen aan de hand van gegevens van de Lower Passaic River (LPR), gelegen in New Jersey, VS. Oorspronkelijk was het een relatief ondiep systeem, maar vanaf het eind van de 19e eeuw is het uitgebaggerd en verdiept voor navigatiedoeleinden, samen met andere aanpassingen zoals het droogleggen van moerasgebieden, oeververstevigingen, de bouw van bruggen, enz. De laatste baggerwerkzaamheden vonden tientallen jaren geleden plaats en hoewel de morfologische tendens op lange termijn er een van opvulling is, zijn de morfologische tendensen op korte termijn (perioden van jaar tot jaar) meer variabel, waarbij er in sommige jaren sprake is van erosie en in andere van opvulling. Dit proefschrift probeert daarom inzicht te krijgen in de processen die de morfologische tendensen op lange en korte termijn aansturen en in de processen die het morfodynamisch evenwicht van het estuarium op lange termijn beheersen. Het proefschrift benadert dit probleem door eerst de kleinschalige (ruimtelijke en tijdsgebonden) transportprocessen te evalueren die verantwoordelijk zijn voor de morfologische evolutie op korte termijn. Vervolgens wordt de grootschalige dynamiek van het systeem beoordeeld vanuit een morfodynamisch perspectief en de processen die de variaties daarin veroorzaken. Ten slotte wordt de informatie die uit de kleinschalige en grootschalige evaluaties is verkregen, gebruikt om de ontwikkeling en toepassing van een morfodynamisch model te ondersteunen.

Sedimenttransport, en bijgevolg morfodynamica, in starved-bed of erosie-beperkt systemen van fijn sediment is een niet-evenwichtsproces dat samenhangt met de beschikbaarheid van mobiel sediment. Dit definieert één tijdschaal van het transport in dergelijke systemen, namelijk die van de getijdenperiode. Onder dergelijke omstandigheden wordt het transport geassocieerd met de dynamiek van een dunne laag (2-4 mm dik in de LPR) van gemakkelijk verwijderbare oppervlaktesedimenten, die de flufflaag wordt genoemd. Op basis van variaties in de concentraties van gesuspendeerd sediment die de oscillerende getijdenstromen volgen, werd een analytische methode, de zogeheten entrainment flux-methode, voor het kwantificeren van de erosie-eigenschappen (met name de kritische schuifspanning voor erosie en de erosiesnelheidscoëfficiënt) van de flufflaag geformuleerd en toegepast. De resultaten van de entrainment flux-methode zijn analoog aan de erosiegegevens die gebruikt worden om de welbekende standaard lineaire erosieformule te formuleren; de afgeleide erosie-eigenschappen zijn ook vergelijkbaar met directe metingen van erosie op sedimentmonsters met behulp van een Gust Microcosm. De positieve vergelijking met de directe metingen suggereert dat de entrainment flux-methode kan worden gebruikt om de erosie van de flufflaag in dergelijke systemen te kwantificeren.

Naast de verschillende tijdschalen voor het fijn-sedimenttransport is er ook nog een andere tijdschaal, namelijk die van episodische erosiegebeurtenissen. In de LPR worden dergelijke erosieomstandigheden vooral geassocieerd met hoge stroomsnelheden

in de rivier welke om de paar jaar voorkomen. In dergelijke omstandigheden kan de erosie, afhankelijk van de stroomsnelheid van de rivier, verder reiken dan de flufflaag en dit tot wel tientallen centimeters diep in de bedding; de sedimentdynamiek in dergelijke omstandigheden is bijgevolg afhankelijk van de fluviatiele krachten. Wanneer deze omstandigheden zich niet voordoen, wordt de sedimentdynamiek echter beheerst door barotropische en baroklinische circulatie. Om de dynamische impact van de verschillende krachten op het transport te begrijpen en te kwantificeren, werd een uitgebreide gegevensverzameling geanalyseerd, bestaande uit de fluxen van gesuspendeerde sedimenten, morfologische veranderingen van jaar tot jaar, erosie van sedimenten, en een numeriek hydrodynamisch model. De eerste twee datasets werden gebruikt om inzicht te krijgen in de sedimentdynamiek over het volledige spectrum van hydrologische omstandigheden, en de laatste twee gegevensverzamelingen werden gebruikt om het gedrag van het systeem te interpreteren. Vervolgens werd een conceptueel beeld ontwikkeld, waarbij de momentane morfologische status van het systeem in drie regimes wordt ingedeeld, afhankelijk van het debiet van de rivier — in regime I voert het systeem sedimenten aan, in regime II voert het systeem sedimenten af door de flufflaag door te spoelen, en in regime III voert het systeem sedimenten af door de minder voor erosie vatbare lagen onder de flufflaag af te schuren. Regime III is van belang voor het morfodynamisch evenwicht van het estuarium op lange termijn, omdat het zorgt voor een mechanisme waardoor sedimenten die zich onder regime I hebben opgehoopt, worden weggespoeld en afgevoerd. De beperkte informatie uit de literatuur suggereert dat een dergelijke conceptualisering van de sedimentdynamiek gebruikelijk kan zijn in estuaria die worden gekenmerkt door starved-bed transport. Deze regimes impliceren ook dat het transport in dergelijke systemen afhangt van de tijdshistorie van het debiet en de morfologische ontwikkeling van het systeem op lange termijn, d.w.z. dat het systeem een geheugen ontwikkelt (vertegenwoordigd door de beschikbaarheid van mobiel sediment) dat de latere morfologische respons beïnvloedt.

De conceptuele en kwantitatieve informatie over het transport en de sedimentdynamiek in de LPR is gebruikt als basis voor de ontwikkeling van een procesgebaseerd morfodynamisch model. De belangrijkste processen die van belang zijn voor fijne sedimenten werden in het model geformuleerd en geparametriseerd. Het gaat daarbij met name om overwegingen van sedimentmobiliteit welke leidt tot een erosiebeperkt transport, hetzij als gevolg van verstevigende effecten, hetzij door een afnemende erosie van sedimenten naarmate de diepte van de bedding toeneemt. Het modelkader omvat ook morfologische opschaling met behulp van de Morfac-benadering, met specifieke formuleringen en overwegingen die relevant zijn voor morfodynamica in een omgeving met fijn sediment. De prestaties van het model werden geëvalueerd aan de hand van verschillende parameters, waaronder de concentraties en fluxen van gesuspendeerde sedimenten, en morfologische veranderingen op korte en lange termijn. Hoewel het model de gemeten morfologische respons op lokale schaal op korte termijn niet weergeeft, voorspelt het wel de morfologische tendensen van het systeem op korte en lange termijn op grote ruimtelijke en temporele schaal (afhankelijk van het debiet van de rivier). Het model werd vervolgens toegepast om de morfodynamische evolutie van het estuarium op lange termijn te beoordelen in reactie op veranderingen in de verschillende krachten, met resultaten die conceptueel en theoretisch verklaarbaar zijn. De resultaten

ondersteunen de toepassing van het morfodynamisch model met behulp van Morfac voor het bestuderen van de morfodynamische evolutie op lange termijn van dergelijke fijn-sediment systemen.

De algemene conceptuele bevindingen en de analytische en numerieke methoden die in dit proefschrift zijn ontwikkeld, zijn algemeen toepasbaar op fijn-sedimentsystemen die worden gekenmerkt door starved-bed omstandigheden. Zo werden bijvoorbeeld kenmerken als de aanwezigheid van een flufflaag en de relatief hoge erosie daarvan, en een door de rivierstroming gemoduleerde transportdynamiek ook in andere systemen waargenomen. Ook de concepten van sedimentmobiliteit en erosiebeperkt transport zijn in de literatuur goed bekend. Dit proefschrift wil een bijdrage leveren aan de kennis over dergelijke systemen door een nieuwe methode te formuleren voor het kwantificeren van de erosiegevoeligheid van de flufflaag, door een conceptualisering te presenteren van de sedimentdynamiek over het volledige spectrum van hydrologische condities, door een morfodynamisch modelkader te presenteren dat rekening houdt met sedimentmobiliteit en erosiebeperkt transport, en door de toepasbaarheid van de Morfacbenadering uit te breiden naar fijn-sediment omgevingen.

1

INTRODUCTION

ESTUARIES, broadly defined (following Cameron and Pritchard [1]) as *a semi-enclosed coastal body of water which has a free connection with the open sea and within which sea water is measurably diluted with fresh water derived from land drainage*, are vitally important for a range of human activities including transportation, trade, fishing, industry, etc. Estuaries also play an important ecological role by providing vital nesting and feeding habitats for aquatic plants and animals. The ecological benefits and the commercial and recreational use of estuaries can be affected by the fate and transport of sediments, and in particular fine sediment (nominally defined as clays and silts, i.e., particle diameters less than 63 μm) which is the subject of this dissertation. For instance, excessive sediment supply to an estuary can result in aesthetic impacts due to enhanced turbidity in the water column, thereby affecting primary production and recreational use of the estuary. Excessive sediment supply can also result in the siltation of navigation channels and harbor basins located within the estuary, thereby affecting navigation and trade. Sediment transport in estuaries is therefore important for various management issues such as contaminant fate and transport, water quality, siltation of navigation channels, dredged material management, etc. Consequently, estuarine sediment dynamics are important for the effective management of estuaries for environmental, commercial, and recreational purposes.

Broadly speaking, the transport of fine sediments in estuarine settings involves the advection and dispersion of sediment originating from freshwater and marine sources, and the bed-water exchange processes of erosion and deposition. Transport is a function of the physical forcings acting upon the given system; these may include the tide, estuarine circulation, river flow, and waves. Erosion and deposition processes for fine sediments are site-specific by nature, with erodibility of fine sediments related to factors such as sediment mobility and consolidation effects, whereas deposition may be a function of flocculation in the water column. Figure 1.1 shows a conceptual representation of these transport processes for an estuarine setting; waves are not included since the analyses presented in this dissertation pertain to settings not subject to waves.

The hydrodynamic forcings acting on the system influence sediment transport at dif-

1

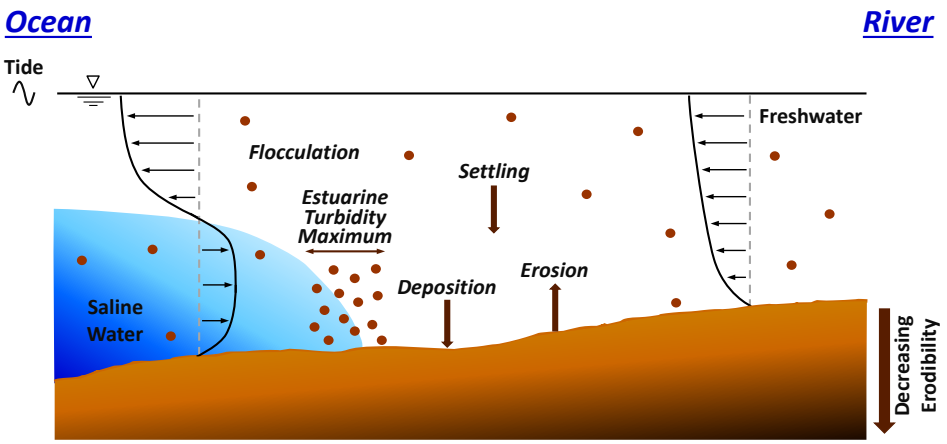

Figure 1.1: Conceptual representation of estuarine fine sediment transport. Adapted from Winterwerp *et al.* [2].

ferent spatial and temporal scales. For instance, transport associated with the tide operates over the time-scale of the tidal period, whereas transport associated with estuarine circulation and river flow can vary in time, e.g., seasonally or episodically in response to changing river flow. Similarly, tidal effects operate over spatial scales corresponding to the tidal excursion length, effects of estuarine circulation operate within the limit of salinity intrusion, and fluvial effects depend on river flow rate, with possibly local effects during low river-flow conditions, and estuary-wide at high river-flow conditions. The individual hydrodynamic forcings can influence transport specifically. For instance, the tide can induce net sediment transport in association with lag effects and tidal asymmetries, whereas estuarine circulation can lead to the formation of an estuarine turbidity maximum co-located with the salt front as shown in Figure 1.1 (Dyer [3]). Furthermore, erosion and deposition processes may also scale over the time-scales of the key hydrodynamic forcings (Dyer [3]). In addition, because of certain non-linearities inherent in fine sediment erosion (e.g., induced by erosion-limited transport due to depth-dependent erodibility), fine sediment transport is subject to limitations of sediment mobility and memory effects related to the time-history of transport regimes (Winterwerp *et al.* [2]).

The interplay between these various governing forcings can result in morphodynamic behavior particular to fine sediment systems. This includes phenomena such as time-history dependent morphological (primarily erosion) response, various time-scales of morphological response, supply constraints on sediment mobility, etc. Consequently, morphological change in fine sediment settings is a non-equilibrium process, largely governed by memory effects. As with sandy systems, morphological change can become part of a feedback loop by modifying the impact of the forcings. For instance, decreasing water depth due to sedimentation at a given location may lead to a local increase in flow velocity, and consequently, a decrease in net sedimentation. This gives rise to the classic morphodynamic feedback loop illustrated in Figure 1.2. Implicit in this schematic is the idea that a change in the physical forcings or in sediment substrate, morphology,

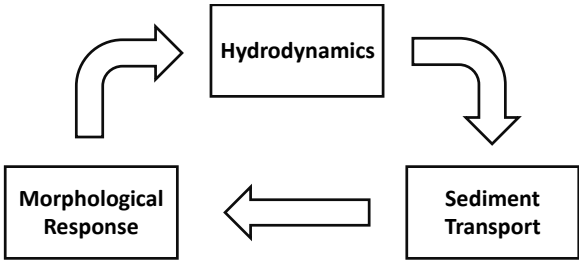

Figure 1.2: Schematic of the morphodynamic feedback loop. Adapted from Winter [4].

or sediment supply may influence morphological evolution and may in some cases result in a new morphodynamic equilibrium for the system. Such changes may be natural (e.g., an extreme storm event), or anthropogenic (e.g., dredging for a navigation channel, construction of river training works, dam construction, climate change, etc.).

This dissertation presents an assessment of sediment dynamics in estuarine settings dominated by fine sediments. Conceptual and quantitative findings pertaining to sediment dynamics are used to support the development and application of a numerical morphodynamic model that represents key processes relevant for fine sediment transport. Because the data, analyses, and model application presented in this dissertation relate to a specific estuary, the Lower Passaic River, the following section presents an overview of the study area, followed by a discussion of the research objectives, and the outline of the dissertation.

1.1. THE LOWER PASSAIC RIVER

THE Lower Passaic River (LPR) is a short, narrow estuary located in New Jersey, USA (Figure 1.3) and is part of New York Harbor. The LPR drains a 2400 km^2 watershed and stretches approximately 28 km long from its mouth in Newark Bay to the head-of-tide at Dundee Dam. Newark Bay is connected to New York Harbor and Raritan Bay (and the Atlantic Ocean) via the tidal inlets Kill van Kull and Arthur Kill, respectively. Historically, the LPR was fringed by tidal wetlands, and although the river planform and width have stayed roughly the same over time (as seen in panel c of Figure 1.3), it was extensively modified in several regards — wetland reclamation, deepening for navigation, shoreline armoring, construction of infrastructure such as bridges and railway crossings, etc. These modifications started in the early 19th century in conjunction with the establishment of various industrial, chemical, and manufacturing facilities along the banks of the river and elsewhere regionally (NOAA and FWS [5]).

In particular, dredging and deepening of the river for navigation purposes started in 1884, with nearly the entire length of the estuary (the lower 24 km) dredged by 1924 (U.S. Army Corps of Engineers [7] and NOAA [6]). The depth of the navigation channel also increased progressively over time, until the last major dredging event in 1950, when depths in the lower reaches were several meters below the original pre-industrial depths. With the exception of a localized dredging event, the upper 13 km of the LPR were last dredged in the 1930s, whereas the lower 11 km was last dredged in 1950. Figure 1.4 shows

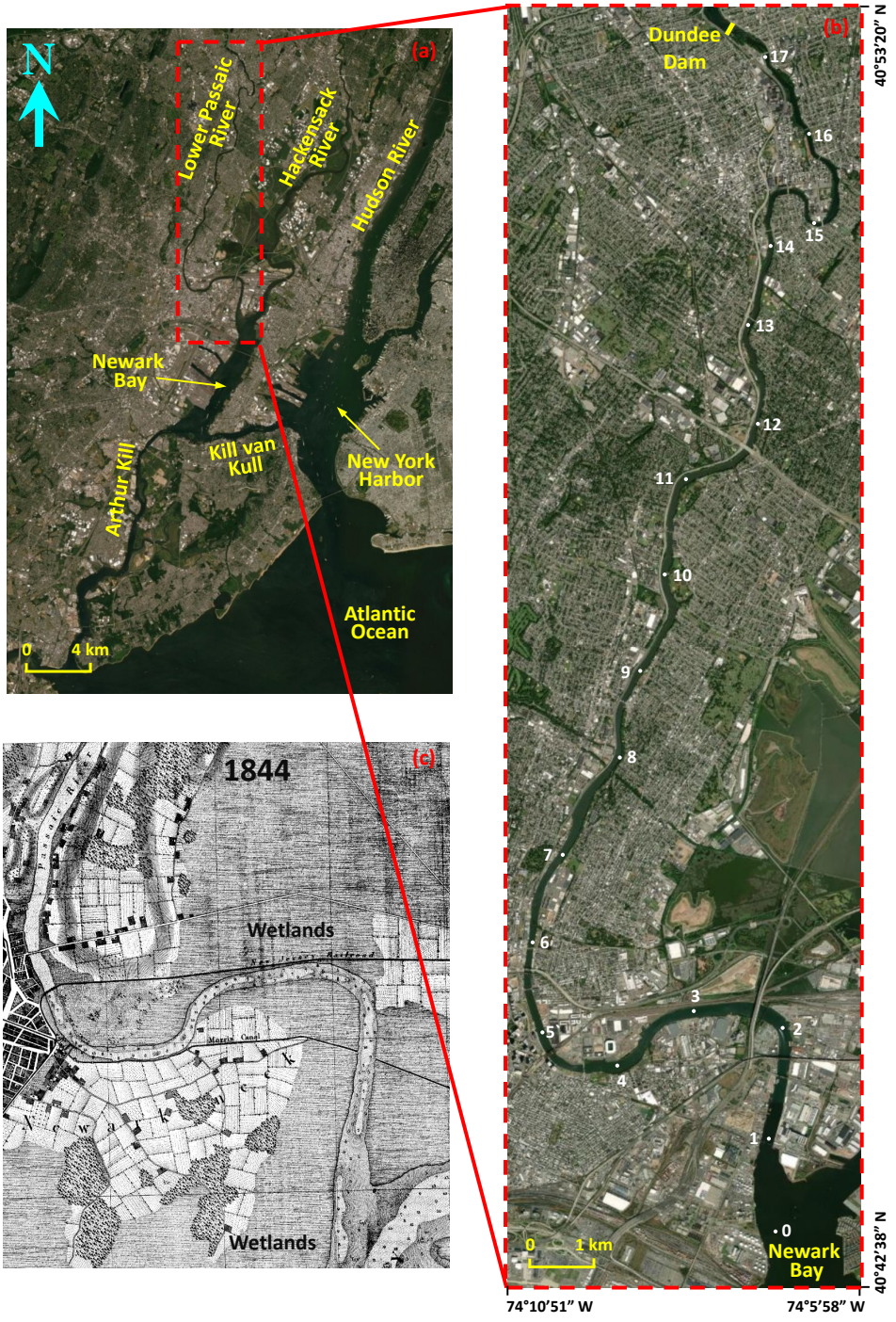

Figure 1.3: Regional (a), local (b), and historical (c) setting of the Lower Passaic River. Numbers along the axis of the river on panel b indicate river mileage. Historical map from [6].

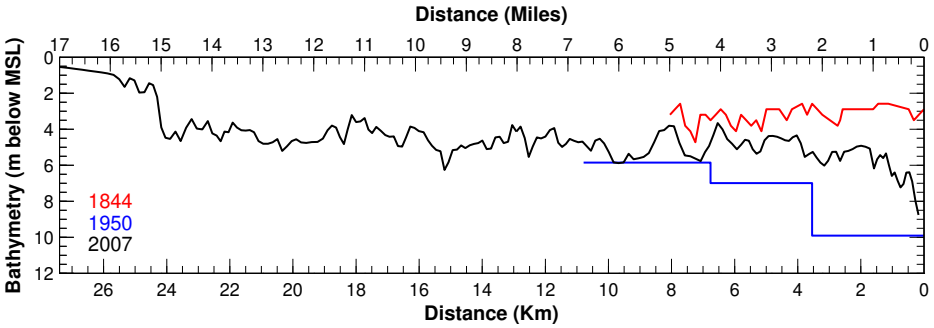

Figure 1.4: Current and historical bathymetry in the navigation channel of the Lower Passaic River. Depths relative to Mean Sea Level (MSL)

the historical (pre-industrial, in 1844) bathymetry in the lower reaches of the LPR relative to the dredged channel depth in 1950, and the current (as measured in 2007) depth in the navigation channel. Although limited by the availability of data in the upper reaches (both historically as well as in 1950), in the lower reaches, the data indicate extensive sedimentation on the order of several meters since the dredging of 1950, with the current bathymetry in some locations tending towards the historical (1844) bathymetry.

The post-dredging infilling of the LPR in the mid-20th century coincided with the release of various contaminants such as dioxins and furans, polychlorinated biphenyls, polycyclic aromatic hydrocarbons, pesticides, and heavy metals (Louis Berger Group *et al.* [8]). Because several of these contaminants are hydrophobic, they tend to preferentially sorb to fine sediments in the water column and in the bed. Consequently, the sediment bed within the LPR is impacted by historical sources of contamination. The LPR is currently the subject of ongoing environmental cleanup and restoration studies aimed at managing the legacy contamination in the sediments. As part of this process, several datasets were collected for quantifying processes and metrics of importance for sediment transport. These include water depths, currents, salinity, suspended sediments, periodic bathymetry surveys, sediment erodibility, sediment substrate (grain size distribution and dry density), etc. These datasets have been used to support the development and calibration of numerical models of the hydrodynamics and sediment transport in the LPR by various entities (Louis Berger Group *et al.* [8] and Moffatt and Nichol and Deltares [9]). Furthermore, with the exception of some portions near the head-of-tide, the majority of the sediment substrate as well as sediment transport in the LPR is characterized by fine sediments. The availability of such extensive empirical datasets characterizing various aspects of fine sediment transport and dynamics over various spatial and temporal scales provides an opportunity for answering a few research questions and objectives as described in the following section.

1.2. RESEARCH OBJECTIVES

THE overall objective of this dissertation is to develop a better understanding of morphodynamics in fine sediment settings. The overall context of the analyses pre-

sented in this dissertation can be seen in the morphological evolution of the LPR presented in Figure 1.4, specifically, the long-term infill of the lower reaches of the LPR since the dredging event in 1950. However, despite this long-term signal of infill, current short-term morphological changes (inter-annual scales; presented in Chapter 3) are more variable, with some years experiencing erosion and other years experiencing deposition. Therefore, this dissertation seeks to understand the processes driving the long-term signal of infill while resulting in a more variable signal over the short-term under current conditions. The dissertation also aims to determine the source of infilling sediment which may include loadings from the head-of-tide, from marine sources (via Newark Bay), and internal restribution. Finally, the dissertation also seeks to understand the processes controlling the long-term equilibrium morphology of the estuary.

The dissertation approaches this problem starting from a fine-scale, by first assessing small-scale (spatial and temporal) transport processes responsible for morphological evolution over the short term. Subsequently, it presents an assessment of large-scale system dynamics from a morphodynamic perspective and the processes driving the variations thereof, from which a conceptual model of transport and sediment dynamics is developed. Finally, the conceptual and quantitative understanding gained from the small- and large-scale assessments are used to support the development and application of a morphodynamic model. Accordingly, the specific research objectives of this dissertation are:

1. **The development of an approach for quantifying the erodibility of surficial sediments in tidal settings**

2. **The development of a conceptual understanding of estuarine sediment dynamics and transport regimes**

3. **The development of a process-based morphodynamic model incorporating various phenomena of relevance in fine sediment settings**

4. **The extension of the morphological upscaling technique for morphodynamic modeling in fine sediment settings**

1.3. DISSERTATION OUTLINE

THIS dissertation is organized following the specific research objectives described in the preceding section. Chapter 2 relates to research objective 1 and presents an evaluation of suspended sediment concentrations in the LPR. This evaluation is used to support the development of an analytical approach to quantify the erodibility of the surficial sediment strata that is responsible for sediment dynamics the majority of the time in such tidal and estuarine systems characterized by fine sediment transport. Chapter 3 relates to research objective 2 and presents an assessment of the large-scale transport dynamics and morphodynamics in the LPR and its relationship with the primary hydrodynamic forcings. The results of this analysis are used to develop a conceptual representation of sediment dynamics and transport regimes in such tidal and estuarine systems characterized by fine sediment transport. Chapter 4 relates to research objective 3 and presents the development of a morphodynamic model of the LPR using the information

presented in Chapters 2 and 3. Chapter 4 also relates to research objective 4 and presents an extension of the morphodynamic upscaling technique which enables computationally efficient morphodynamic simulations — as part of the research presented in this dissertation, specific formulations and methods were developed to support application of morphodynamic upscaling to fine sediment settings. The morphodynamic model is also used to assess the projected long-term and large-scale morphodynamic evolution of the LPR in response to various external forcings. Finally, Chapter 5 integrates the key findings in relation to the research objectives of this dissertation, presents the main conclusions, and provides recommendations for further research. Furthermore, the bulk of the analyses in this dissertation (representing Chapters 2, 3, and 4) consists of two published and one submitted manuscript.

REFERENCES

[1] W. M. Cameron and D. W. Pritchard, *Estuaries,* in *The Sea, Vol. II*, edited by M. N. Hill (John Wiley and Sons, New York, NY, 1963).

[2] J. C. Winterwerp, T. van Kessel, D. S. van Maren, and B. C. van Prooijen, *Fine Sediment in Open Water — From Fundamentals to Modeling* (World Scientific, in press, 2021).

[3] K. R. Dyer, *Estuaries: A Physical Introduction*, 2nd ed. (John Wiley and Sons, New York, 1997).

[4] C. Winter, *Observation- and modelling of morphodynamics in sandy coastal environments,* Habilitationsschrift zur Erlangung der venia legendi im Fachbereich Geowissenschaften der Universität Bremen (2011).

[5] NOAA and FWS, *Natural Resource Damage Asssessment Plan for the Diamond Alkali Superfund Site,* (2020).

[6] NOAA, *Historical Map and Chart Collection,* https://historicalcharts.noaa.gov, accessed: March 8, 2021.

[7] U.S. Army Corps of Engineers, *Lower Passaic River Commercial Navigation Analysis* (New York, NY, USA, 2010).

[8] Louis Berger Group, Battelle, and HDR|HydroQual, *Remedial Investigation Report for the Focused Feasibility Study of the Lower Eight Miles of the Lower Passaic River,* (2014).

[9] Moffatt and Nichol and Deltares, *Appendix M: Sediment transport model of the Lower Passaic River, Lower Passaic River RI/FS* (Cooperating Parties Group, Newark, NJ, 2019).

2

SURFICIAL SEDIMENT ERODIBILITY

Numerical models of fine sediment transport depend on different approaches to parameterize the erosion properties of surficial sediment strata. These properties, namely the critical shear stress for erosion and the erosion rate coefficient, are crucial for reproducing the short-term and long-term sediment dynamics of the system. Methods to parameterize these properties involve either specialized laboratory measurements on sediment samples or optimization by model calibration. Based on observations of regular patterns in the variation of suspended sediment concentrations (SSC) over the tidal cycle in a small, narrow estuary, an alternate approach, referred to as the entrainment flux method, for quantifying the erosion properties of surficial bed strata is formulated and applied. The results of this method are shown to be analogous to the erosion data used to formulate the standard linear erosion formulation developed by various authors. The erosion properties inferred from the entrainment flux method are also compared to direct measurements of erodibility on sediment samples from the same site using the Gust Microcosm apparatus. The favorable comparison of the two approaches suggests that the entrainment flux method can be used to infer and quantify the erodibility of surficial sediment strata in similar small and narrow estuaries. This method has certain advantages, chiefly its ease of implementation and the fact that it uses SSC time-series which would typically be expected to be available for the study of or for model application at a given site. Guidelines for selecting the appropriate dataset for the application of the method are also presented.

This chapter has been published in the journal Ocean Dynamics:
R. Mathew and J. C. Winterwerp, *Surficial sediment erodibility from time-series measurements of suspended sediment concentrations: Development and validation*, Ocean Dynam **67**, 691–712 (2017)

2.1. INTRODUCTION

FINE sediment (generally defined as clays and silts with particle diameters less than 63 µm) transport in aquatic systems is a subject of considerable study and interest from environmental and commercial perspectives. Fine sediment transport is of consequence to various sediment management problems such as contaminant fate and transport, water quality, siltation of navigation channels, dredged material management, etc. Broadly speaking, the transport processes for fine sediments involve advection and dispersion in the water column and the bed-water exchange processes of erosion and deposition. The former bed-water exchange process represents the mobilization of sediments from the bed followed by entrainment into the water column, and the latter process represents the settling of suspended sediment through the water column followed by deposition onto the bed surface. This chapter focuses on the erosion dynamics of fine sediments.

Erosion of fine sediments in the natural environment occurs under the action of shear stresses imposed at the bed-water interface by waves and currents. As such, erosion can be distinguished into four different modes, roughly in increasing order with respect to the magnitude of shear stress responsible and the resulting erosion rate — floc erosion, surface erosion, mass erosion, and liquefaction (Mehta [1]; Winterwerp and van Kesteren [2]). Floc erosion refers to the removal of individual sediment flocs from the bed surface. Floc erosion occurs when the mean bed shear stress is at or just below some nominal critical threshold shear stress for surface erosion. Surface erosion is a drained process that occurs when the mean bed shear stress exceeds the mean critical threshold shear stress. This causes a rupture of the physicochemical bonds between flocs at the bed surface, followed by the detachment of flocs from the bed, and entrainment into the water column by hydrodynamic drag and lift. In contrast, mass erosion is an undrained process typically associated with much larger bed shear stresses than surface erosion and occurs due to a failure of the sediment matrix along a shear plane in the bed, leading to the erosion of clumps of sediment from the bed. Finally, liquefaction refers to the structural breakdown of the bed sediment matrix, typically under the action of waves, forming a layer of fluid-supported slurry known as fluid mud from which sediment can be entrained into the overlying water column by flow-induced turbulent mixing. The analysis presented in this chapter includes shear stress regimes characteristic of floc erosion and surface erosion. Therefore, the formulations used to describe these processes and the laboratory methods used to measure and quantify them are reviewed.

Fine sediment erosion was first studied in a systematic manner by Partheniades [3] and Partheniades [4]; also summarized in Partheniades [5]. Using measurements of erosion in flume tests using cohesive sediments from San Francisco Bay, he developed a relationship between the imposed bed shear stress and resulting erosion rate. The data indicated a "hockey-stick"-type response, with a shallower slope in the shear stress-erosion rate relationship at low shear stresses (indicative of floc erosion), changing to a steeper slope beyond some threshold shear stress (indicative of surface erosion). However, floc erosion is the subject of some debate in the literature; Piedra-Cueva and Mory [6] in a targeted experimental study did not find any measurable evidence of floc erosion. More recently, however, Winterwerp *et al.* [7], and van Prooijen and Winterwerp [8] consider floc erosion to be a consequence of turbulent fluctuations in the mean bed shear stress and the stochastic nature of the critical threshold shear stress for surface erosion.

Accordingly, floc erosion occurs when the instantaneous bed shear stress exceeds the local critical threshold shear stress for surface erosion even though the time-averaged bed shear stress may be at or below the spatial-mean critical threshold shear stress for surface erosion. The floc erosion rate was parameterized by these authors as an empirical third-order polynomial function of the turbulence-mean bed shear stress and the critical shear stress for erosion.

In contrast, surface erosion has been well established and studied by various authors; typical numerical sediment transport models include formulations of surface erosion. Using the data indicative of surface erosion as measured by Partheniades [3] and Partheniades [4], Kandiah [9] and Ariathurai and Arulanandan [10] formulated the erosion rate function as:

$$E = M\left(\frac{\bar{\tau}_b - \tau_{Cr}}{\tau_{Cr}}\right), \text{for } \bar{\tau}_b > \tau_{Cr} \tag{2.1}$$

where, E (M/L^2/T) is the erosion rate or mass flux, $\bar{\tau}_b$ (M/L/T^2) is the turbulence mean bed shear stress, M (M/L^2/T) is the erosion rate coefficient, and τ_{Cr} (M/L/T^2) is the critical threshold shear stress for erosion. The latter two represent empirical parameters determined from erosion measurements. Eq. 2.1 is also referred to as the standard linear erosion formulation. Note that other authors (Sanford and Halka [11]; Sanford *et al.* [12]) use Eq. 2.1 without the normalization by τ_{Cr}, in which case the units for M change accordingly. Eq. 2.1 is used to model what is referred to as unlimited or Type II erosion where M and τ_{Cr} do not change with time or depth in the sediment bed (Mehta and Partheniades [13]). However, sediments in nature typically exhibit depth-dependence in their erosion properties. For instance, τ_{Cr} commonly increases with depth due to the effects of consolidation, thereby limiting the extent of erosion under a given bed shear stress. The erosion behavior under such conditions is referred to as depth-limited or Type I erosion (Mehta and Partheniades [13]) and can be formulated as (Parchure and Mehta [14], Amos *et al.* [15]):

$$E = E_f \exp\left\{\alpha\left(\frac{\bar{\tau}_b - \tau_{Cr,z}}{\tau_{Cr,z}}\right)^{\beta}\right\} \tag{2.2}$$

where E_f (M/L^2/T) is referred to as the floc erosion rate, α and β are empirical, material-dependent parameters, and $\tau_{Cr,z}$ is the depth-dependent critical shear stress for erosion. Note that this definition of E_f as the floc erosion rate is different from that of others such as Winterwerp *et al.* [7], and van Prooijen and Winterwerp [8]. Sanford and Maa [16] subsequently showed that Eq. 2.1 and 2.2 yield identical results simply by allowing M and τ_{Cr} in Eq. 2.1 to vary with depth z.

Eq. 2.1 and its variants have been implemented in numerical sediment transport models for numerous applications around the world. Such applications typically rely on either parameterization derived from physical measurements of the erosion properties, achieved using a number of different devices and approaches such as the Gust Microcosm (Gust and Mueller [17]), Sedflume (McNeil *et al.* [18]), carousels (Parchure and Mehta [14]; Amos *et al.* [15]; Maa *et al.* [19]), soil mechanical properties (Winterwerp *et al.* [7]), etc., or rely on model calibration to suspended sediment concentrations (SSC)

measurements (van Kessel *et al.* [20]; van Maren *et al.* [21]). The experimental methods vary in complexity in terms of sample requirements (for example, undisturbed cores versus grab samples), ex situ versus in situ measurements, laboratory equipment (for example, specialized flumes versus conventional soil mechanical measurements), sediment strata sampled (for example, thin layers near the bed surface versus larger depth intervals but deeper in the bed), etc.

Here we propose an alternative approach for quantifying the erosion properties of surficial bed strata, also referred to in the literature as the fluff layer, in tidal and estuarine systems. This approach uses high-frequency time-series measurements of SSC, water depths, and currents to assess the erosion properties of the fluff layer. As validation of this method, the results are compared against direct measurements of erosion properties on sediment cores measured using the Gust Microcosm apparatus. It is also worth noting that the focus of this alternate method is on the development of appropriate parameter values for ultimate use in a numerical sediment transport model. The following sections provide an overview of the study area, the relevance of the fluff layer for sediment dynamics in tidal and estuarine systems, the data used, the analytical procedures involved, followed by a discussion of the results.

2.2. SITE OVERVIEW AND BACKGROUND

THE data presented in this chapter come from the Lower Passaic River (LPR), a tidal estuary that is part of New York Harbor (Figure 2.1). The LPR stretches approximately 28 km long from its mouth in Newark Bay to the head-of-tide at Dundee Dam. Newark Bay is connected to New York Harbor and Raritan Bay (and the Atlantic Ocean) via the tidal inlets Kill van Kull and Arthur Kill, respectively. The river width ranges from approximately 600 m at its mouth, declining to about 200 m at River Mile (RM) 1.4 (about 2.25 km from the mouth), and about 150 m near RM 4.2 (about 6.75 km from the mouth); the latter two locations are pertinent to the analysis in this chapter. The LPR is the subject of an ongoing environmental cleanup and restoration process and as part of this process, a number of datasets, including the data presented here, have been collected to support the development and calibration of numerical models of the hydrodynamics, sediment transport, and contaminant fate and transport.

The hydrodynamics and sediment dynamics within the LPR are controlled by the tide, estuarine (gravitational) circulation, and river flow. Semi-diurnal tides (dominant period of 12.42 h, corresponding to the semi-diurnal M_2 constituent) entering Newark Bay through the Kill van Kull and Arthur Kill propagate to the LPR and the head-of-tide at Dundee Dam, forming an almost standing wave and with maximum currents typically occurring around mid-tide. The tidal range varies from 0.9 m to 2.1 m from neap to spring; the corresponding flow rates due to tidal exchange (based on current measurements at RM 1.4) range approximately 150 m^3/s to 300 m^3/s (averaged over the half tidal cycle). In comparison to the flow rates associated with tidal exchange, the annual average river flow over Dundee Dam is only about 34 m^3/s (a few minor tributaries contribute approximately an additional 15% freshwater flow). Therefore, river discharge accounts for a relatively small fraction of the total flow in the LPR during low–average flow conditions. Consequently, salinity intrusion occurs during low–average river flow conditions, resulting in a partially-mixed water column within the LPR. Salinity intrusion occurs due

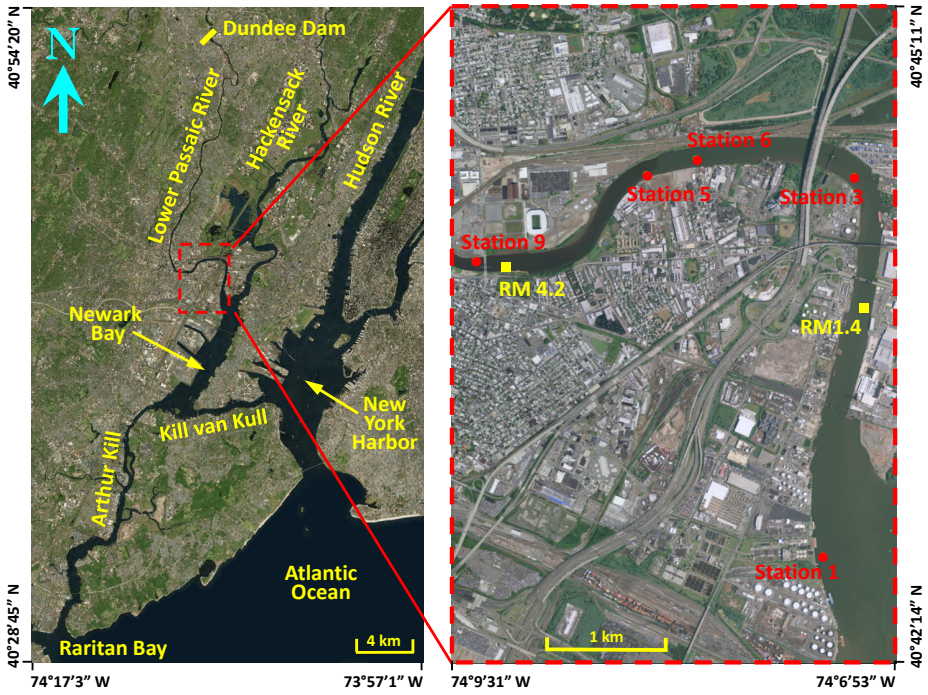

Figure 2.1: Location map of the Lower Passaic River along with the locations of the in situ moorings (squares) and sediment core samples (circles).

to the tides and estuarine circulation (defined as the density-driven circulation resulting in tidally-averaged residual currents directed up-estuary in the lower portion of the water column and down-estuary in the upper portion of the water column). The extent of salinity intrusion, as indicated by the location of the salt front, is a function of the tidal phase, river flow, spring–neap cycle, as well as offshore mean water level fluctuations due to set-up and set-down events. The salt front moves down-estuary with the ebb tide, increasing river flow, increasing tidal range (spring tides), and offshore set-down events. Conversely, up-estuary movement of the salt front occurs during conditions of flood tide, decreasing river flow, decreasing tidal range (neap tides), and offshore set-up events. The salt front is also typically co-located with the Estuarine Turbidity Maximum (ETM), a region characterized by relatively high SSC and sediment trapping (Dyer [22]). The hydrodynamics and sediment dynamics during typical tidal and low–average flow conditions in the LPR are also characterized by tidal asymmetry, with higher peak currents and SSC during flood than on ebb. As a result, depth- and tidally-integrated suspended sediment (SS) fluxes are directed up-estuary at low river flow and down-estuary at high river flow (Chant *et al.* [23]). Note that the term typical tidal condition is used to refer to tides with expected spring–neap variability in tidal range (0.9 m to 2.1 m) as opposed to periods affected by storm surges or offshore set-up or set-down events since

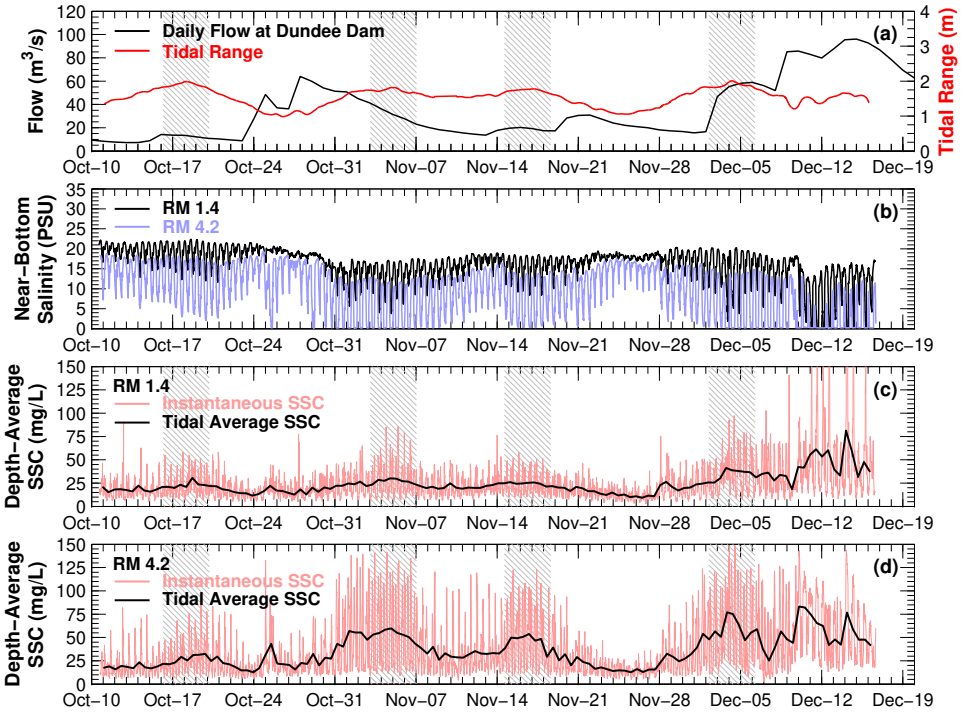

Figure 2.2: Time series of (a) the Dundee Dam discharge and spring–neap variability in tidal range, (b) near-bottom salinity, (c) instantaneous and tidally averaged depth-average SSC at RM 1.4, and (d) instantaneous and tidally averaged depth-average SSC at RM 4.2. Hatched regions indicate 2 days before and after the twice-monthly maximum in tidal range — nominally, spring tide conditions.

such events may augment bed shear stresses generated by the tidal currents.

Figure 2.2 provides an overview of the SSC dynamics over a two-month period using measurements at two locations near the mouth of the LPR, at RM 1.4 and RM 4.2. The SSC dynamics are shown in relation to the river flow, tidal range (as a proxy for spring–neap variability), and near-bottom salinity (as a proxy for the location of the salt front and the ETM). Instantaneous depth-average SSC ranges from intra-tidal lows of about 10 mg/L to highs of about 75 mg/L at both locations typically, except for higher values co-occurring with the passage of the salt front (and the ETM) at RM 4.2, and during high-flow periods such as the one in early-mid December.

As seen in a two-day snapshot in Figure 2.3 of the tide, depth-average velocity and SSC at RMs 1.4 and 4.2, and the vertical distribution of SSC at RM 4.2 (along with the vertical salinity gradient), the SSC data also show systematic patterns with velocity within the tidal cycle — SSC and velocity magnitudes are positively correlated within the tidal cycle, increasing and decreasing approximately in phase. Near-bottom and depth-average SSC increases as velocity increases, reaching a maximum around the time of maximum velocity and decreasing thereafter to a minimum around slack water, a general pattern

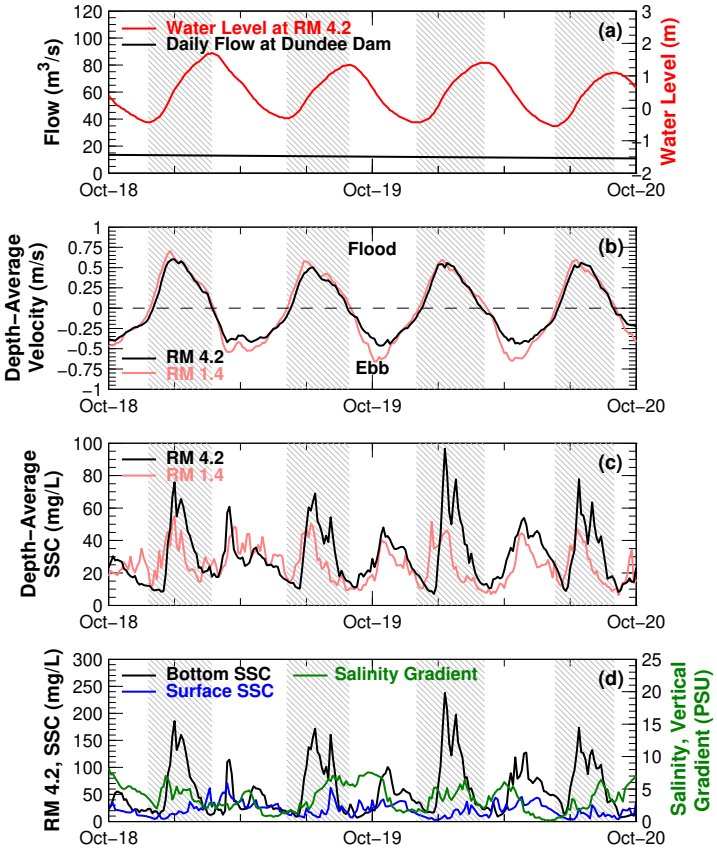

Figure 2.3: Time-series of (a) Dundee Dam discharge, water level at RM 1.4, (b) the depth-average velocity at RMs 1.4 and 4.2, (c) the depth-average SSC at RMs 1.4 and 4.2, and (d) the vertical distribution of SSC and salinity gradient at RM 4.2. Hatched regions indicate period of increasing water level.

true of both ebb and flood tides. During the period of accelerating velocity, near-bottom SSC increases rapidly, with somewhat smaller increase in near-surface SSC. The vertical gradient in SSC may be influenced by salinity stratification, with stratification (as seen in the time-series of the salinity gradient on the bottom panel of Figure 2.3) increasing during flood and possibly reducing vertical mixing. The rapid increase in SSC during the accelerating phase of the flood/ebb currents followed by the rapid decrease during the decelerating phase indicates erosion and deposition from/to the sediment bed over tidal time-scales. The notion of erosion and deposition within the flood and ebb phases of the tide is supported by the fact that the SSC signal is in phase with velocity rather than with the tidal water levels. The correlation with velocity is further explored in Figure 2.4 and discussed later in the text. Comparison of the depth-average SSC at RMs 1.4 and 4.2 also shows that both locations attain approximately similar values during slack water, which implies similar SSC over the entire reach between these two locations during slack water.

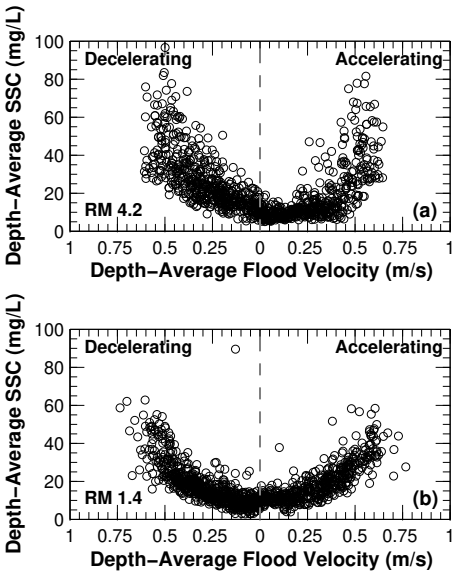

Figure 2.4: SSC as a function of depth-average velocity during the flood phase of the tidal cycle at (a) RM 4.2, and (b) RM 1.4. Data measured during Oct 11-24, 2009 and Nov 22-27, 2009.

Furthermore, the travel time between RMs 1.4–4.2 is in excess of 3 h, depending on the magnitude of tidal currents which vary over the spring–neap cycle. These observations suggest that the SSC fluctuations are locally driven, i.e., due to erosion and deposition between RMs 1.4–4.2 during the flood- and ebb-phases of the tide. Focusing on the first half of the flood tide at RM 4.2 (i.e., accelerating currents), a period that is the subject of the analysis presented in this chapter, the increase in SSC during this period is not due to the advection of a SSC plume from locations down-estuary of RM 1.4. If the advection of such a plume were responsible, SSC would not scale with velocity every tidal cycle, a feature further examined in Figure 2.4 and discussed later in the text. Rather, the increase in SSC at RM 4.2 during flood is driven by local erosion in the reach between RMs 1.4–4.2 and advection of the eroded sediment to RM 4.2.

The intra-tidal variability of SSC described above is indicative of the bed-water exchange dynamics, suggesting a small pool of easily-erodible sediment, termed the fluff layer, overlying less-erodible strata. The fluff layer is comprised of sediments deposited to the bed during slack water and resuspended during the following flood or ebb tide. The excess sediment (when deposition exceeds erosion), if any, in the fluff layer consolidates over time forming less-erodible strata. Additional lines of evidence that support the presence of the fluff layer are summarized in Appendix A. Similar sediment dynamics have also been observed in other tidal and estuarine systems (Maa *et al.* [24]; van Maren *et al.* [21]; van Kessel *et al.* [20]; El Ganaoui *et al.* [25]; Wang [26]; Bedford *et al.* [27]). Using the intra-tidal range in depth-average SSC of ~10 mg/L to ~75 mg/L within the salt wedge, with tidally-averaged water depth of 6 m, and assuming a dry density of 200 kg/m^3 (for the sediments comprising the fluff layer) results in an estimated fluff layer

thickness of about 2 mm. The sediment mass contained within this fluff layer is more or less in equilibrium with the sediments suspended in the water column every tidal cycle. Furthermore, the tidally-averaged SSC in Figure 2.2 also support observations of the relative importance of fluff layer dynamics for sediment transport in the LPR. The tidally-averaged SSC varies within a fairly narrow range during October and November (period with river flows less than about 60 m^3/s), mainly showing variability in response to the spring–neap cycle, and tending to higher values only at flows greater than about 60 m^3/s in December. This suggests that the bed-water exchange is dominated by fluff layer dynamics during river flows less than about 1.7 times the annual average flow, i.e., the majority of the time. Therefore, the erosion properties of the fluff layer are important for reproducing SSC dynamics and SS fluxes within the system over intra- and inter-tidal time-scales during typical tidal conditions and river flows up to about 1.7 times the annual average, i.e., the majority of the time.

The concept of a fluff layer has also been implemented in numerical sediment transport model applications, most notably by van Maren *et al.* [21] and van Kessel *et al.* [20]. However, some relevant information about the fluff layer such as its spatial distribution, composition, structure, and density are currently not well understood. Nonetheless, theoretical considerations as well as empirical evidence allow for some inference about these features. Review of longitudinal SSC profile surveys in the LPR, as well as SSC data from fixed moorings at RMs 1.4, 4.2, and 6.7, 10.2, and 13.5 (respectively located 10.8 km, 16.4 km, and 21.7 km from the mouth of the LPR; data not presented here) during typical tidal and low–average flow conditions suggests that fluff layer dynamics are most prominent down-estuary of the salt front and within the ETM. Although the SSC time-series shows some intra-tidal variability at locations up-estuary of the salt front and the ETM, the fluctuations are not similar in magnitude as locations further down-estuary. During such low–average river flow conditions, grain size distribution measurements on water samples show composition of nearly 100% fine sediments entering the study area. Therefore, the fluff layer may predominantly be comprised of fine sediments. Fine sediments in suspension, especially in estuarine settings, are expected to be flocculated, with a range of floc diameters and associated settling velocities (Winterwerp and van Kesteren [2]). As the flocs deposit to the bed, they form a space-filling network structure called a gel. The concentration at which this happens is called the gelling point; it is also known as the structural density (Winterwerp [28]). Based on analysis of unpublished data from a location in Newark Bay close to the mouth of the LPR, the gelling point is estimated to be in excess of 100 kg/m^3. This provides a conservative lower bound on the dry density of the fluff layer; an average dry density of 500 kg/m^3 measured over the top 15 cm of the sediment bed between RMs 1.4 and 4.2 provides a conservative upper bound. In summary, even though theoretical considerations and empirical evidence provide some information on the afore-mentioned properties of the fluff layer, these topics may require more elaborate studies. The remainder of the analysis presented in this chapter relates only to the erosion properties of the fluff layer.

2.3. MATERIALS

A number of datasets were used in the analysis presented in this chapter. The data include time-series of SSC, currents, salinity, and water depth measurements, as well

as direct measurements of surficial sediment erodibility using a Gust Microcosm. These data are described next.

2.3.1. SSC AND CURRENT DATA

THE SSC and current data presented in this chapter come from a moored deployment over a two-month period (October 10, 2009 to December 16, 2009) at several locations within the LPR. Figure 2.1 shows the locations of two such moorings relevant to this analysis, at RMs 1.4 and 4.2. The deployment included moored (1) Acoustic Doppler Current Profilers (ADCP), (2) Conductivity-Temperature-Depth (CTD) sensors, and (3) Optical Backscatter (OBS) sensors. The sensors performed in situ measurements at a relatively high frequency, every 12 minutes, compared to the tidal period of 12.42 h. The ADCPs were deployed in the bottom-mounted, upward-facing configuration and measured the depth-profile of flow velocity and echo intensity. The CTD and OBS sensors were deployed 0.9 m above the bed and 0.9 m below the water surface for measurements of surface and bottom salinity, temperature, and turbidity along with water depth. The data recorded by the moored instruments were periodically recovered (approximately 1-month intervals), and the instruments serviced and redeployed. In addition, water samples were regularly collected at the mooring locations and measured for SSC. These SSC measurements were used to relate the measured turbidity to SSC and acoustic backscatter (ABS; calculated from echo intensity following the methods of Deines [29] and Wall *et al.* [30]) to SSC. The resulting turbidity-SSC and ABS-SSC relationships were applied to the continuous time-series measurements of turbidity and ABS to estimate time-series of SSC at the mooring locations. The turbidity-SSC relationship followed a power-law form, with a relatively high $R^2 = 0.84$ (single relationship for all the LPR stations). The ABS-SSC relationships followed a logarithmic form, and were more variable, with $R^2 = 0.65$ and $R^2 = 0.87$ at RMs 1.4 and 4.2, respectively. As an additional check on data quality, the ABS-derived SSC time-series were also compared to the turbidity-derived SSC, with the comparison showing reasonably compatible estimates from both sensors. The analysis presented in this chapter relies on the ABS-estimated SSC time-series.

Since the ADCP sensors were mounted on a tripod placed on the sediment bed, a fraction of the water column near the bed was not measured by the ADCP profile measurements. Similarly, a fraction near the surface of the water column was not measured due to interference and binning artifacts. Both velocity and ABS-estimated SSC in these unmeasured depths were estimated by extrapolation. Velocity in the unmeasured near-surface zone was estimated by assuming that fluid shear stress decreases linearly from measured values to zero at the surface of the water column. Fluid shear stress is calculated as:

$$\tau = \mu \frac{\mathrm{d}u}{\mathrm{d}z} \tag{2.3}$$

where, τ = fluid shear stress, μ = dynamic viscosity of water, u = flow velocity, and z = vertical coordinate ($z = 0$ at bottom of water column). Velocity in the unmeasured near-bottom zone was estimated assuming a logarithmic profile:

$$u_z = \frac{u_*}{\kappa} \ln\left(\frac{z}{z_0}\right) \tag{2.4}$$

where, u_* = the bottom friction velocity, $\kappa = 0.4$ = the von Karman constant, and z_0 = bottom roughness length = 1 mm, taken from a previous hydrodynamic modeling study of the LPR (HydroQual [31]). SSC in the unmeasured near-bottom and near-surface zones was extrapolated assuming that the vertical SSC profile follows the Rouse distribution (van Rijn [32]):

$$\frac{c}{c_a} = \left[\frac{a\left(1-\frac{z}{h}\right)}{z\left(1-\frac{a}{h}\right)} \right]^{\beta} \tag{2.5}$$

where, c = SSC measured at level z, c_a = SSC at reference height a, h = total water depth, and β = the Rouse number. β was estimated by a least-squares fitting of the measured SSC profiles. It is also worth noting that other extrapolation methods were tested for both velocity and SSC. However, the overall results presented here did not change appreciably, suggesting that the results are relatively insensitive to the extrapolation technique.

Due to the tidal nature of the system, the measured velocity profiles include a variable number of constant thickness ADCP bins with velocity data over time. In order to assist with subsequent data analysis of the flow field, the velocity profiles were converted from this fixed coordinate system based on depth within the water column, to a sigma (σ) coordinate system. The latter coordinate system allows for velocity profiles with a constant number of layers but of variable thickness over time. The σ coordinate system is defined as:

$$\sigma = \frac{z-\eta}{H+\eta} \tag{2.6}$$

where, η = the instantaneous water level with respect to the reference height H. The instantaneous velocity profiles were interpolated to a 20-layer σ grid. This transformation of the velocity profile enables calculations described subsequently that involve the tidal-period averaging of currents in individual layers in the water column.

2.3.2. GUST MICROCOSM EROSION DATA

THE direct measurements of erosion properties presented in this chapter were performed by Chesapeake Biogeochemical Associates [33] using a Gust Microcosm (Gust and Mueller [17]) on undisturbed sediment cores collected from the LPR in May 2005, about 4 years before the mooring deployment described previously. The river flow averaged about 10 m^3/s during the period of core collection, similar to the river flow over the first 2 weeks of the deployment in Figure 2.2. During this period, the salt front (and therefore the ETM) is seen to be located up-estuary of RM 4.2 (as seen in the near-bottom salinity on panel b of Figure 2.2). Therefore, the salt front and ETM are estimated to have been located up-estuary of the core locations during the period when the cores were collected. Shallow cores (~10 cm) were collected from five locations (Stations 1, 3, 5, 6, and 9 as shown in Figure 2.1) located within 7 km from the mouth of the LPR. The cores were located in different parts of the river cross-section, with average water depths ranging from about 2 m to 8 m. Duplicate cores were collected at each location for an assessment of the variability in erodibility. With the exception of Station 5, which was collected about 2 h after slack water, the remainder of the cores were collected around slack water when the fluff layer would be expected to be at its maximum thickness. The cores were

collected using either a piston push corer (at the shallow locations) or by subsampling from a small box corer (at the deeper locations). Each core was extruded until the sediment surface was 10 cm from the top of the core tube and was then carefully transported by boat to the testing facility located nearby. The erosion measurements were conducted within a few hours of core collection to minimize core disturbance and consolidation.

The cores were subject to erosion measurements using a Gust Microcosm apparatus (Gust and Mueller [17]). The Gust Microcosm apparatus utilized by Chesapeake Biogeochemical Associates [33] simultaneously measured the erodibility of the duplicate cores collected at each station. The experimental setup consisted of two core tubes, with a rotating disc within each core tube, and a layer of continually-refreshed water separating the discs from the sediment-water interface. The rotation speed of the disc was controlled to impose varying shear stresses, with a suction pipe located at the center of the disc to extract the water containing eroded sediments and for minimizing secondary currents. The shear stresses generated by the rotating disc was calibrated in the laboratory using hot-film sensors. The experiment consisted of seven 20 minute intervals, with increasing shear stress (0.01, 0.05, 0.1, 0.15, 0.2, 0.3, and 0.45 Pa). The effluent of the system, containing the eroded sediment, was passed through a turbidimeter and collected. The collected effluent water samples were filtered and weighed to determine the exact sediment mass eroded during each step as well as a calibration for the turbidimeter for each step. The calibrated turbidimeter data provides a time-series of SSC for each step. The sediment erosion rate was subsequently calculated as the product of the pumping rate and SSC. Further to the discussion above, it is noted that the applied shear stresses are expected to be too low to erode consolidated sediments. The Gust Microcosm is therefore considered to measure the erodibility of the fluff layer.

2.4. METHODS

2.4.1. ENTRAINMENT FLUX

THE analysis for the erosion properties of the fluff layer derives from the following observations of the SSC time-series measurements. Figure 2.3 shows a two-day snapshot of the flow at Dundee Dam and the tide at RM 1.4, the depth-average velocity at RMs 1.4 and 4.2, the depth-average SSC at RMs 1.4 and 4.2, and the vertical distribution of SSC at RM 4.2. This period is associated with below-average river flows and typical tidal conditions, i.e. not affected by offshore set-up or set-down events, both of which can alter the shear stress regime in the estuary. The shaded area indicates the duration of the flood tide (four flood tides during this two-day period). Due to flood-dominance in tidal currents (and therefore higher range of velocities during flood than on ebb), this analysis is restricted to SSC measured during the flood tide.

The SSC time-series shows the cyclic behavior and correlation with velocity described earlier, with concentration increasing as velocity increases and decreasing as velocity decreases. Comparison of the depth-average SSC at RMs 1.4 and 4.2 also shows that concentrations at both locations attain approximately similar values during slack water. For instance, during the first low-water slack period on October 19, SSC at both locations is about 10 mg/L. During the following flood tide, concentrations increase at both locations, to ~50 mg/L at RM 1.4, and about twice as high (~100 mg/L) at RM 4.2. During this

time period, the salt front and therefore the ETM are located up-estuary of RM 4.2 (at least 4 km up-estuary of RM 4.2, based on other data not shown here), thereby ruling out the possibility that the additional SSC during the flood tide at RM 4.2 could reflect the up-estuary transport of the ETM. The location of the ETM up-estuary of RM 4.2, and the similarity of the slack-water concentrations at RMs 1.4 and 4.2 during this period leads to the consideration that slack-water concentrations in the entire reach between RM 1.4–4.2 may be similar to the ~10 mg/L values measured at RM 1.4 and RM 4.2. With this assumption, the increase in SSC measured at RM 4.2 during the following flood tide, can only be associated with erosion down-estuary of RM 4.2. Restricted to the duration of accelerating flood velocities, which is also associated with increasing SSC, this increase in SSC at RM 4.2 thus represents gross erosion rather than net erosion (defined as the sum of gross erosion and gross deposition) between RM 1.4–4.2.

The relationship between the flow velocity and SSC can also be seen more clearly in Figure 2.4 which includes pairs of the depth-average SSC and velocity at RMs 1.4 and 4.2 during the flood tides between October 11–24, 2009 and November 22–27, 2009 (note that these periods cover a full spring–neap cycle). The sediment dynamics during these periods are not affected by (1) presence of the ETM, or (2) above-average river flows, or (3) offshore set-up/set-down events. The latter two conditions are expected to be associated with above-average flow-velocities and shear stresses, whereas considering only periods when the ETM is known to be located up-estuary of RM 4.2 ensures consistency with the Gust Microcosm erosion measurements since those were performed on sediment cores collected from locations down-estuary of the ETM. The data in Figure 2.4 are divided by the phase of flood currents (accelerating versus decelerating velocity). On average, the SSC data are seen to follow a predictable pattern. Starting from low-water, as flood velocities increase (the right hand side of both panels), on average, SSC increases, reflecting erosion from the fluff layer. Following peak velocity, as flood velocity decreases (the left hand side of both panels), on average, SSC decreases, reflecting deposition and thereby reestablishing the fluff layer. The fact that SSC scales as a function of velocity also indicates that the SSC signal reflects erosion from and deposition to the bed within the tidal cycle. Since erosion and deposition during such typical tidal and low–average flow conditions are expected to be dominated by the fluff layer dynamics, this increase in SSC during the accelerating phase of the flood currents is analyzed for an assessment of the erosion properties of the fluff layer. However, since this analysis uses an indirect measurement (SSC) rather than a direct measurement of erosion, the results are presented in terms of the entrainment process rather than erosion. Accordingly, the term entrainment flux is used rather than erosion rate.

Figure 2.5 shows an idealized conceptualization of the velocity and SSC fluctuations over the tidal cycle (in panels b and c, respectively) in a Eulerian frame of reference, similar to Figure 2.3. Low water (T_0) coincides with slack water (V_0) and also minimum SSC over the tidal cycle (C_0) at RMs 1.4 and 4.2. As the tide starts flooding, flow velocity increases to V_1 and subsequently V_2 at time T_1 and T_2, respectively; simultaneously, SSC increases to C_1 and subsequently C_2. This conceptualization is also depicted in panel d of Figure 2.5 in a Lagrangian frame of reference. Consider three fluid parcels at slack tide (T_0), located at x (RM 4.2), and at x' and x'', some distance down-estuary of RM 4.2. Note that x' and x'' are not fixed in time but a function of the time-variable currents. At

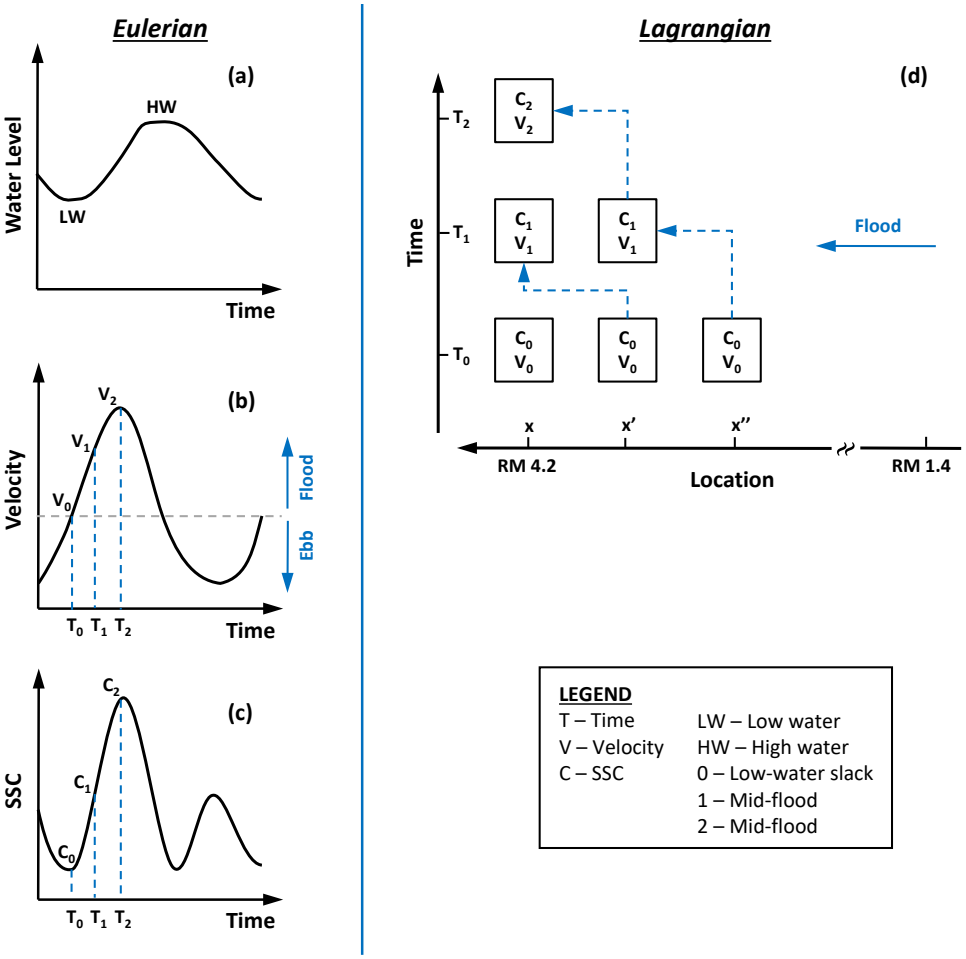

Figure 2.5: Idealized conceptualization of velocity and SSC fluctuations, and schematization of the entrainment process over the flood tide in the LPR. In Eulerian frame of reference (a, b, and c), and in Lagrangian frame of reference (d).

T_0, concentrations in the reach between RM 1.4–4.2 are assumed to be uniform (C_0). As the tide starts flooding, at T_1, the first fluid parcel is transported up-estuary of RM 4.2, and the second fluid parcel moves from x' to x (RM 4.2) influenced by some erosion and entrainment over distance x'–x and attaining concentration C_1. At the same time, the third fluid parcel moves from x'' to x' and is also assumed to attain concentration C_1 due to erosion and entrainment over distance x''–x'. At T_2, the third fluid parcel is transported up to x, associated with concentration C_2 reflecting the effect of some erosion and entrainment in the time interval from T_1 to T_2 and over distance x'–x. Therefore,

the time-derivative of the depth-average SSC at RM 4.2, adjusted for the water depth, is the entrainment flux experienced by given fluid parcel over distance x'–x:

$$E' = \frac{\mathrm{d}(\bar{c}h)}{\mathrm{d}t} \tag{2.7}$$

where, E' = entrainment flux (kg/m^2/s), $\bar{c}$ = depth-average SSC (kg/m^3), t = time (s), and h = instantaneous water depth (m). Note that E' has the same units as the erosion rate E in Eq. 2.1. The time-interval associated with the application of Eq. 2.7 derives from the frequency of SSC time-series data (every 12 minutes). As mentioned previously, review of the SSC time-series relative to the velocity and salinity time-series suggests that the increase in SSC at RM 4.2 is locally-driven, i.e., due to erosion between RMs 1.4 and 4.2. Therefore, it is hypothesized that E' is a function of the shear stress experienced by given fluid parcel during transit from x' to x, i.e., the spatial-average Lagrangian shear stress. The entrainment flux is therefore paired with the Lagrangian shear stress and examined for this hypothesis.

The entrainment flux calculation was applied to the time-series of SSC measured at RM 4.2 over the same period used for Figure 2.4, subject to a few restrictions. The first restriction derives from one of the assumptions of the entrainment flux method that the minimum SSC attained around low-water slack is relatively uniform in the reach between RM 1.4 and RM 4.2. Since the SSC field down-estuary of RM 1.4 is unknown, this assumption implies the need to restrict the entrainment flux analysis to data reflective of erosion only between RMs 1.4–4.2, i.e., avoiding data that may reflect SSC dynamics originating from down-estuary of RM 1.4. Another restriction derives from subtle phase differences between the velocity and SSC time-series as seen in Figure 2.3. Moving from low-water slack to flood, SSC is typically seen to decline for some time even as flood velocity increases, reaching a minimum some time following initiation of flood currents. For the examples in Figure 2.3, this lag is seen to be about 1–2 h; this phenomenon is well known in the literature and is referred to as scour lag (Postma [34]; Dronkers [35]). Subsequently, as flood velocity increases, SSC increases and reaches a maximum after maximum flood velocities are attained. Therefore, the entrainment flux calculation is performed over the duration of minimum to maximum SSC during the flood tide at RM 4.2, a period on the order of 1–2 h per tidal cycle. These considerations, along with the need to pair the entrainment flux over a given time interval with the spatial-average Lagrangian velocity and shear stress over that time interval (defined as the spatially averaged velocity and shear stress experienced by given fluid parcel over that time interval), necessitates the use of a numerical model to provide a high spatial- and temporal-resolution description of currents in the reach between RMs 1.4 and 4.2 as described in the next section.

2.4.2. NUMERICAL MODEL

THE temporally- and spatially-variable description of currents in the reach between RMs 4.2 and 1.4 was developed using the velocity and water depth measurements to solve the continuity equation for flow rate at a high spatial and temporal resolution. The 1D continuity equation for unsteady open-channel flow is written as:

$$\frac{dQ}{dx} = -\frac{dA}{dt} \tag{2.8}$$

where, Q = flow rate, x = longitudinal coordinate (along flow direction), and A = cross-sectional area.

The availability of high-frequency current measurements at RMs 1.4 and 4.2 paired with water levels, provides the information necessary to solve Eq. 2.8) at intermediate locations. Limited shipboard instantaneous cross-sectional measurements (not included here) do not suggest significant cross-sectional variations in velocity. Therefore, the calculations were performed for cross-section averaged conditions. Similarly, the calculations were performed using the depth-averaged velocities, with the velocity component due to estuarine circulation zeroed out as a consequence of depth-averaging. However, as mentioned subsequently, the estuarine circulation component is included in the post-processing of the results. It should also be noted that although the term 1DH model is used subsequently to describe this application of the 1D continuity equation, this is only a direct solution of the continuity equation for flow — given the inflow rate and the change in storage within given reach, the outflow rate from the reach and flow rate at intermediate locations within the reach are solved by numerically integrating Eq. 2.8 over the reach.

The model application consisted of a series of evenly-spaced cross-sections (approximately every 50 m) to represent the reach between RMs 1.4 and 4.2. The bathymetry associated with each cross-section was based on a multi-beam bathymetric survey performed in November 2008. The bathymetry data were also used to determine the variation in submerged cross-sectional area (and volume) associated with tidal water level variations for each cross-section. The model takes as a boundary condition the depth-average currents measured at RM 1.4 (on flood), and RM 4.2 (on ebb). However, the results are only considered for the period of flood currents which is the period of interest for the entrainment flux analysis described previously. In addition, the variation in water levels measured at RMs 1.4 and 4.2 were also specified as boundary conditions, with the water levels at intermediate locations assumed to vary linearly as a function of distance. Using these inputs and boundary conditions, the model calculates time-series of the depth-averaged and cross-section averaged flow rates (and therefore velocities) at intermediate locations using Eq. 2.8.

The model performance was evaluated by comparison with measured velocities at RM 4.2, as shown in panel a of Figure 2.6 for the depth-average velocities, and in panel b of Figure 2.6 for the near-bottom velocities, both for the periods of flood currents. The near-bottom velocity at RM 4.2 was calculated from the depth-average velocity in the model following Eq. 2.4. However, the measured near-bottom velocity includes a component due to estuarine circulation (the other components being tidal exchange and river flow; the component due to Stokes drift is zero in this case because the tide behaves as a standing wave in the LPR). In contrast, the model computations only reflect components due to tidal and river flows as mentioned previously. Therefore, the estuarine circulation component was estimated from the data and added to the model computed near-bottom velocity for an appropriate comparison with data. The estuarine circulation component was estimated using the method of tidal averaging (Costa [36]; Siegle

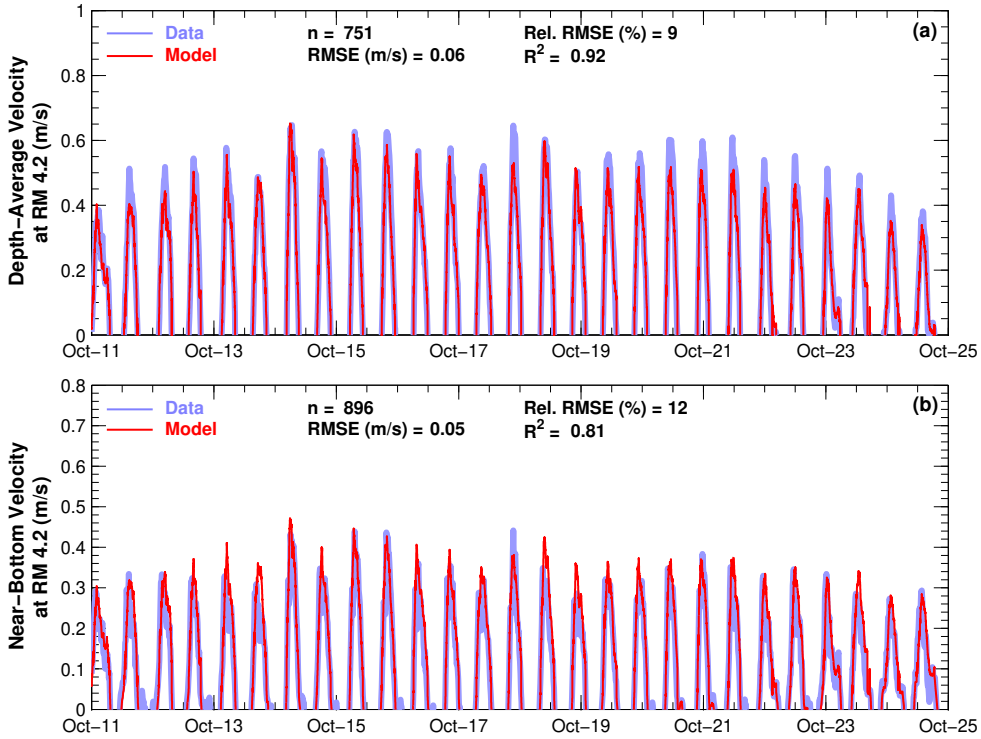

Figure 2.6: Comparison of measured and model-calculated (a) depth-average flood velocity, and (b) near-bottom flood velocity at RM 4.2.

et al. [37]; Sommerfield and Wong [38]):

$$u_{z,E} = \frac{1}{2T\Delta z}\int_0^{2T}\left[u_z\Delta z - \frac{\Delta z}{h}\int_0^h u_z \mathrm{d}z\right]\mathrm{d}t \tag{2.9}$$

where, $u_{z,E}$ = velocity component associated with estuarine circulation at depth z, T = tidal period (in practice, due to the inequality in the semi-diurnal tides, the tide-averaging was performed over two tidal cycles), Δz = the instantaneous thickness of σ layer at depth z, and u_z = measured instantaneous velocity at depth z. The near-bottom estuarine circulation velocity component (directed up-estuary) thus estimated at RM 4.2 using Eq. 2.9 averaged about 0.04 m/s during October 11–24, 2009, and about 0.07 m/s during November 22–27, 2009. Similar calculations performed following methods involving signal processing techniques used by others (Lerczak *et al.* [39]; Chant *et al.* [23]) yielded similar results for the estuarine circulation velocity component.

Both the comparisons seen in Figure 2.6 suggest a reasonably good performance by the model. A few statistical metrics quantifying the model-data comparisons are also included in Figure 2.6. These include the root mean square error (RMSE), a measure of the error between the model and data as expressed by:

$$RMSE = \sqrt{\frac{\sum (u_{Data} - u_{Model})^2}{n}} \tag{2.10}$$

where, u_{Data} = measured velocity, u_{Model} = model-calculated velocity, and n = number of pairs of model and data. Another metric quantifying the model-data performance is the relative RMSE (%), defined as the RMSE relative to the data range. The data range is the difference between the minimum and maximum of the measured values. Finally, the correlation coefficient, R^2, between model and data is also included.

Although the model captures the temporal variability and magnitude of the depth-average velocity several times during this period, it tends to under-predict the peak velocities during other periods. However, the depth-average velocities calculated by the model are of secondary importance; it is mainly used for the travel time and distance calculations associated with estimating the average Lagrangian near-bottom velocities. In this regard, the near-bottom velocities calculated by the model (and adjusted to include the estuarine circulation component), are more relevant and compare quite well with measured values as seen in panel b of Figure 2.6, with both temporal variability and magnitude well reproduced by the model. The statistical assessment of model performance shows reasonable performance — the relative RMSE is 9% and 12% for depth-average and near-bottom velocity, respectively. Similarly, the correlation coefficient is also relatively robust, at 0.92 and 0.81 for depth-average and near-bottom velocity, respectively. Both the relative RMSE and correlation coefficient are within the bounds of acceptability for such numerical models (Meselhe and Rodrigue [40]). These statistical metrics comparing the model and data, therefore, provide confidence in the performance of the model at RM 4.2 and by extension its ability to reproduce currents in the reach between RM 1.4 and 4.2.

Following standard assumptions for hydrodynamic interactions at the bottom boundary, the effective bottom roughness used in Eq. 2.4 is assumed to be composed of form-related and grain-related fractions (van Rijn [41]). The grain-related roughness, calculated as a function of the surficial sediment texture, is considered to generate the skin friction forces relevant to the sediment dynamics of erosion and deposition. Therefore, the calculated near-bottom velocity was used to calculate skin friction as:

$$\tau_{SF} = \rho \left[\frac{u_b \kappa}{\ln\left(\frac{z_b}{z_{0G}}\right)} \right]^2 \tag{2.11}$$

where, τ_{SF} = skin friction, ρ = density of water, u_b = near-bottom velocity calculated by the 1DH model and adjusted to include the estuarine circulation component, z_b = distance to the mid-point of the bottom-most σ layer, and z_{0G} = grain roughness height, calculated as:

$$z_{0G} = \frac{k_s}{30} = \frac{3D_{90}}{30} \tag{2.12}$$

where, k_s = Nikuradse grain roughness (van Rijn [41]), D_{90} = particle diameter representing the 90% cumulative percentile of the sediment grain size distribution, calculated as 140 μm using grain size distribution measurements in the sediment bed in the reach

between RMs 1.4 and 4.2. The resulting spatial and temporal distributions of depth-average velocity and skin friction were used to calculate the average Lagrangian shear stress to pair with entrainment flux values over the same period.

2.4.3. ASSUMPTIONS OF ENTRAINMENT FLUX METHOD

THE calculation of the entrainment flux and the pairing with Lagrangian velocities and shear stresses involve a few assumptions and simplifications as listed below:

- The minimum SSC observed around low-water slack is uniform in the reach between RM 1.4-4.2.
- The horizontal dispersion of the SSC field is ignored.
- The horizontal shearing of the SSC profile due to flow components associated with estuarine circulation, river flow, and tidal shear is ignored.
- The increase in SSC at RM 4.2 over given duration is associated solely with resuspension over the travel path of that fluid parcel over that duration.
- The effect of local velocity gradients on erosion and deposition between RM 1.4-4.2 is not considered. Locally, there may exist areas of higher velocity where larger or more resistant particles may be eroded which may be deposited a short distance away in an area of lower velocity, both within the period of accelerating flood currents and SSC.
- During periods of accelerating flood currents and SSC, gross erosion is the same as net erosion (e.g. we ignore deposition).
- No significant cross-sectional variations exist in currents or SSC.

In addition, the analysis does not distinguish between the various modes of erosion. However, the shear stress regime involved is expected to be characteristic of floc and surface erosion.

2.4.4. GUST MICROCOSM EROSION DATA

THE data from the Gust Microcosm experiments consists of time-series of erosion rate and imposed shear stress. The data was analyzed by Chesapeake Biogeochemical Associates [33] using the erosion formulation of Sanford and Maa [16]. This formulation assumes an exponentially decreasing erosion rate for each shear stress level:

$$E_t = E_0 e^{-\lambda t} \tag{2.13}$$

Based on this assumption, the erosion rate time-series was extrapolated to determine the total erodible mass for each applied shear stress level. Using the applied shear stress (τ_b) and total erodible mass, a profile of critical shear stress for erosion was generated. From this profile, the excess shear stress ($\tau_b - \tau_{Cr}$) at the beginning of the step was determined. The initial erosion rate for each step was then divided by the excess shear stress to calculate the erosion rate coefficient, M:

$$M = \frac{E_0}{\tau_b - \tau_{Cr}} \tag{2.14}$$

The results of the data analysis include the eroded mass (which is a measure of the depth of erosion), critical shear stress for erosion, and erosion rate coefficient for the various shear stress levels for each core.

2.5. RESULTS

THE results of the Gust Microcosm experiments are presented first followed by the entrainment fluxes assessed with the 1DH model and a discussion of the comparison between the two methodologies.

2.5.1. GUST MICROCOSM EROSION DATA

FIGURE 2.7 shows the measured depth profile of the critical shear stress for erosion from the Gust Microcosm experiments. Each panel includes results for the duplicate cores at each location. The measurements of cumulative eroded mass for each core were converted to an equivalent depth in the bed assuming a dry density of 200 kg/m^3. Note that the exact value assumed for dry density is of secondary importance, it is only used here to transform the results of the erosion experiments, in units of eroded mass per unit area, into depth in the bed which is only used as a more intuitive parameter in the explanation of the erosion results. The resulting depth-interval sampled by the Gust Microcosm is seen to range only up to a few millimeters indicating the shallow pool of sediments eroded during the experiments. The main feature apparent in the data is an order of magnitude increase in the strength of the bed, or the critical shear stress for

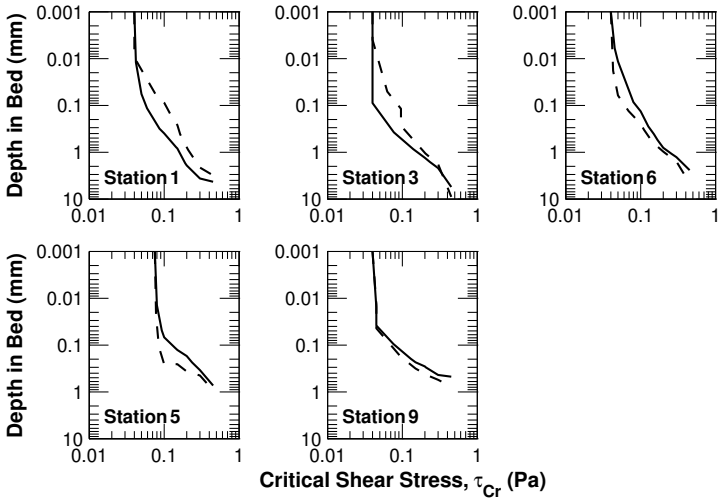

Figure 2.7: Depth-profile of measured critical shear stress for erosion from the Gust Microcosm experiments. Solid and dashed lines indicate data for the duplicate cores at each station.

erosion, within the top 1–2 mm of the cores. The critical shear stress increases from 0.04 Pa at the surface of the cores (except station 5, at 0.075 Pa) up to 0.4 Pa within the top 2 mm of the cores. In the case of stations 5 and 9, the critical shear stress reaches 0.4 Pa at depths <1 mm. These critical shear stresses are also within the range of shear stresses experienced in the LPR under typical tidal conditions (this is discussed in more detail in the next section), indicating that this shallow pool of sediments within the top 1–2 mm of the bed is available for resuspension under typical tidal conditions.

This pattern of a rapid increase in the near-surface strength of the bed and the comparability of critical shear stresses in this near-surface depth-interval and the typical tidal shear stresses in the LPR is supportive of the notion of a fluff layer, where the limited residence time and lack of consolidation limit the development of significant bed strength. This depth-interval (top 1–2 mm) with a rapid increase in measured bed strength also compares well with the thickness of the fluff layer in the LPR presented in Section 2.2, estimated as 2 mm. This has implications for the development of numerical sediment transport models for estuaries, where typically the hydrograph (on an annual basis) may be dominated by long periods of low–average river flows during which the sediment dynamics are dominated by fluff layer dynamics. During the remainder of the year, the hydrograph may be dominated by high-flow events, resulting in higher shear stresses than usual, as a result of which the bed strata underlying the fluff layer could be exposed and subject to erosion. Therefore, for numerical modeling studies of the long-term sediment transport dynamics in estuaries, it is important to appropriately parameterize the erosion properties of the fluff layer (as well as the underlying, more resistant layers).

Figure 2.8 shows the depth profile of the erosion rate coefficient M (see Eq. 2.14) from the Gust Microcosm experiments examined in a similar fashion as the critical shear

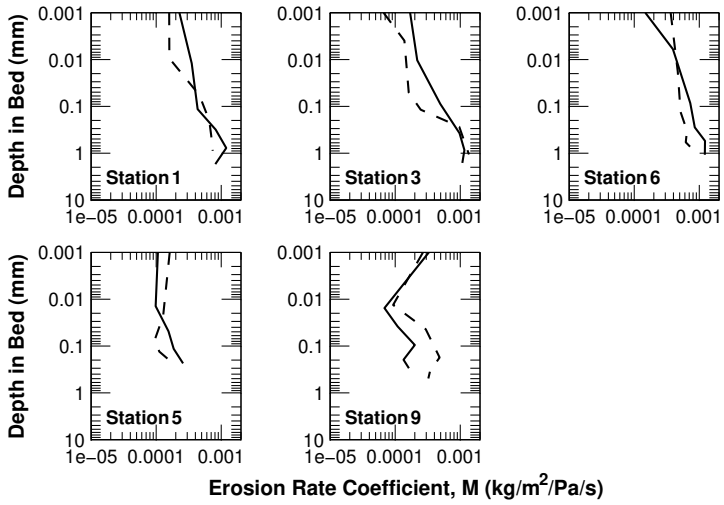

Figure 2.8: Depth-profile of measured erosion rate coefficient from the Gust Microcosm experiments. Solid and dashed lines indicate duplicate cores at each station.

stress for erosion. Although several cores tend to show an increase in the value of M with depth in the bed, others show a variable trend with depth. Both the critical shear stresses as well as the erosion rate coefficients are compared with the results of the entrainment flux analysis in the following section.

2.5.2. ENTRAINMENT FLUX ANALYSIS AND VALIDATION WITH GUST MICROCOSM EROSION DATA

FIGURE 2.9 shows the calculated entrainment flux plotted as a function of the average Lagrangian velocity and the average Lagrangian shear stress, both calculated using the results of the 1DH model. The range of skin-friction related shear stresses (<0.425 Pa) in the LPR is seen to be comparable to the range of shear stresses tested in the Gust Microcosm experiments (0.01 Pa to 0.45 Pa), indicating that the laboratory measurements and the field data provide results over comparable shear stress regimes. Therefore, the erosion process (floc erosion and surface erosion) and resulting parameter estimates from the two methods should also be expected to be comparable.

Since the entrainment flux is calculated from high-frequency SSC measurements, they are susceptible to variability in the SSC time-series. The variability in SSC may be real or may also be an artifact of the uncertainty in the ABS-SSC relationship used to derive the SSC time-series. This variability manifests itself in the entrainment flux data included in Figure 2.9 (as seen in the more than an order of magnitude range in entrainment flux seen at the lower shear stresses), as well as in negative entrainment flux (when SSC at given instant is lower than the SSC at preceding time record). The latter data (instances of negative entrainment flux) is not included here and comprised about 20% of the dataset. The former manifestation of variability is seen to be more prominent at the lower shear stresses (and lower SSC occurring after slack water) than at higher shear stresses typically during mid-tide. Nonetheless, the overall trend is a positive relationship between the entrainment flux and the velocity/shear stress. The issue of variability

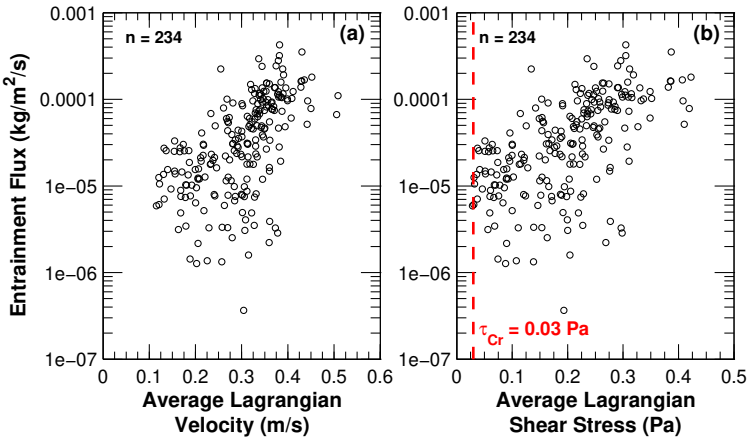

Figure 2.9: Calculated entrainment flux relative to the Lagrangian (a) near-bottom velocity, and (b) shear stress.

in entrainment flux and therefore uncertainty in the dependency with shear stress is examined in further detail subsequently.

One important erosion property apparent from Figure 2.9 is the threshold for initiation of motion or the critical shear stress for erosion; entrainment is noted to occur only at shear stresses greater than 0.03 Pa, which indicates the critical shear stress for the fluff layer. This can be compared to the direct measurements presented in Figure 2.7, which show near-surface critical shear stresses starting at 0.04 Pa and increasing by an order of magnitude within the top 1–2 mm of the bed. Although the entrainment flux analysis does not provide information on the profile of the critical shear stress with depth, the estimated value for critical shear stress of 0.03 Pa (which would be expected to correspond to the surficial bed strata) is within a factor of two of the surficial critical shear stresses (0.04 Pa) measured in the Gust Microcosm experiments. Besides deviations arising from any mismatch between actual currents (and shear stress) and that predicted by the numerical model, the model results of shear stress in particular are also sensitive to other factors such as the parameterization of the Nikuradse roughness height used to compute skin friction. Furthermore, even direct measurements of the critical shear stress for erosion using different erosion devices do not result in identical parameter values. For instance, Tolhurst *et al.* [42] compared measurements of the critical shear stress for erosion of surficial sediments in the Humber estuary (UK) using a Gust Microcosm and three other laboratory devices for measuring sediment erodibility. The reported values of the critical shear stress for erosion using the various methods varied by a factor of two. This implies some uncertainty in the results of Gust Microcosm experiments in the LPR as well. The difference of 0.01 Pa between the estimates from the Gust Microcosm experiments and the entrainment flux analysis is also relatively small (2.5%) compared to the full range of shear stresses under typical tidal and low–average river flow conditions (up to 0.4 Pa as seen in Figure 2.9). Therefore, the results of the entrainment flux method and the Gust Microcosm in the LPR are considered comparable for the critical shear stress for erosion of the surficial sediments. This value for the critical shear stress is also comparable to measurements for the fluff layer at other sites (0.05 Pa reported by Wang [26]; 0.025–0.05 Pa reported by El Ganaoui *et al.* [25]; 0.05 Pa reported by Maa *et al.* [24]; <0.015 Pa for surficial sediments reported by Sanford and Maa [16]; 0.016 Pa reported by Sanford *et al.* [12]).

Another trend apparent in Figure 2.9 is a relationship between the entrainment flux and the average Lagrangian velocity and shear stress. The individual data points for entrainment flux are somewhat variable, probably reflecting several factors such as natural variability in SSC, uncertainties due to the fact that the SSC time-series are based on indirect measurements using ABS and converted to SSC using a regression of ABS and SSC with its accompanying variability, uncertainties due to lack of information on the exact temporal and spatial distribution of velocity and shear stress between RMs 1.4 and 4.2, etc. However, on average, the data suggest a dependency of entrainment flux with velocity and shear stress, with entrainment flux increasing with increasing velocity and shear stress. Functionally, the trend is similar to the relationship inferred from the erosion rate experiments by Partheniades [3] and Partheniades [4], and used to formulate Eq. 2.1 by Kandiah [9] and Ariathurai and Arulanandan [10]. Therefore, the entrainment flux data is binned in increments of 0.02 Pa to quantify its relationship with shear stress.

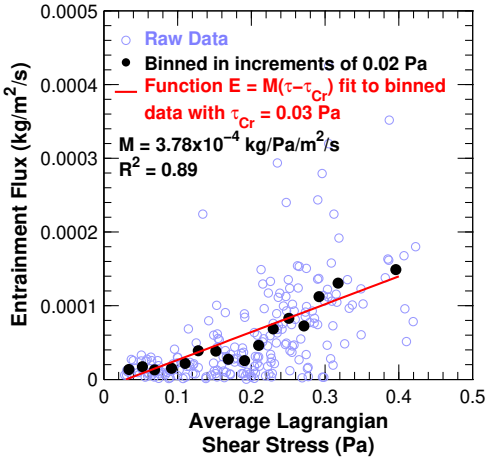

Figure 2.10: Entrainment flux as a function of the shear stress.

Figure 2.10 shows the individual entrainment flux data illustrated in panel b of Figure 2.9, along with the mean entrainment flux for each of the shear stress bins. The binned entrainment fluxes range over an order of magnitude, from ~1×10^{-5} to ~1.5×10^{-4} kg/m^2/s over the entire range of typical tidal shear stresses. These values, which reflect the erosion rate of the fluff layer, are more or less comparable to values reported by others (constant 5×10^{-6} kg/m^2/s reported by Wang [26] and 1×10^{-8} – 6×10^{-5} kg/m^2/s reported by El Ganaoui *et al.* [25], both over the same shear stress range; up to 2×10^{-5} kg/m^2/s reported by Bedford *et al.* [27] over shear stresses up to 0.2 Pa). The binned entrainment fluxes are also a function of the Lagrangian shear stress, thus verifying the hypothesis formulated in Section 2.4.1. The binned entrainment fluxes tend to asymptote to an entrainment flux of about 1.5×10^{-5} kg/m^2/s at shear stress less than 0.1 Pa, a trend similar to what has been attributed to floc erosion by Partheniades [3] and Partheniades [4]. However, since the formulation of the entrainment flux method does not permit distinction between floc erosion and surface erosion, and in the interest of comparing the results of the entrainment flux method to the measurements from the Gust Microcosm, no distinction is made between floc erosion and surface erosion.

Working under the assumption that the entrainment flux during the period of accelerating flood currents is an approximation of the gross erosion rate, a linear relationship (also shown in Figure 2.10) is developed using the binned entrainment fluxes and following Eq. 2.1 but without the normalization by τ_{Cr}, and assuming τ_{Cr} = 0.03 Pa. The slope of this relationship (= 3.78×10^{-4} kg/Pa/m^2/s) is comparable to the erosion rate coefficient M presented in Figure 2.8 based on the Gust Microcosm experiments. The value of M inferred from the entrainment flux analysis can also be compared against the values measured in the Gust Microcosm experiments as a validation of the entrainment flux analysis for inferring the erosion properties of surficial sediments. This comparison is shown in Figure 2.11 as a probability distribution of measured values for the individual shear stress levels by core (blue squares), and the average erosion rate coefficient by

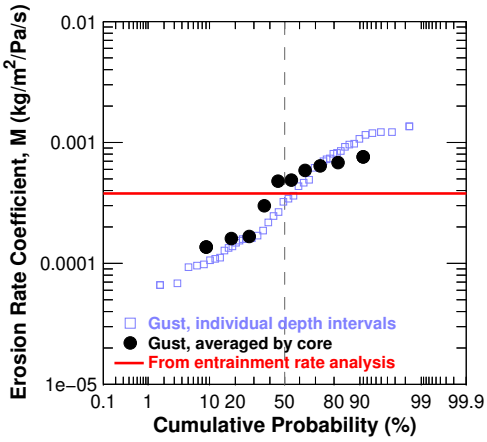

Figure 2.11: Probabilistic comparisons of the erosion rate coefficient, M, estimated by the entrainment flux analysis (solid horizontal line), and that measured in the Gust Microcosm experiments (squares and circles).

core (black circles) against the erosion rate coefficient estimated from the entrainment flux analysis (horizontal red line). The value of M inferred from the entrainment flux analysis is similar to the median of the measured values, a reasonable finding since the entrainment flux analysis provides a measure of the spatially integrated erosion properties in the river, whereas the individual cores would be expected to be more variable in response to features such as the shear stress regime at the core locations (which affects the type of particles expected to be present in the bed), shear stress history, location in the cross-section which affects the type and magnitude of sediment supply, etc. The erosion rate coefficient estimated from the entrainment flux analysis is also within the overall range of values reported by others for surficial sediment strata (5×10^{-5} – 1.6×10^{-4} kg/Pa/m^2/s reported by El Ganaoui *et al.* [25]; 2×10^{-3} – 9×10^{-3} kg/Pa/m^2/s reported by Sanford and Maa [16]; 8.8×10^{-5} kg/Pa/m^2/s reported by Sanford *et al.* [12]).

2.5.3. EROSION PARAMETERS FROM ENTRAINMENT FLUX ANALYSIS — VARIABILITY AND UNCERTAINTY

A statistical analysis was performed to examine the impact of the variability inherent in the entrainment flux data on the resulting erosion properties. Similar approaches have been proposed for assessing the effect of data outliers on regression model parameters (Tsao and Ling [43]). Briefly, the procedure consists of sub-sampling the entrainment flux dataset (pairs of entrainment flux and shear stress) iteratively, fitting the linear erosion function to each of the sub-sampled datasets, and then assessing the variability in the erosion parameters calculated for the sub-sampled datasets. The overall entrainment flux dataset shown in Figure 2.9 and Figure 2.10 consists of data from October 11–24 and November 22–27, 2009. This period covers a full spring–neap cycle and comprises 36 separate flood tides. The data were first segregated into low, medium, and high tidal range datasets, with twelve tides in each group. The sub-sampling was performed by randomly selecting three separate tides from each of these tidal range groups (to char-

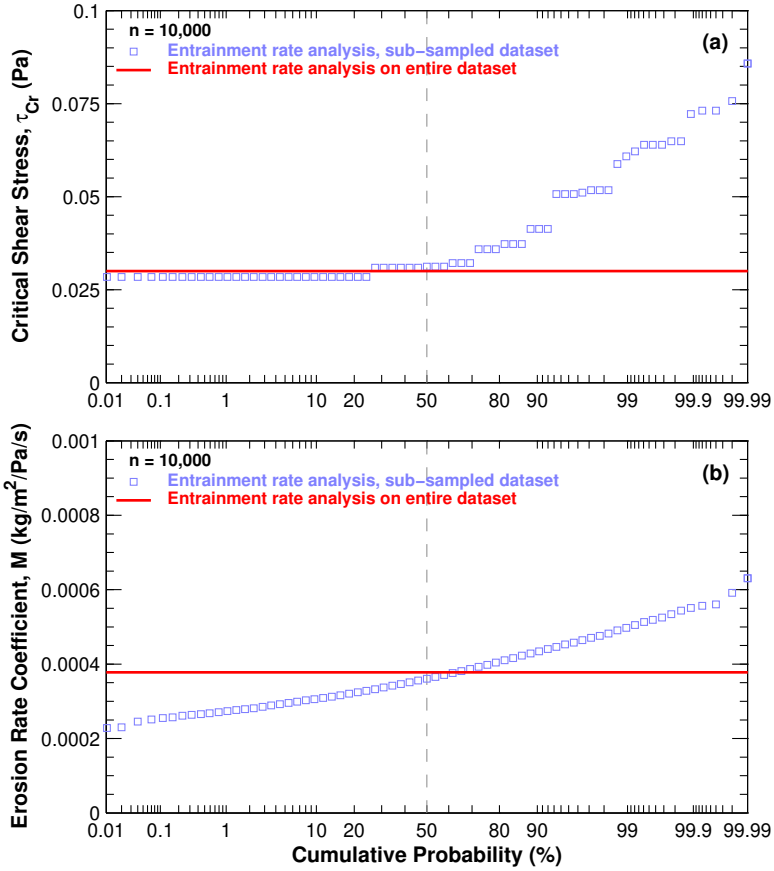

Figure 2.12: Probabilistic comparisons of parameter estimates from entrainment flux analysis on the entire dataset (solid horizontal line) against population estimates from sub-sampling the entrainment flux dataset (squares). Comparisons of the critical shear stress for erosion (a), and the erosion rate coefficient (b).

acterize the full range of shear stresses over the spring–neap cycle), for a total of nine tides per sub-sample. The critical shear stress for erosion was defined as the minimum shear stress within each sub-sampled dataset, and a linear erosion function developed for each sub-sample following the procedure described previously in association with Figure 2.10.

The sub-sampling and parameter estimation procedure was implemented a large number of times ($n = 10,000$) to estimate the variability in erosion parameters. Figure 2.12 shows the results of this exercise. The individual values of the erosion rate coefficient and the critical shear stress for erosion calculated for the sub-sampled data are shown as a cumulative probability distribution (squares). The parameter estimates developed from the entire dataset (in Figures 2.9 and 2.10) are included with a horizontal red line. The parameter estimates for both the erosion rate coefficient and the critical shear stress for erosion from the entire dataset are seen to be very similar to the median

value from the sub-sampled data. Furthermore, about 70% of the time, the sub-sampled data indicate a critical shear stress for erosion about the same as estimated from the entire dataset (0.03 Pa). Similarly, the entire range of values for the erosion rate coefficient in the sub-sampled data is within a factor of two of the value estimated from the entire dataset. Even though the individual measurements of entrainment flux shown in Figure 2.9 tend to be variable by an order of magnitude or more, this does not translate to similar variability in the erosion parameter estimates. The erosion rate coefficient varies by only about a factor of three from the lower to upper end of the distribution based on sub-sampled data. Similarly, the distribution of the critical shear stress for erosion in the sub-sampled data tends to be relatively constant over the vast majority of the data, deviating from 0.03 Pa appreciably (by more than 50%) only within the upper 10^{th} percentile. The sub-sampling of the overall dataset allows for an assessment of the potential variability in the estimates of the erosion rate coefficient and the critical shear stress for erosion. These comparisons suggest that although the entrainment flux data from individual tidal cycles may be somewhat variable, when aggregated over several tidal cycles, the entrainment flux method tends to produce erosion parameter estimates that are relatively robust.

2.6. DISCUSSION

ESTUARINE sediment transport dynamics reflect a balance between tidal and fluvial transport processes. Tidal processes result in SSC dynamics that follow the tidal currents, often with erosion and deposition over tidal time-scales, resulting in the creation (by deposition) and destruction (by erosion) of a thin layer of easily erodible sediments termed the fluff layer overlying more consolidated and less erodible strata. During episodic high river flow periods, the SSC dynamics are altered such that fluvial processes become more relevant due to the higher flow velocities and shear stresses generated under such conditions. During such conditions, the fluff layer dynamics become of secondary importance, and the less erodible strata underlying the fluff layer may be exposed, and become more relevant for sediment dynamics. These flow-dependent dynamics are apparent in the tidally-averaged SSC time-series described previously in association with Figure 2.2.

In a system such as the LPR, where the hydrograph is dominated by long periods of below-average flows interrupted by episodic above-average periods, the SSC dynamics can be said to be dominated by tidal processes the majority of the time. Therefore, the erosion properties of the fluff layer are of primary importance in reproducing the SSC dynamics the majority of the time and particularly relevant for the up-estuary transport of fine sediments during typical tidal conditions by estuarine circulation and tidal asymmetries. In addition to the SSC fluctuations, the fluff layer dynamics also influence the phenomenon of ETM formation, as well as the patterns of deposition during such periods. Three approaches that have been reported in the literature for parameterizing the erosion properties of the fluff layer include, (1) direct measurements using an apparatus such as the Gust Microcosm, Sea Carousel, etc. (Gust and Mueller [17]; Parchure and Mehta [14]; Amos *et al.* [15]; Maa *et al.* [19], (2) model calibration to SSC measurements (van Kessel *et al.* [20]; van Maren *et al.* [21]), and (3) using field measurements (Wang [26]; Sanford *et al.* [12]; deVries [44]). The entrainment flux method is an additional

approach using field measurements that can serve as a useful alternative in situations where direct measurements of erosion may be difficult or cost-prohibitive. For instance, even though the Gust Microcosm experiments can be performed ex situ, the experimental apparatus still needs to be set up on site in order to minimize transport of the sediment cores and the potential for disturbance of the cores during transit. Furthermore, given the extremely low shear stresses and depth intervals involved in the erosion of the fluff layer, the erosion of the fluff layer is somewhat difficult to measure. Alternatively, the entrainment flux method can also serve to reduce the number of model calibration parameters in cases where the erosion properties of the fluff layer are aimed to be determined by calibration of a numerical model. Such calibration exercises typically involve a large number of iterative simulations to optimize the calibration parameters (the critical shear stress for erosion and the erosion rate coefficient for the fluff layer).

The entrainment flux method derives from certain systematic patterns in the SSC signal in relation to the tidal currents. As described in connection with Figure 2.3, the increase in SSC during flood is restricted to about 1–2 h (the erosion is preceded by a duration of ~1 h associated with scour lag). This duration of ~1–2 h with increasing SSC (from minimum to maximum SSC within the tidal cycle) typically extends from somewhat low velocities following slack-water to past peak flood velocities. In other words, SSC scales as a function of the tidal velocity. This is a signal consistent with erosion and entrainment from the fluff layer rather than the advection of a SSC plume from elsewhere within the estuary. Subsequently, SSC decreases due to deposition. The increase in SSC during this period of up to ~1–2 h can be used to calculate the entrainment flux, which is a function of the shear stress regime and can be used to infer the erosion properties of the fluff layer. These inferred erosion properties are comparable to direct measurements using the Gust Microcosm apparatus. The similarity of the results of the Gust Microcosm experiments and the results of the entrainment flux analysis is an important finding because the former is based on direct measurements of erosion properties, whereas the latter is inferred from indirect measurements of SSC. This provides a validation of the method and the results of the entrainment flux analysis. This is the more remarkable because the two datasets were collected more than four years apart, with several major storm events associated with significant river flows in the intervening period which would be expected to alter the sediment dynamics in the river, albeit over short-term time-scales. The fact that erosion properties inferred from the analysis of measured SSC time-series are consistent with the Gust Microcosm data also suggests that the direct measurements of erosion parameters are consistent with the SS dynamics in the LPR under low–average flow and typical tidal conditions. This comparison also implies that the fluff layer maintains its erosion properties over long periods of time despite the fact that the fluff layer is reformed every tidal cycle, i.e., is continually renewed. This implies that the erosion properties of the fluff layer are an inherent physical property of the system, and a constant feature at least over the four-year time-period examined here. This validation also suggests that the results of the entrainment flux analysis can be used to infer the average erosion properties of surficial sediment strata in such systems characterized by regular, periodic fluctuations in SSC.

Similar procedures to infer erosion properties from indirect measurements, i.e., SSC time-series have been applied by others (Sanford *et al.* [12]; deVries [44]). However, these

studies were limited in scope, with data from a limited number of tidal cycles, and using the local shear stress rather than the Lagrangian shear stress. The analysis presented here uses data over a larger period of time, and covers the full range of spring to neap shear stresses expected in the estuary during typical tidal and flow conditions. In addition, the comparison with the results of the Gust Microcosm experiments provides a validation of the entrainment flux method for inferring the erosion properties of the fluff layer. However, unlike the Gust Microcosm experiments, the entrainment flux method does not provide information on the depth-profile of the critical shear stress for erosion. As seen in Figure 2.7, the critical shear stress for erosion may increase by nearly an order of magnitude within the top few millimeters of the sediment bed, a depth interval that corresponds to the thickness of the fluff layer. However, typical state of practice numerical sediment transport model applications do not resolve the vertical structure in the bed at such a high resolution; the typical resolution in the bed is on the order of millimeters to centimeters, with a unique value for the critical shear stress for erosion associated with a given bed layer. From this perspective, it is more important to resolve the overall depth-profile of the critical shear stress at length scales relevant to the numerical model. The results of the entrainment flux method provides a starting point to parameterize the critical shear stress of the fluff layer within the numerical model. Empirical methods such as Sedflume (McNeil *et al.* [18]) or based on soil mechanical properties (Winterwerp *et al.* [7]) can be used to determine the critical shear stress of the more consolidated bed underneath the fluff layer.

The validation of the entrainment flux method also suggests that this method can be used for inferring the erosion properties of similar systems elsewhere. The main advantages of this method are that it is relatively easy and straightforward to implement, and it makes use of SSC time-series that may be collected and required for purposes such as model calibration, or developing a data-based understanding of the sediment dynamics in given system. However, the SSC data needs to be carefully reviewed and screened in order to select an appropriate dataset for analysis. Since the entrainment flux method is constructed to infer the erosion properties of the fluff layer, which is the layer responsible for the bed-water exchange dynamics under typical tidal and low–average riverflow conditions, the SSC time-series should be screened to filter out periods of elevated river flows, or off-shore set-up and set-down events, all of which can result in elevated SSC as a consequence of above-average shear stresses and therefore erosion potentially extending to sediment strata below the fluff layer. Finally, given the inherent variability associated with such observations in natural systems, an appropriately large dataset (e.g. data from several tides rather than a single tide) should be considered for a truly representative estimate of the erosion properties of the fluff layer.

2.7. CONCLUSIONS

AN alternate approach, referred to as the entrainment flux method, for quantifying the erodibility of fine sediments from the surficial sediment strata in a small estuary was formulated and applied. The results of this method are analogous to the erosion rate data used to fit the well-known and widely applied standard linear erosion formulation. The method helps to infer the critical shear stress for erosion and the erosion rate coefficient of the surficial sediment strata, both of which are important inputs in

the application of numerical sediment transport models in estuaries and tidal systems. The erosion properties inferred from this approach are also compared to direct measurements of erodibility using the Gust Microcosm apparatus. The favorable comparison of the two methods suggests that the entrainment flux method can be used to infer and quantify the erodibility of the surficial sediment strata in such systems. The entrainment flux method has certain advantages, chiefly its ease of implementation and the fact that it uses SSC time-series which would typically be expected to be available for the study of or for the model application at a given site. Guidelines for selecting the appropriate dataset for the application of the method are also developed. The expected applications of this method are in relatively narrow estuaries without significant lateral (across the cross-section) variations in currents or SSC, unless if suitable information on lateral variability is available.

REFERENCES

[1] A. J. Mehta, *Characterization of Cohesive Soil Bed Surface Erosion, With Special Reference to the Relationship between Erosion Shear Strength and Bed Density* (UFL/COEL/MP-91/4, Univ. of Florida, Gainesville, FL, 1991).

[2] J. C. Winterwerp and W. G. M. van Kesteren, *Introduction to the Physics of Cohesive Sediments in the Marine Environment, Vol. 56* (Elsevier, New York, 2004).

[3] E. Partheniades, *A Study of Erosion and Deposition of Cohesive Soils in Salt Water*, PhD dissertation, Univ. of Calif., Berkeley (1962).

[4] E. Partheniades, *Erosion and deposition of cohesive soils,* J Hydraul Div-ASCE **91**, 105 (1965).

[5] E. Partheniades, *Cohesive Sediments in Open Channels: Properties, Transport, and Applications* (Elsevier, New York, 2010).

[6] I. Piedra-Cueva and M. Mory, *Erosion of a deposited layer of cohesive sediment,* in *Proceed Marine Sci*, Vol. 3, edited by W. H. McAnally and A. J. Mehta (Elsevier, 2000) pp. 41–51.

[7] J. C. Winterwerp, W. G. M. van Kesteren, B. van Prooijen, and W. Jacobs, *A conceptual framework for shear flow-induced erosion of soft cohesive sediment beds,* J Geophys Res **117**, C10020 (2012).

[8] B. C. van Prooijen and J. C. Winterwerp, *A stochastic formulation for erosion of cohesive sediments,* J Geophys Res **115**, C01005 (2010).

[9] A. Kandiah, *Fundamental Aspects of Surface Erosion of Cohesive Soils*, PhD dissertation, Univ. of Calif., Davis (1974).

[10] C. R. Ariathurai and K. Arulanandan, *Erosion rates of cohesive soils,* J Hydraul Div-ASCE **104**, 279 (1978).

[11] L. P. Sanford and J. P. Halka, *Assessing the paradigm of mutually exclusive erosion and deposition of mud, with examples from Upper Chesapeake Bay,* Mar Geol **114**, 37 (1993).

[12] L. P. Sanford, W. Panageotou, and J. P. Halka, *Tidal resuspension of sediments in Northern Chesapeake Bay,* Mar Geol **97**, 87 (1991).

[13] A. J. Mehta and E. Partheniades, *Resuspension of deposited cohesive sediment beds,* in *18th International Conference on Coastal Engineering* (Coastal Engineering Research Council, Cape Town, South Africa, 1982).

[14] T. M. Parchure and A. J. Mehta, *Erosion of soft cohesive sediment deposits,* J Hydraul Eng-ASCE **111**, 1308 (1985).

[15] C. L. Amos, G. R. Daborn, H. A. Christian, A. Atkinson, and A. Robertson, *In situ erosion measurements on fine-grained sediments from the Bay of Fundy,* Mar Geol **108**, 175 (1992).

[16] L. P. Sanford and J. P. Y. Maa, *A unified erosion formulation for fine sediments,* Mar Geol **179**, 9 (2001).

[17] G. Gust and V. Mueller, *Interfacial hydrodynamics and entrainment functions of currently used erosion devices,* in *Cohesive Sediments*, edited by N. Burt, W. R. Parker, and J. Watts (John Wiley and Sons, New York, 1997) pp. 149–174.

[18] J. McNeil, C. Taylor, and W. Lick, *Measurements of erosion of undisturbed bottom sediments with depth,* J Hydraul Eng-ASCE **122**, 316 (1996).

[19] J. P. Y. Maa, L. D. Wright, C. H. Lee, and T. W. Shannon, *VIMS Sea Carousel: A field instrument for studying sediment transport,* Mar Geol **115**, 271 (1993).

[20] T. van Kessel, J. C. Winterwerp, B. van Prooijen, M. van Ledden, and W. Borst, *Modeling the seasonal dynamics of SPM with a simple algorithm for the buffering of fines in a sandy seabed,* Cont Shelf Res **31**, 124 (2011).

[21] D. S. van Maren, T. van Kessel, K. Cronin, and L. Sittoni, *The impact of channel deepening and dredging on estuarine sediment concentration,* Cont Shelf Res **95**, 1 (2015).

[22] K. R. Dyer, *Estuaries: A Physical Introduction*, 2nd ed. (John Wiley and Sons, New York, 1997).

[23] R. J. Chant, D. Fugate, and E. Garvey, *The shaping of an estuarine Superfund site: Roles of evolving dynamics and geomorphology,* Estuar Coast **34**, 90 (2011).

[24] J. P. Y. Maa, L. Sanford, and J. P. Halka, *Sediment resuspension characteristics in Baltimore Harbor, Maryland,* Mar Geol **146**, 137 (1998).

[25] O. El Ganaoui, E. Schaaff, P. Boyer, M. Amielh, F. Anselmetc, and C. Grenz, *The deposition and erosion of cohesive sediments determined by a multi-class model,* Estuar Coast Shelf S **60**, 457 (2004).

[26] Y. H. Wang, *The intertidal erosion rate of cohesive sediment: A case study from Long Island Sound,* Estuar Coast Shelf S , 56 (2003).

[27] K. W. Bedford, W. Onyx, C. M. Libicki, and R. Van Evra, *Sediment entrainment and deposition measurements in Long Island Sound,* J Hydraul Eng **113**, 1325 (1987).

[28] J. C. Winterwerp, *On the flocculation and settling velocity of estuarine mud,* Cont. Shelf Res **22**, 1339 (2002).

[29] K. L. Deines, *Backscatter estimation using broadband acoustic doppler current profilers,* in *Oceans 99 MTS/IEEE Conference Proceedings* (Seattle, WA, 1999).

[30] G. R. Wall, E. A. Nystrom, and S. Litten, *Use of an ADCP to Compute Suspended-Sediment Discharge in the Tidal Hudson River, New York* (USGS SIR 2006-5055, 2006).

[31] HydroQual, *Final Hydrodynamic Modeling Report: Lower Passaic River Restoration Project and Newark Bay Study* (Mahwah, NJ, 2008).

[32] L. C. van Rijn, *Sediment transport part II: Suspended load transport,* J Hydraul Eng-ASCE **110**, 1613 (1984).

[33] Chesapeake Biogeochemical Associates, *Passaic River Erosion Testing and Core Collection: Field Report and Data Summary* (2006).

[34] H. Postma, *Transport and accumulation of suspended matter in the Dutch Wadden Sea,* Neth. J. Sea Res **1**, 148 (1961).

[35] J. Dronkers, *Tide-induced residual transport of fine sediment,* in *Proceedings of the Symposium on the Physics of Shallow Bays and Estuaries, Miami 1984* (Springer-Verlag, 1985).

[36] R. G. Costa, *Flow-fine sediment hysteresis in sediment-stratified coastal waters,* (MS Thesis, University of Florida, Gainesville, 1989).

[37] E. Siegle, C. A. F. Schettini, A. H. F. Klein, and E. E. Toldo, *Hydrodynamics and suspended sediment transport in the Camboriu estuary Brazil: Pre jetty conditions,* Braz J Oceanogr **57**, 123 (2009).

[38] C. K. Sommerfield and K. C. Wong, *Mechanisms of sediment flux and turbidity maintenance in the Delaware estuary,* J Geophys Res **116**, C01005 (2011).

[39] J. A. Lerczak, W. R. Geyer, and R. J. Chant, *Mechanisms driving the time-dependent salt flux in a partially stratified estuary,* J Phys Oceanogr **36**, 2283 (2006).

[40] E. A. Meselhe and M. D. Rodrigue, *Mississippi River Hydrodynamics and Delta Management Study (MRHDM): Models Performance Assessment Metrics and Uncertainty Analysis* (Baton Rouge, LA, 2013).

[41] L. C. van Rijn, *Principles of Sediment Transport in Rivers, Estuaries, and Coastal Seas* (Aqua Publications, Emmeloord, The Netherlands, 1993).

[42] T. J. Tolhurst, K. S. Black, D. M. Paterson, H. J. Mitchener, G. R. Termaat, and S. A. Shayler, *A comparison and measurement standardisation of four in situ devices for determining the erosion shear stress of intertidal sediments,* Cont Shelf Res **20**, 1397 (2000).

[43] M. Tsao and X. Ling, *Subsampling method for robust estimation of regression models,* Open J Stat **2**, 281 (2012).

[44] J. W. deVries, *Field measurements of the erosion of cohesive sediments,* J Coast Res **8**, 312 (1992).

3

SEDIMENT DYNAMICS AND TRANSPORT REGIMES

Estuarine sediment dynamics are a consequence of various forcings (barotropic, estuarine circulation, and fluvial) that vary in space and time. Here we present a study examining sediment dynamics in a narrow microtidal estuary, the Lower Passaic River in New Jersey, USA. The analysis incorporates measurements of suspended sediments, morphological change, sediment erodibility, and a numerical hydrodynamic model. The former two datasets are used to develop an understanding of sediment dynamics over the full range of hydrologic conditions, and the latter two datasets are used to interpret the behavior of the system. Subsequently, a conceptual picture is developed, one that classifies the morphological status of the system at any given time into three regimes dependent on river flow — Regime I includes conditions when the system is importing sediments, Regime II includes conditions when the system is exporting sediments by flushing a thin easily erodible surficial stratum termed the fluff layer, and Regime III includes conditions when the system is exporting sediments by scouring more consolidated strata underneath the fluff layer. Regime III is relevant for the long-term morphodynamic equilibrium of the estuary by providing a mechanism that erodes and exports sediment accumulated under Regime I conditions. Consequently, sediment dynamics depend not only on short timescale processes such as the instantaneous river flow-rate, but also on the time-history of river flow, and the long-term morphological progression of the system. These regimes represent a conceptualization of estuarine sediment transport dynamics and can be useful in the development of effective estuarine sediment management strategies.

This chapter has been published in the journal Ocean Dynamics:
R. Mathew and J. C. Winterwerp, *Sediment dynamics and transport regimes in a narrow microtidal estuary,* Ocean Dynam **70**, 435–462 (2020)

3.1. INTRODUCTION

ESTUARINE sediment dynamics are a consequence of the advective and dispersive transport of suspended sediment originating from freshwater and marine sources, and the bed-water exchange processes of erosion and deposition. These sediment fate and transport processes are a function of the hydrodynamic forcings involved, and the local bathymetry. The primary hydrodynamic forcings typically include barotropic circulation induced by the tide, estuarine circulation, and river flow, i.e., freshwater inflow from the head-of-tide (Dyer [1]). Additional, primarily episodic, forcings that can influence sediment dynamics include barotropic circulation induced by coastal setup and setdown, wind-induced circulation and mixing, local wind-waves, and ocean waves (Dyer [1]). The latter three are mainly relevant for relatively wide estuaries, estuaries subject to the propagation of ocean waves, and/or estuaries with large tidal shallows. Since the estuary reported upon in this chapter is relatively narrow (i.e., fetch-limited for wind-waves), and is not directly influenced by ocean waves, the impacts of winds and waves are not examined further in this chapter. Given their relevance to the analyses in this chapter, the impact of the primary forcings (barotropic, estuarine, riverine) on sediment dynamics are briefly summarized first followed by a discussion of the present research.

3.1.1. BAROTROPIC EFFECTS

NON-LINEAR tidal distortion in shallow water (Dronkers and Schönfeld [2]; Friedrichs and Aubrey [3]) and the spatially-variable and oscillatory nature of estuarine tidal currents give rise to several residual sediment transport mechanisms, grouped into what is referred to as tidal asymmetries and lag effects, respectively. Dronkers [4] and Gatto *et al.* [5] provide a detailed review of the various transport mechanisms summarized here. These transport mechanisms, as described below with respect to their impact on residual sediment transport, assume that suspended sediment concentrations (SSC) scale over tidal time-scales.

The impact of tidal distortion on sediment transport is apparent in a Eulerian frame of reference and is driven by asymmetries in peak currents and in slack-water duration. Residual (fine) sediment transport follows the asymmetry in peak currents, with flood-dominant systems (peak flood currents greater than peak ebb currents) exhibiting net up-estuary transport and vice versa for ebb-dominant systems (Dronkers [6]; van de Kreeke and Robaczewska [7]). Slack-water asymmetry originates from differences in the deceleration and acceleration of currents in the transition from flood to ebb and vice versa. Residual sediment transport follows the asymmetry in slack water duration, with longer slack water duration at the end of flood than ebb associated with net up-estuary transport, and vice versa for longer slack water duration at the end of ebb than flood. In addition to asymmetries generated by tidal distortion, the interaction between certain principal astronomic tidal constituents can also lead to the development of tidal asymmetries and residual sediment transport (Hoitink *et al.* [8]). Lag effects are conceptualized in a Lagrangian frame of reference and refer to residual sediment transport induced by the oscillatory and spatially variable nature of tidal currents in combination with certain sediment transport parameters, namely the critical shear stress for erosion, τ_{Cr}, and a corresponding threshold for deposition (Postma [9], Postma [10], van Straaten

and Kuenen [11] and van Straaten and Kuenen [12]). Lag effects can further be categorized into settling lag and scour lag; both generally promote up-estuary residual transport. In addition to the periodic barotropic circulation induced by the tide, episodic subtidal variations in sea-level (induced by coastal setup and setdown) also result in volume fluxes into and out of estuaries (Salas-Monreal and Valle-Levinson [13]). However, the importance of such events on sediment transport dynamics is not straight-forward, depending on the interaction of these events with the other forcings. The use of the term barotropic in the remainder of this chapter is limited to only the tide.

The barotropic effects on sediment dynamics are also collectively referred to as tidal pumping in the literature (Geyer *et al.* [14]; Scully and Friedrichs [15]; Sommerfield and Wong [16]). Tidal pumping has been shown by these authors to be a significant mechanism responsible for the up-estuary transport of sediments. Tidal pumping has also been shown to be dependent on river flow and the spring–neap cycle. Tidal pumping can influence the formation of estuarine turbidity maxima (ETM), a zone of elevated SSC and enhanced sediment trapping, in the tidal freshwater regions of an estuary due to the convergence of up-estuary barotropic transport and down-estuary fluvial transport (Burchard *et al.* [17]).

3.1.2. ESTUARINE CIRCULATION

ESTUARINE circulation includes several processes such as baroclinic (gravitational) circulation, shear induced by river flow, lateral and longitudinal advection, eddy viscosity-shear covariance, etc. (Dijkstra *et al.* [18]) resulting in residual near-bottom currents directed up-estuary and near-surface currents directed down-estuary. In combination with a vertical gradient in SSC (typically increasing from surface to bottom of water column), estuarine circulation induces an up-estuary flux of sediment that extends up to the limit of salinity intrusion and resulting in the formation of ETMs co-located with the salt front (Festa and Hansen [19]; Burchard and Baumert [20]; Sanford *et al.* [21]; Burchard *et al.* [17]).

3.1.3. FLUVIAL EFFECTS

IN addition to delivering sediment to the estuary, freshwater inflow varying seasonally or episodically in response to rainfall runoff events can impact sediment dynamics within the estuary by pushing the salt-front seaward, enhancing bed shear stress, and potentially causing erosion and export of sediments from the estuary (Ralston *et al.* [22]). In addition, the direction of residual sediment transport can depend on river flow, with net up-estuary flux of sediments during low-flow conditions and net down-estuary flux during high-flow conditions (Geyer *et al.* [14]). The additional freshwater flow during runoff events can also impact tidal asymmetries by altering the relative magnitudes of net ebb and flood currents (Winterwerp *et al.* [23]; Guo *et al.* [24]).

3.1.4. PRESENT RESEARCH

THE gross sediment dynamics described above have been assessed both numerically (Gatto *et al.* [5]; Guo *et al.* [24]), and using empirical data from estuaries such as the Hudson River (Geyer *et al.* [14]), Lower Passaic River (Chant *et al.* [25]), Huangmaohai Estuary (Gong *et al.* [26]), Delaware River (McSweeney *et al.* [27]), and Wairoa River

(Pritchard and Green [28]). These studies have focused on the role of barotropic and estuarine circulation in promoting up-estuary residual sediment transport, and on the role of river flow in promoting down-estuary residual sediment transport. As such, sediment dynamics in these estuaries have been classified into an importing and an exporting regime. In some cases, the exporting regime is described as primarily a flushing event where sediments trapped within the ETM zone are exported during the above-average river flows associated with the spring freshet (Pritchard and Green [28], and Geyer *et al.* [14]). Less studied is the impact of extreme or relatively infrequent river flow events on estuarine sediment dynamics and morphological evolution. For instance, in the Hudson River estuary, Geyer *et al.* [14] hypothesize the occurrence of major erosion events occurring at roughly decadal time-scales. Similarly, a model application by Ralston *et al.* [22] calculated significant erosion within the lower Hudson River estuary during an extreme event. Nonetheless, empirical evidence and understanding of sediment dynamics during extreme events is incomplete and is a subject of ongoing research (Ouillon [29]).

Here we present an analysis of sediment dynamics in a short, narrow, microtidal estuary over short-term and long-term time-scales. The key objectives of our study are to assess estuarine suspended sediment dynamics over the full range of hydrologic conditions including extreme river flow events and to relate suspended sediment dynamics to the response of the bed in the particular estuary that is the focus of the analyses presented herein. The findings from this study are subsequently examined in the context of the long-term morphological evolution of estuaries. Furthermore, reliance on any single empirical line-of-evidence in developing a conceptual picture of sediment dynamics in such systems may lead to a biased result due to factors such as limited availability of measurements, episodic variations in the behavior of the system, etc. Therefore, a secondary objective of our study was to use a multiple lines-of-evidence approach including five separate and independent metrics in order to account for the limitations and uncertainties inherent in any single line of evidence. The analysis involves (1) measurements of residual sediment transport from a moored deployment over a range of river flows, (2) along-channel water column measurements over a range of river flows, (3) measurements of morphological change over the full range of river flows, (4) measurements of sediment erodibility, and (5) the results of a numerical hydrodynamic model. The mooring data are first used to assess sediment dynamics and relevant forcings during a limited range of river flows. The conclusions inferred from the analysis of the mooring data are compared against the along-channel water column measurements and measurements of morphological change for an assessment of sediment dynamics during a larger range of river flows including extreme events. The sediment dynamics are interpreted with the aid of a numerical hydrodynamic model and related to measurements of sediment erodibility for an assessment of bed dynamics driving sediment transport. Finally, the results are synthesized into a conceptual picture of sediment dynamics in the estuary. The following sections provide an overview of the study area, the data used, the analytical procedures involved, followed by a discussion of the results.

3.2. SITE OVERVIEW

THE data presented in this chapter come from the Lower Passaic River (LPR), a tidal estuary that is part of New York Harbor (Figure 3.1). The LPR stretches approximately

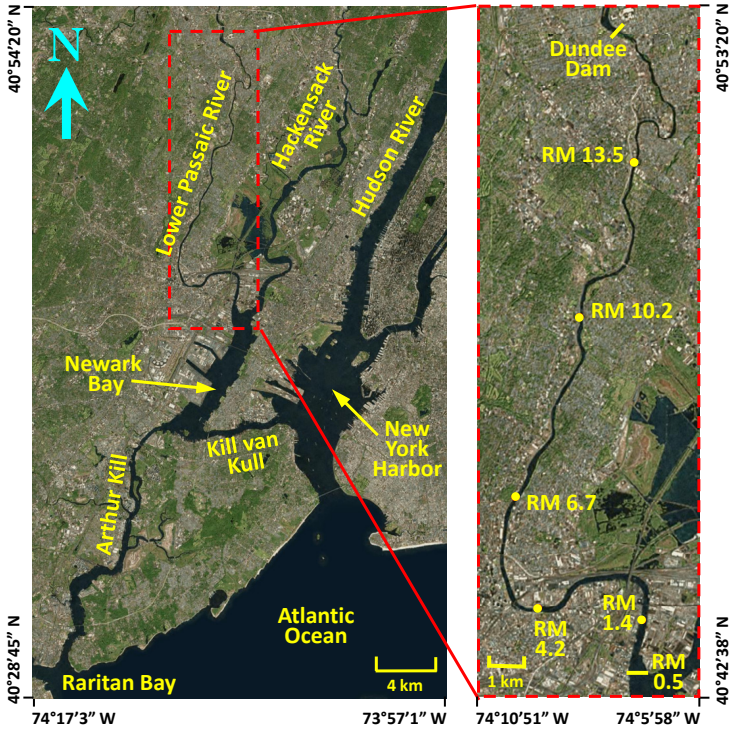

Figure 3.1: Location map of the Lower Passaic River along with the locations of the in situ moorings.

28 km long from its mouth in Newark Bay at approximately River Mile (RM) 0.5, to the head-of-tide at Dundee Dam (approximately RM 17.5). Newark Bay is connected to New York Harbor and Raritan Bay (and the Atlantic Ocean) via the tidal inlets Kill van Kull and Arthur Kill, respectively. The width of the LPR ranges from approximately 600 m at its mouth, declining to about 200 m at RM 1.4, 150 m at RM 4.2, 120 m at RM 6.7, 90 m at RM 10.2, and 75 m at RM 13.5, i.e. locations about 2.25 km, 6.75 km, 10.75 km, 16.5 km, and 21.75 km, respectively, from the mouth of the river and relevant to the analyses presented here. Typical water depths along the thalweg in the LPR currently range between 5 m to 7 m (with respect to mean sea level) and up to 17 m in the navigation channels in Newark Bay and Kill van Kull (Chant *et al.* [25]; Sommerfield and Chant [30]). The LPR is characterized by the remnants of a former navigation channel that was last dredged several decades ago and is no longer actively maintained at design depths (which ranged from about 10 m near the mouth of the river to about 4 m in the upper reaches; Chant *et al.* [25]). The LPR has relatively few sub-tidal shallows or tidal wetlands, features that have a bearing on the hydrodynamics of the system. The sediment substrate in the LPR is comprised of predominantly fine sediments (particle diameters less than 63 µm; Moffatt and Nichol and Deltares [31]). Therefore, the sediment dynamics presented here relate primarily to fine sediments. The LPR is the subject of ongoing environmental cleanup

and restoration studies; the data presented here were collected as part of this process.

The hydrodynamic forcings within the LPR include the tides, estuarine circulation, and river flow. Semi-diurnal tides (period of 12.42 h, corresponding to the dominant semi-diurnal M_2 constituent) entering Newark Bay through the Kill van Kull and Arthur Kill propagate to the LPR and the head-of-tide at Dundee Dam, forming an almost standing wave, with maximum currents typically occurring around mid-tide (Mathew and Winterwerp [32]). The tidal range varies from 0.9 m to 2.1 m from neap to spring; the corresponding flow rates due to barotropic circulation (estimated from current measurements at RM 1.4) range approximately 150 m^3/s to 300 m^3/s (averaged over the half tidal cycle). In comparison, the annual average river flow over Dundee Dam is only about 34 m^3/s (a few minor tributaries contribute approximately an additional 15% freshwater). Based on an extensive dataset of measurements, Chant *et al.* [25] found salinity intrusion within the LPR during periods of low–average river flow (resulting in a partially-mixed water column), with the saline water flushed out of the LPR during periods of high river flows. The extent of salinity intrusion, as indicated by the location of the salt front, is a function of the tidal phase, river flow, spring–neap cycle, as well as offshore mean water level fluctuations. Chant *et al.* [25] also show an ETM co-located with the salt front, with its location and average SSC a function of the river flow.

3.3. MATERIALS AND METHODS

SEVERAL lines of evidence are presented in this chapter. These include (1) fixed mooring measurements of SSC, currents, salinity, and water depth, (2) along-channel shipboard measurements of SSC, salinity, and water depth, (3) multi-beam bathymetry data, (4) measurements of sediment erodibility, and (5) a numerical hydrodynamic model. These data sources are described next followed by a discussion of the analytical methods used in this chapter.

3.3.1. WATER COLUMN: MOORING DATA

THE mooring data presented in this chapter was collected during a period of several months (October 10, 2009 to December 16, 2009, and March 22, 2010 to July 24, 2010) at several locations within the LPR (shown in Figure 3.1). The mooring locations span a range of salinity regimes during this period, ranging from freshwater tidal at RM 13.5, mostly freshwater tidal at RM 10.2, alternating freshwater and brackish at RM 6.7, and mostly brackish at RM 1.4 (with the exception of two days in the 2010 deployment when the salt front was located further seaward). The deployment also spanned a range of river flows, from below-average flows of about 5 m^3/s to above-average flows up to 280 m^3/s.

The deployment included moored (1) Acoustic Doppler Current Profilers (ADCP), (2) Conductivity-Temperature-Depth (CTD) sensors, and (3) Optical Backscatter (OBS) sensors performing in situ measurements every 12 minutes. The ADCPs were deployed in the bottom-mounted, upward-facing configuration and measured the depth-profile of flow velocity and echo intensity. The CTD and OBS sensors were deployed floating 0.9 m below the water surface and fixed 0.9 m above the bed for measurements of surface and bottom salinity, temperature, water depth, and turbidity. Water samples were reg-

ularly collected at the mooring locations and measured for SSC and related to turbidity measured by OBS, and to acoustic back-scatter (ABS; calculated from echo intensity following the methods of Deines [33], and Wall *et al.* [34]). The resulting turbidity-SSC and ABS-SSC relationships were applied to the continuous time-series measurements of turbidity and ABS to estimate time-series of SSC at the mooring locations. The analysis presented in this chapter relies on the ABS-estimated SSC time-series since it provides data on time-variable vertical profiles of SSC and primarily use data from the 2009 deployment. For reasons not well understood, ABS-SSC relationships for the 2010 deployment required separate regressions (yielding somewhat poorer correlation) for the relatively high river flow periods in the first half of the deployment and for the relatively low river flow periods in the second half of the deployment. Therefore, the data from the 2010 deployment are used in a limited manner as described subsequently.

Since the ADCP sensors were mounted on a tripod placed on the sediment bed, a fraction of the water column near the bed was not measured. Similarly, a fraction near the surface of the water column was not measured due to interference and binning artifacts. Both velocity and ABS-estimated SSC in these unmeasured zones were estimated by different methods as described next. Velocity in the unmeasured near-surface zone was estimated by assuming that fluid shear stress decreases linearly from measured values to zero at the surface. Fluid shear stress is calculated as:

$$\tau = \mu_t \frac{\mathrm{d}u}{\mathrm{d}z} \tag{3.1}$$

where, τ = fluid shear stress, μ_t = turbulent eddy viscosity, u = turbulent flow velocity, and z = vertical coordinate ($z = 0$ at the sediment-water interface). Velocity in the unmeasured near-bottom zone was estimated assuming a logarithmic profile:

$$\bar{u}_{z,t} = \frac{u_*}{\kappa} \ln\left(\frac{z}{z_0}\right) \tag{3.2}$$

where, $\bar{u}$ = the turbulence-mean velocity, u_* = the bottom friction velocity, $\kappa = 0.4$ = the von Karman constant, and z_0 = bottom roughness length = 1 mm, taken from a hydrodynamic modeling study of the LPR (HydroQual [35]). SSC in the unmeasured near-bottom and near-surface zones was extrapolated assuming that the vertical SSC profile follows the Rouse distribution (van Rijn [36]):

$$\frac{c}{c_a} = \left[\frac{a\left(1-\frac{z}{h_t}\right)}{z\left(1-\frac{a}{h_t}\right)}\right]^{\beta} \tag{3.3}$$

where, c = SSC measured at level z, c_a = SSC at reference height a, h_t = instantaneous water depth, and β = the Rouse number. β was estimated by a least-squares fitting of the measured instantaneous SSC profiles.

Due to tidal variations, the measured profiles include a variable number of constant thickness ADCP bins with data over time. In order to assist with subsequent data analysis, the velocity and SSC profiles were converted to a sigma (σ) coordinate system which results in profiles with a constant number of layers but of variable thickness over time. The σ coordinate system is defined as:

$$\sigma = \frac{z-\eta}{H+\eta} \tag{3.4}$$

where, η = the instantaneous water level with respect to the reference height H. The instantaneous velocity profiles were interpolated to a 20-layer σ grid.

3.3.2. WATER COLUMN: SHIPBOARD DATA

THE shipboard data span a wide range of river flows and include measurements of salinity and SSC (using CTD and OBS casts) over depth in the water column at several locations along the LPR and extending into Newark Bay. Some of this data is presented in Chant *et al.* [25]; the data presented here were collected by the same authors. Data during a below-average river flow condition of 8 m^3/s on June 23, 2005 and an extreme event on March 16, 2010 with river flow of about 450 m^3/s (corresponding to a return period of 25 years) are presented subsequently.

3.3.3. BATHYMETRY DATA

THE bathymetry data consists of a series of multi-beam surveys performed in September 2007, November 2008, June 2010, October 2011, and September 2012. The freshwater inflow from Dundee Dam during this 5-year period is shown in Figure 3.2 in relation to the annual average river flow rate. The river flow ranged from a low of about 1 m^3/s in October 2007, to highs of 450 m^3/s in March 2010 and March 2011 (return period of 25 years), and 700 m^3/s in August 2011 (return period of 90 years). The surveys extended from the mouth of the river to RM 14.5 (about 23.3 km from the mouth), with data from individual surveys mapped to a 1.5 m by 1.5 m resolution grid. The various surveys were referenced to the same horizontal datum (North American Datum 1983, New Jersey State Plane) and vertical datum (National Geodetic Vertical Datum of 1929). River flow in the intervening periods between surveys varied, with certain periods (2007–2008,

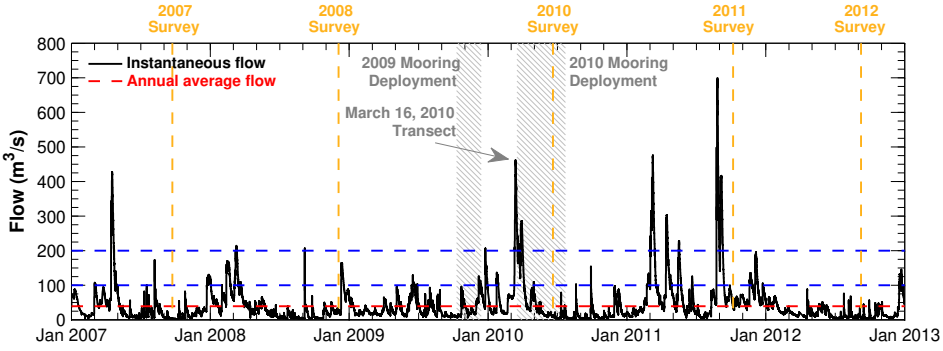

Figure 3.2: Time-series of measured river flow at Dundee Dam during the periods encompassing the water column data and the various bathymetry surveys in the LPR in relation to the annual average river flow (red dashed line), and two morphologically relevant river flow thresholds discussed in this chapter (blue dashed lines).

and 2011–2012) encompassing predominantly low-flow periods (i.e., no events greater than about 200 m^3/s — return period of 2 years), and other periods (2008–2010, and 2010–2011) encompassing events greater than 200 m^3/s (the relevance of the 200 m^3/s threshold is discussed subsequently). Morphological change during these periods was calculated by performing bathymetric differencing of consecutive surveys.

3.3.4. SEDIMENT ERODIBILITY DATA

THE sediment erodibility data used to support the analyses presented here is based on a series of erodibility measurements performed on surficial sediment cores from several locations in the LPR (Chesapeake Biogeochemical Associates [37]; measurements also presented in Mathew and Winterwerp [32]). Briefly, the measurements consisted of shallow cores collected from the LPR and subject to erosion experiments using a Gust Microcosm device. The resulting data were analyzed to calculate a depth-profile of τ_{Cr}.

3.3.5. NUMERICAL HYDRODYNAMIC MODEL

THOUGH not explicitly necessary for the present analyses, we use a three-dimensional hydrodynamic model, as this was available and well-calibrated. This model was developed by HydroQual [35] using the Estuarine, Coastal and Ocean Model (ECOM) framework and applied as part of the environmental restoration activities in the LPR (U.S. Environmental Protection Agency [38]). The model was applied over a domain that includes the LPR, Hackensack River, Newark Bay, and extending to the ends of the Arthur Kill and Kill van Kull — roughly the spatial extent shown in Figure 3.1 (excluding the Hudson River and New York Harbor). The model grid resolution in the LPR ranges from 5 cells across the river at the mouth, decreasing to 4 cells near RM 1.4, to 3 cells near RM 4.2, and 2 cells above RM 15.7 (about 25 km from the mouth of the river). The average grid resolution in the LPR is about 40 m wide and 180 m long with 10 vertical layers (in a sigma coordinate system). Boundary conditions for the model include the measured river flow entering from the head-of-tide in the LPR and tributaries, and the water level, salinity, and temperature at the Kill van Kull and Arthur Kill boundaries (specified using the results of a regional-scale hydrodynamic model also described in HydroQual [35]). The model also includes meteorological forcings (winds, air temperature, relative humidity, barometric pressure, shortwave solar radiation and cloud cover). It was calibrated against measured water levels, currents, temperature, and salinity at several locations within the model domain as well as validated against measurements from the 2009 and 2010 moored deployments described previously. The calibrated model was used for an assessment of currents and bed shear stresses under various steady-state river flows.

Following standard assumptions for hydrodynamic interactions at the bottom boundary, the effective bottom roughness used in Eq. 3.2 was assumed to be composed of form-related and grain-related fractions (van Rijn [39]). The grain-related roughness, calculated as a function of the surficial sediment texture, is considered to generate the skin friction relevant for erosion. Therefore, skin friction was calculated as:

$$\tau_{SF} = \rho \left[\frac{\bar{u}_t \kappa}{\ln\left(\frac{h_t}{2z_{0G}}\right)} \right]^2 \tag{3.5}$$

where, τ_{SF} = skin friction, ρ = density of water, the overbar represents depth-averaging, and z_{0G} = grain roughness height, calculated as:

$$z_{0G} = \frac{k_s}{30} = \frac{3D_{90}}{30} \tag{3.6}$$

where, k_s = Nikuradse grain roughness (van Rijn [39]), D_{90} = particle diameter representing the 90% cumulative percentile of the sediment grain size distribution. The D_{90} was calculated using surficial sediment grain size distribution measurements in the LPR.

3.3.6. DECOMPOSITION METHODS

THE majority of the analyses presented here relates to sediment dynamics using the mooring data. The analysis involves the decomposition of suspended sediment flux (SSF) into components attributable to the primary hydrodynamic forcings. This was accomplished by first decomposing the measured flow rates into barotropic, estuarine, and residual components followed by calculation of SSF associated with these processes. The term residual flow in the context of the analyses presented in this chapter refers to the depth- and tidally-integrated quantity which in this case is mainly the river (freshwater) flow and flow induced by episodic subtidal barotropic events. Due to the lack of cross-sectional coverage in the mooring data, unless otherwise noted, the flow rates and SSF discussed in the remainder of the text refer to their channel width-normalized equivalents.

FLOW DECOMPOSITION

THE flow decomposition uses a combination of analytical formulations and harmonic analysis of the σ-transformed measured currents and flow rates. Given the co-variance of tidal water depths and currents, in order to perform a mass conservative decomposition, the decomposition is applied to flow rates instead of currents. The measured instantaneous depth-dependent flow rate $q_{z,t}$ is:

$$q_{z,t} = u_{z,t}\Delta z_t \tag{3.7}$$

where, $u_{z,t}$ is the measured instantaneous velocity for sigma layer z in the water column with directionality assigned positive during flood and negative during ebb, and Δz_t is the instantaneous thickness of the corresponding sigma layer. This instantaneous flow rate represents the combination of several components — a high-frequency component associated with barotropic circulation ($q_{z,T}$), a low-frequency component associated with estuarine circulation ($q_{z,E}$), and a low-frequency residual component that in this case is associated with the river (freshwater) flow ($q_{z,R}$). High-and low-frequency are relative to the tidal period T (12.42 h). Accordingly, the instantaneous depth-dependent flow rate is:

$$q_{z,t} = q_{z,T} + q_{z,E} + q_{z,R} \tag{3.8}$$

Various approaches were tested to perform the flow decomposition described by Eq. 3.8. The approach used in the analysis presented herein was chosen primarily for its ability to estimate the estuarine circulation component at locations that are relatively

dynamic with respect to the salt front (freshwater and brackish). Appendix B presents the various approaches, along with a comparative evaluation of the results from these approaches.

The flow components in Eq. 3.8 were calculated by first applying an analytical formulation to extract the estuarine circulation component, followed by harmonic analysis to separate the barotropic and residual components. Estuarine circulation is classically defined as the tidally-averaged deviation of the velocity profile from the depth-averaged velocity (Dyer [1]):

$$u_{z,E} = \langle u_{z,t} - \bar{u}_t \rangle \tag{3.9}$$

where, the overbar represents depth-averaging, angled brackets represent tidal-averaging, and $u_{z,E}$ is the velocity component associated with estuarine circulation. However, this definition includes vertical shearing by the logarithmic profile in Eq. 3.2. Application of Eq. 3.9 leads to results such as estuarine circulation being calculated landward of the salt front (see Appendix B) due to deviations from the depth-averaged velocity (e.g., the logarithmic velocity profile). Such artifacts are avoided by modifying Eq. 3.9 to incorporate the logarithmic velocity profile using analytical formulations for velocity profiles that include the effects of bottom roughness and the pressure gradient induced by the longitudinal density gradient. Accordingly, Eq. 3.9 is rewritten as:

$$u_{z,Tot} = \langle u_{z,t} - \bar{u}_t \rangle \tag{3.10}$$

where, $u_{z,Tot}$ is the total measured residual vertical circulation which represents the effects of estuarine circulation $u_{z,E}$ and the logarithmic velocity profile $u_{z,log}$. To obtain a best estimate of $u_{z,E}$ from the data, $u_{z,Tot}$ is corrected for $u_{z,log}$. In the presence of baroclinic effects, the velocity profile differs from the logarithmic profile, thus affecting the effective u_*. The logarithmic contribution is therefore obtained from the first-order analytical velocity profile for shear flow under the influence of a longitudinal salinity gradient (Winterwerp *et al.* [40]). This analytical velocity is indicated with the symbol v, to distinguish from the measured value u:

$$\begin{aligned} v_{z,t} &= -\frac{v_*}{\kappa} \ln\left(\frac{z}{z_0}\right) + \frac{1}{2}\frac{\alpha g h_t}{\kappa v_*}(z - z_0)\frac{1}{\rho}\frac{\partial S}{\partial x} \\ &= v_{z,t,log} + v_{z,t,bcl} \end{aligned} \tag{3.11}$$

where,$\alpha = 0.8$, g is the gravitational constant, $\partial S/\partial x$ is the measured longitudinal salinity gradient, and $v_{z,t}$ represents the analytical depth-dependent velocity. The first term on the right-hand side of Eq. 3.11 is the barotropic logarithmic velocity profile $v_{z,t,log}$ and the second term $v_{z,t,bcl}$ accounts for the contribution from the longitudinal density gradient. The analytical shear velocity, v_*, is calculated using Eq. 3.12 which represents the depth-integration of Eq. 3.11:

$$\begin{aligned} \bar{v}_t &= -\frac{v_*}{\kappa}\left[\ln\left(\frac{h_t}{z_0}\right) - 1\right] + \frac{1}{4}\frac{\alpha g {h_t}^2}{\kappa v_*}\frac{1}{\rho}\frac{\partial S}{\partial x} \\ &= \bar{v}_{t,log} + \bar{v}_{t,bcl} \end{aligned} \tag{3.12}$$

Substituting the measured $\bar{u}_t$ for the analytical $\bar{v}_t$ in Eq. 3.12 resolves the analytical shear velocity v_* which includes contributions from barotropic and baroclinic components. Subsequently, the barotropic logarithmic velocity profile $v_{z,t,log}$ is assessed using Eq. 3.11 and used to calculate the estuarine circulation component $u_{z,E}$ by modifying Eq. 3.10 to include a correction for the logarithmic velocity profile (estimated as $v_{z,t,log} - \bar{v}_{t,log}$):

$$\begin{aligned} u_{z,E} &= \left\langle u_{z,t} - \bar{u}_t - \left(v_{z,t,log} - \bar{v}_{t,log}\right) \right\rangle \\ &= \left\langle u_{z,t} - \bar{u}_t - v_{z,t,log} + \bar{v}_{t,log} \right\rangle \end{aligned} \tag{3.13}$$

Given the tidal variations in water depth, the flow rate associated with estuarine circulation is calculated by incorporating the instantaneous sigma layer thickness in Eq. 3.13:

$$q_{z,E} = \left\langle \left(u_{z,t} - \bar{u}_t - v_{z,t,log} + \bar{v}_{t,log}\right) \Delta z_t \right\rangle \tag{3.14}$$

Given the inequality in the semi-diurnal tides, the tidal-period averaging was performed over two tidal cycles (2*12.42 h) using a centered moving-window scheme. Note that the estuarine component thus calculated does not explicitly meet the constraint:

$$\int q_{z,E}\, \mathrm{d}z = 0 \tag{3.15}$$

However, review of the residual from depth-integration of the calculated $q_{z,E}$ as well as comparison of the calculated near-bottom $q_{z,E}$ to the measured near-bottom salinity (presented subsequently) serve as a check on the decomposition formulations.

The difference of $q_{z,t}$ and $q_{z,E}$ represents the advection term, $q_{z,A}$, which is the sum of the barotropic and residual flow components, as in Eq. 3.16:

$$q_{z,A} = q_{z,t} - q_{z,E} = q_{z,T} + q_{z,R} \tag{3.16}$$

The depth-dependent barotropic and residual flow components were separated using a 35 h low-pass filter applied to the constituent periods of the Fourier-transformed $q_{z,A}$ time-series. Constituents with periods less than 35 h were considered to represent the barotropic component $q_{z,T}$ and constituents with periods greater than 35 h were considered to represent the residual flow component $q_{z,R}$. Therefore, the barotropic component represents primarily tidal transport, whereas the residual flow component can include river flow, low frequency barotropic events such as storm surges, as well as the effect of lateral variations in flow due to presence of river bends, etc.

Such flow decomposition techniques have been applied by other authors (Uncles and Jordan [41]; Winterwerp [42]; Costa [43]; Dyer [1]; Jay *et al.* [44]; Siegle *et al.* [45]). Alternative approaches using signal processing techniques have also been developed by other authors; see Lerczak *et al.* [46] and Chant *et al.* [25]. These approaches were also applied to the data presented here; Appendix B includes a comparison of results from these approaches to the flow decomposition formulations described by Eq. 3.8–3.16.

SUSPENDED SEDIMENT FLUX DECOMPOSITION

THE various flow components and SSC time-series data were used to calculate SSF. Although decomposition techniques have been applied by others to separate SSC into components equivalent to that resulting from flow decomposition (Geyer *et al.* [14]; Scully and Friedrichs [15]; Siegle *et al.* [45]; Sommerfield and Wong [16]; Chant *et al.* [25]; Becherer *et al.* [47]), it was not applied in the present analysis for two inter-related reasons (see Appendix C for additional description of both arguments). The first reason involves the fact that the decomposition results in fluctuating SSC components that are often negative. Although mathematically tractable, negative SSC components are physically meaningless. The second reason is that integrated over depth and the tidal cycle, the scale of interest for the analyses presented here, SSF calculated with and without SSC decomposition are identical. Therefore, the tide- and depth-integrated SSF, F_X, associated with given flow component was calculated as:

$$F_X = \int_0^T \int_0^{h_t} q_{z,X} c_{z,t} \, \mathrm{d}z \mathrm{d}t \tag{3.17}$$

where, subscript X refers to the various flow components described previously (residual, estuarine, and barotropic circulation), and c_z, t is the measured depth-dependent instantaneous SSC. The net SSF representing the integrated effect of the individual components was calculated as the sum of the SSF associated with the individual flow components.

The SSF associated with the various flow components is subject to some uncertainty originating from the fact that the SSF decomposition procedure considers the various flow components and SSC as independent variables. However, SSC has a boundary condition (at the river bed) that scales over tidal time-scales. In other words, erosion from the bed scales as a function of the net force (i.e., the skin friction generated by the sum of the individual flow components) which varies over the tidal period. As shown in the next section, because the current associated with river flow adds to and enhances the ebb tidal currents, SSC during a given ebb tide is greater during periods of high river flow than during periods of lower river flow. However, the SSF decomposition does not apportion the incremental SSC generated by the higher river flow entirely to the SSF associated with river flow; such attribution implies that SSF associated with barotropic circulation would be independent of river flow which is the theoretically expected result. Rather, the SSF decomposition formulation associates the barotropic ebb flow rate with the net SSC, potentially resulting in depth- and tidally-average SSF associated with barotropic circulation directed down-estuary during periods of high river flow. This limitation is entirely related to the use of empirical SSC data and is expected to be most prominently apparent in the SSF associated with barotropic circulation. SSC (and SSF) can reliably be attributed to the individual flow components only by using a numerical model such as used by Gatto *et al.* [5]. Nonetheless, the empirical data and SSF decomposition presented here helps inform sediment transport dynamics and the relevance of various transport processes; the exact magnitude of impact of given forcing on SSF may be somewhat different.

3.4. RESULTS

THE results of the decomposition formulations include time-series of flow rates and SSF which are examined next for dependencies with the measured river flow and salinity over a limited range of hydrologic conditions. The findings of sediment dynamics inferred from the review of SSF are also compared against morphological trends measured in the bathymetry data. The bathymetry data are also used to assess sediment dynamics over the full range of hydrologic conditions. The bed-water exchange processes of erosion and deposition inferred from the SSF and bathymetry data are interpreted with the aid of the hydrodynamic model and reviewed in the context of measurements of the vertical profile of in the bed. These results are described in the following subsections, starting with an overview of SSC dynamics in relation to the primary hydrodynamic forcings.

3.4.1. SSC DYNAMICS

FIGURE 3.3 shows a detailed view of SSC at RM 6.7 over a 2-day window to illustrate various sediment transport processes and the different dynamics during low and high river flow conditions. In general, during the low river flow period (left column of Figure 3.3), SSC is in phase with current speed (and salinity), implying local resuspension of bed sediments. Also, both currents and SSC attain higher magnitudes during flood than ebb, indicating advection and net SSF directed up-estuary over the tidal cycle. During low river flow, due to its morphology, the LPR is characterized by flood-dominance in currents and consequently, SSC tends to be higher during flood than ebb. Similarly, acceleration/deceleration asymmetries are apparent in the velocity data, with acceleration at the start of flood seen to be faster than deceleration at the end of flood, and vice-versa during ebb. The effect of acceleration/deceleration asymmetries is also apparent in SSC, with SSC increasing relatively rapidly at the start of flood than at the start of ebb. In other words, SSC persists at a relatively low value of about 20 mg/L for a longer duration around high-water slack than around low-water slack. Therefore, both tidal asymmetry mechanisms described previously are apparent in the data at RM 6.7 during low river flow conditions implying that depth- and tidally-integrated net SSF are directed up-estuary during this period. As mentioned previously, the other category of transport mechanisms, namely lag effects, are apparent only in a Lagrangian frame of reference and are therefore not explicitly apparent in Figure 3.3.

The trends during high river flow (right column of Figure 3.3) contrast in several respects with trends during low river flow. Although SSC is in phase with current speed during high river flow, in contrast to low river flow, both SSC and currents attain higher magnitudes during ebb than flood, thus indicating advection from up-estuary potentially in combination with erosion. The additional freshwater during high river flow (in conjunction with a setdown event apparent during the second half of December 11) results in higher currents during ebb than during flood. At the same time, the salt front is pushed down-estuary because of the higher river flow. Furthermore, during certain flood tides such as during the latter half of December 11th, SSC does not exhibit a peak as seen during other flood periods. This is due to the relatively low peak flood currents during this period, indicating that bed shear stresses are too low to cause erosion. In addition to the afore-mentioned trends in currents and SSC, during high river flow con-

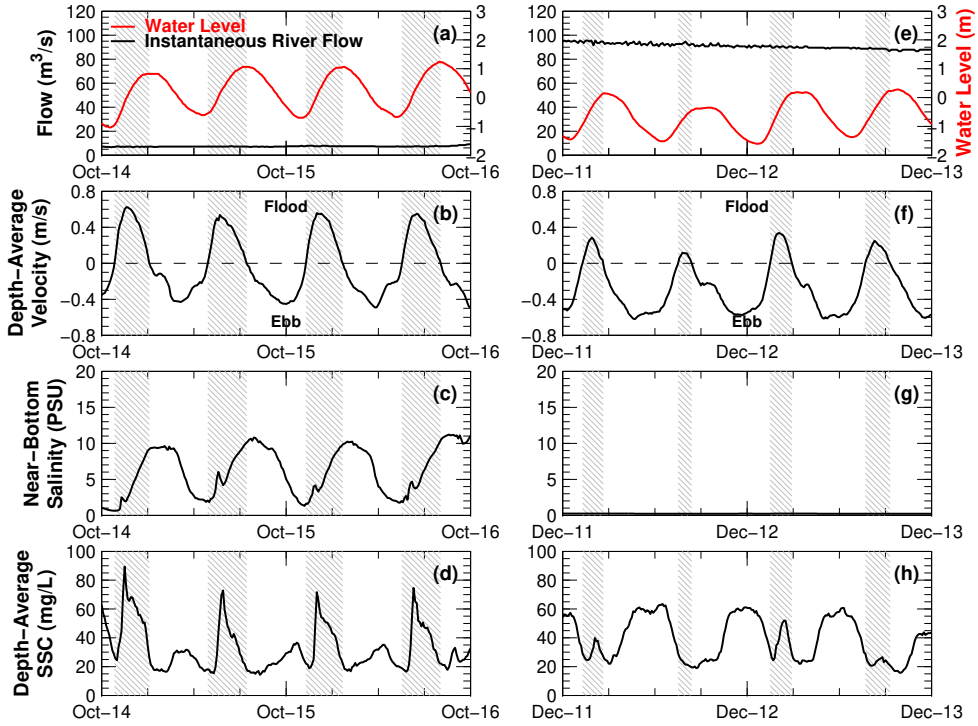

Figure 3.3: Time-series of (a & e) the Dundee Dam discharge and water level at RM 6.7, (b & f) depth-average currents, (c & g) near-bottom salinity, and (d & h) instantaneous and tidally-averaged depth-average SSC at RM 6.7. Hatched regions indicate duration of flood currents, i.e., directed up-estuary. Left and right columns show data during low and high-flow periods, respectively.

ditions, ebb duration is longer than flood duration. These trends imply that depth- and tidally-integrated net SSF are directed down-estuary during this period.

Figure 3.4 includes along-channel transects in the LPR and in Newark Bay showing the measured bathymetry, salinity, and SSC during a below-average river flow condition of 8 m^3/s on June 23, 2005, and an extreme event on March 16, 2010 with river flow of about 450 m^3/s (return period of 25 years). Both transects show evidence of a well-developed ETM in the vicinity of the salt front (nominally defined as the location of the 2 PSU isohaline). The salt front and ETM respond to river flow — during the low-flow event, both the salt front and the ETM are located at RM 7, with depth-average SSC of about 75 mg/L within the ETM whereas during the high-flow event, the salt front and ETM are pushed to the mouth of the LPR with much higher depth-average SSC of about 250 mg/L within the ETM. The presence of the ETM co-located with the salt front within the LPR is indicative of the relevance of estuarine circulation to sediment dynamics in the LPR. The response to river flow is apparent in the SSC landward of the ETM which ranges about 20–40 mg/L during the low-flow event but increases to about 120 mg/L during the high-flow event.

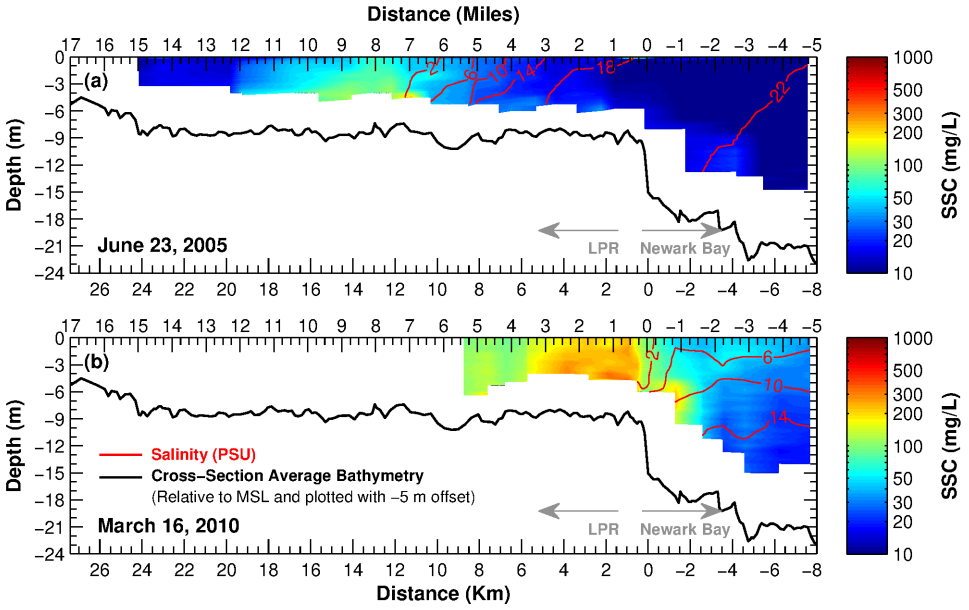

Figure 3.4: Along-channel transects showing the cross-sectionally averaged bathymetry within the LPR (measured in 2007) and within the navigation channel in Newark Bay (both shown with an offset of -5 m for plotting purposes). Also included are salinity contours and SSC (shaded colors) measured during (a) low river flows of about 8 m^3/s, and (b) during high river flows of about 450 m^3/s and plotted relative to the measured water depth at the time of measurement. Both transects measured during mid-ebb.

The sediment dynamics and the residual sediment transport apparent in Figure 3.3 and Figure 3.4 are further explored using the flow and SSF decomposition methods.

3.4.2. HYDRODYNAMIC MODEL AND SEDIMENT ERODIBILITY

THE hydrodynamic model was used to perform a series of simulations under constant salinity (at the marine boundaries in the Arthur Kill and Kill van Kull), over a spring–neap cycle, and for various river flow rates. Applied freshwater flow rates at the head-of-tide ranged from 0 m^3/s to 500 m^3/s (representing an event with a return period slightly greater than 25 years). These simulations help understand the response of the LPR to river flow and the impact on sediment dynamics. Figure 3.5 and Figure 3.6 show various metrics from these simulations, calculated using the spring–neap mean of various cross-sectionally averaged quantities. Figure 3.5 shows results for computed currents and salinity, and Figure 3.6 shows results for computed skin friction. The impact of localized variations such as a reduction in cross-sectional area due to a rock outcrop immediately up-estuary of RM 8, and an increase in cross-sectional area due to a widening of the river at RM 4.2 are apparent in the calculated peak tidal currents and skin friction. Asymmetry in peak tidal currents was quantified as the ratio of the peak flood-current to peak ebb-current, with values greater than one denoting flood-dominance and values less than one denoting ebb-dominance. At any given location, the system is flood-

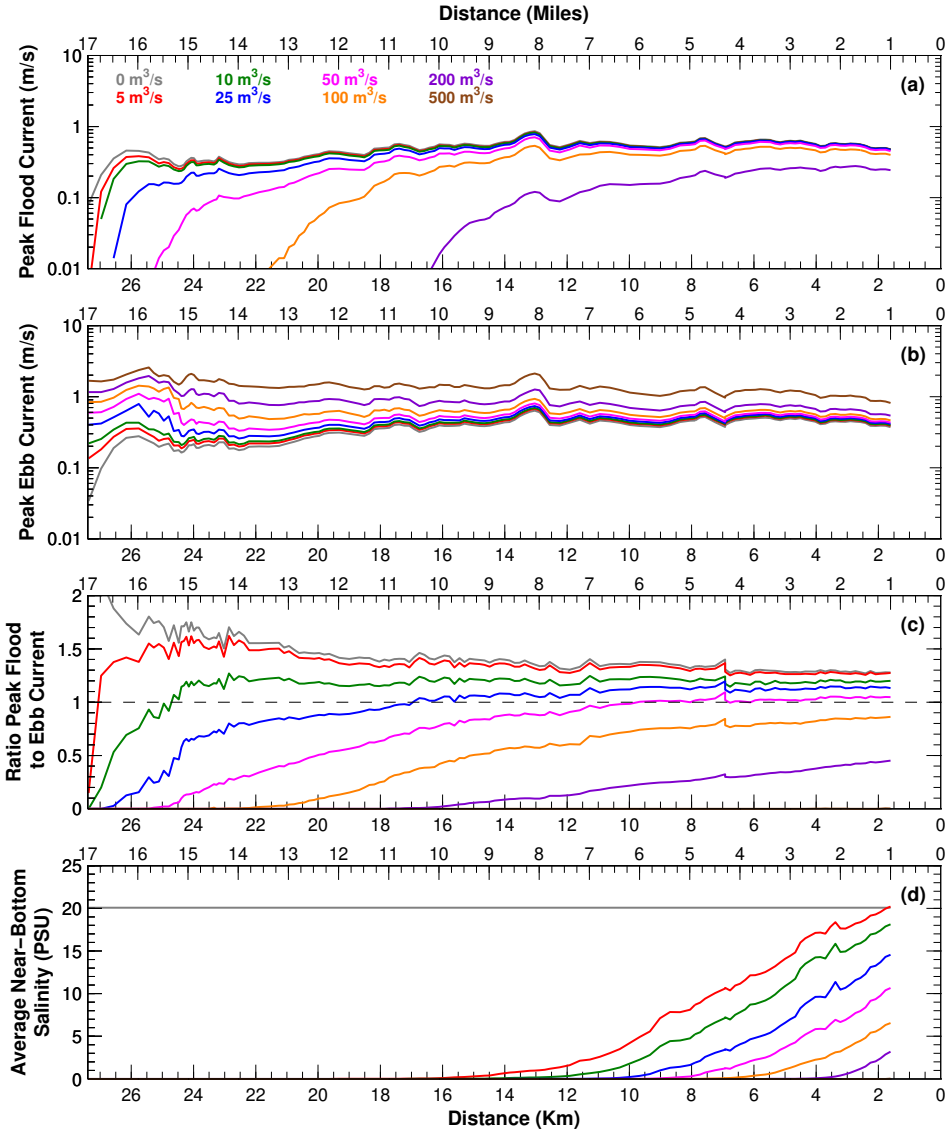

Figure 3.5: Results of a numerical model showing impact of river flow rate on (a) peak flood-phase currents, (b) peak ebb-phase currents, (c) asymmetry in peak currents, and (d) salinity.

dominant at low river flows, transitioning to ebb-dominance with increasing river flow. The river flow associated with the transition from flood- to ebb-dominant increases with distance down-estuary and the entire river exhibits ebb-dominance at river flow slightly greater than 50 m^3/s. Salinity responds in a similar manner, with the salt front pushed seaward as river flow increases and pushed out of the river at flow greater than 200 m^3/s.

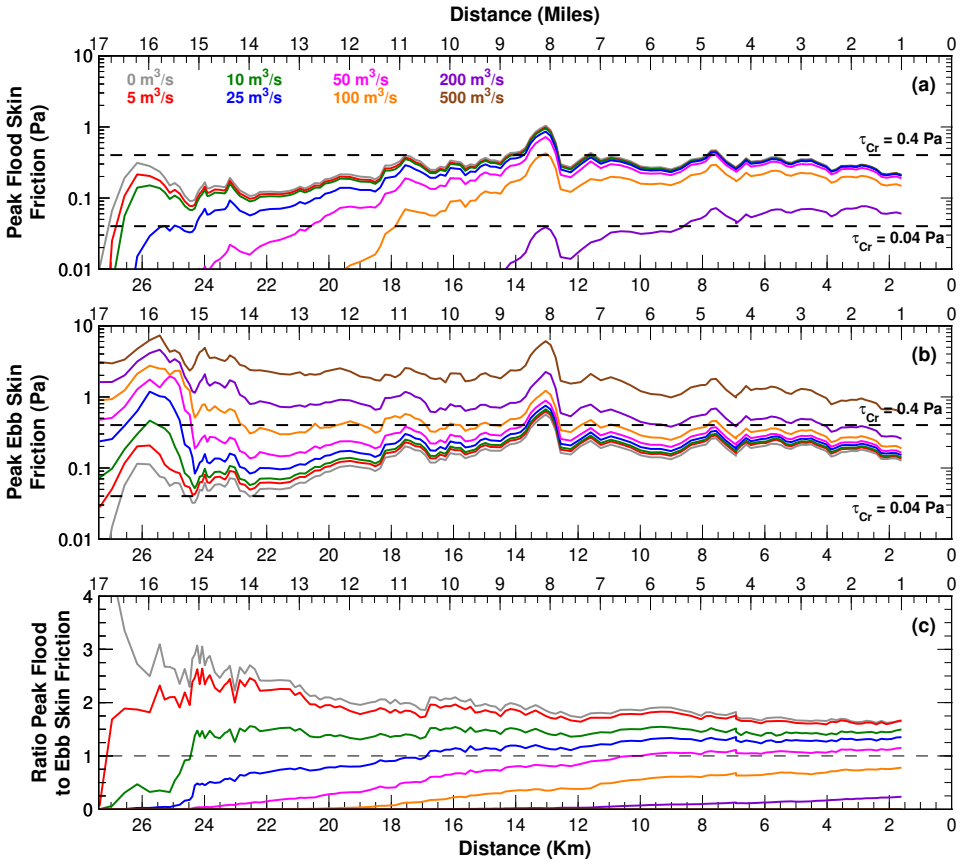

Figure 3.6: Results of a numerical model showing impact of river flow rate on (a) peak flood-phase skin friction, (b) peak ebb-phase skin friction, and (c) asymmetry in peak skin friction.

Skin friction at the bed-water interface shown in Figure 3.6 responds in a similar manner as currents. The upper two panels in Figure 3.6 also show the τ_{Cr} measured on sediment cores. As shown in Mathew and Winterwerp [32], typical values of τ_{Cr} in the LPR ranges from about 0.04 Pa at the surface of the cores, increasing to 0.4 Pa at a depth of about 2–4 mm below the surface. This thin layer (2-4 mm thick) of easily-erodible sediments at the surface of the cores was shown to be indicative of a pool of sediment (referred to as the fluff layer) that is resuspended every tidal cycle (once during flood and again during ebb) and redeposited around slack water. Mathew and Winterwerp [32] also present arguments supporting the importance of the fluff layer for the net transport of fine sediments against the direction of residual (river) flow. This is also seen in the skin friction results presented in Figure 3.6 — during low river flows (nominally defined as 0–10 m^3/s in this context), peak skin friction ranges between 0.04 to 0.4 Pa over nearly the entire length of the LPR. In other words, erosion is expected to be restricted to the fluff layer during such conditions. Only when bed skin friction exceeds about 0.4 Pa is erosion

expected to extend to deeper depths. The results for peak ebb skin friction show that as river flow increases beyond 25 m^3/s, progressively larger areas of the LPR experience skin friction greater than 0.4 Pa. At river flows greater than about 100 m^3/s, areas landward of RM 8 experience skin friction greater than 0.4 Pa, and at river flows beyond 200 m^3/s, the entire river experiences skin friction greater than 0.4 Pa. These relative comparisons of τ_{Cr} for various sediment strata, and the system response to increasing river flow are used to inform the interpretation of sediment dynamics and morphological change from the analysis of SSF and bathymetry data. Note that the values of τ_{Cr} presented here are associated with predominantly cohesive sediments. In particular, the sediment substrate in areas above RM 14.5 is predominantly composed of sand and gravel, and therefore, the values of τ_{Cr} presented here are not representative of the sediments in those areas.

3.4.3. FLOW DECOMPOSITION

THIS section presents a validation of the decomposition procedure, by comparing two of the three calculated flow components against measured metrics.

RESIDUAL FLOW

THE residual flow rate is estimated to represent primarily river flow; this was assessed by comparison against the measured freshwater inflow from the head-of-tide. The calculated depth-integrated residual flow rate at given location was extrapolated over the cross-section using the effective channel width (calculated as the ratio of cross-sectional area to water depth at the mooring location; both at mean sea level). Figure 3.7 shows the results of this comparison for the 2009 moored deployment, including quantitative metrics. The calculated flow rates at all locations tends to reproduce the general temporal trends seen in the measured river flow, with episodic high-flow events during the last week of October, and during the first half of December. However, the magnitudes differ — at the two seaward locations (RM 1.4 and RM 4.2), calculated and measured flow rates are more comparable during high-flow periods than during low-flow periods. Occasionally, during low-flow periods, the flow decomposition procedures also result in calculated residual (river) flow rate directed up-estuary which is a spurious result. The alternative approaches applied in Appendix B also give such spurious results suggesting that this is not an artifact related to the flow decomposition formulations. Rather, these artifacts at RM 1.4 and RM 4.2 likely relate to uncertainties in measurement, sampling location, cross-sectional averaging and possibly secondary flows and preferential flow paths induced by sharp bends in the river. Such errors are inherent in the estimation of residual terms from gross fluxes in tidal and estuarine settings (Jay *et al.* [44]).

In contrast, calculated flow rates at the three up-estuary locations are more comparable to measured flow rates over the full range of flows. The relatively consistent tendency for over-prediction at these three locations may be an indication of cross-channel variations in currents not captured by the mooring data. It should be noted that the decomposition of sediment fluxes is performed on a channel width-normalized basis and is therefore not affected by potential artifacts associated with cross-channel variations. The comparison of the calculated and measured river flow rates at the three up-estuary locations is taken as a validation of the flow decomposition formulations, thus supporting its use in SSF decomposition.

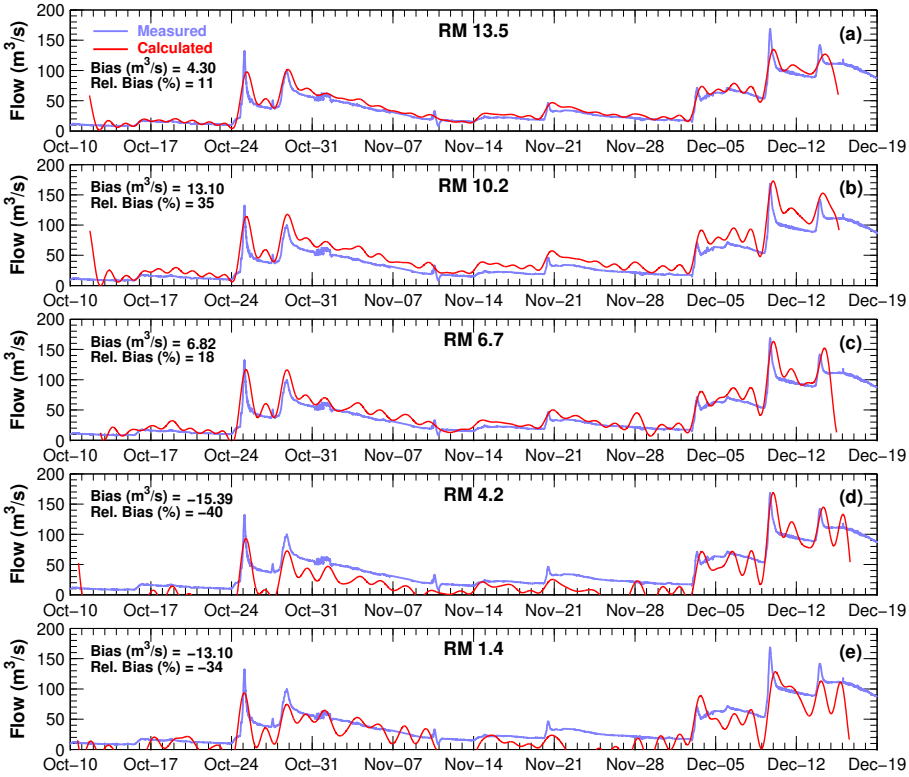

Figure 3.7: Time-series comparison of measured river flow rate at the head-of-tide and calculated residual (river) flow rate at the various mooring locations for the 2009 moored deployment. Performance metrics shown include the bias (calculated as the difference of mean calculated and mean measured flow rate, with the mean values calculated over the duration of the deployment), and the relative bias (calculated as the ratio of bias to the mean measured flow rate). Comparisons at (a) RM 13.5, (b) RM 10.2, (c) RM 6.7, (d) RM 4.2, and (e) RM 1.4.

ESTUARINE EXCHANGE FLOW

THE calculated flow rates associated with estuarine circulation were also validated, albeit in a qualitative manner, using measured near-bottom salinity data. Since estuarine circulation is expected only seaward of the salt front, the presence or absence of salinity at a given location is indicative of the presence or absence of estuarine circulation. Therefore, the presence or absence of calculated estuarine circulation is compared against the presence or absence of salinity at given location as a qualitative check on the flow decomposition formulations. Figure 3.8 shows the results of this comparison for the 2009 moored deployment. At RM 6.7, which is the most dynamic location with respect to the salt front, the calculated near-bottom flow component associated with estuarine circulation shows consistent temporal trends as near-bottom salinity. Estuarine circulation is seen to occur only when the salt front is located landward of RM 6.7, a result consistent with theoretical expectations. The other locations are less dynamic with

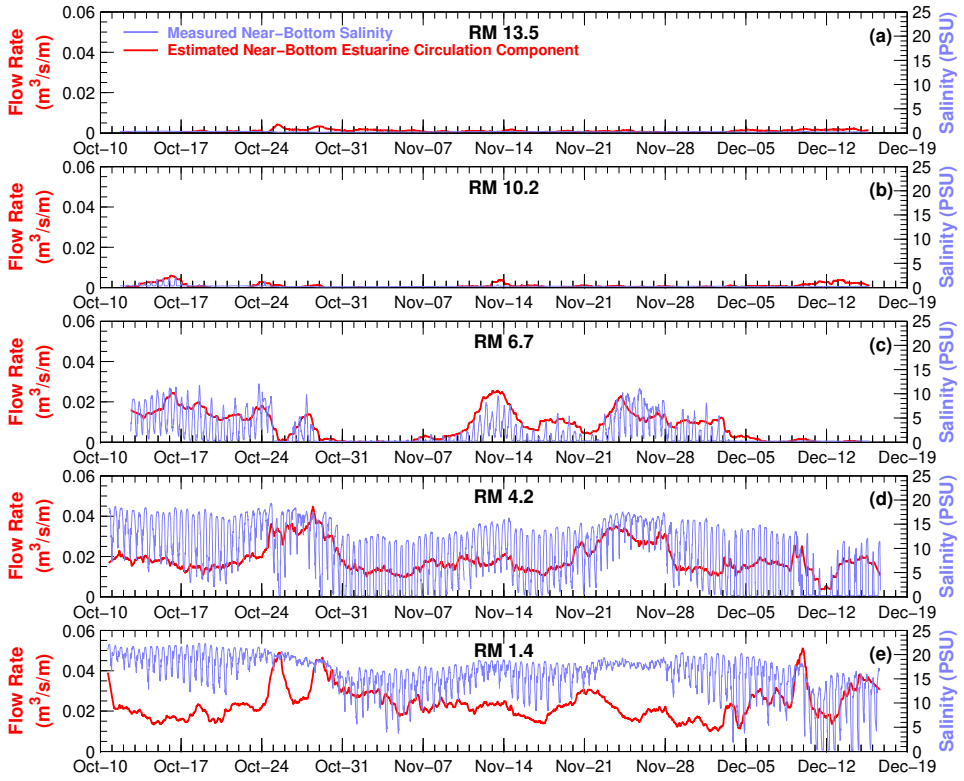

Figure 3.8: Time-series comparison of measured near-bottom salinity and calculated near-bottom flow rate associated with estuarine circulation at the various mooring locations for the 2009 moored deployment. Comparisons at (a) RM 13.5, (b) RM 10.2, (c) RM 6.7, (d) RM 4.2, and (e) RM 1.4.

respect to estuarine circulation, with estuarine circulation persisting at RM 1.4 and RM 4.2 over the entire deployment. Similarly, the salt front and estuarine circulation is seen to extend up to RM 10.2 for a few days preceding October 17. Although estuarine circulation is calculated during brief periods at RM 10.2 (October 24 and November 14), and RM 13.5 (October 25 through November 2), during periods when the salt front is located seaward of these stations, the magnitude of the calculated flow rate is small. These false signals are likely related to deviations from the theoretical logarithmic vertical profile for currents. The significantly higher flow rates associated with estuarine circulation at the other locations, and its co-dependence with measured salinity is taken as a validation of the flow decomposition methods, thus supporting its use for SSF decomposition. It should be noted that neglecting the correction for the logarithmic velocity profile results in artifacts such as estuarine circulation being calculated even at RM 13.5 which is located landward of the salt front during the entire deployment. This is further elaborated in Appendix B.

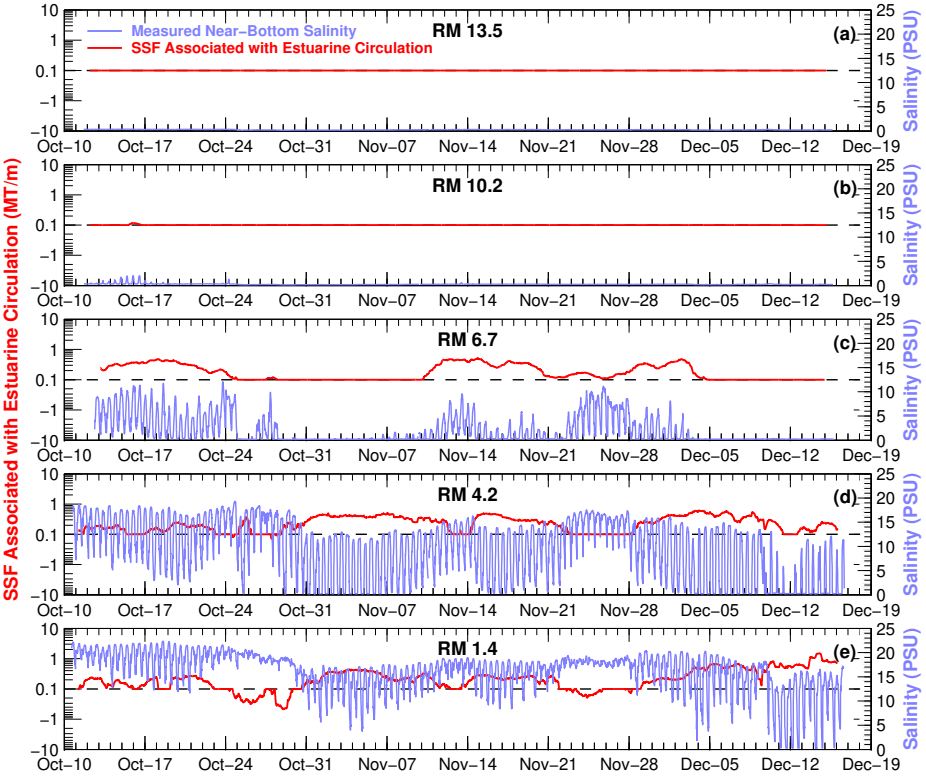

Figure 3.9: Time-series comparison of measured near-bottom salinity and calculated SSF associated with estuarine circulation for the 2009 moored deployment. Comparisons at (a) RM 13.5, (b) RM 10.2, (c) RM 6.7, (d) RM 4.2, and (e) RM 1.4. Fluxes calculated by integrating over depth and over time (two tidal cycles) using a moving-window scheme. Positive and negative values indicate fluxes directed up-estuary and down-estuary, respectively.

3.4.4. SUSPENDED SEDIMENT FLUXES

THE results of the SSF decomposition includes time-series of the net SSF and SSF associated with various flow components. These are evaluated for their dependency with the primary hydrodynamic forcings.

SSF ASSOCIATED WITH ESTUARINE CIRCULATION

FIGURE 3.9 shows the time-series of SSF associated with estuarine circulation relative to the measured near-bottom salinity for the 2009 moored deployment. As with the estuarine circulation flow rates, SSF associated with estuarine circulation tends to be correlated with the salt front location and is directed up-estuary at locations seaward of the salt front. The only exceptions are during the neap tides of October 24–30, and November 22–28 at RMs 4.2 and 1.4. This is due to a combination of low tidal energy (i.e., lesser amplitude of tidal currents and therefore lesser sediment resuspension and lower near-bottom SSC), strong stratification (also seen in the relatively small intra-tidal

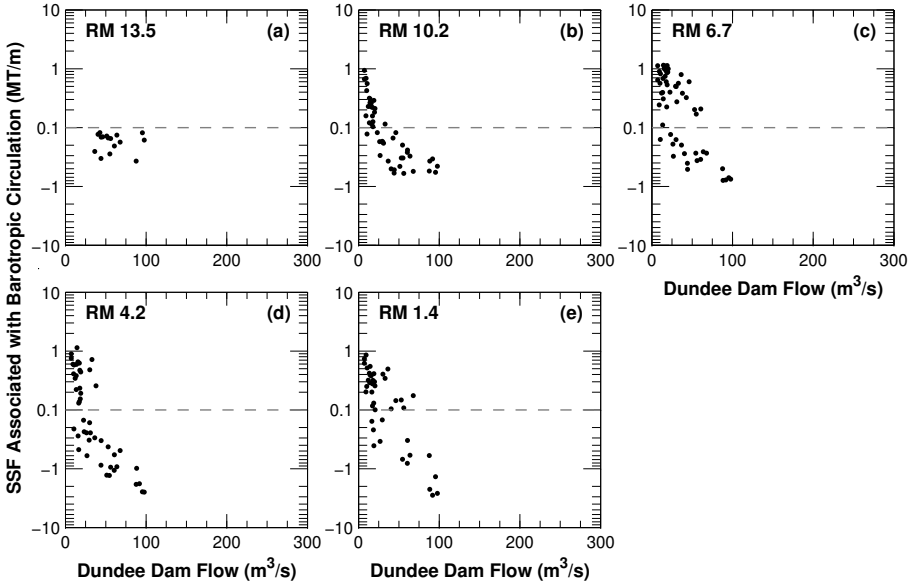

Figure 3.10: Calculated SSF associated with barotropic processes as a function of the measured river flow rate at the head-of-tide for the 2009 moored deployment. Comparisons at (a) RM 13.5, (b) RM 10.2, (c) RM 6.7, (d) RM 4.2, and (e) RM 1.4. Fluxes calculated by integrating over depth and over time (two tidal cycles) using a fixed-window scheme. Positive and negative values indicate fluxes directed up-estuary and down-estuary, respectively.

fluctuations in near-bottom salinity) which dampens vertical mixing, and elevated river flow (on October 25 and 28). The runoff events likely resulted in additional SSC loadings to the river (from the head-of-tide as well as stormwater outfalls in the estuary), resulting in measurements of higher near-surface SSC than near-bottom SSC (also seen in the turbidity-estimated SSC; concentrations on the order of 10–20 mg/L). Although not definitively related to a runoff event, the period of November 22–28 also experiences strong salinity stratification, and higher near-surface SSC than near-bottom SSC. The net result is a negligible up-estuary or even down-estuary SSF despite estuarine circulation during these periods, especially at RM 1.4.

SSF Associated with Barotropic Circulation

Figure 3.10 shows the calculated SSF associated with barotropic circulation as a function of the measured freshwater flow rate at Dundee Dam for the 2009 moored deployment. The comparison indicates SSF dynamics that are dependent on river flow, with low river flows generally associated with up-estuary SSF and high river flows associated with down-estuary SSF. The up-estuary SSF at low river flows can be attributed to the various barotropic processes described previously — lag effects and tidal asymmetries. Two of these processes can be seen in the results for the zero river flow case shown in Figure 3.5 — the decrease in tidal currents with distance up-estuary, and flood dominant tidal currents. Theoretically, the barotropic lag effects and tidal asymmetries, and by extension their role in promoting net up-estuary SSF, are independent of river

flow. However, as explained previously, the lack of reliable decomposition of SSC results in the apparent dependency of SSF with river flow and specifically, the down-estuary SSF at high river flows. Nonetheless, as apparent from the up-estuary SSF at low river flows, Figure 3.10 shows that in the LPR as a whole (landward of RM 1.4), lag effects and tidal asymmetries influence sediment dynamics and induce up-estuary flux of sediments. Although we cannot distinguish between lag effects and tidal asymmetry, the former is probably more important in transporting sediment up-estuary because up-estuary transport is measured only at low river flows (below erosion threshold of parent bed), and Figure 3.3 suggests only a limited amount of sediment is mobilized in a short period during the flood tide.

SSF ASSOCIATED WITH RESIDUAL FLOW

FIGURE 3.11 shows the calculated SSF associated with the residual flow as a function of the measured freshwater flow rate at the head-of-tide at Dundee Dam for the 2009 moored deployment. As expected, net SSF associated with the residual flow follows the direction of the residual current, i.e., river flow, and is directed down-estuary at all locations. The only exceptions are net up-estuary SSF at RMs 4.2 and 1.4 during a handful of tidal cycles during low river flows. These are associated with the artifacts associated with the estimated river flow rate at these locations discussed previously in association with Figure 3.7.

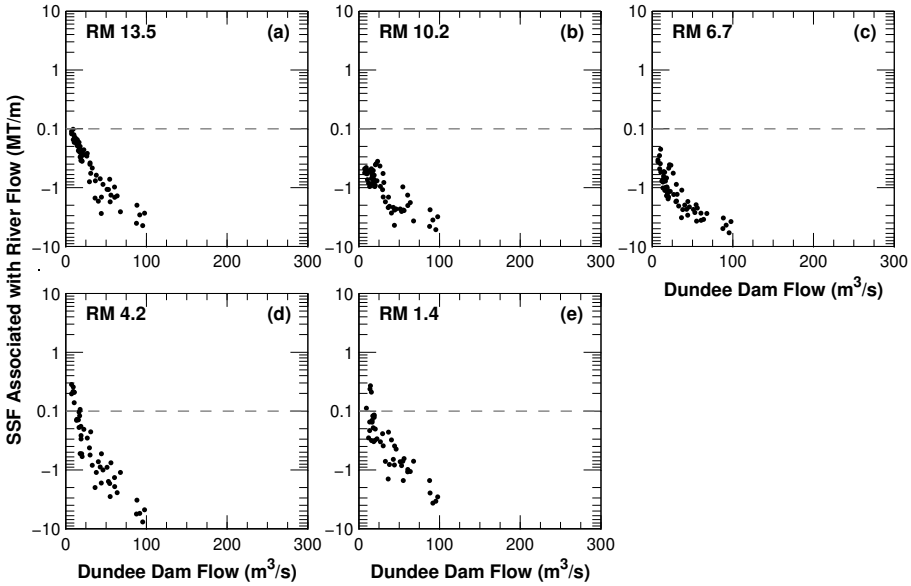

Figure 3.11: Calculated SSF associated with the residual flow as a function of the measured river flow rate at the head-of-tide for the 2009 moored deployment. Comparisons at (a) RM 13.5, (b) RM 10.2, (c) RM 6.7, (d) RM 4.2, and (e) RM 1.4. Fluxes calculated by integrating over depth and over time (two tidal cycles) using a fixed-window scheme. Positive and negative values indicate fluxes directed up-estuary and down-estuary, respectively.

The relationship between SSF and river flow shows certain patterns that inform erosion and deposition patterns in the LPR. In general, as river flow increases, net down-estuary SSF increases due to a combination of additional sediment load from the head-of-tide as well as erosion within the LPR. Comparing the SSF at RM 13.5 to locations down-estuary shows the impact of erosion within the LPR. There is a general trend of increasing SSF from RM 13.5 to RM 6.7, indicating erosion within this reach, and a general trend of decreasing SSF from RM 6.7 to RM 1.4, indicating deposition within this reach. These patterns of erosion and deposition show a dynamic system, with spatially variable patterns of erosion and deposition that are dependent on river flow and are further elaborated upon in the following section. The SSF trends with river flow were also assessed using SSF calculated using the measured river flow instead of the calculated residual flow as an assessment of the uncertainty in the calculated residual flow rates presented in Figure 3.7. The resulting trends were generally similar to Figure 3.11 suggesting that the previously noted errors in the calculated residual flow do not impact the overall conclusions presented here.

NET SSF

THE net SSF represents the integrated result of all the transport processes described previously (barotropic, estuarine, and fluvial). As seen in Figure 3.12 for the 2009

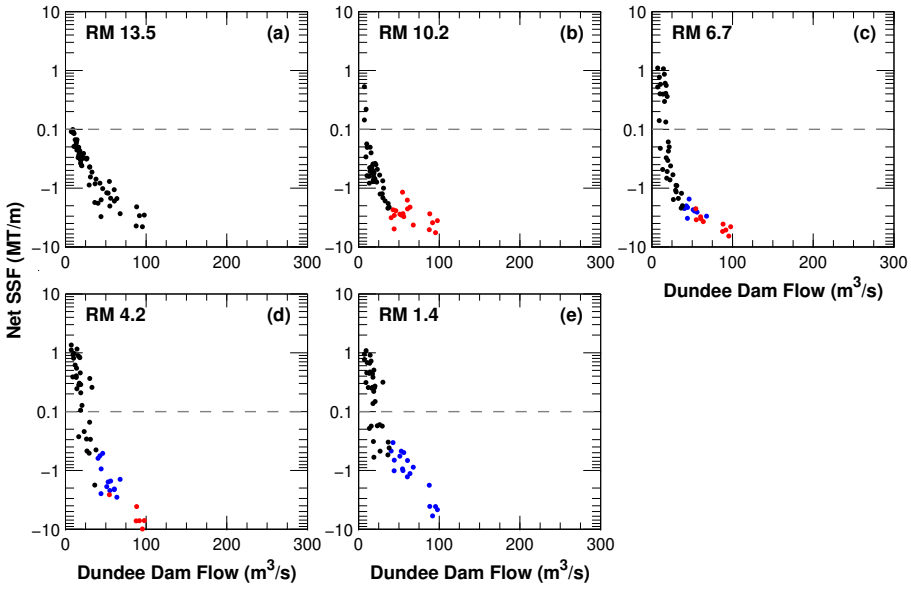

Figure 3.12: Calculated net SSF (integrating all transport processes) as a function of measured river flow rate at the head-of-tide for the 2009 moored deployment. Comparisons at (a) RM 13.5, (b) RM 10.2, (c) RM 6.7, (d) RM 4.2, and (e) RM 1.4. At locations seaward of RM 13.5, during above-average river flows, SSF is color-coded relative to the magnitude of SSF at the location immediately landward, with red and blue indicating erosion and deposition, respectively, in the intervening reach. Fluxes calculated by integrating over depth and over time (two tidal cycles) using a fixed-window scheme. Positive and negative values indicate fluxes directed up-estuary and down-estuary, respectively.

moored deployment, the magnitude and direction of net SSF is strongly dependent on the river flow rate. With the exception of RM 13.5, areas landward of which are characterized by predominantly sandy sediments, the general trend is of net up-estuary SSF at low river flow, i.e., importing conditions, and a transition to net down-estuary SSF at higher river flows, i.e., exporting conditions. During low river flow, the up-estuary transport is driven by estuarine circulation, and barotropic lag effects and tidal asymmetries. The latter two transport mechanisms also persist landward of the salt front. Increasing river flow reduces and/or eliminates the processes responsible for up-estuary SSF (for instance, increasing river flow reverses the flood dominance in currents), increases ebb currents, and consequently, net SSF transport is directed down-estuary at high river flows. The river flow rate associated with the transition from net up-estuary to down-estuary SSF increases towards the mouth of the LPR.

The SSF in Figure 3.12 during above-average river flows is also color-coded to indicate whether SSF at given location is greater or less than the SSF at the location immediately landward, thus indicating erosion or deposition in the intervening reach. The data show a general trend of erosion at the more landward locations (e.g., between RM 13.5 and RM 10.2) gradually transitioning to deposition at the more seaward locations (e.g., between RM 4.2 and RM 1.4) during above-average river flows. For context, using dry density of 0.5 MT/m^3 (based on measurements in the LPR; see Moffatt and Nichol and Deltares [31]), 1 MT/m of erosion in the reach from RM 13.5 to RM 10.2 is equivalent to a depth of erosion of approximately 0.4 mm which is less than the estimated thickness of the fluff layer. The erosional response at the up-estuary locations can be interpreted using Figure 3.6 — barring a few localized exceptions seaward of RM 13.5 and the area above RM 15, skin friction is less than the threshold of 0.4 Pa in the majority of the LPR for river flows up to 100 m^3/s. Therefore, the more consolidated bed underneath the fluff layer is likely not eroded during such river flows, thus limiting scour depths and net down-estuary SSF. In other words, erosion is limited to the fluff layer in the majority of the LPR during river flows up to 100 m^3/s, with some of the eroded material deposited at locations farther seaward. Furthermore, as seen in Figure 3.6, peak ebb skin friction exceeds 0.4 Pa at the more seaward locations (e.g., in the vicinity of RM 1.4) only when river flow exceeds about 200 m^3/s. Therefore, erosion is expected to be limited to the fluff layer for river flows up to about 200 m^3/s at the more seaward reaches.

Figure 3.13 shows the tidally-integrated net SSF for the 2010 moored deployment as a function of river flow. The general trends noted in Figure 3.12 are apparent in this dataset as well, with the magnitude and direction of net SSF dependent on river flow, low river flow periods associated with net up-estuary SSF, and a transition to net down-estuary SSF at higher river flows. Note the higher range of river flow rates for this dataset, up to 280 m^3/s, as compared to the 2009 moored deployment. Although the 2010 moored deployment includes river flows greater than 200 m^3/s (threshold based on river-wide impacts as seen from the peak ebb skin friction in Figure 3.6), sediment dynamics in this dataset are subject to certain qualifiers that are also relevant to one of the findings of this chapter. In contrast to the erosional response noted in the more landward reaches during above-average river flows in the 2009 moored deployment, comparison of the net SSF during flow rates greater than 200 m^3/s at the various locations shows relatively similar values between RM 13.5 to RM 4.2, with only RM 1.4 showing somewhat higher SSF.

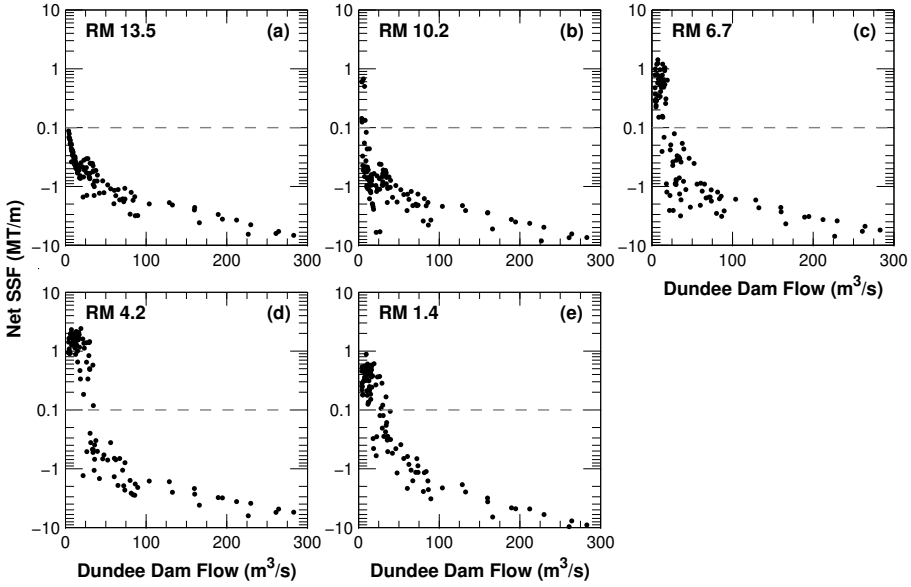

Figure 3.13: Calculated net SSF (integrating all transport processes) as a function of measured river flow rate at the head-of-tide for the 2010 moored deployment. Comparisons at (a) RM 13.5, (b) RM 10.2, (c) RM 6.7, (d) RM 4.2, and (e) RM 1.4. Fluxes calculated by integrating over depth and over time (two tidal cycles) using a fixed-window scheme. Positive and negative values indicate fluxes directed up-estuary and down-estuary, respectively.

The time-history of river flow is relevant in interpreting sediment dynamics during river flows greater than 200 m^3/s in this dataset. The 2010 deployment started on March 22, 2010 following a high river flow event of 450 m^3/s (return period of 25 years) on March 16, 2010. Subsequently, river flow decreased to 170 m^3/s on March 22, decreased further to 120 m^3/s on March 28, before increasing to 280 m^3/s on April 1. As elaborated in the following section, the 450 m^3/s event on March 16 caused significant erosion (nominally defined as depths in excess of the fluff layer thickness) within the LPR which influenced the sediment dynamics of the system during the subsequent 280 m^3/s event. Measurements of sediment erodibility in the LPR (Borrowman *et al.* [48]) show decreasing erodibility (τ_{Cr} increasing) with depth in the bed (measurements up to about 40 cm deep). This suggests that the less erodible bed strata exposed as a consequence of erosion during the 450 m^3/s event would not be expected to erode under the relatively lower skin friction of the following 280 m^3/s event. The lack of significant erosion noted in Figure 3.13 during flows greater than 200 m^3/s is consistent with this explanation derived from empirical measurements of sediment erodibility. Furthermore, this pattern of significant erosion during the 450 m^3/s event on March 16 and relatively little erosion during the subsequent 280 m^3/s event was also reproduced by numerical sediment transport models (U.S. Environmental Protection Agency [38]; Moffatt and Nichol and Deltares [31]). Therefore, the lack of significant erosion in the river during flows greater than 200 m^3/s in the 2010 moored deployment dataset is related to time-history of river flow

rather than being indicative of sediment dynamics had these flow conditions occurred sufficiently removed in time from the preceding 450 m^3/s event.

Although the SSF from the mooring data do not allow for evaluation of events exhibiting signification erosion, the periodic bathymetry surveys encompassed periods with river flows up to 700 m^3/s as well as below-average river flows, allowing for an evaluation of the river dynamics under importing, exporting, and erosional conditions. The along-channel transect during the 450 m^3/s event on March 16, 2010 presented in Figure 3.4 also provides evidence of significant erosion and is discussed in the next section.

3.4.5. SEDIMENT DYNAMICS FROM MORPHOLOGICAL DATA

THE series of consecutive multi-beam bathymetry surveys during 2007 through 2012 were analyzed to calculate morphological changes during the intervening periods. The calculated bathymetric changes between successive individual surveys were averaged cross-sectionally and longitudinally over 1 mile (1.6 Km) intervals for an assessment of large-scale morphological changes. Figure 3.14 shows the results of this analysis,

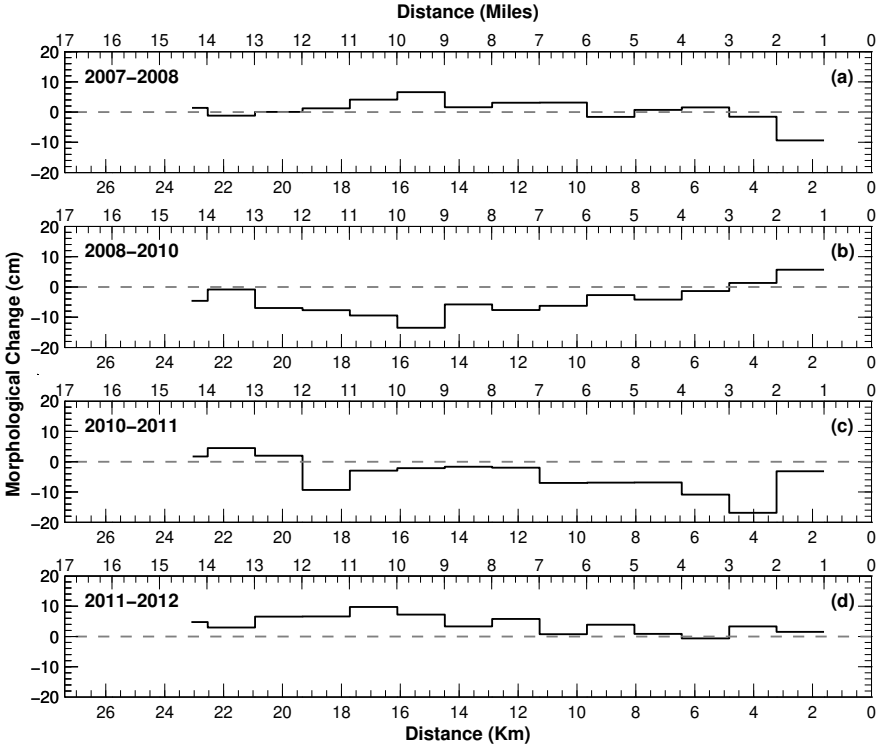

Figure 3.14: Longitudinal profile of measured bathymetric changes over various survey periods laterally and longitudinally averaged over 1.6 km (1 mile) intervals. Positive values indicate net deposition and negative values indicate net erosion. Morphological change over the (a) 2007–2008, (b) 2008–2010, (c) 2010–2011, and (d) 2011–2012 survey periods (see also Figure 3.2 for the hydrograph during these periods). Positive and negative values indicate deposition and erosion, respectively.

plotted as a profile of morphological change along the longitudinal axis of the LPR.

The morphological changes show a correspondence with river flow that is similar to the SSF trends in the mooring data. For instance, river flow in the periods encompassed by the 2007–2008 and 2011–2012 surveys was relatively low compared to the periods encompassed by the 2008–2010 and 2010–2011 surveys. The former periods had only three events and one event, respectively, above 100 m^3/s, and no events above 200 m^3/s (see Figure 3.2). However, the latter periods had several events above 100 m^3/s as well as 200 m^3/s, with 450 m^3/s events in March 2010 and March 2011 and a 700 m^3/s event in August 2011. The impact of river flow is seen in the morphological changes measured during these periods, with the 2007–2008 and 2011–2012 periods exhibiting a generally depositional signal, albeit with some localized erosion, whereas the high river flow periods (2008–2010 and 2010–2011) show generally erosion over much of the LPR. It should be noted that the erosion measured between RM 1–2 during the 2007–2008 period is mostly due to ship-induced scour; this reach of the LPR includes several active maritime terminals. With the exception of a few events with river flow between 100–200 m^3/s during 2007–2008 and 2011–2012, the LPR mostly experienced river flows corresponding to importing regimes. Therefore, the net infilling during these periods is considered to be associated with the estuarine circulation and barotropic processes as seen in the analysis of SSF from the mooring data.

In contrast, the two high river flow periods (2008–2010 and 2010–2011) experienced events with river flow in excess of 200 m^3/s when the consolidated bed underneath the fluff layer are expected to be subject to scour (as seen from Figure 3.6). This helps explain the erosion noted in the 2008–2010 and 2010–2011 periods. There are certain localized signals such as (1) relatively lower erosion landward of RM 7 during 2010–2011 than during 2008–2010 which may be caused by armoring of the bed in these areas during the 2008–2010 period, (2) relatively large erosion between RM 11–12 during 2010–2011 which was caused by a temporary constriction of the river due to bridge construction, and (3) erosion extending farther seaward during 2010–2011 than during 2008–2010 due to the higher river flow during the former period. The overall pattern noted during these two high river flow periods is one of scour, with scour depths largely in excess of the fluff layer thickness, a result consistent with the estimates of skin friction from the numerical model and its comparison to the for the fluff layer and the more consolidated bed underneath. Furthermore, the pattern of significant erosion during the 450 m^3/s and 700 m^3/s events was also reproduced by numerical sediment transport models (U.S. Environmental Protection Agency [38]; Moffatt and Nichol and Deltares [31]).

The erosion noted in the 2008–2010 period is also seen directly in the water column data. Specifically, the 450 m^3/s event on March 16, 2010 was the largest event measured during the 2008–2010 period and the likely cause of the erosion measured in the bathymetry data. Measurements during this event are presented in panel b of Figure 3.4 — both the salt front and ETM were pushed to mouth of the LPR, with elevated SSC within the ETM as well as landward of the ETM (as compared to the low river flow transect in panel a of Figure 3.4). Depth-average SSC landward of the ETM averaged approximately 120 mg/L whereas SSC at the head-of-tide (estimated using a rating curve) is only about 50 mg/L (Moffatt and Nichol and Deltares [31]) indicating significant erosion landward of the ETM. Two similar transects (data not shown) collected during other phases

of the tide during this same event show similar trends. This is a direct line of evidence indicating scouring conditions at river flows greater than 200 m^3/s and is consistent with the measured morphological change during 2008–2010. Both the 450 m^3/s and 700 m^3/s events in 2010 and 2011 represent extreme river flow conditions where the salt front is pushed to the mouth of the river and the entire river experiences skin friction greater than 0.4 Pa, with erosion of the more consolidated bed beneath the fluff layer.

Therefore, the erosion measured in the morphological data over the 2008–2010 and 2010–2011 periods is considered to have been caused by the relatively extreme 450 m^3/s and 700 m^3/s river flow events during these periods. Although not direct evidence linking the measured erosion to the extreme river flow events, the various lines of evidence discussed above support the notion of significant estuary-wide scour during river flows in excess of 200 m^3/s. The findings from the analysis of the morphological changes are combined with the results of SSF dynamics from the mooring data and used to develop a conceptual picture of estuarine sediment dynamics in the following section.

3.5. DISCUSSION

THE results of the SSF decomposition allows for an assessment of the various hydrodynamic forcings on sediment transport in the LPR. Since the residual, i.e., river flow, is directed down-estuary, net sediment transport associated with river flow is also directed down-estuary. In contrast, barotropic and baroclinic processes promote up-estuary transport. During low river flow, lag effects and tidal asymmetries induced by barotropic circulation, and estuarine circulation induced by salinity intrusion and mixing typically lead to net up-estuary transport of sediment. Increasing river flow modifies both the barotropic and baroclinic transport pathways. The additional freshwater inflow pushes the salt front seaward, thus limiting the spatial extent of estuarine circulation as a transport mechanism. Similarly, increasing freshwater inflow reverses the flood-dominance in barotropic currents and also alters lag effects resulting in net SSF directed down-estuary during high river flows.

The primary finding of this chapter is a conceptual picture of sediment dynamics, with the estuary following one of three modes — importing, flushing, or scouring. During low river flow conditions, tidal and estuarine processes dominate sediment transport and the system imports sediments from locations farther seaward (as well as from the head-of-tide) and is a net sink for sediments. In general terms, low river flow conditions represent an importing regime (Regime I). Conversely, increasing river flow is associated with net down-estuary SSF at all locations, and a net export of sediment from the system. In other words, high river flow conditions represent an exporting regime, when the system is a net source of sediments and exports sediments to locations farther seaward. The exporting regime can be further divided into two conditions, distinguished by morphological impact — flushing conditions, thus referred to since only the easily-erodible sediment in the fluff layer are expected to be eroded (Regime II), and scouring conditions, thus referred to since the more consolidated bed layers underneath the fluff layer are eroded (Regime III). In the LPR, the threshold between flushing and scouring regimes is estimated to be approximately 200 m^3/s for the system as a whole, although locally, such as in the areas landward of RM 8, the threshold is lower. The threshold of 200 m^3/s also represents conditions when the salt front is located near the mouth of the

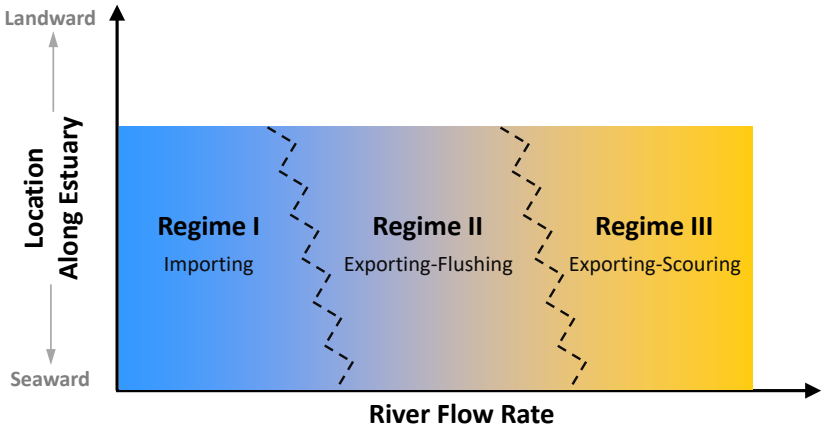

Figure 3.15: Conceptual picture of estuarine sediment transport regimes — importing, exporting-flushing, and exporting-scouring. The gradient in colors indicates the increasing SSC and increasing potential for morphological change from Regime I to Regime III. The lines separating the regimes are inclined to indicate the generally decreasing river flow thresholds between regimes with distance up-estuary. The lines separating the regimes are jagged to indicate that local variations are possible around this general pattern of decreasing river flow threshold between regimes with distance up-estuary; for instance, in response to local changes in cross-sectional area. The lines separating the regimes are dashed to indicate that temporal variations are possible for the river flow threshold separating the regimes; for instance, in response to local erosion and deposition, dredging, etc.

river.

Figure 3.15 shows a conceptual picture of the sediment dynamics in the LPR following the three regimes. The freshwater flow rates associated with the thresholds between regimes are spatially variable. For instance, as seen in Figure 3.12, the threshold between Regimes I and II is estimated to be about 10 m^3/s at RM 10.2, and between 20–30 m^3/s at RM 1.4, and as seen in panel b of Figure 3.6, the threshold between Regimes II and III is estimated to be about 100 m^3/s at RM 8, and about 200 m^3/s at RM 1.4. The spatial variation in flow thresholds means that these regimes may not be synchronous along the length of the river, e.g., an event that produces Regime II behavior at an up-estuary location may induce a Regime I behavior at a down-estuary location. Comparison of these flow thresholds to the long-term (over a hundred years) hydrograph in the LPR shows the temporal prevalence of these regimes. Freshwater flow rate of 30 m^3/s is exceeded about 40% of the time, 100 m^3/s about 5% of the time, and 200 m^3/s less than 1% of the time. In other words, importing regimes persist the majority of the time and exporting regimes, in particular, exporting-scouring regimes, occur only during a relatively small fraction of the time. However, as seen in Figure 3.12 and Figure 3.13, net down-estuary SSF at high river flows are orders-of-magnitude larger than the up-estuary SSF at low river flows, suggesting that even though exporting regimes occur a small fraction of the time, net export during such conditions is a significant fraction of the long-term sediment mass budget. As seen from the infill rate during 2011–2012 following the erosional events of 2008–2010 and 2010–2011, the recovery (infilling) time is estimated to be on

the order of about one year or more (depending on the magnitude of the event). This implies that the impact of these extreme events persists for an extended period.

With the exception of Regime III, the general conceptual picture of importing and exporting regimes described here is consistent with studies of other estuaries around the world. Based on analysis of SSF in the Hudson River, USA, Geyer *et al.* [14] concluded net import of sediments during average flow conditions, and net export during elevated river flow (coincident with spring tides). Similar observations have also been reported in other estuaries (Huangmaohai Estuary, China by Gong *et al.* [26]; Delaware River, USA by McSweeney *et al.* [27]; and Wairoa River, New Zealand by Pritchard and Green [28]) as well as in the LPR by Chant *et al.* [25]. River discharge (possibly in combination with spring tides) is the main factor in determining the transition from importing to exporting regimes. Wider estuaries with significant inter-tidal areas or shallow tidal flats may also show cross-channel variations in importing and exporting regimes. For example, in the Delaware River, USA, McSweeney *et al.* [27] show net sediment export across the entire cross-section during high river flow periods, but net import along the deeper portions of the channel and net export along the shallow flanks during low river flow periods. A similar result was also reported by Scully and Friedrichs [15] in the York River, USA. The main contribution of this chapter towards the understanding of estuarine sediment dynamics is the assessment of sediment dynamics over the full range of hydrologic conditions and over longer timescales which results in the delineation of the exporting regime into exporting-flushing and exporting-scouring regimes.

The finding of Regime III is relevant in the context of the long-term morphological evolution of estuaries. Meade [49] noted that the typical morphological behavior of estuaries in the Holocene epoch is a slow infill with sediment originating from fluvial and marine sources, eventually reaching a (dynamic) equilibrium between sediment supply and export. Furthermore, the exporting conditions necessary for maintaining the long-term equilibrium are thought to be extreme events when the flow is directed seaward at all depths within the estuary and the salt front is pushed out of the estuary (Meade [49]). This general narrative was also proposed by Geyer *et al.* [14] who found the short-term sediment import from fluvial and marine sources in the Hudson River estuary to be significantly higher than the long-term net sedimentation rate measured from radionuclide data. Since the Hudson River is at morphodynamic equilibrium, Geyer *et al.* [14] hypothesized the occurrence of episodic events at decadal time-scales as the mechanism causing erosion and export of accumulated sediments, thus maintaining the long-term morphodynamic equilibrium and accounting for the difference between the short-term and long-term sedimentation rates. The hypothesis of episodic erosion in the lower Hudson River estuary was also verified by Ralston *et al.* [22] who calculated significant erosion in model simulations of a river flow event with a return period of 60 years. The finding of Regime III events in the LPR is consistent with the hypothesis of Meade [49] and Geyer *et al.* [14]. Therefore, Regime III events may be considered representative of the mechanism responsible for maintaining long-term estuarine morphodynamic equilibrium in such estuaries.

The conceptual picture outlined in Figure 3.15 is also responsive to morphological change. For instance, deepening of the system (due to dredging or erosion) or a reduction in water depths due to sedimentation may change the threshold river flow rates

separating the three regimes (in addition, tidal propagation may also be impacted by morphological change). In other words, the morphodynamic response of the system at any given time is a function of the existing river flow rate, as well as the time-history of river flow rate and the morphological state of the system. This is seen in the lack of significant erosion during above-average river flows in the 2010 moored deployment data which is likely related to the armoring effects of the preceding 450 m^3/s event on March 16, 2010. Another example relates to the long-term (decadal-scale) morphological evolution of the LPR relative to the short-term event-driven dynamics conceptualized by Figure 3.15. As shown in Chant *et al.* [25], the long-term large-scale morphological behavior of the LPR is an infilling trend following the dredging of the navigation channel in the late 1940s which deepened the LPR below its morphological equilibrium. However, despite this long-term infilling trend, short-term trends are more variable — high-flows induce erosion as seen in the morphological change during 2008–2010 and 2010–2011, whereas low–average river-flows promote infilling as seen in the morphological change during 2007–2008 and 2011–2012, and in the mooring data. This implies that it is not possible to assess whether a river is in morphodynamic equilibrium on the basis of short-term measurements. Furthermore, the infilling trend noted in the mooring data under low–average river flows may also be altered by the time-history of river flow. For instance, the 2009 mooring data were collected during a prolonged period of infill (mostly Regime I) following a Regime III event in April 2007 (see Figure 3.2). Measurements during similar river flows during other periods may show a slightly different picture, primarily for the river flow thresholds separating the three regimes. Therefore, the analysis of sediment dynamics in such systems also needs to consider the long-term response of the system (morphological status relative to the long-term equilibrium morphology), river flow at given time, and the time history of river flow in the system (for example, occurrence of Regime III events which may promote Regime I behavior during subsequent periods).

In addition to its morphodynamic relevance, the conceptual picture outlined in Figure 3.15 also indicates the relevance of the fluff layer for estuarine sediment dynamics (note that this point is mainly relevant for transport associated with barotropic circulation). Sediment dynamics (erosion and deposition) are mostly restricted to the fluff layer during Regimes I and II which persist about 95% of the time landward of RM 8, and about 99% of the time landward of RM 1.4. In other words, fluff layer dynamics dominate sediment dynamics in the system the majority of the time. Therefore, reproducing the spatial and temporal trends in SSC and SSF in a numerical model under such conditions is dependent on the appropriate parameterization of the erodibility of the fluff layer.

It should be noted that there is some uncertainty associated with the river flow thresholds characterizing the various regimes. The uncertainty derives from potential cross-channel variations in flow rates (the mooring data represents measurements at a single location in the cross-section), and variability in the ABS-SSC relationships used to estimate SSC, and subsequently, SSF at the mooring locations. Such artifacts mainly affect the river flow threshold separating Regimes I and II rather than the conceptual definition of these regimes and relevant transport processes. Another uncertainty described previously relates to the use of empirical SSC measurements, and the limitation of the SSF decomposition approach in accurately ascribing SSF to the various flow components. However, the various lines of evidence (SSF dynamics, along-channel transects, mor-

phological changes measured in the bathymetry surveys, sediment erodibility measurements, and the numerical model) tend to a single conceptual picture of sediment dynamics. Therefore, the overall conclusions from the analysis of sediment dynamics and the conceptual picture of sediment transport presented here are valid.

3.6. CONCLUSIONS

ESTUARINE sediment dynamics reflects a complex interplay between barotropic, estuarine, and fluvial forcings. The relative importance of these forcings can vary spatially along the length of the system as well as laterally (in relatively wide systems). Sediment dynamics during low river flow conditions are primarily influenced by the formation and persistence of a thin layer of easily erodible sediments termed the fluff layer, deposited around slack water and eroded during the following flood or ebb phase of the tide. In the LPR, for the system as a whole, fluff layer dynamics persist and are relevant for sediment dynamics about 99% of the time. The net direction of sediment transport during low river flow is typically up-estuary, induced by barotropic lag effects and tidal asymmetries, and estuarine circulation. Increasing river flow causes an increase in currents and shear stresses during ebb, resulting in net erosion and flushing of the sediments contained within the fluff layer (up to a certain river flow threshold, estimated as 200 m^3/s for the LPR), and net export of sediments from the estuary. Only when river flow exceeds 200 m^3/s, is erosion expected to scour the more consolidated bed underneath the fluff layer and cause estuary-wide erosional impacts. Depending on the magnitude of the event, the impact of these extreme events may persist and influence sediment dynamics for an extended period (on the order of over a year for the events examined in this chapter). The analyses presented in this study allow for the classification of a given estuary at any given time into one of three regimes — importing, exporting-flushing, and exporting-scouring, in decreasing order of temporal prevalence. The morphodynamic response and categorization of the system into one of these three regimes at any given time also depends on the long-term morphological progression, river flow rate at given time, and time-history of river flow. The exporting-scouring regime represents an important aspect of the hydro-sedimentological behavior of estuaries and likely represents the conditions responsible for maintaining long-term morphodynamic equilibrium in estuaries.

REFERENCES

[1] K. R. Dyer, *Estuaries: A Physical Introduction*, 2nd ed. (John Wiley and Sons, New York, 1997).

[2] J. J. Dronkers and J. C. Schönfeld, *Tidal computations in shallow water – Report on hydrostatic levelling across the Westerschelde* (Rijkswaterstaat, The Netherlands, 1959).

[3] C. T. Friedrichs and D. G. Aubrey, *Non-linear tidal distortion in shallow well-mixed estuaries: a synthesis,* in *Estuar Coast Shelf S*, Vol. 27 (1988) pp. 521–545.

[4] J. Dronkers, *Dynamics of coastal systems,* in *Advanced Series on Ocean Engineering*, Vol. 25 (World Scientific, 2005).

[5] V. M. Gatto, B. C. van Prooijen, and Z. B. Wang, *Net sediment transport in tidal basins: quantifying the tidal barotropic mechanisms in a unified framework,* Ocean Dynam **67**, 1385 (2017).

[6] J. Dronkers, *Tidal asymmetry and estuarine morphology,* Neth J Sea Res **20**, 117 (1986).

[7] J. van de Kreeke and K. Robaczewska, *Tide-induced residual transport of coarse sediment: Application to the Ems estuary,* Neth J Sea Res **31**, 209 (1993).

[8] A. J. F. Hoitink, P. Hoekstra, and D. S. van Maren, *Flow asymmetry associated with astronomical tides: Implications for the residual transport of sediment,* J Geophys Res **108**, 3315 (2003).

[9] H. Postma, *Hydrography of the Dutch Wadden Sea,* Arch Neerl Zool **10**, 405 (1954).

[10] H. Postma, *Transport and accumulation of suspended matter in the Dutch Wadden Sea,* Neth. J. Sea Res **1**, 148 (1961).

[11] L. M. J. U. van Straaten and P. H. H. Kuenen, *Accumulation of fine grained sediments in the Dutch Wadden Sea,* Geologie en Mijnbouw **19** (1957).

[12] L. M. J. U. van Straaten and P. H. H. Kuenen, *Tidal action as a cause of clay accumulation,* J Sediment Petrol **28**, 406 (1958).

[13] D. Salas-Monreal and A. Valle-Levinson, *Sea-level slopes and volume fluxes produced by atmospheric forcing in estuaries: Chesapeake Bay case study,* J Coastal Res **24**, 2 (2008).

[14] W. R. Geyer, J. D. Woodruff, and P. Traykovski, *Sediment transport and trapping in the Hudson River estuary,* Estuaries **24**, 670 (2001).

[15] M. E. Scully and C. T. Friedrichs, *Sediment pumping by tidal asymmetry in a partially mixed estuary,* J Geophys Res **112**, 07028 (2007).

[16] C. K. Sommerfield and K. C. Wong, *Mechanisms of sediment flux and turbidity maintenance in the Delaware estuary,* J Geophys Res **116**, C01005 (2011).

[17] H. Burchard, H. M. Schuttelaars, and D. K. Ralston, *Sediment trapping in estuaries,* Annu Rev Mar Sci **10**, 371 (2018).

[18] Y. M. Dijkstra, H. M. Schuttelaars, and H. Burchard, *Generation of exchange flows in estuaries by tidal and gravitational eddy viscosity-shear covariance (ESCO),* J Geophys Res Oceans **122**, 4217 (2017).

[19] J. F. Festa and D. V. Hansen, *Turbidity maxima in partially mixed estuaries: A two-dimensional numerical model,* Estuar Coast Mar Sci **7**, 347 (1978).

[20] H. Burchard and H. Baumert, *The formation of estuarine turbidity maxima due to density effects in the salt wedge: A hydrodynamic process study,* J Phys Oceanogr **28**, 309 (1998).

[21] L. P. Sanford, S. E. Suttles, and J. P. Halka, *Reconsidering the physics of the Chesapeake Bay estuarine turbidity maximum,* Estuaries **24**, 655 (2001).

[22] D. K. Ralston, J. C. Warner, W. R. Geyer, and G. R. Wall, *Sediment transport due to extreme events: The Hudson River estuary after tropical storms Irene and Lee,* Geophys Res Lett **40**, 5451 (2013).

[23] J. C. Winterwerp, J. Vroom, Z. B. Wang, M. Krebs, E. C. M. Hendriks, D. S. van Maren, K. Schrottke, C. Borgnsmuller, and A. Schol, *SPM response to tide and river flow in the hyper-turbid Ems river,* Ocean Dynam **67**, 559 (2017).

[24] L. Guo, M. van der Wegen, J. A. Roelvink, and Q. He, *The role of river flow and tidal asymmetry on 1-D estuarine morphodynamics,* J Geophys Res Earth Surf **119**, 2315 (2014).

[25] R. J. Chant, D. Fugate, and E. Garvey, *The shaping of an estuarine Superfund site: Roles of evolving dynamics and geomorphology,* Estuar Coast **34**, 90 (2011).

[26] E. Gong, L. Jia, J. Shen, and J. T. Liu, *Sediment transport in response to changes in river discharge and tidal mixing in a funnel-shaped micro-tidal estuary,* Cont Shelf Res **76**, 89 (2014).

[27] J. M. McSweeney, R. J. Chant, and C. K. Sommerfield, *Lateral variability of sediment transport in the Delaware estuary,* J Geophys Res-Oceans **121**, 725 (2016).

[28] M. Pritchard and M. Green, *Trapping and episodic flushing of suspended sediment from a tidal river,* Cont Shelf Res **143**, 286 (2017).

[29] S. Ouillon, *Why and how do we study sediment transport? Focus on coastal zones and ongoing methods,* Water **10**, 390 (2018).

[30] C. K. Sommerfield and R. J. Chant, *Mechanisms of Sediment Trapping and Accumulation in Newark Bay, New Jersey: An Engineered Estuarine Basin* (Hudson River Foundation, New York, NY, 2010).

[31] Moffatt and Nichol and Deltares, *Appendix M: Sediment transport model of the Lower Passaic River, Lower Passaic River RI/FS* (Cooperating Parties Group, Newark, NJ, 2019).

[32] R. Mathew and J. C. Winterwerp, *Surficial sediment erodibility from time-series measurements of suspended sediment concentrations: Development and validation,* Ocean Dynam **67**, 691 (2017).

[33] K. L. Deines, *Backscatter estimation using broadband acoustic doppler current profilers,* in *Oceans 99 MTS/IEEE Conference Proceedings* (Seattle, WA, 1999).

[34] G. R. Wall, E. A. Nystrom, and S. Litten, *Use of an ADCP to Compute Suspended-Sediment Discharge in the Tidal Hudson River, New York* (USGS SIR 2006-5055, 2006).

[35] HydroQual, *Final Hydrodynamic Modeling Report: Lower Passaic River Restoration Project and Newark Bay Study* (Mahwah, NJ, 2008).

[36] L. C. van Rijn, *Sediment transport part II: Suspended load transport,* J Hydraul Eng-ASCE **110**, 1613 (1984).

[37] Chesapeake Biogeochemical Associates, *Passaic River Erosion Testing and Core Collection: Field Report and Data Summary* (2006).

[38] U.S. Environmental Protection Agency, *Record of Decision, Lower 8.3 miles of the Lower Passaic River, Part of the Diamond Alkali Superfund Site* (US EPA Region 2, New York, USA, 2016).

[39] L. C. van Rijn, *Principles of Sediment Transport in Rivers, Estuaries, and Coastal Seas* (Aqua Publications, Emmeloord, The Netherlands, 1993).

[40] J. C. Winterwerp, Z. B. Wang, T. van der Kaaij, K. Verelst, A. Bijlsma, Y. Meersschaut, and M. Sas, *Flow velocity profiles in the Lower Scheldt estuary,* Ocean Dynam **56**, 284 (2006).

[41] R. J. Uncles and M. B. Jordan, *Residual fluxes of water and salt at two stations in the Severn estuary,* Estuar Coast Mar Sci **9**, 287 (1979).

[42] J. C. Winterwerp, *Decomposition of the mass transport in narrow estuaries,* Estuar Coast Shelf S **16**, 627 (1982).

[43] R. G. Costa, *Flow-fine sediment hysteresis in sediment-stratified coastal waters,* (MS Thesis, University of Florida, Gainesville, 1989).

[44] D. A. Jay, R. J. Uncles, J. Largier, W. R. Geyer, J. Vallino, and W. R. Boynton, *A review of recent developments in estuarine scalar flux estimation,* Estuaries **20**, 262 (1997).

[45] E. Siegle, C. A. F. Schettini, A. H. F. Klein, and E. E. Toldo, *Hydrodynamics and suspended sediment transport in the Camboriu estuary Brazil: Pre jetty conditions,* Braz J Oceanogr **57**, 123 (2009).

[46] J. A. Lerczak, W. R. Geyer, and R. J. Chant, *Mechanisms driving the time-dependent salt flux in a partially stratified estuary,* J Phys Oceanogr **36**, 2283 (2006).

[47] J. Becherer, G. Flöser, L. Umlauf, and H. Burchard, *Estuarine circulation versus tidal pumping: Sediment transport in a well-mixed tidal inlet,* J Geophys Res Ocean **121**, 6251 (2016).

[48] T. D. Borrowman, E. R. Smith, J. Z. Gailani, and L. Caviness, *Erodibility study of Passaic River sediments using USACE Sedflume* (ERDC TR-06-7, Kansas City, Missouri, 2006).

[49] R. H. Meade, *Landward transport of bottom sediments of the Atlantic coastal plain,* J Sediment Petrol **39**, 222 (1969).

4

MORPHODYNAMIC MODELING AND MORPHOLOGICAL UPSCALING

Sediment transport and morphodynamics in fine sediment systems is a non-equilibrium process related to sediment mobility and memory effects induced by the time-history of morphological development. These phenomena have been observed empirically in the Lower Passaic River estuary, with transport following various time-scales and river-flow dependent regimes. Here we present a process-based morphodynamic model using an extensive dataset of relevant physical measurements and extended to include morphological upscaling using the Morfac approach. Although the model performance does not capture measured morphological response at local scales over the short term, it predicts the large-scale short- and long-term morphological response. The model also confirms the empirically-derived conceptual picture of sediment dynamics. The model is subsequently applied to assess the long-term morphodynamic evolution of the estuary in response to changes in various forcings. The results support the application of the Morfac approach for assessing the long-term morphodynamics of such fine sediment systems.

This chapter is under review for publication in the journal Advances in Water Resources:
R. Mathew and J. C. Winterwerp, *Morphodynamic modeling and morphological upscaling in a fine sediment system*, Adv Water Resour [under review]

4.1. INTRODUCTION

THE morphological evolution of estuaries is of consequence for various management problems such as contaminant fate and transport, water quality, siltation of navigation channels, dredged material management, impact of engineering works, etc. Morphological change is a function of the bed-water exchange processes of erosion and deposition, and the water column transport processes of advection and dispersion. These processes are often parameterized and simulated in process-based numerical morphodynamic models for an assessment of morphological response to external forcings or to engineering works in the system. Such morphodynamic models have been developed and applied more commonly in sand-dominated [1] systems (Lesser *et al.* [1] and Roelvink [2]) than in fines-dominated systems (Vested *et al.* [3]), likely due to the site-specific, spatially-variable, and temporally-variable nature of various fine sediment transport processes that typically requires extensive data for representation and parameterization in numerical models. In addition, there are several important differences between sand and fine sediment transport that require examination in the context of process-based morphodynamic models.

Sand transport is typically an equilibrium process characterized by capacity load conditions, i.e., an equilibrium exists between the (local) sediment load and the (local) turbulent flow velocity. As this equilibrium is rapidly established under alluvial bed conditions, these systems are not affected by memory effects (e.g., related to the availability of mobile sediment in the bed) on shorter time scales. Consequently, morphological change in sandy settings is a function of gradients in transport and is generally calculated using equilibrium transport formulations (van Rijn [4]), although pick-up functions for prescribing bed-water exchange processes may be used as well. In contrast, fine sediment transport is typically characterized by non-equilibrium conditions with respect to the carrying capacity of the flow. This implies that the bed-water exchange processes have to be modeled explicitly through pick-up and deposition functions and cannot be described with equilibrium transport formulations. Specifically, non-linearities related to the supply of sediments in the bed, erodibility of sediments in the bed, or the settling velocity of fines can result in supply-limited, erosion-limited, and/or settling-limited conditions, respectively, that control local bed-water exchange (Winterwerp *et al.* [5]). In general, these conditions refer to beds comprised of a mixture of sands and fines that limits erosion of fines, beds with a vertical gradient in erodibility[2] that limits erosion under given shear stress, or systems where settling velocities are too low to achieve significant deposition of fines and thus limiting sediment availability for erosion. This implies that the amount of mobile sediment (i.e., the volume of sediment available for transport under given flow regime) is generally not constant, even over very small time-scales — this is in particular the case during short-lived events, such as storms, river floods, etc. The availability of mobile fine sediment therefore exhibits profound memory ef-

[1] Sand and fine-sediment are nominally defined as particle sizes greater than and less than 63 μm, respectively. Moreover, we implicitly assume that fines exhibit cohesive behavior.

[2] Erodibility in the context of this chapter refers to the critical shear stress for erosion, τ_{Cr}, the threshold bed shear stress required to be exceeded for surface erosion to occur following the Partheniades erosion formulation (Partheniades [6]). An increase in the critical shear stress for erosion with depth represents a decrease in sediment erodibility with depth.

fects, affected largely by past conditions and events. This steers the morphodynamic development on short (up to the tidal time-scale) and long time-scales (many years) and consequently, morphodynamics in fine sediment settings can be highly non-linear.

Related to the notion of erosion-limited transport is the effect of armoring, stratification, and consolidation of the sediment bed, primarily in causing a decrease in erodibility with depth for fine sediments (Mehta [7] and Sanford and Maa [8]) and thus limiting sediment mobility. A decrease in erodibility with depth implies that morphological response to a given event is dependent on the time-history of events (Vested *et al.* [3]). In other words, the system develops a memory (represented by the availability of mobile sediment) that influences subsequent morphological response. Such erosion-limited transport can occur during non-event (e.g., tide-dominated) conditions when erosion may be limited to a thin layer (thickness on the order of millimeters) of easily-erodible surficial sediments termed the fluff layer, as well as during episodic events when erosion may extend deeper into the bed (Winterwerp *et al.* [5], Mathew and Winterwerp [9], and Mathew and Winterwerp [10]). Morphological response to events may also exhibit a stepwise pattern. For instance, erosion during relatively small events (i.e., relatively low shear stress) may be restricted to the fluff layer and limited by the erodibility of more consolidated layers underneath, with only relatively large events (i.e., relatively high shear stress) causing erosion of the less erodible subsurface layers (Mathew and Winterwerp [10]). The availability of mobile sediment in the fluff layer is also dependent on the supply of sediments from the head-of-tide (generally event-dominated for fines), thus affecting sediment availability for subsequent redistribution.

The erosion-limited, supply-limited, and time-dependent morphological response governs the time-scales associated with morphological evolution in fines-dominated systems. One time-scale is that of the tidal period during non-event conditions, when erosion is limited to the fluff layer and residual transport associated with the tide and estuarine circulation dominates, modulated by the spring–neap cycle (Mathew and Winterwerp [10], Geyer *et al.* [11], and McSweeney *et al.* [12]). Another time-scale is that of episodic events (e.g., associated with elevated river flow) when erosion extends to the less erodible parent bed underneath the fluff layer and morphological response may be limited by erodibility and related to the time-history of events (Vested *et al.* [3] and Mathew and Winterwerp [10]). A third, intermediate time-scale is that of low-to-moderate events when erosion is limited to the fluff layer but transport (from the head-of-tide) is important for sediment supply considerations (Mathew and Winterwerp [10]). The morphodynamic evolution of fines-dominated systems is therefore governed by non-linear processes operating over various time-scales that induce a memory to the system response, as a result of which the order of events becomes important. This poses challenges for the morphodynamic modeling of such systems, beyond those encountered in sandy systems.

Typically, morphodynamic models for sandy systems are based on sediment transport models calibrated for relatively short-term periods, and then used to perform long-term simulations, sometimes up to centuries. Therefore, the first objective of this chapter is to investigate whether a similar procedure may be applied in erosion-limited, fine sediment settings where memory effects are prominent. We start from a mixed (sands and fines) sediment transport model, calibrated over a range of hydrologic conditions

and using various calibration metrics. The model is then run in morphodynamic mode, prescribing all hydrodynamic forcing in detail — we refer to brute-force morphodynamic simulations for periods of multiple years, with model performance assessed using measured morphological change. This is similar to the setup of morphodynamic models for sandy systems.

Further to morphodynamic process-based modeling in sandy systems, recent advances in this subject area include the development of the morphological acceleration factor (Morfac) technique for morphodynamic upscaling which enables simulations of morphological evolution over extended time-scales in a computationally efficient fashion (Lesser *et al.* [1], Roelvink [2], Ranasinghe *et al.* [13], and Lesser [14]). The Morfac approach has been successfully applied in sandy systems over multi-year to millennial time-scales by various authors (van der Wegen and Roelvink [15], Dam *et al.* [16], and Styles *et al.* [17]). Although not as extensively applied as for sandy systems, the Morfac approach has also been applied to fine sediment systems (Ganju *et al.* [18], George *et al.* [19], and van der Wegen and Jaffe [20]). However, as it is not obvious that the Morfac approach can yield realistic results for fine sediment systems with large memory effects at all time scales, the second objective of this chapter is to investigate the application and viability of the Morfac approach for erosion-limited fine sediment settings. Subsequently, the morphodynamic model using Morfac is used to address a few specific research questions related to long-term morphodynamic evolution.

Accordingly, the chapter is divided into three major parts. The first part describes the development, calibration, and analysis of the morphodynamic model for the particular estuary used here as a case study. The second part describes the extension of the morphodynamic model to include the Morfac approach and includes a comparison of results from the morphodynamic model with Morfac to the results of the morphodynamic model without Morfac (i.e., the results presented in the first part of the chapter). The second part also presents a comparison of performance of the morphodynamic model with Morfac to decadal-scale data for morphological change. Finally, the third part of the chapter presents the application of the morphodynamic model with Morfac to address a few questions pertaining to long-term morphodynamics — in particular, the role of navigation which is specific to the particular estuary presented here, the role of episodic storm events, and the impact of climate change. The following section presents an overview of morphodynamics in the estuary used here as a case study, followed by the afore-mentioned three major parts of the chapter and a discussion.

4.2. SITE OVERVIEW AND SEDIMENT DYNAMICS

THE data presented in this manuscript come from the Lower Passaic River (LPR), an estuary that is part of New York Harbor (Figure 4.1). The LPR is the subject of an ongoing environmental cleanup and restoration study and as part of this process, several datasets, including the data presented here, were collected to support the development and calibration of numerical hydrodynamic, sediment transport, and contaminant fate and transport models. The LPR stretches approximately 28 km long from its mouth in Newark Bay at approximately River Mile (RM) 0.5, to the head-of-tide at Dundee Dam (approximately RM 17.5). Newark Bay is connected to New York Harbor and Raritan Bay (and the Atlantic Ocean) via the tidal inlets Kill van Kull and Arthur Kill, respectively.

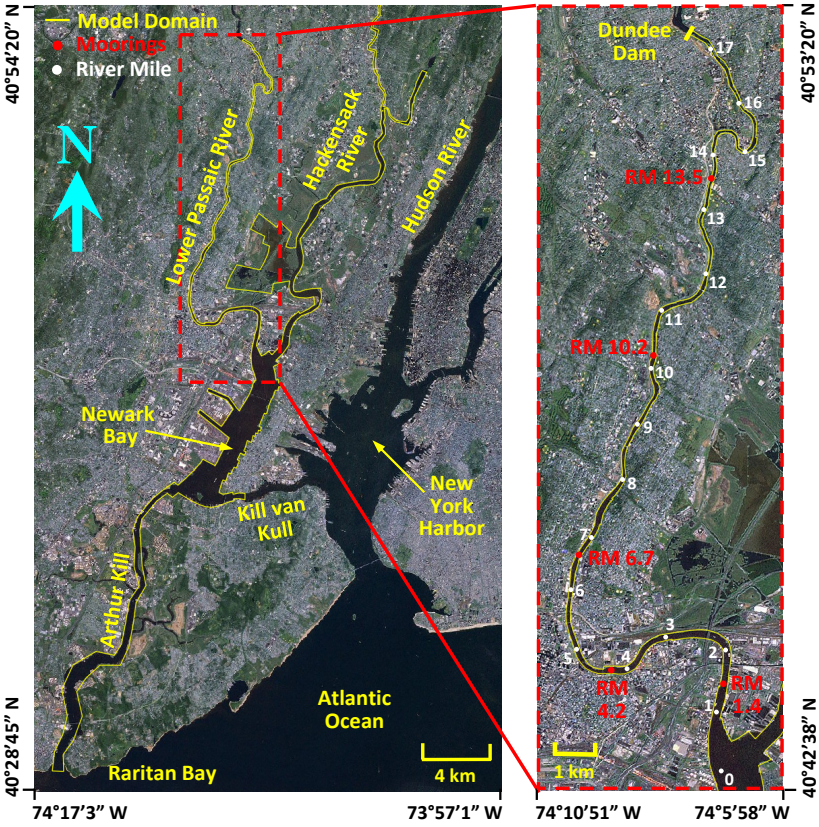

Figure 4.1: Location map of the Lower Passaic River along with the locations of in situ moorings and outline of model domain.

The width of the LPR ranges from approximately 600 m at its mouth, declining to about 200 m at RM 1.4, 150 m at RM 4.2, 120 m at RM 6.7, 90 m at RM 10.2, and 75 m at RM 13.5, i.e., locations about 1.5 km, 6 km, 10 km, 15.5 km, and 21 km, respectively, from the mouth of the river. These were also the locations of months-long (October 10, 2009 to December 16, 2009, and March 22, 2010 to July 24, 2010) in situ measurements of salinity, temperature, velocity, water depth, and suspended sediment concentrations (SSC; estimated using surrogate measurements of acoustic backscatter and a correlation of acoustic backscatter to SSC) used to calibrate the numerical model presented here. Typical water depths along the thalweg in the LPR currently range between 5 m to 7 m (with respect to mean sea level; MSL) and up to 17 m in the navigation channels in Newark Bay and Kill van Kull. The LPR is characterized by the remnants of a navigation channel dredged several decades ago and no longer actively maintained at design depths (which ranged from about 10 m at the mouth of the river to about 4 m in the upper reaches).

The hydrodynamics and sediment dynamics in the LPR were analyzed by Mathew

and Winterwerp [10] using the in situ data and are summarized here. The primary hydrodynamic forcings within the LPR include barotropic and baroclinic circulation, and river flow. Semi-diurnal tides (period of 12.42 h, corresponding to the dominant semi-diurnal M_2 constituent, and tidal range of 0.9 m to 2.1 m from neap to spring) entering Newark Bay through the Kill van Kull and Arthur Kill propagate to the LPR and the head-of-tide at Dundee Dam, forming an almost standing wave. Salinity intrusion occurs under most river flows (annual average river flow at Dundee Dam is about 34 m^3/s), with the saline water flushed out of the LPR at high river flows (>200 m^3/s; return period of 2 years). The extent of salinity intrusion, as indicated by the location of the salt front, is a function of the tidal phase, river flow, spring–neap cycle, as well as offshore mean water level fluctuations due to set-up and set-down events. The salt front also determines the location of the estuarine turbidity maximum (ETM), a zone of elevated SSC and enhanced sediment trapping.

Suspended sediments in the LPR varies over tidal time-scales, responding to the cyclic variations in tidal currents by eroding and replenishing (by deposition) the sediment inventory in the fluff layer. The presence of the fluff layer in the LPR has been observed in erodibility measurements using a Gust Microcosm on shallow sediment cores, as well as other lines of evidence (Mathew and Winterwerp [9]). The data show a thin pool (2–4 mm thick) of easily-erodible sediments overlying less-erodible strata and comprised of sediments that are resuspended twice every tidal cycle (once during flood and again during ebb) and redeposited around slack water. Increasing river flow alters these dynamics in two respects — by preventing deposition around slack water (i.e., preventing replenishment of the fluff layer), and by causing erosion of the more consolidated sediments underneath the fluff layer. Consequently, sediment transport, as inferred from the tidally-integrated net suspended sediment flux (SSF), is influenced by barotropic and baroclinic circulation, with the magnitude and direction of SSF modulated by river flow. During low river flow, lag effects and tidal asymmetries induced by barotropic processes, and baroclinic circulation induced by salinity intrusion and mixing result in net up-estuary transport of sediment. Increasing river flow reduces the influence of these up-estuary transport pathways, delivers additional sediment loading from the head-of-tide, causes erosion, and results in net down-estuary SSF.

The integrated impact of these various transport pathways is a system that imports sediment from Newark Bay (and from the head-of-tide) during low river flow conditions and exports sediment during high river flow conditions. Conceptually, sediment dynamics in the LPR follows one of three modes depending on river flow at any given time — importing, flushing, scouring (Mathew and Winterwerp [10]). In general terms, low river flow conditions are associated with net up-estuary SSF and represent an importing regime (Regime I), and conversely, increasing river flow is associated with net down-estuary SSF and export of sediment from the system. The exporting regime can be further distinguished into two conditions, distinguished by morphological impact — flushing conditions, thus referred to since only (mainly) the sediments within the fluff layer are eroded (Regime II), and scouring conditions, thus referred to since the more consolidated layers underneath the fluff layer are eroded (Regime III). In other words, during low-to-moderate river flows (Regimes I and II), erosion is limited to the fluff layer, and only during high river flows (nominally Regime III), are shear stresses high enough

to cause erosion of the less-erodible strata underlying the fluff layer (Mathew and Winterwerp [10]). Although variable locally, for the system as a whole, the river flow rate thresholds between Regimes I and II and between Regimes II and III are approximately 20–30 m^3/s and 200 m^3/s, respectively. This implies that sediment transport in the LPR is dominated by fluff layer dynamics, i.e., erosion-limited, the majority of the time. The availability of sediments in the fluff layer is responsible for the net transport of fine sediments by barotropic and baroclinic circulation against the direction of residual (river) flow. Therefore, the infill of the estuary with fines from down-estuary is governed by the fluff layer dynamics which therefore needs to be accounted for in the morphodynamic model.

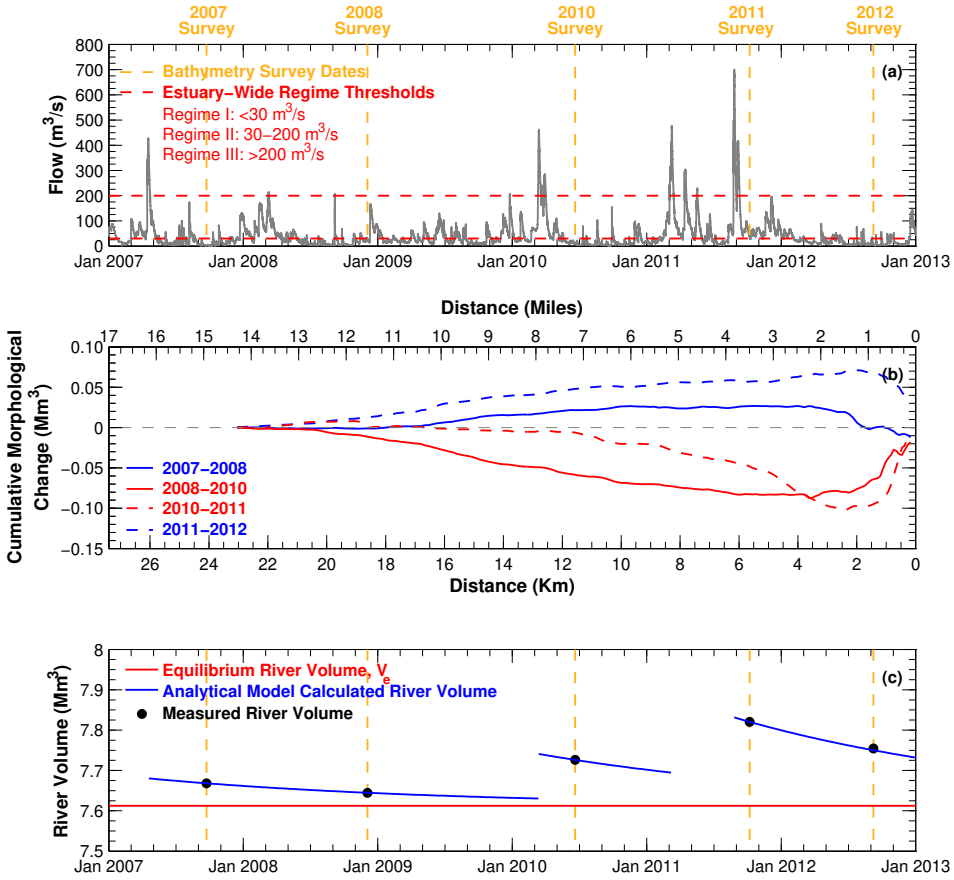

Figure 4.2: Time-series of (a) measured flow rate at the head-of-tide in the LPR over the period of the bathymetry surveys, (b) measured longitudinal profile of cumulative (in the seaward direction) volumetric morphological change in the LPR with positive and negative slopes indicating deposition and erosion, respectively, and (c) measured and the analytical model-calculated river volume landward of RM 2 (at mean sea level).

The general process of sediment import during low river flow periods and export during high river flow periods is also apparent in the morphological change measured in a series of inter-annual multi-beam bathymetric surveys performed in September 2007, November 2008, June 2010, October 2011, and September 2012 (Mathew and Winterwerp [10]). The cumulative volumetric change between consecutive surveys is shown in Figure 4.2 along with the river flow rate during this five-year period. River flow ranged from a low of about 1 m^3/s in October 2007, to highs of 450 m^3/s in March 2010 and March 2011 (return period of 25 years), and 700 m^3/s in August 2011 (return period of 90 years). The periods between the 2007–2008 and 2011–2012 surveys represent relatively low-flow conditions, with generally Regimes I and II events whereas the periods between the 2008–2010 and 2010–2011 surveys included several Regime III events and represent relatively high-flow conditions. The impact of the varying flow regimes is apparent in the measured morphological change, with different behavior for the reaches seaward and landward of RM 2. Landward of RM 2, the low-flow periods (2007–2008 and 2011–2012) experienced deposition whereas the high-flow periods (2007–2008 and 2011–2012) experienced erosion. The 2010–2011 period experienced erosion at locations further seaward than seen in the 2008–2010 period, an observation that is consistent with expectations given the greater magnitude of river flow events during the former period. In addition, effects of bed armoring are apparent in the morphological change over 2010–2011. Specifically, the reach landward of RM 7 does not show significant erosion during 2010–2011 which is in contrast to the significant erosion in this reach during 2008–2010. It is likely that a highly consolidated fine sediment layer and/or armoring by coarser sediment exposed during the Regime III event in 2008–2010 prevented further erosion in 2010–2011. Such erosion-limited behavior therefore needs to be accounted for in the morphodynamic model. In contrast, the reach seaward of RM 2 experienced deposition during the high-flow years because of the increasing river cross-section, and experienced erosion during the low-flow years because of the impact of ongoing shipping. This reach contains several active shipping terminals (U.S. Army Corps of Engineers [21]), and as explained subsequently, shipping-induced scour maintains a state of dynamic morphological equilibrium that is different than would be expected under natural conditions. Review of the bathymetry in the vicinity of the shipping terminals shows signification accretion in these areas during high-flow years, followed by erosion and a return to a near-equilibrium bathymetry under mean conditions.

The infill landward of RM 2 during the low-flow years was examined analytically for an assessment of large-scale morphodynamics. Assuming the infill as a diffusive process over longer time-scales, a heuristic exponential infill formulation is defined based on the "Volume-of-Cut method" described in Winterwerp *et al.* [5]:

$$V_t = V_e - (V_e - V_0) \exp\left(\frac{-V_e t}{V_0 k}\right) \tag{4.1}$$

where, k is the time-constant for the infill process, and V is the cumulative submerged river volume (calculated at MSL) landward of RM 2, with subscripts t, e, and 0 representing instantaneous, equilibrium, and initial quantities. Eq. 4.1 was used to describe the infill process between the 2007–2008 and 2011–2012 surveys using the measured initial and final river volumes, and the two unknowns, V_e and k, calculated as 7.61 Mm^3 and

795 days, respectively. The application of Eq. 4.1 to model infill over time in Figure 4.2 shows that measured river volumes in 2010 and 2011 were only 1.5% and 2.7% greater, respectively, relative to V_e, and the measured river volumes in all five surveys is very similar to V_e. This indicates that, as a whole, the reach landward of RM 2 is at or near morphodynamic equilibrium, with episodic Regime III events causing only a relatively small deviation from equilibrium.

The overall morphodynamic status of the LPR is also apparent from an assessment of two common morphodynamic relationships (longitudinal convergence of river cross-section, and tidal prism to cross-section relation [Winterwerp *et al.* [5] and D'Alpaos *et al.* [22]]) as shown in Figure 4.3. Between RM 2 and RM 15, the LPR conforms to the following trends:

- An exponentially converging form — given the cross-sectional area A_x at given location x, and the relationship $A_x = A_0 \exp(-x/L_A)$, the reference cross-section at RM 2, A_0, is calculated as 615 m^2, and convergence length, L_A, as 24.7 km. This indicates that even though the river was modified in the past (e.g., dredged for navigation, shorelines hardened, and inter-tidal wetlands reclaimed), it has retained an exponential cross-section distribution.

- A relationship between the cross-section area and tidal prism — given the cross-sectional area A_x and tidal prism $P_{T,x}$ at given location x, and the relationship $A_x = A_0 (P_{T,x}/P_{T,0})^{\alpha}$, the reference cross-section at RM 2, A_0, is calculated as 560 m^2, and the exponent, α, as 0.43. The exponent α is typically in the range of 0.85-1.1 in tidal inlets (D'Alpaos *et al.* [22]). The reason for the lower value noted in the LPR is further explored subsequently using the morphodynamic model presented here.

Seaward of RM 2, the river cross-section increases, and the relationship with tidal prism changes because of the morphological impact of shipping. The contrast with the trends landward of RM 2 suggests that the reach seaward of RM 2 is currently not at morphodynamic equilibrium (given natural hydrodynamic forcings) and is likely to experience infilling in the absence of shipping. Such infilling would be consistent with the historical morphological evolution of the LPR shown in Figure 4.3. As mentioned previously, the LPR was dredged for navigation purposes historically, with the last major dredging events occurring in 1950–1951 (between RM 0 to RM 6.7), and in 1983 (between RM 0 to RM 1.5) (U.S. Army Corps of Engineers [21]). Comparison of the post-dredging and current cross-sections in Figure 4.3 shows the morphodynamic response of the river to the disequilibrium induced by the dredging, with significant infilling between RM 0 to RM 6.7. This infilling was likely a combination of sediment deposited during Regime III events, and sediment transported up-estuary during Regime I and II conditions. The larger river cross-sections historically also imply that sediment trapping efficiency was greater historically and has decreased over time in response to the evolving morphology.

In summary, the availability of data describing short-term and long-term morphological change, along with data for parameterizing and calibrating a numerical model therefore provides opportunity for developing a morphodynamic model. The conceptual model of sediment dynamics (the three transport regimes, erosion-limited transport, fluff layer dynamics) described in this section was therefore used as the basis of

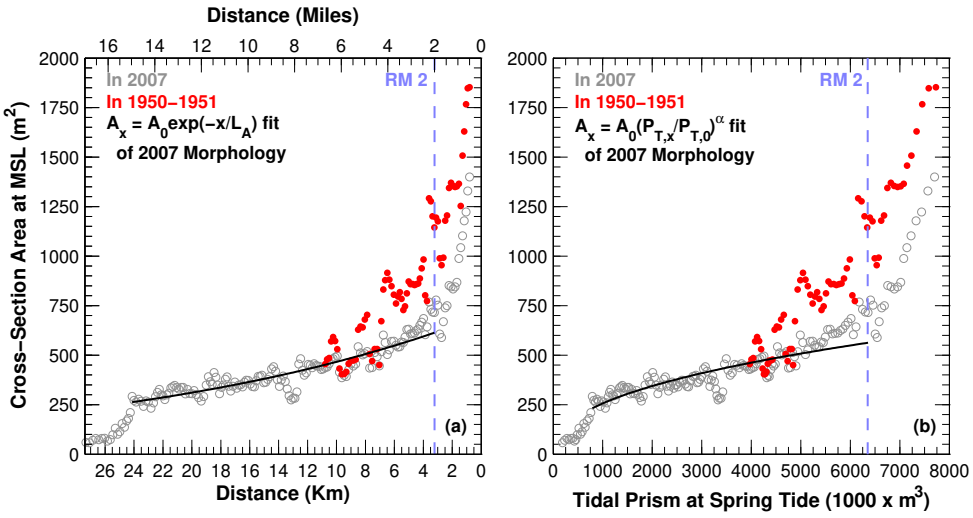

Figure 4.3: Relationship of submerged cross-sectional area (at MSL) with (a) distance along the river and (b) with tidal prism at spring tide. Cross-section area based on bathymetry in 2007 and 1950–1951. Tidal prism calculated using the numerical hydrodynamic model described in this chapter.

the morphodynamic model of the LPR, and subsequently, for application of the Morfac approach.

4.3. MORPHODYNAMIC MODEL

THE morphodynamic model presented in this chapter uses the Estuarine, Coastal and Ocean Model (ECOM) framework developed by Blumberg and Mellor [23], which includes integrated hydrodynamic and sediment transport sub-models. As part of the environmental studies of the LPR, ECOM was used for a regional-scale hydrodynamic model application (HydroQual [24]) as well as a sediment transport model application (Moffatt and Nichol and Deltares [25]) of the LPR. Model inputs and calibration parameters established as part of the hydrodynamic application were used in the morphodynamic model presented here. Although the sediment transport model application by (Moffatt and Nichol and Deltares [25]) used somewhat different formulations, some inputs such as initial conditions, erodibility inputs, boundary conditions, etc., used in the morphodynamic model presented here are based on the model application developed by Moffatt and Nichol and Deltares [25]. The formulations and setup of the morphodynamic model is presented next followed by the model performance.

4.3.1. MODEL SETUP

THE morphodynamic model involves a three-dimensional time-variable application over a domain that includes the LPR, Hackensack River, Newark Bay, Arthur Kill, and Kill van Kull (model domain shown in Figure 4.1). The spatial domain is resolved using a shoreline-fitted variable-resolution curvilinear orthogonal grid. Grid resolution

in the LPR ranges from seven cells across the river at RM 1.4 and decreasing to three cells across the river at RM 13.5. Average grid resolution in the LPR is 35 m wide and 140 m long, with a ten-layer σ-coordinate system in the water column. Boundary conditions for the hydrodynamic model include the measured river flow entering from the head-of-tide in the LPR and tributaries, and the tide, salinity, and temperature at the marine boundaries (Kill van Kull and Arthur Kill; boundary conditions specified using the results of the regional-scale hydrodynamic model. The hydrodynamic model was calibrated by adjusting bottom roughness and the horizontal eddy mixing to reproduce measured water level, and measured three-dimensional velocity, temperature, and salinity. Table 4.1 provides a tabulation of the major parameter values in the model.

Table 4.1: Parameter values for the hydrodynamic and sediment transport models

Parameter	**Value**
Bottom roughness, z_0 (mm)	1
Coefficient in Smagorinsky horizontal turbulence closure scheme	0.01
Fluff and transition layer thickness (mm)	2
Channel, Fluff and transition layer erosion rate coefficient, M (kg/m^2/Pa/s)	5×10^{-4}
Channel, Fluff layer critical shear stress, τ_{Cr} (Pa)	0.03
Channel, Transition layer critical shear stress, τ_{Cr} (Pa)	0.2
Shallows, Fluff and transition layer erosion rate coefficient, M (kg/m^2/Pa/s)	1.5×10^{-3}
Shallows, Fluff layer critical shear stress, τ_{Cr} (Pa)	0.01
Shallows, Transition layer critical shear stress, τ_{Cr} (Pa)	0.07
Consolidated layers, thickness at bed surface (mm)	25
Consolidated layers, critical shear stress at bed surface, τ_{Cr} (Pa)	0.5
Consolidated layers, critical shear stress at depth in bed, τ_{Cr} (Pa)	1.8
Consolidated layers, for $\bar{\tau}_b = 0.5 - 2$ Pa, erosion rate at surface, E (mm/s)	$2.5 \times 10^{-3} - 7.8 \times 10^{-2}$
Consolidated layers, for $\bar{\tau}_b = 0.5 - 2$ Pa, erosion rate at depth, E (mm/s)	$1 \times 10^{-4} - 3.2 \times 10^{-3}$
Critical shear stress for deposition, τ_{Dep} (Pa)	∞
Settling velocity of poorly-flocculated fines (mm/s)	0.20
Settling velocity of flocculated fines (mm/s)	0.40
Settling velocity of bed fines (mm/s)	0.80

The sediment transport model calculates the advection and dispersion of suspended sediments originating from the boundaries, and the bed-water exchange processes of erosion and deposition. As discussed in the preceding section, the LPR is characterized by erosion-limited transport, i.e., erosion is a function of the sediment substrate and stratigraphy. Accordingly, the classical morphodynamic feedback loop commonly used in sandy settings was modified for application to fine sediment settings as shown in Figure 4.4. The primary refinement is the consideration of the availability of mobile sediment in the transport formulations. Note that the morphological acceleration factor included in Figure 4.4 is not applicable to the analyses in this section but rather the following sections. The spatially and temporally varying erosion and deposition fluxes computed by the model in response to the non-equilibrium transport formulations are used to compute the changing bed stratigraphy, composition, mass, and consequently, the bed thickness. The resulting morphological change is used to update the bathymetry used for hydrodynamic calculations in the following timestep. Thus, the hydrodynamic solution adapts and self-adjusts in response to the evolving bathymetry during the sim-

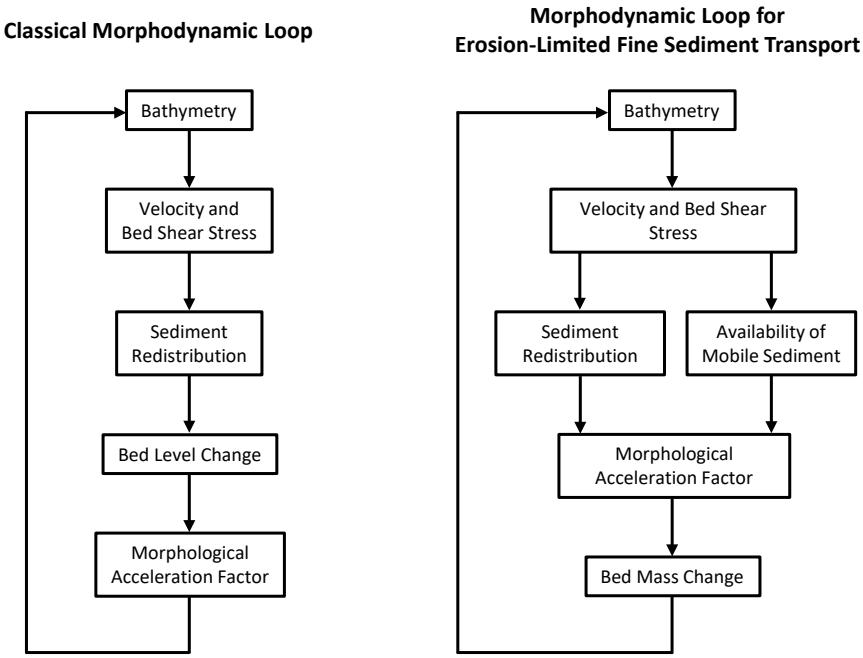

Figure 4.4: Schematic of classical morphodynamic loop (for sandy settings; adapted from Ranasinghe *et al.* [13]) and refined schematic for erosion-limited fine sediment settings.

ulation.

The conceptual description and quantitative parameterization of erosion-limited transport in the model is based on erodibility measurements. As mentioned previously, erodibility measurements using a Gust Microcosm (and other lines of evidence) show the presence of a 2-4 mm thick fluff layer (comprised of easily-erodible sediments) overlying less-erodible strata (Mathew and Winterwerp [9]). Within the fluff layer, τ_{Cr} values increase by approximately an order of magnitude. Erodibility measurements using a Sedflume device (Borrowman *et al.* [26]) and analyzed by Moffatt and Nichol and Deltares [25] show approximately an additional four-fold increase in τ_{Cr} over the top 30 cm of the bed. This conceptual description of depth-dependent erodibility was used as the basis for a multi-layer bed model.

Figure 4.5 shows a schematic of the bed layering developed to represent the depth-dependent erodibility along with a conceptual description of the hydrodynamic conditions that can potentially scour through the various strata. The fluff layer is located at the bed-water interface and is subject to erosion and deposition. During erosional conditions (e.g., the first half of the flood tide), the fluff layer may be depleted and disappear. During the following depositional condition (e.g., the second half of the flood tide and high-water slack), depositing sediments first recreate the fluff layer. When the fluff layer exceeds its pre-determined maximum thickness, the excess sediment is transferred to the underlying layer. Given the order of magnitude difference in erodibility between the

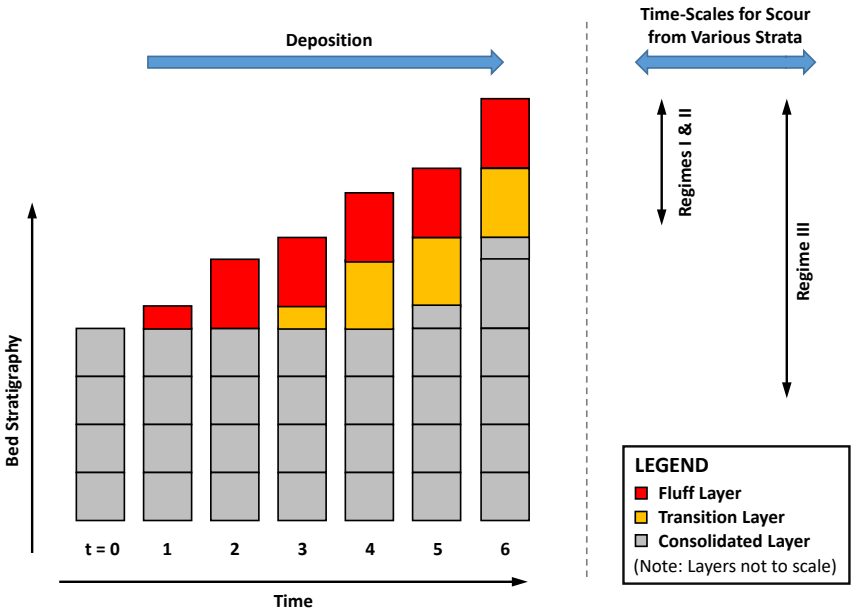

Figure 4.5: Schematic of bed layering and conceptual representation of hydrodynamic conditions potentially responsible for erosion from various strata.

fluff layer and the underlying less erodible layer, the model includes a transition layer (with same maximum allowable thickness as the fluff layer) with intermediate strength and located between the fluff and less-erodible layers underneath. When both the fluff and transitional layers reach their pre-determined maximum thickness, new layers are created underneath the transitional layer. Under depositional conditions, sediment is transferred from the fluff layer through the transitional layer and to layer underneath. Under erosional conditions, layer depletion proceeds in a logical sequence with the fluff layer eroded first, followed by the underlying layers. Erosion rate for the fluff and transition layers follows a modification of the Partheniades formulation for surface erosion:

$$E = M\left(\bar{\tau}_b - \tau_{Cr}\right), \text{ for } \bar{\tau}_b > \tau_{Cr} \tag{4.2}$$

where, E is the erosion rate (mass flux), $\bar{\tau}_b$ is the turbulence mean bed shear stress, and M is the erosion rate coefficient. Within the relatively deep channel, parameters τ_{Cr} and M were specified using the approach of Mathew and Winterwerp [9] and marginally adjusted (within the estimated uncertainty limits) during calibration. However, the subtidal shallows outside the channel were parameterized as three times more erodible (i.e., parameters τ_{Cr} and M reduced and increased, respectively, by a factor of three) than the channel areas, primarily by calibration. Though this model describes the vertical response of the bed to erosive forcing, it basically parameterizes spatial variability within grid cells, as elaborated by Winterwerp and van Kesteren [27].

The less-erodible layers underneath the fluff and transitional layers are treated some-

what differently. In order to enable efficient management of the bed layers, mainly with respect to depth- and time-dependent erodibility, these layers are formulated using the consolidation model of Sanford [28]. Briefly, the consolidation model prescribes an equilibrium depth-profile of bed density ρ_{eq} as:

$$\rho_{eq} = \rho_\infty - (\rho_\infty - \rho_0)\exp^{-cO} \tag{4.3}$$

where, ρ_0 is the density at the bed surface, ρ_∞ is the asymptotic density at depth, O is the mass of sediment above given depth in the bed (referred to as the overmass), and c is an empirical parameter. Given the equilibrium density profile, at any point in time t and depth within the bed, the instantaneous density ρ approaches equilibrium following the first-order approximation:

$$\frac{\partial \rho}{\partial t} = r_c(\rho_\infty - \rho)H(\rho_\infty - \rho) - r_s(\rho_\infty - \rho)H(\rho - \rho_\infty) \tag{4.4}$$

where, H is the Heaviside step function ($H = 1$ when its argument is ≥ 0 and $H = 0$ otherwise), r_c is the first-order consolidation rate, and r_s is the first-order swelling rate. The instantaneous depth-dependent density is related to the erosion rate using a power-law formulation (Roberts *et al.* [29]):

$$E = A\bar{\tau}_b^n \rho^m \tag{4.5}$$

where, A, n, and m are empirical parameters. Finally, the time- and depth-dependent τ_{Cr} is estimated by rearranging Eq. 4.5 such that τ_{Cr} is calculated as that shear stress which results in given critical threshold erosion rate E_{Cr} (Roberts *et al.* [29]). Parameters c, A, n, m, and E_{Cr} in Eq. 4.3 and Eq. 4.5 were determined by fitting the measured density, erosion rate, and τ_{Cr} profiles (Borrowman *et al.* [26] and Moffatt and Nichol and Deltares [25]). Parameter r_c was estimated as 0.25 (d^{-1}) using the results of Sedflume erosion experiments on cores reconstituted in settling columns and tested at different intervals after self-weight consolidation (Sea Engineering Inc. [30]), whereas parameter r_s was defined as $0.01 r_c$ based on Sanford [28]. Although the application of the consolidation model involves the determination of several fitted parameters, the resulting metrics of interest (erosion rates, τ_{Cr}, and ρ) are constrained by measured values. The parameterization of the consolidation model results in equilibrium profiles with increasing density, decreasing τ_{Cr}, and decreasing erosion rate (for given shear stress) with depth in the bed. The consolidation model also allows for the instantaneous profile of these metrics to deviate from the equilibrium profile as a function of the time history of erosion and deposition, and eventually tending to the equilibrium profile. In other words, a less-erodible layer exposed by erosion will swell and become more erodible over time, a temporal trend that is conceptually reasonable and relevant for long-term morphological simulations in dynamic settings. Furthermore, the depth- and time-dependent erodibility parameterized in the bed layering (via the fluff and transition layers, and the consolidation model) allows for representation of the various time-scales responsible for morphological evolution in fine sediment systems, affecting the availability of mobile sediment over time. This is a key aspect of the modification to the morphodynamic loop for representing the availability of mobile sediment presented in Figure 4.4.

It should be noted that only bed layers comprised of predominantly fine sediments (fines fraction >15%; [Winterwerp and van Kesteren [27]]) are subject to consolidation, with erosion defined using Eqs. 4.3–4.5. Bed layers comprised predominantly of sand (fines fraction <15%) do not consolidate and have erosion properties (coefficients A and n in Eq. 4.5) defined using Sedflume experiments on quartz particles (Roberts *et al.* [29]) with erosion rates calculated using a simplified version of Eq. 4.5 that does not include the dependency with density. The model includes six particle classes, of which three are sand-sized (effective diameters 150 µm, 750 µm, and 4000 µm; calculated using grain size distribution measured in sediment cores), and three are fine sediment classes representing fines originating from freshwater sources (head-of-tide), from marine sources (Arthur Kill and Kill van Kull), and from the bed by erosion. Although the various fine sediment classes do not interact, i.e., flocculation is not modeled explicitly, as discussed in the following paragraph, the impact of flocculation is parameterized in the model. The two larger sand fractions are limited to a small part of the LPR, predominantly towards its head, with significant loadings of fine sand entering the LPR only during episodic events.

Initial conditions corresponding to the mass fractions of the various classes in the sediment bed (fines in bed at initialization were assigned to the bed fines class) and dry density were defined using measurements on sediment cores from the LPR (Moffatt and Nichol and Deltares [25]) and assigned as averages over large reaches. The fluff and transition layers were also initialized at their maximum allowable thickness. Temporally varying SSC boundary conditions were defined at the head-of-tide (varying in response to river flow), and at the marine boundaries (varying within the tidal cycle as a function of tidal currents) using rating curves (Moffatt and Nichol and Deltares [25]). The settling velocities of the sand classes were determined using the formulation of Cheng [31]. The settling velocity of fines originating from the head-of-tide was calculated using Cheng [31] using an effective diameter measured with laser diffraction on deflocculated suspended sediment samples (Moffatt and Nichol and Deltares [25]). Effectively, this assumes that fines originating from the freshwater sources are poorly flocculated, an assumption verified during model performance assessment. In contrast, the settling velocities of fines originating from marine sources and from the bed were developed by calibration to SSC/SSF and morphological change data, respectively; these correspond to higher values than the fines from the head-of-tide, likely reflecting the effect of floc formation in the water column and in the bed (Winterwerp [32] and Tran and Strom [33]). Furthermore, in an approximation of aggregation processes in the bed (Tran and Strom [33]), fines from freshwater and marine sources that accumulate underneath the fluff and transition layers (i.e., implicitly have been residing in the bed for one or more tidal cycles) are instantaneously transferred to the bed fines class, i.e., after deposition, these particles have lost their original properties. Probability of deposition for the sand classes is defined using Gessler [34] whereas probability of deposition for the fines is set to 1 (i.e., allowing deposition under all conditions; see Winterwerp and van Kesteren [27]). Table 4.1 provides a tabulation of the major parameter values used in the model.

Finally, the effect of shipping at locations seaward of RM 2 was parameterized for simulations spanning the 2007–2008 and 2011–2012 bathymetry surveys by using the measured morphological change over these periods. The measured morphological change (erosion) was used to specify a constant rate of erosion at the locations of observed scour,

and the scoured sediment assigned as a continuous and vertically-uniform sediment loading to the water column. There is some uncertainty associated with the representation of shipping-induced scour. For instance, in reality, erosion will be limited to the periods of ship transit, and ship traffic could potentially be limited to periods of high water in case of depth-limited navigation. Similarly, propeller-wash generated by ships scales as a function of the draft and power applied by the propellers, which implies that the resulting erosion rates scale accordingly. However, there is no information available to parameterize shipping-induced scour in such a fashion mechanistically.

4.3.2. MODEL PERFORMANCE

MODEL performance was evaluated by comparison against various metrics — currents, salinity, SSC, SSF, and morphological change over a range of river flows and time periods. Figure 4.6 shows a comparison of model performance relative to the measured depth-average velocity, near-bottom salinity, and depth-average SSC at the in situ moorings (locations shown in Figure 4.1) over October 14–15, 2009 when river flow rate at Dundee Dam averaged 8 m^3/s (Regime I, infilling conditions). During this period, the model reproduces several key features apparent in the data:

- Tidal asymmetry (flood dominance) in currents
- The magnitude and intra-tidal trends in salinity and SSC
- The location of the salt front generally in the reach between RM 6.7 and RM 10.2
- Increasing SSC in the up-estuary direction, with maximum SSC generally in the reach between RM 6.7 and RM 10.2. In combination with the location of the salt front in this reach, this is indicative of the ETM location, and SSC dynamics within the ETM.
- The effect of tidal asymmetry on SSC, primarily manifest as higher SSC during flood than during ebb
- Relatively low SSC and relatively low intra-tidal variability in SSC at the freshwater tidal station (RM 13.5), which is an indication of solids with relatively lower settling velocity entering from the head-of-tide. This is in contrast to the locations within the salt wedge (RM 1.4, RM 4.2, RM 6.7) which experience higher intra-tidal variability in SSC and indicative of solids with relatively higher settling velocity. These spatially varying dynamics are reproduced by the model primarily by having higher settling velocity for solids originating from marine sources as compared to the freshwater sources.

Model performance was also assessed using along-channel transects of water depth, salinity, and SSC within the LPR and within the navigation channel in Newark Bay. Figure 4.7 shows such a comparison for June 23, 2005 and March 16, 2010 when river flow rate at Dundee Dam averaged 8 m^3/s (Regime I conditions) and 450 m^3/s (Regime III; return period of 25-years), respectively. Within the LPR, the model reproduces major features in the data such as the salt front and its location, and the presence of the ETM associated

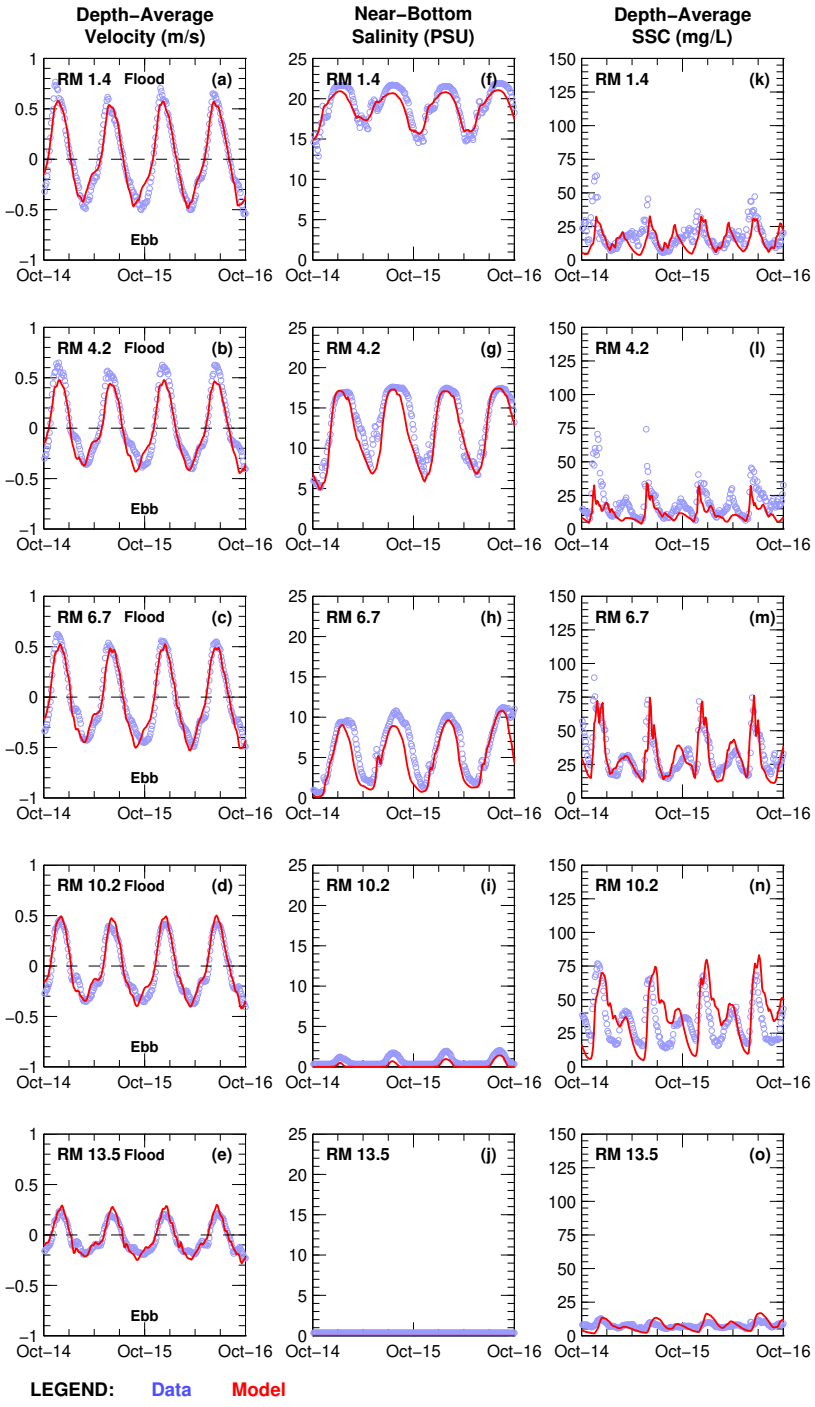

Figure 4.6: Comparison of model performance for (a–e) currents, (f–j) near-bottom salinity, and (k–o) SSC to measurements at the in situ moorings in the LPR during low river flow conditions (Regime I).

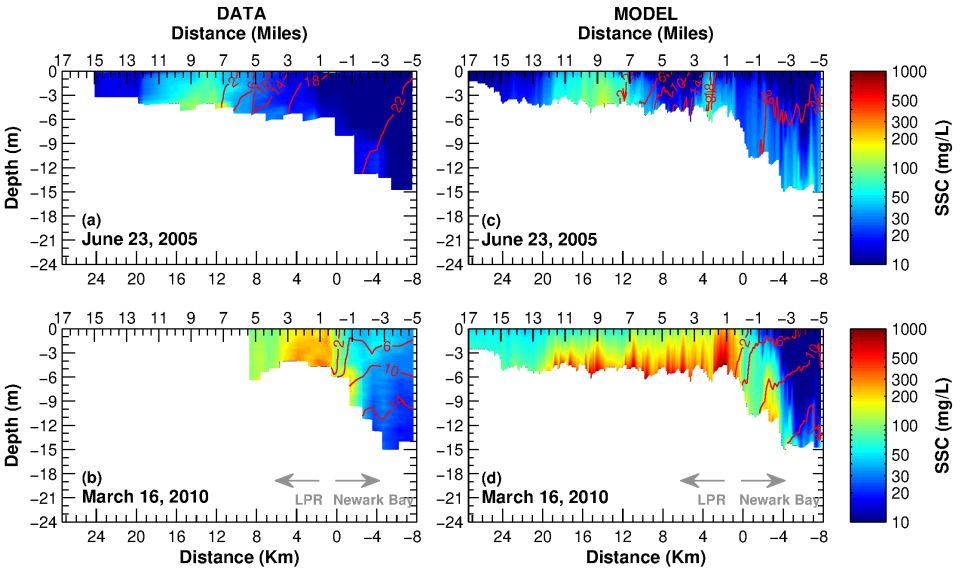

Figure 4.7: Comparison of model performance (c–d) for salinity (contours) and SSC (shaded colors) to along-channel transect measurements (a–b) within the LPR and the navigation channel in Newark Bay during low river flow conditions (Regime I; a and c), and during high river flow conditions (Regime III; b and d).

with the salt front. In addition, the model reproduces the difference in SSC values within the ETM between the two events, with higher SSC during the March 16, 2010 event as compared to the June 23, 2005 event.

The measurements of velocity and SSC at the in situ moorings were used to calculate the tidally-integrated net SSF at these locations over the years 2009 and 2010. The resulting net SSF shows a relationship with river flow rate as seen from the upper row in Figure 4.8, a trend that is reproduced by the model as seen in the bottom row of Figure 4.8. Statistical metrics quantifying the model-data comparisons are also included — these include the root mean square error (RMSE), a measure of the error between the model and data as expressed by:

$$RMSE = \sqrt{\frac{\sum (SSF_{Data} - SSF_{Model})^2}{n}} \tag{4.6}$$

where, SSF_{Data} = measured tidally-integrated SSF, SSF_{Model} = model-calculated tidally-integrated SSF, and n = number of pairs of model and data. Another metric quantifying the model-data performance is the relative RMSE (%), defined as the RMSE relative to the data range (the difference between the minimum and maximum measured value). Within the predominantly estuarine locations (RM 1.4, RM 4.2, and RM 6.7), low river flows are associated with net up-estuary SSF, with net down-estuary SSF as river flow increases. In contrast, net SSF at the freshwater tidal location (RM 13.5) is consistently directed down-estuary. At RM 1.4, during river flows ranging between about 30–150 m^3/s model performance is somewhat inconsistent with data — the magnitude of net SSF

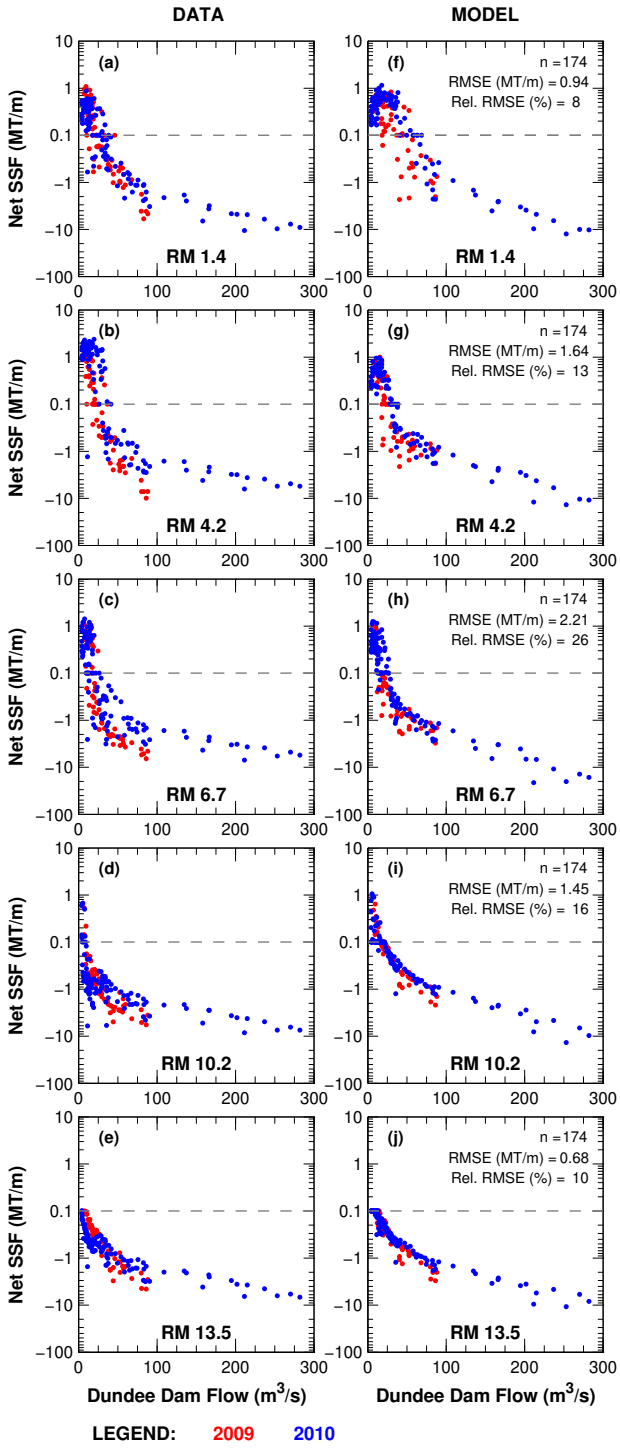

Figure 4.8: Comparison of model performance (f–j) for the trend of SSF versus river flow rate to the measured trend (a–e) at the in situ moorings in the LPR over an extended range of river flows (Regimes I, II, and III). Positive and negative values indicate fluxes directed up-estuary and down-estuary, respectively.

tends to be biased low compared to the data. Assessment of model performance at RM 4.2 and RM 6.7 over this range of flow rates shows a similar bias at these locations as well. This suggests that the model does not calculate enough erosion in the more landward reaches of the LPR. This limitation in model performance may partly be related to the time-history of events and the ability of the model to capture variations in sediment erodibility at small spatial and temporal scales — this is one of the difficulties involved in modeling fine sediment transport in such erosion-limited settings. Furthermore, as indicated by Mathew and Winterwerp [10], erosion during such conditions, which are nominally representative of Regime II, is limited to the fluff layer (and the transition layer) and is therefore less significant from a morphological perspective as compared to Regimes I and III.

Model performance was also compared to the measured morphological change in bathymetric surveys measured over 2007–2012. The morphodynamic model was used to perform four separate simulations spanning the periods of the various bathymetry surveys, with each simulation initialized using measured bathymetry at the start of the particular period. Each simulation also included a spin-up period; however bathymetric changes calculated during the spin-up period were discarded. The measured and calculated morphological changes were averaged cross-sectionally and longitudinally over 1-mile (1.6 Km) intervals for an assessment of large-scale morphological changes and are shown in Figure 4.9. Overall, the model reproduces the large-scale flow-dependent morphological trends apparent in the data with maximal errors smaller than 10 cm (averaged over the spatial scales presented in Figure 4.9). Consistent with the data, model results for the low-flow periods (2007–2008 and 2011–2012) generally show infilling landward of RM 2, and the high-flow periods (2008–2010 and 2010–2011) show erosion landward of RM 2 and deposition seaward of RM 2. In the model, erosion scales with the magnitude of river flow — for instance, the 2008–2010 period included a 450 m^3/s event whereas the 2010–2011 period included a 700 m^3/s event, and accordingly, the model responds with more erosion during the latter period. The data show such flow-dependent erosion depths in some reaches, e.g., between RM 2 to RM 6. However, in other reaches, specifically between RM 7 to RM 11, while the data shows evidence of armoring during the 2010–2011 period, the model does not capture the armoring effects. Although the model reproduces the large-scale flow-dependent erosional and depositional trends, and the large-scale morphological changes, it tends to under-perform at local scales.

The comparison of large-scale flow-dependent morphological trends is seen more clearly in Figure 4.10), which shows the measured and model-calculated cumulative (starting from the landward end) volumetric morphological change over the various time-periods. Overall trends are consistent between the model and data — landward of RM 2, the model reproduces the depositional trends in 2007–2008 and 2011–2012, and the erosional trends in 2008–2010 and 2010–2011. Similarly, seaward of RM 2, the model reproduces the depositional trends in 2008–2010 and 2010–2011 (as mentioned previously, the erosional trend seaward of RM 2 during 2007–2008 and 2011–2012 is driven by the parameterized shipping scour process). During the low-flow periods (2007–2008 and 2011–2012), the model-calculated magnitude of infill landward of RM 2 is comparable to the data. However, model performance of erosion landward of RM 2 during the high-flow periods (2008–2010 and 2010–2011) is more variable, with a bias towards

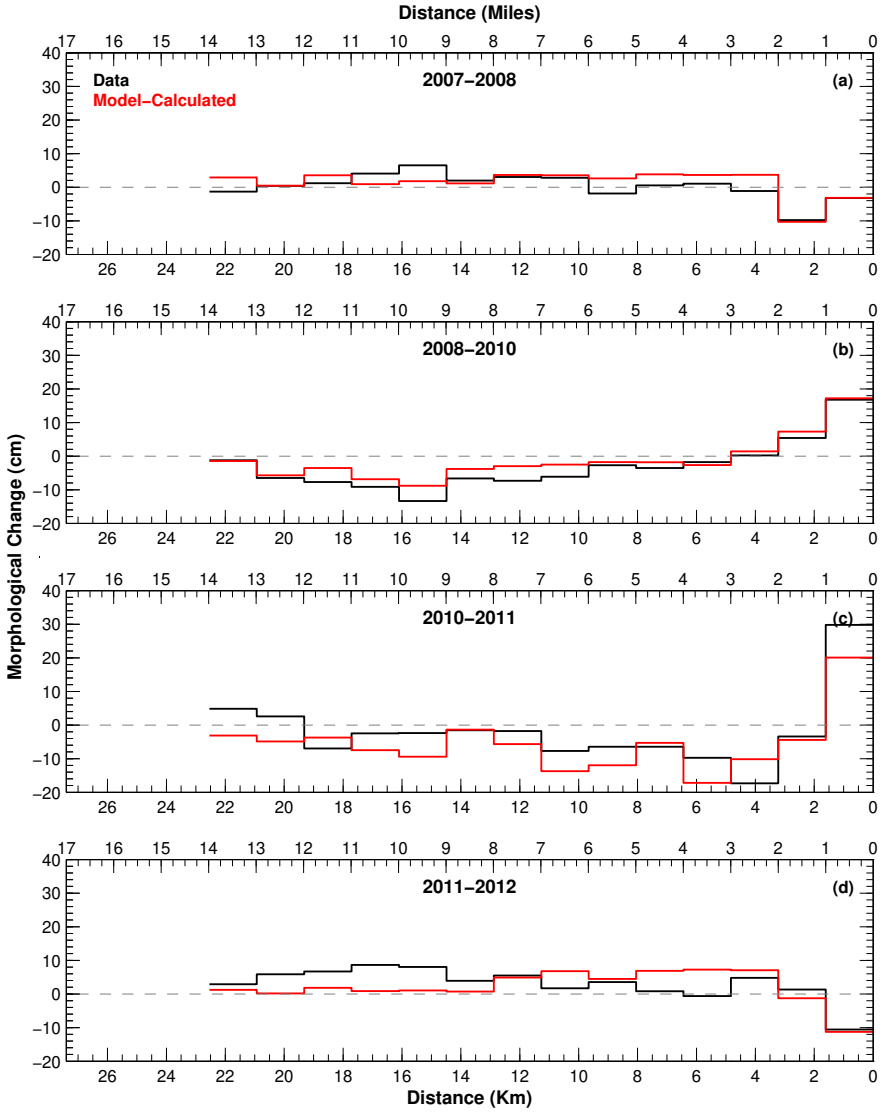

Figure 4.9: Comparison of measured and model-calculated longitudinal profile of morphological change in the LPR over various survey periods laterally and longitudinally averaged over 1.6 km (1 mile) intervals. Positive values indicate net deposition and negative values indicate net erosion. Morphological change over the (a) 2007–2008, (b) 2008–2010, (c) 2010–2011, and (d) 2011–2012 survey periods.

under-prediction during the former period and over-prediction during the latter period.

The model-calculated change in river volume in the simulations covering the 2007–2012 period was also compared to the results of the analytical infill model presented previously in Figure 4.2. Figure 4.11 shows the comparison of the numerical and analyt-

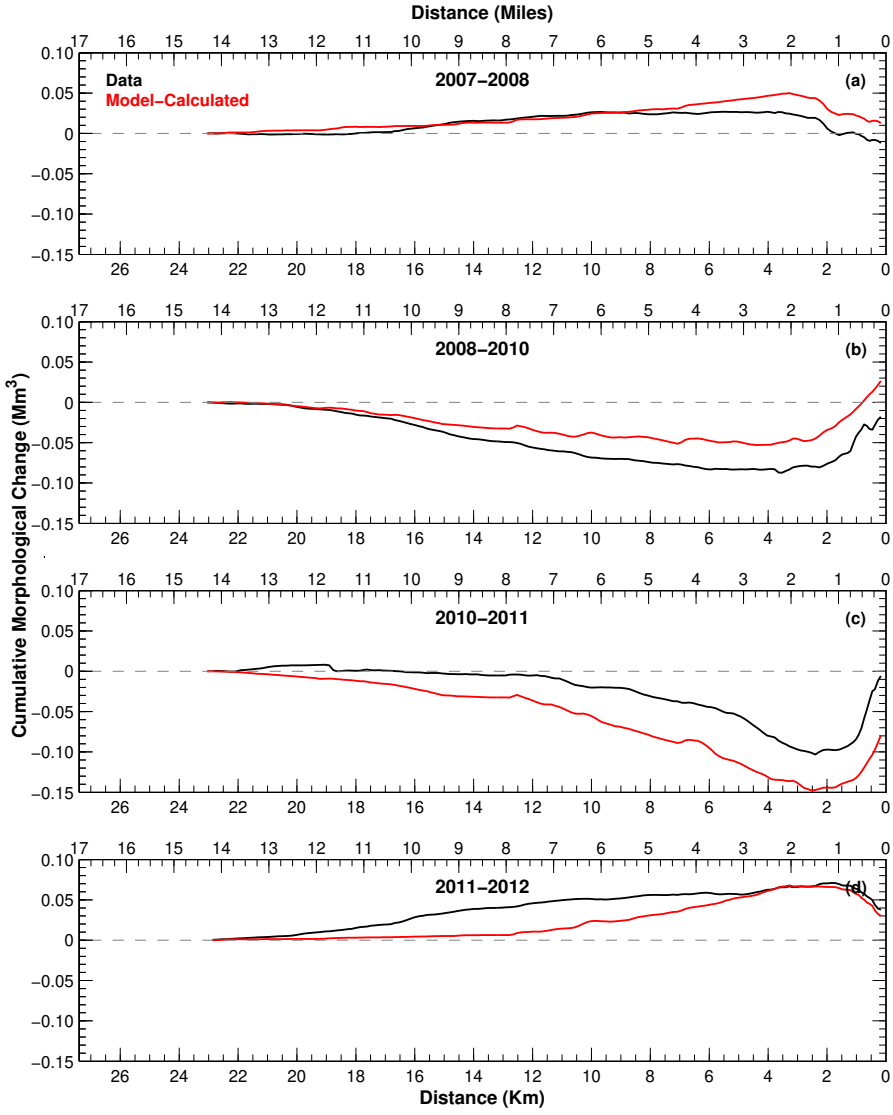

Figure 4.10: Comparison of measured and model-calculated longitudinal profile of cumulative (in the seaward direction) volumetric morphological change in the LPR. Positive slope indicates deposition and negative slope indicates erosion. Morphological change over the (a) 2007–2008, (b) 2008–2010, (c) 2010–2011, and (d) 2011–2012 survey periods.

ical models. Over these large spatial scales, with some notable exceptions, the numerical model shows trends that are generally consistent with estimates from the analytical model. Figure 4.11 also shows that measured river volumes in 2007 and 2011 were only 0.7% and 2.7% greater, respectively, relative to the equilibrium volume. River cross-

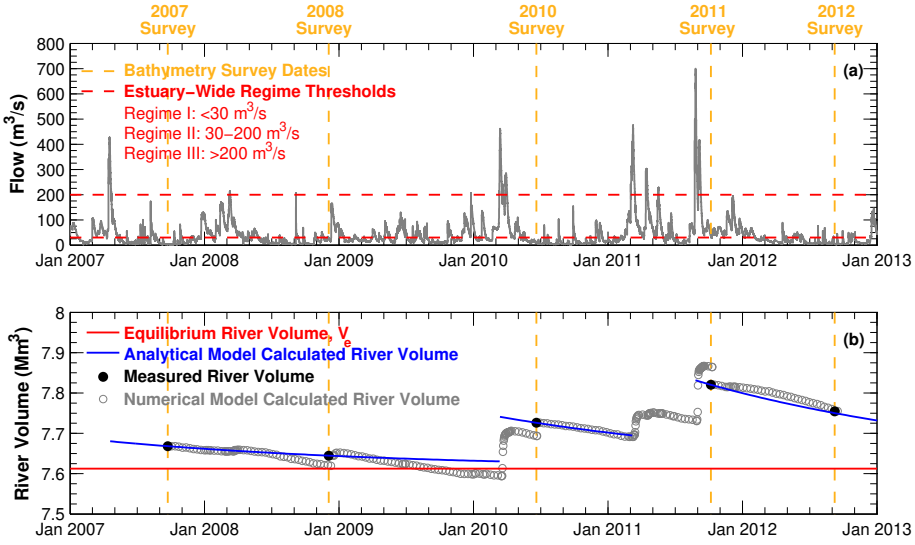

Figure 4.11: Time-series of measured flow rate at the head-of-tide in the LPR over the period of the bathymetry surveys, and comparison of measured and model-calculated (analytical and numerical) river volume (at mean sea level).

sections calculated using measured bathymetry in the individual years is also very similar to the values and trends presented in Figure 4.3 (which use the 2007 bathymetry). This suggests possible explanations for the under-performance of the model with respect to small-scale spatial erosion and infill patterns. Specifically, scour in erosion-limited conditions is very sensitive to local variations in bed stratigraphy, both with respect to the armoring effects of sand lenses as well as low erodibility, consolidated layers. Model results are therefore limited due to the lack of data characterizing such spatially- and depth-varying properties. Similarly, because the change in river volume by erosion is not significant enough to significantly enhance trapping efficiency in the following periods, local patterns of infill are expected to be more sensitive to the availability of sediment at the mouth of the LPR and its synchronization with import mechanisms, especially in the case of shipping-induced scour. For instance, in locations where navigation is limited by water depth, ship traffic may be limited to the period of the rising or flood tide, which implies greater potential for sediment import into the LPR than if the scour is distributed equally over the entire tidal cycle as assumed in the numerical model.

The under-performance of the model with respect to morphological change over inter-annual periods is consistent with the findings of Dam *et al.* [16], who found temporal trends in the performance of a hindcast morphological simulation (over 110 years) in the Western Scheldt estuary. Although a sand dominated system, the authors found that model performance (relative to measured morphological change) tended to show a progressive worsening up to about 20–30 years after model initialization, followed by a consistent improvement in model performance. Over time, as the measured signal

(i.e., measured morphological change) increased and artifacts of model setup and initialization were attenuated, the error in model results tended to become progressively smaller in relative terms, thus leading to an improvement in model performance over time. Qualitatively, this is similar to the rationale presented in the preceding paragraph — the measured signal (infill or erosion) in the inter-annual bathymetric surveys in the LPR is a relatively small response/perturbation, and model performance shows a relatively large error.

Additional potential explanations why the model does not capture local-scale changes over inter-annual scales include limitations related to various model inputs and formulations:

- Bed initial conditions — The core profile measurements used to define model initial conditions are somewhat sparse and do not capture the full range of spatial and depth-dependent heterogeneity. Moreover, they may not necessarily match the equilibrium solution of the model.

- Erodibility — The available data for erodibility of the parent bed (Borrowman *et al.* [26]) were conducive to the development of only a single set of erodibility inputs over the entire LPR (Moffatt and Nichol and Deltares [25]) which is likely to be a simplification of the spatial heterogeneity in reality. Moreover, these may vary over time inducing the memory effects discussed in Section 4.1.

- Grid resolution — The resolution of the model grid, limited by computation time, is not sufficient to resolve small-scale features such as bridge support pillars, shoreline structures, etc., which cause local scour during high river flow events, with infill of the scoured areas during low river flow conditions.

- Shipping-induced scour — The exact timing and magnitude of this source term is unknown. For the model simulations presented here, the locations of scour and scour rate were parameterized using the measured bathymetry, and the scour rate was assumed to be constant in time, all of which are simplified representations of the process.

- Consolidation time-scales — Consolidation time-scales and their impact on erodibility are not very well characterized, both generally as well as specifically in the case of the LPR. For instance, at initialization, the model assumes that sediments in the bed to be fully consolidated (and therefore, less erodible) whereas in reality, some surficial sediments may be newly deposited and not fully consolidated (i.e., more erodible).

- Flocculation effects — Although the model includes parameterized approximations of flocculation effects on settling velocity, it does not capture the full range of spatial and temporal heterogeneity of this process, neither in the sediment bed, nor in the water column. For example, the model only includes two representative floc classes, whereas in reality, floc sizes and settling velocities are expected to vary over large range.

However, such limitations may impact model performance more over short-term simulations such as the inter-annual periods presented here than over the long-term (Dam *et al.* [16]). Therefore, the application of the Morfac approach to the LPR presented in the next section also includes a validation of model performance over a multi-decadal period.

4.4. MORPHODYNAMIC UPSCALING USING MORPHOLOGICAL ACCELERATION

THE morphodynamic model of the LPR was used in the development and application of the Morfac approach for fine sediment settings. The Morfac approach derives from the following key concepts (Lesser *et al.* [1], Roelvink [2], Ranasinghe *et al.* [13], and Lesser [14]):

- Time-scales of morphological change are typically greater than time-scales of change in hydrodynamic forcings.
- Morphological change or net change in bed sediment mass (e.g., in response to a repeated sequence of identical hydrodynamic forcings) is assumed to be linear within the morphological timestep. This implies that morphological change or net change in bed sediment mass calculated over a single tidal cycle can be upscaled to n tidal cycles using the morphological acceleration factor, $f_{mor} = n$.

This gives rise to the notion of the morphological timestep, Δt_{mor}:

$$\Delta t_{mor} = f_{mor} \Delta t_{hyd} \tag{4.7}$$

where, Δt_{hyd} is the hydrodynamic timestep (which we implicitly assume equals the sediment transport time step). Net change in bed sediment mass over the morphological timestep is calculated using erosion and deposition fluxes over the hydrodynamic timestep:

$$\Delta S_{mor} = f_{mor}(D - E)\Delta t_{hyd} \tag{4.8}$$

where, D is the deposition flux, and ΔS_{mor} is the mass change in the bed over the morphological timestep. In the LPR, where the river flow regime is the primary determinant of sediment dynamics (see Figure 4.8, and Mathew and Winterwerp [10]), morphological acceleration is achieved by upscaling the morphological response to given river flow rate. In other words, the net change in sediment mass in the bed associated with a given river flow that repeats over n tidal cycles is calculated by simulating a single tidal cycle for that river flow and scaling the resulting bed mass change to n tidal cycles using Eq. 4.8.

Note that in contrast to Eq. 4.8 (i.e., morphological upscaling applied to bed mass change), the classical approach to morphodynamic upscaling using the Morfac approach consists of multiplying bed level changes with to calculate bathymetry at the end of the morphological timestep (Roelvink [2] and Ranasinghe *et al.* [13]) as shown in the left

panel of Figure 4.4. The classical approach was tested initially as part of the current research. However, as explained in Appendix D, the classical approach is appropriate only in settings where armoring of the bed and/or erosion-limited transport is not a factor, e.g., typically, problems of sand transport in coastal settings. Morphodynamic upscaling in settings where depth-dependent erodibility and/or armoring are relevant for transport can be successfully achieved only by applying upscaling to the bed mass change. Appendix D also presents a comparison of model performance with morphological upscaling applied to bed mass change and to bed level change.

The Morfac approach involves input reduction for the hydrodynamic forcings, which in the case of the LPR includes the river flow and barotropic forcing. Briefly, input reduction for the barotropic forcing seeks *to replace the complex time series of tidal water level and current fluctuations occurring in nature with a simplified tide that produces the same residual sediment transport and morphological change patterns as the naturally varying tides* (Lesser [14]). In the case of fine sediment systems, the representative tide should also reproduce the effects of sediment availability and erosion-limited transport on residual sediment transport. The harmonics of this representative tide used for boundary conditions in the application of the Morfac approach include the semi-diurnal M_2 and diurnal O_1 and K_1 constituents along with the M_4 and M_6 overtides, with the representative tide (tidal range of 1.5 m) synthesized following the methods of Lesser [14]. Simulations using the representative tide were compared to simulations using the spring–neap tidal cycle in order to ensure that the representative tide preserves the long-term net sediment transport. SSC boundary conditions at the marine boundaries were specified using the rating curve approach described previously and using tidal currents corresponding to the representative tide. Input reduction for river flow is discussed in the following section.

4.4.1. CONSIDERATIONS FOR MORFAC APPROACH IN FINE SEDIMENT SETTINGS AND SPECIFICALLY FOR APPLICATION TO THE LPR

SECTION 4.1 includes discussion of phenomena specific to fine sediment transport. Specific formulations and careful selection of model inputs were required for appropriate representation of these phenomena within the context of the Morfac approach. These considerations maintain the assumption of linearity within the morphological timestep that is key to the Morfac approach, separate conditions when the assumption of linearity cannot be met, and preserve the various time-scales of morphological response in fine sediment systems. These are summarized below:

- Residual sediment transport — Morphological change due to residual sediment transport associated with barotropic and baroclinic circulation (relevant during Regimes I and II) scales as a function of time. For instance, a sediment particle located at the mouth of the river at the start of a flood tide will move a certain distance up-estuary after one tidal cycle due to tidal asymmetries and lag effects (assuming flood dominance), and estuarine circulation. During the following tidal cycle, it will move some distance further up-estuary. In other words, net sediment transport in a simulation of two tidal cycles with $f_{mor} = 1$ will not be identical to a simulation of one tidal cycle with $f_{mor} = 2$. This implies a practical upper-

bound on the value of f_{mor}, established by trial-and-error as 7 and applicable during Regimes I and II in the current application.

- Depth-dependent erodibility — Consider a time-series of two identical erosional events occurring sequentially and in short order. High shear stress during the first event can cause erosion of surficial sediments, thus exposing a bed layer with τ_{Cr} greater than the maximum bed shear stress during the event. Therefore, the second event, which experiences the same time-history and magnitude of bed shear stress as the first event, would not be expected to cause any further erosion. However, a simulation of a single event with $f_{mor} = 2$ will overestimate the magnitude of erosion compared to a simulation of two sequential events with $f_{mor} = 1$; the latter will preserve the erosion-limited morphological response. In the LPR, depth-dependent erodibility is a factor in limiting erosion primarily under Regime III conditions (river flow rate greater than 200 m^3/s for the system as whole, although this threshold decreases in the landward direction). Therefore, in order to appropriately represent the effects of depth-dependent erodibility, for the current application, morphological acceleration is not employed (i.e.,) when river flow rate exceeds 50 m^3/s which is a threshold established using maps of bed shear stress under different steady-state river flow rates and is the estimated threshold above which erosion of the consolidated layers may occur.

- Supply-limited transport — The supply of fine sediments from the head-of-tide generally tends to be event-dominated, i.e., episodic high-flow events are responsible for a significant fraction of the annual sediment delivery to the river and affect sediment availability for redistribution during subsequent periods. Morphological acceleration under such conditions may not accurately reproduce sediment transport patterns. For instance, for a high-flow event loading with a travel time of 10 days from the head-of-tide to the area of interest, a one-day simulation with $f_{mor} = 10$ will not capture transport to the area of interest. Therefore, in order to appropriately represent such supply-limited transport, for the current application, morphological acceleration is not employed (i.e., $f_{mor} = 1$) when river flow rate exceeds 50 m^3/s. This threshold is also consistent with the rating curve used to define SSC boundary conditions at the head-of-tide which includes relatively constant SSC at river flow rate of less than 60 m^3/s and increasing with increasing river flow.

- Fluff layer dynamics — In order to preserve the intra-tidal SSC and SSF dynamics, which depend on sediment inventory in the fluff layer and is relevant for residual transport, only the sediment flux over the hydrodynamic timestep, i.e., $(D - E)\Delta t_{hyd}$, is added to or sourced from the fluff layer. Sediment flux over the remainder of the morphological timestep, i.e., $(f_{mor} - 1)(D - E)\Delta t_{hyd}$, is added to or sourced from subsurface layers. This preserves the timing of erosion (and deposition) within the tidal cycle, thus preserving residual transport over the tidal cycle, and is important for maintaining the condition of linearity in morphological change during the morphological timestep that is key to morphological upscaling.

These considerations have resulted an approach that includes river flow-dependent

values of f_{mor} for the current application, with f_{mor} of 7 or 1 when river flow rate is less than or greater than 50 m^3/s, i.e., Regime I/II or Regime II/III conditions, respectively. The selected river flow threshold separates conditions where erosion is limited to the fluff layer (river flows <50 m^3/s) from conditions where the consolidated layers underneath the fluff layer may be eroded. This definition of conditions without morphological acceleration preserves erosion-limited dynamics and preserves supply-limited transport which are relevant during high river flows. Furthermore, the selected f_{mor} value of 7 in combination with the formulation described previously that preserves fluff layer dynamics, helps preserve residual sediment transport which is a key driver of morphological change during low–moderate river flow conditions.

The river flow boundary conditions are a synthesized sequence of flow rates designed to represent the river flow-dependent location of the salt-front and ETM, and effects of barotropic and baroclinic circulation on net sediment transport. This was accomplished by sorting the measured river flows (averaged over the period of two tidal cycles in order to account for the inequality in the semi-diurnal representative tide), followed by a moving-window average (over seven two-tide cycles) of river flows for flow rates less than 50 m^3/s. For simulations covering the periods of the inter-annual bathymetry surveys, this sorting and sequencing was performed separately for periods before and after significant high-flow events between two surveys, with the synthesized river flow rate increasing from the start of the simulation up to the peak of the high-flow event, followed by decreasing river flow rate. This preserves the timing of the high-flow event in a fashion analogous to the brute-force simulations (i.e., simulations performed without morphological acceleration and using the measured sequence and magnitude of river flow and tide; results presented in Figure 4.9). SSC boundary conditions at the head-of-tide were defined using rating curves as described previously.

4.4.2. MODEL PERFORMANCE

WITH the exception of the boundary conditions for tide, river flow rate, and SSC (which were defined as described above), the remainder of the model setup and parameterization for the morphodynamic model using Morfac is identical to the setup presented in the preceding section. The performance of the morphodynamic model using Morfac is first compared against the brute-force simulations over the period of the inter-annual bathymetry surveys (2007–2012). This serves as test of the Morfac approach in its ability to reproduce the results of the more computationally-intensive approach. Subsequently, as a validation, the morphodynamic model using Morfac is applied for a multi-decadal hindcast simulation and its results compared against the measured morphological change.

MODEL TESTS — 2007–2012

THE value of f_{mor} used for periods simulated with morphological acceleration and the flow threshold used to separate periods with and without morphological acceleration were developed based on the results of morphological change in test simulations covering the period of the inter-annual bathymetry surveys over 2007–2012. Table 4.2 presents a quantitative model performance assessment for various parameter values for f_{mor} and the threshold river flow. The performance of the individual test simulations

was assessed against the results of the brute-force simulations (using model results in individual grid cells) using the Brier-Skill Score (BSS) as defined by van Rijn *et al.* [35] and Sutherland *et al.* [36]:

$$BSS = 1 - \frac{\langle (Y - X)^2 \rangle}{\langle (B - X)^2 \rangle} \tag{4.9}$$

where, X can be the measured bed level (if comparing model results to data) or the calculated bed level from the brute force simulations (if as in this case comparing to the performance of the model using Morfac), Y is the model-calculated bed level (in simulations using the Morfac approach), B is the initial bed level, and the angled-brackets denote an arithmetic mean. A BSS of 1 indicates a perfect match whereas decreasing value of BSS indicates increasing divergence between the two sets of model results.

Table 4.2: Quantitative performance assessment of model simulations using the Morfac approach compared to the brute force simulations for various combinations of f_{mor} and the flow threshold separating the conditions with variable values of f_{mor}.

Morfac Approach — Simulation Scenario			**Simulation Performance — BSS**			
Regime I & II f_{mor}	**Regime II & III f_{mor}**	**Flow Threshold (m^3/s)**	**2007–2008**	**2008–2010**	**2010–2011**	**2011–2012**
1	1	–	0.96	0.92	0.93	0.96
3	1	50	0.96	0.92	0.91	0.94
5	1	50	0.96	0.92	0.91	0.93
7	1	50	0.95	0.91	0.91	0.92
10	1	50	0.91	0.90	0.91	0.90
15	1	50	0.87	0.89	0.90	0.85
7	1	25	0.95	0.91	0.90	0.93
7	1	75	0.93	0.91	0.92	0.90
7	1	100	0.92	0.91	0.92	0.89
7	3	50	0.84	0.65	0.72	0.88
7	5	50	0.74	0.46	0.63	0.88

The results in Table 4.2 show progressively worsening results with (1) increasing value of f_{mor} for the periods with morphological acceleration (during Regime I & II flows), (2) morphological acceleration during Regimes II and III, and (3) increasing flow threshold used to separate periods with and without morphological acceleration. These comparisons were used to support the choice of $f_{mor} = 7$ for periods simulated with morphological acceleration and the flow threshold of 50 m^3/s. In addition, the results for the simulation without morphological acceleration (i.e., $f_{mor} = 1$ for all flows) also shows the impact of the representative tide and the synthesized flow sequencing applied as part of the Morfac approach — overall, these simplifications of the boundary conditions do not significantly impact the results for morphological change, i.e., the accuracy of the predictions.

Figure 4.12 shows comparisons of model results for the brute-force simulations, and for simulations using Morfac (using $f_{mor} = 7$ for periods with morphological acceleration and flow threshold of 50 m^3/s). Both graphical as well as quantitative comparisons indicate a high degree of similarity between the two sets of model results. Minor differences apparent in the comparisons are primarily related to factors not included in

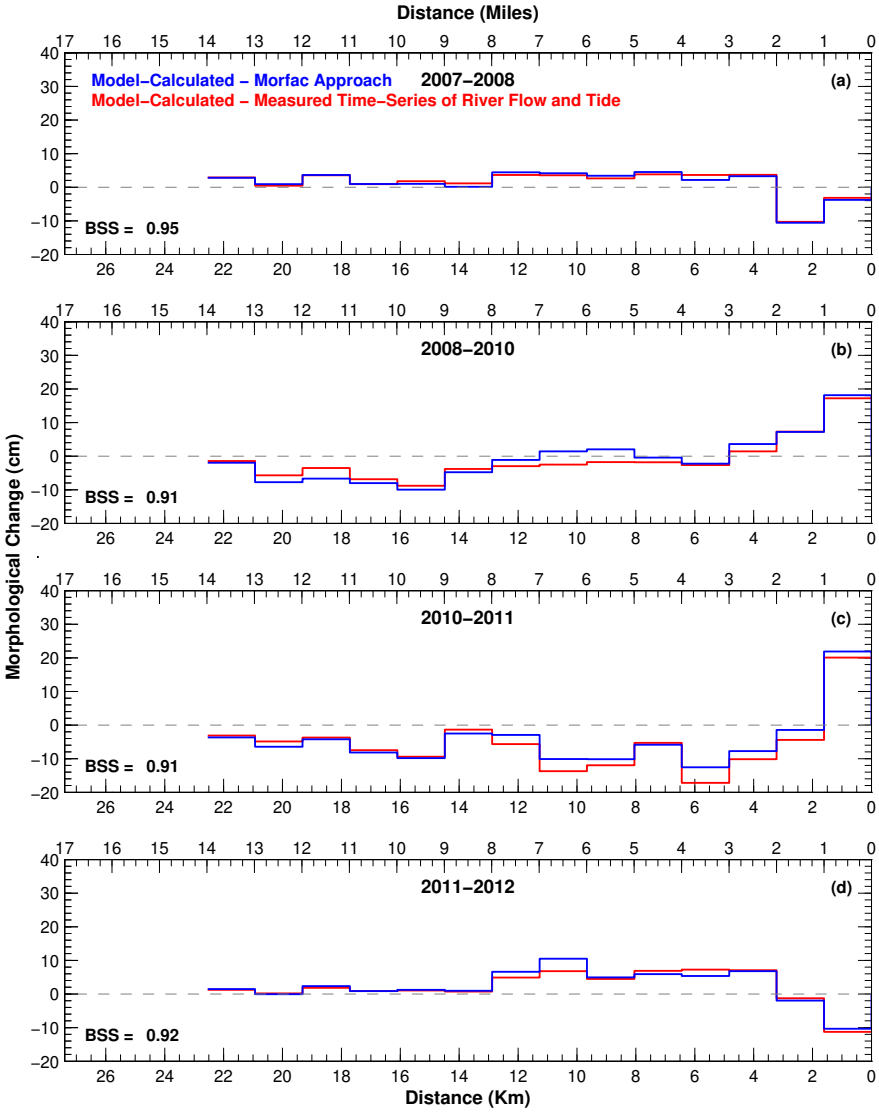

Figure 4.12: Comparison of model-calculated longitudinal profile of morphological change in the LPR over various survey periods laterally and longitudinally averaged over 1.6 km (1 mile) intervals. Positive values indicate net deposition and negative values indicate net erosion. Morphological change over the (a) 2007–2008, (b) 2008–2010, (c) 2010–2011, and (d) 2011–2012 survey periods. Results for model simulations using the measured time-series of river flow and tide, and for model simulations using Morfac.

the simulations using Morfac, e.g., coincident spring tide during some of the high-flow events, effect of the somewhat randomly varying river flow on residual sediment transport, etc. Nonetheless, overall, the simulations using Morfac reproduce the large-scale as well as local-scale (with some minor exceptions) performance of the brute-force simula-

tions. Therefore, the morphodynamic model using Morfac is concluded to be reasonably similar to the more computationally intensive approach, and subject to the validation presented in the following sub-section, a valid approach for computationally efficient morphological simulations in fine sediment settings.

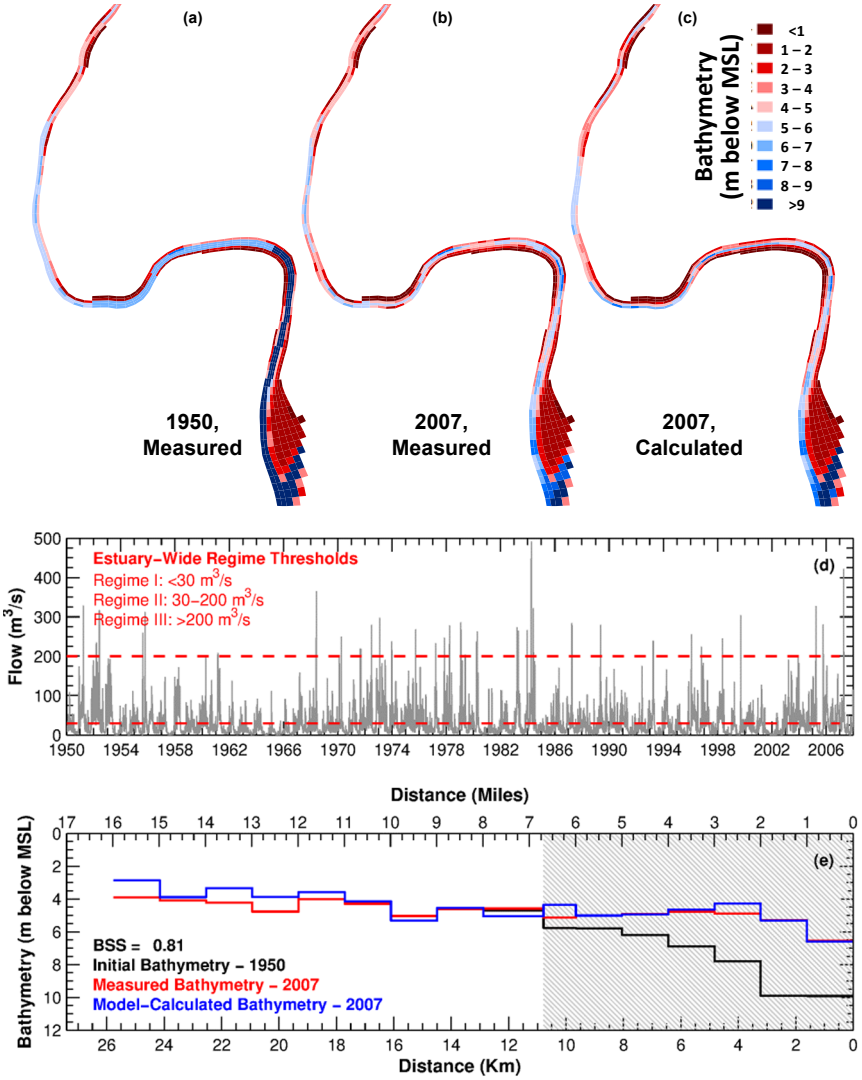

Figure 4.13: Validation of morphological model using Morfac using the measured infill of the LPR between RM 0 and RM 6.7 over 1950–2007. Maps of bathymetry at various times (a-c), time-series of river flow during 1950–2007 (d), and longitudinal profiles of bathymetry (e) in the navigation channel post-dredging in 1950–1951, measured in 2007, and model-calculated in 2007 (hatched region indicates extent of dredging in 1950–1951).

MODEL VALIDATION — 1950–2007

THE hindcast simulation used to validate the long-term performance of the morphodynamic model using Morfac involves the historical infill of the navigation channel in the LPR. The last major dredging in the LPR occurred in 1950–1951 between RM 0 to RM 2.2, RM 2.2 to RM 4.2, and RM 4.2 to RM 6.7, to depths of 9.9 m, 6.8 m, and 5.6 m, respectively (depths relative to MSL), with maintenance dredging (to depth of 9.9 m) between RM 0 to RM 1.5 in 1983 [21]. Figure 4.3 also includes the cross-section in 1950–1951 for comparison to the 2007 configuration — significant deviations from the near-equilibrium conditions in 2007 are apparent, especially between RM 2 and RM 5. Subsequent infill of the navigation channel ranges up to about 5 m in some locations. Therefore, the morphodynamic model using Morfac was applied for a simulation over the period 1950–2007 with the bathymetry in the navigation channel between RM 0 to RM 6.7 initialized at the design dredge depths, and bathymetry between RM 0 to RM 1.5 reset to the design dredge depths in 1983. Periodic changes in the geometry and morphology within Newark Bay (U.S. Army Corps of Engineers [37]) were also represented in the simulation. Input reduction for river flow at the head-of-tide was performed in annual cycles using the historic river flow data from 1950–2007. The impact of navigation in the channel between RM 0 and RM 2 was included by constraining deposition as a depth-limited process in this reach, with the limiting depth being the measured bathymetry in 2007. Figure 4.13 shows the hydrograph during this period; key observations include the extended period from the mid-1950s to late-1960s when river flow was relatively low (mostly Regime I, i.e., infilling), with only one Regime III event. In contrast, the remainder of this 58-year period experienced thirty-two Regime III events.

Figure 4.13 shows a comparison of the measured and model-calculated bathymetry in 2007. Overall, the model reproduces various spatial and temporal trends apparent in the data. These include the magnitude of infill at local scales, trend of decreasing infill with distance in the landward direction, and relatively lower infill in the vicinity of bends in the river. Quantitative assessment of the model-calculated and measured bathymetry in 2007 shows BSS value of 0.81 which represents an "excellent" model performance accordingly to the performance classification scheme of van Rijn *et al.* [35]. Therefore, this validation using multi-decadal data provides demonstration of the applicability of the Morfac approach for performing long-term morphological simulations in fine sediment settings.

4.5. MODEL APPLICATION

THE morphodynamic model using Morfac was applied to answer a few specific and general questions regarding the current morphological status of the LPR and the impact of specific forcings on the morphology of the system. The specific question pertains to the impact of navigation seaward of RM 2, and the general questions pertain to the current morphological status of the LPR landward of RM 2, the role of episodic Regime III events, and the impact of climate change. The prognostic simulations used to address these issues were initialized using the measured bathymetry in 2007. The hydrograph over 1950–2007 is representative of the long-term measured river flow (over 1897–2020). Therefore, except as described later in the context of episodic Regime III events and climate change, the prognostic simulations use the river flow hydrograph from 1950–2007

described in the preceding section. These simulations do not include shipping-induced scour in the LPR.

4.5.1. ROLE OF NAVIGATION AND CURRENT MORPHOLOGICAL STATUS

SEVERAL lines of evidence indicate that the reach between RM 0 and RM 2 in the LPR is impacted by shipping activities:

- a change in the trend of current river cross-section area with distance and with tidal prism at RM 2 as presented in Figure 4.3,
- erosional trends between RM 0 to RM 2 during the low-flow periods (2007–2008 and 2011–2012) in the inter-annual morphological changes as presented in Figure 4.2, and the consideration that the erosion cannot be caused by natural hydrodynamic forcings — model-calculated bed shear stresses during the periods of erosion are not high enough to cause the noted magnitude of erosion, and
- local-scale spatial patterns of erosion that are consistent with ship tracks developed from marine traffic data (Moffatt and Nichol and Deltares [25]).

Collectively, these lines of evidence indicate that this reach of the LPR is in a state of dynamic equilibrium with the ongoing shipping activities. Therefore, the impact of navigation in the morphological equilibrium of the LPR was assessed using a prognostic simulation that does not include shipping-induced scour in the LPR. Figure 4.14 shows the resulting comparison of initial and calculated bathymetry at the end of the simulation, and the cross-section area and its relationship with tidal prism using the initial and final model-calculated bathymetry. The comparisons indicate that the reach between RM 0 and RM 2 which currently experiences shipping-induced scour, will infill by up to 2-3 m in some areas in the absence of navigation. The infilling sediment is a combination of sediment scoured from landward locations during Regime III events as well as sediments transported from Newark Bay by the tide and estuarine circulation. Consequently, the cross-section adapts, and seaward of RM 2, both the longitudinal profile of cross-section area and the trend of cross-section with tidal prism tend towards a continuation of trends measured in 2007 at more landward locations. These results are consistent with the hypothesis that this reach of the LPR is currently in a state of dynamic morphological equilibrium with the ongoing shipping activities. In the absence of navigation, substantial infill will occur, reaching an equilibrium cross-section that is similar to that expected based on morphodynamic relationships apparent in more landward reaches.

Furthermore, using the river morphology at the end of the prognostic simulation, the convergence length and exponent of 26.6 km and 0.42, respectively, are only marginally different from values based on the current morphology (presented in Section 4.2). These results indicate that the reach landward of RM 2 is largely at morphodynamic equilibrium, which is a finding that is consistent with the results of the analytical infill model presented in Section 4.2.

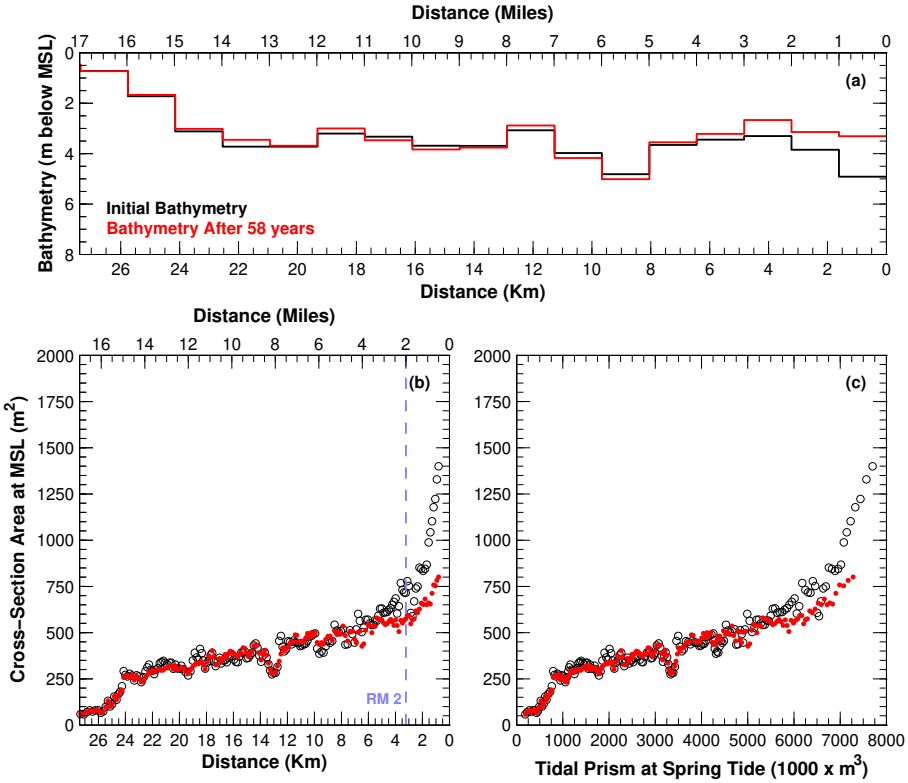

Figure 4.14: Application of the morphodynamic model using Morfac to assess the impact of navigation between RM 0 and RM 2 in the LPR. Longitudinal profiles of bathymetry (a) and cross-sectional area (b), and tidal prism to cross-section relationship (c) measured in 2007, and model-calculated after a 58-year prognostic simulation.

4.5.2. IMPACT OF REGIME III EVENTS

EPISODIC events causing significant erosion and export of sediments are considered to be the mechanism responsible for maintaining the long-term morphological equilibrium in an estuary, which may otherwise experience infilling due to import of sediments from both landward and seaward directions (Geyer *et al.* [11] and Meade [38]). In the context of the LPR, Regime III events are considered to be representative of such erosional and exporting conditions (Mathew and Winterwerp [10]). Therefore, in order to assess the significance of Regime III events on long-term morphological behavior, the results of a prognostic simulation using the measured river flow hydrograph were compared to a simulation where river flow was capped at 100 m^3/s, which is the local threshold for Regime III events for the reach landward of RM 8.

Figure 4.15 shows the resulting comparison of initial and calculated bathymetry at the end of the simulation, and the cross-section area and its relationship with tidal prism using the initial and final model-calculated bathymetry. Similar to the results presented in Figure 4.14 (which includes the impact of Regime III events), the results in Figure 4.15

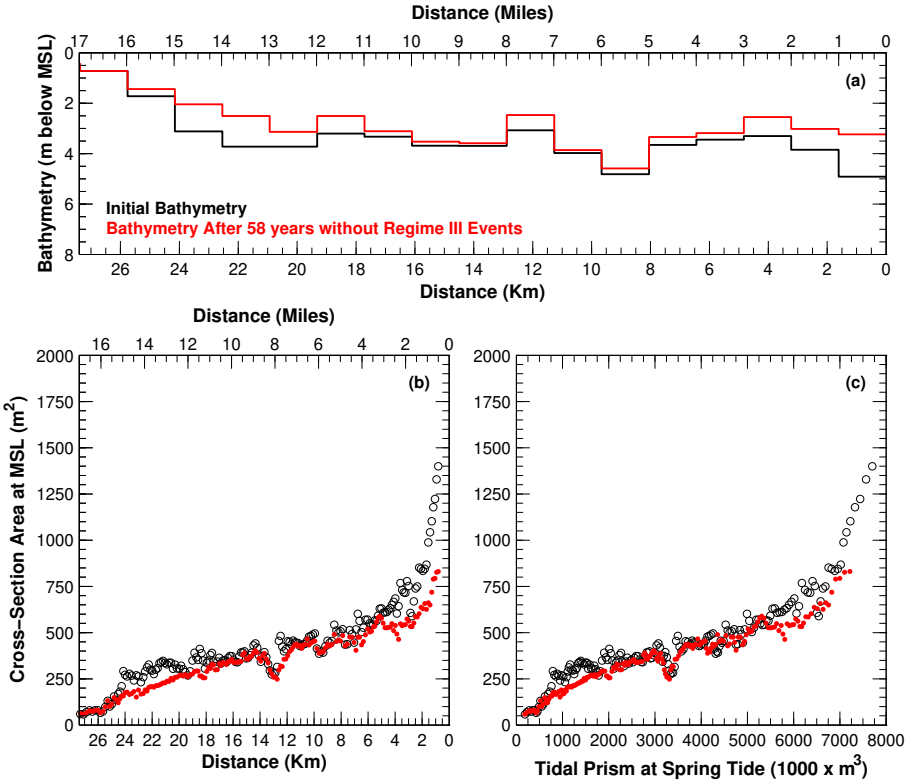

Figure 4.15: Application of the morphodynamic model using Morfac to assess the impact of episodic Regime III events. Longitudinal profiles of bathymetry (a) and cross-sectional area (b), and tidal prism to cross-section relationship (c) — measured in 2007, and model-calculated after a 58-year prognostic simulation without Regime III events.

show significant infilling in the reach seaward of RM 2. However, in contrast to the results in Figure 4.14, the results in Figure 4.15 show infilling throughout the length of the estuary, and most markedly in the upper reaches (between RM 15 and RM 11). These results indicate a difference in the equilibrium morphology of the river in the absence of Regime III events, with a shallower equilibrium bathymetry than in the presence of Regime III events. These results tend to confirm the hypothesis of Geyer *et al.* [11] and Meade [38], and the empirical observations of Mathew and Winterwerp [10] on the role of Regime III events in the long-term morphological equilibrium of estuaries.

Regime III events also impact the morphodynamic relations of cross-section profile and relationship with tidal prism. In contrast with the values for the current morphology presented in Section 4.2, the results in Figure 4.15 show that in the absence of Regime III events, the convergence length L_A and exponent α, decrease to 19.1 km, and increase to 0.58, respectively. The decrease in convergence length is consistent with the findings of Dronkers [39] who showed convergence length to be a positive function of river flow velocity. Accordingly, a decrease in river flow rate (e.g., due to the lack of Regime III events),

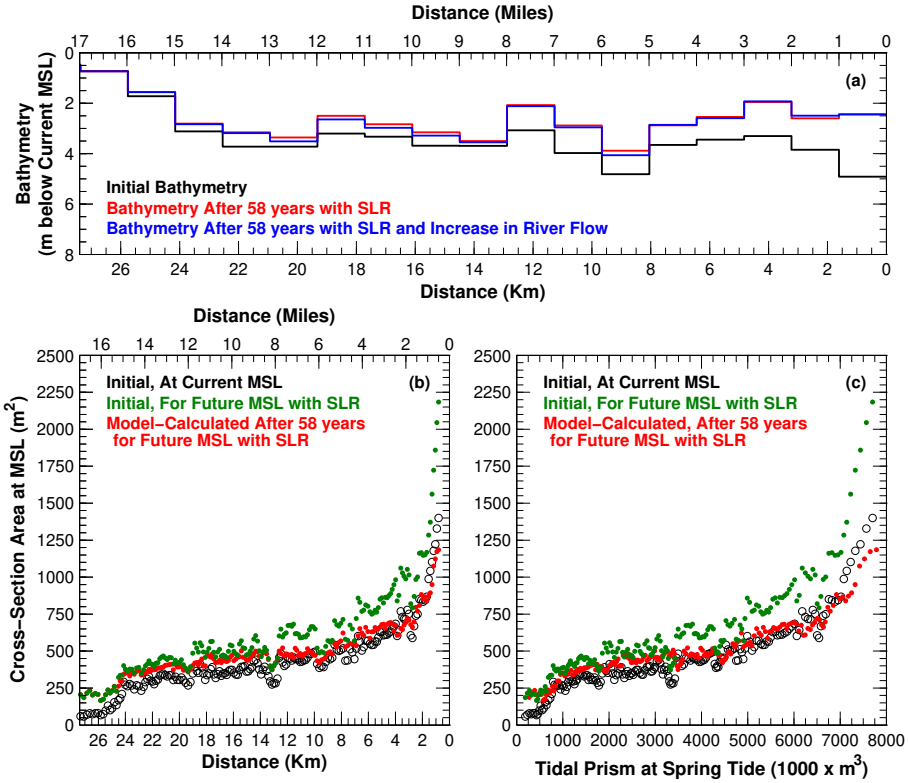

Figure 4.16: Application of the morphodynamic model using Morfac to assess the impacts of SLR and increasing river flow due to climate change. Longitudinal profiles of bathymetry — measured in 2007, and model-calculated after 58-year prognostic simulations with SLR and with increasing river flow (a). Longitudinal profiles of cross-sectional area (b), and tidal prism to cross-section relationship (c). Cross-sections in panels b and c shown for current bathymetry at current MSL, current bathymetry for future MSL with SLR, and for calculated bathymetry after a 58-year simulation with SLR.

would result in a decrease in the convergence length which is consistent with the numerical model results. The decrease in cross-section area in the upper reaches also leads to the increase in the value of α, tending towards values more commonly observed for tidal inlets (in the range of 0.85-1.1; D'Alpaos *et al.* [22]). In other words, in the absence of Regime III events, river flow becomes a relatively less important forcing compared to the barotropic forcing in shaping the equilibrium morphology of the estuary. Therefore, in addition to maintaining the long-term morphological equilibrium, Regime III events are also responsible for shaping the morphodynamic equilibrium profile of the estuary.

4.5.3. IMPACT OF CLIMATE CHANGE

BROADLY speaking, the projected impact of climate change relevant for morphological development is two-fold and includes sea level rise (SLR) and changes in river flow rate. SLR in the LPR, under an extreme scenario, is projected to be about 1.3 m (relative

to the year 2000) by the year 2070 (Kopp *et al.* [40]). Although climate change impacts on river flow in the LPR are not known precisely, projections from global climate models generally indicate an increase in total precipitation during storm events. For instance, in the LPR, compared to the historical conditions, total precipitation during a 4-day storm event with a return period of 100 years is projected to increase by about 20% by the year 2080 (CDM Smith and Matrix New World [41]). Therefore, assuming linearity, river flow rate in the future is expected to be higher than current conditions. However, SLR and increasing river flow may have opposing morphological impacts. Specifically, SLR will cause a decrease in currents, thus promoting infilling, whereas increasing river flow will cause an increase in currents, especially during storm events, which could cause erosion and export of sediments from the estuary. Therefore, the relative impact of SLR and increasing river flow was assessed using two incremental prognostic simulations using (1) the projected SLR and current river flow rates, and (2) the projected SLR and projected river flow rates (calculated by enhancing current river flow by 20% as a crude approximation of the additional precipitation due to climate change).

Figure 4.16 shows the resulting comparison of initial bathymetry in the prognostic simulations, and calculated bathymetry at the end of the two incremental prognostic simulations. These comparisons show significant infilling over nearly the entire length of the estuary, primarily due to the decrease in currents associated with the increase in water depth due to SLR. These results also indicate that SLR rather than increased river flow rate has a greater impact on the morphological evolution of the estuary, with the overall impact of climate change being infill of the LPR. Possibly, also the sediment loading may increase with increasing river flow, which would shorten the time scales to attain the new equilibrium. Since no predictions exist on changes in sediment loading due to climate change, this subject was not addressed in this scenario. Furthermore, the longitudinal profiles of river cross-section and trend of cross-section area with tidal prism shown in Figure 4.16 indicate that the estuary adapts to the disequilibrium caused by SLR by infilling and tending towards a morphodynamic profile similar to current conditions (for the current morphology and current MSL) in most of the estuary. However, as seen from localized differences between the cross-section at the end of the prognostic simulation and the cross-section under the current MSL, the 58-year duration of the prognostic simulations is likely not sufficient to attain the equilibrium profile. Nonetheless, the overall response of the system to SLR is consistent with theoretical and historical response to SLR (Meade [38]).

4.6. DISCUSSION

THE LPR is characterized by predominantly fine sediment transport, although the bed in places is mixed (fines and sands). Consequently, transport (mainly erodibility) is influenced by stratified, armored conditions, and by consolidation effects. As a result, the transport of fines in the system is below capacity conditions, i.e., no equilibrium exists between the sediment load and the local hydraulic conditions. The amount of mobile sediment, actively forming the river's morphology, is largely influenced by past hydrodynamic conditions, in particular by episodic erosional events (Mathew and Winterwerp [10]). The morphodynamic development of the LPR thus exhibits profound memory effects at various time scales, from the tidal period to multi-year periods spanning

episodic erosional events. At short to intermediate time-scales, the response to hydrodynamic forcing is characterized by three regimes, mainly governed by the river flow. Regime I reflects the dynamics of a limited amount of fines contained within an easily-erodible fluff layer overlying less-erodible parent layers, and that is resuspended and deposited every tidal cycle. During Regime II, this fluff layer is washed out of the river, while the parent bed remains largely untouched. Reestablishment of the Regime I volume of fines characterizes the first memory effect. However, the fluff layer is relatively thin and does not affect the morphodynamic state of the river on short time scales, although the fluff layer dynamics do control net infilling and accumulation of sediments during prolonged periods of low-moderate river flows. During Regime III conditions, the parent bed is scoured as well, although somewhat unevenly because of the many structures in the river (e.g., bridges), and the uneven composition and erodibility of the sediment bed. Reestablishment of the pre-Regime III conditions can only take place through the fluff layer dynamics. Hence, the amount of sediment scoured, its fate, and time of re-infill of the river defines another memory effect. Furthermore, shipping impacts near the mouth of the LPR mobilizes sediment at a greater rate than the natural hydrodynamic forcings, and hence affects the memory of the river as well. Because the morphodynamic development and relevant time scales are steered by the amount of mobile sediment in the river, strong non-linear hysteresis effects are introduced — for the same hydrodynamic conditions (river flow, tide, salinity intrusion), the river response may be quite different depending on the time-history of river flow. While quantified for the LPR, this type of response is characteristic of fine sediment dynamics in rivers characterized by erosion-limited conditions (Winterwerp *et al.* [5]).

The sediment dynamics pertaining to sediment mobility, memory effects, and consequently, the three transport regimes in the LPR are generally confirmed by the application of the morphodynamic model presented here. The model formulation, specifically the bed schematization with an easily-erodible fluff layer overlying less erodible parent bed, reproduces the short-term dynamics in SSC and SSF, and the large-scale spatial and temporal (flow-dependent) trends in morphological change over short-term (inter-annual) periods. However, the model response is less accurate at local scales, especially for short-term (inter-annual) morphological change. Model performance is limited by the fact that bed composition and stratigraphy cannot be reproduced in detail because they depend on initial conditions and memory effects that are not known precisely. Nonetheless, the model captures the long-term (decadal-scale) morphological trend, specifically when the system was under a state of morphological disequilibrium caused by navigational dredging. The long-term performance of the model further confirms the system dynamics inferred using empirical lines-of-evidence (Mathew and Winterwerp [10]).

The morphodynamic model framework using Morfac allows for assessment of the current morphological status of the LPR and its long-term response to external forcings. Currently, the majority of the LPR (i.e., landward of RM 2) is in a state of dynamic morphological equilibrium under the natural forcings (barotropic, baroclinic and river flow). However, the reach seaward of RM 2 is in different equilibrium, one controlled by the ongoing shipping activities in this reach. In absence of any shipping, the reach seaward of RM 2 is projected to infill and tend towards an equilibrium profile similar

to more landward reaches. Conceptually, this is consistent with expectations based on the relationship of estuarine convergence length and tidal prism to cross-section area. Episodic Regime III events are especially important for maintaining the current equilibrium morphodynamic profile landward of RM 2 by providing a mechanism for erosion and export of sediments that accumulate under Regimes I and II, consistent with the hypothesis of others (Geyer *et al.* [11] and Meade [38]). In the absence of Regime III events, the estuarine convergence length would decrease, consistent with theoretical expectations (Dronkers [39]), and the tidal prism to cross-section area relationship would tend towards trends in tidal inlets (D'Alpaos *et al.* [22]). In the future, because of climate change (primarily SLR), the LPR is projected to experience infilling over nearly its entire length, with the morphodynamic profile tending towards the current equilibrium profile. However, it should be noted that the time to attain morphodynamic equilibrium may be somewhat different than inferred from the results presented here, primarily because of uncertainties in future sediment loadings, transport in Newark Bay, etc. Overall, the prognostic assessments using the morphodynamic model are conceptually explainable, consistent with theoretical expectations, and consistent with observations of other authors.

The assessment of the morphodynamic model using Morfac shows that morphological upscaling may be deployed in fine sediment systems between relatively large episodic erosional events, provided that the morphological upscaling is applied to the sediment mass in the bed rather than bed level. The response to episodic erosional events (involving erosion of the parent bed underneath the fluff layer) cannot be represented with the Morfac approach, as this response is too non-linear. This implies that the morphodynamic modeling of rivers under erosion-limited conditions requires a thorough analysis of the hydrograph, including the recurrence intervals and order of occurrence of the relatively large episodic events. These inherent uncertainties are reflected directly in the uncertainties of model predictions, the results of which should therefore be interpreted accordingly. When the system is in a state of morphodynamic disequilibrium, the Morfac approach is feasible over the long time-scales needed to attain equilibrium. This was the case in the LPR, which was dredged several meters below its equilibrium depth in 1950, and has since infilled over time.

The model framework presented here, specifically the bed structure for parameterizing and representing erosion-limited conditions, is generally similar to numerical models of such fine sediment systems developed by other authors (van Maren *et al.* [42]). The model framework is generally applicable to settings with erosion-limited transport associated with either consolidation effects in the bed (e.g., in a purely fine sediment system), or due to armoring in mixed sediment systems. Furthermore, both settings (purely fine sediment and mixed) may occur in the same system, for instance, between the thalweg and adjacent inter-tidal areas. However, such non-linearities driving the system response in fine sediment settings implies that appropriate representation of such systems in morphodynamic models requires a significant amount of site-specific data describing spatial and temporal variations in key transport parameters. These include the erodibility of sediments (for the fluff layer and the parent bed), sediment stratigraphy, temporal trends in erodibility due to consolidation/swelling, and settling velocities for fine sediments in suspension. In practical terms, the relatively large data requirements

imply that numerical models of fine sediment systems are almost invariably limited by the availability of data for model parameterization and calibration (Vested *et al.* [3]).

These considerations indicate the potential for limitations in numerical models of fine sediment systems. While certain limitations (e.g., more spatial discretization of the physical transport processes) may be addressed computationally (e.g., using smaller model grid cells), others require extensive site-specific data. For instance, conceptually, a sediment bed formed by sedimentation in a dredged navigation channel is expected to be more erodible than an undisturbed bed created over millennial timescales. Similarly, a newly-deposited sediment bed is expected to consolidate and decrease in erodibility over time. Both effects can be parameterized by appropriate spatially and temporally comprehensive measurements of sediment erodibility. Other limitations may require alternate formulations than traditionally implemented in numerical models. For instance, based on application to data from erosion experiments, van Prooijen and Winterwerp [43] propose a model formulation that includes a Gaussian distribution of turbulent bed shear stress, a stochastic distribution of critical shear stress and using dozens of fine sediment classes. In contrast, typical model formulations characterize the turbulence-mean shear stress at the bed-water interface and parameterize the mean critical shear stress along with one or, at most, a few fine sediment classes.

Finally, another conceptual and philosophical aspect to consider in the application of such models over long-term or to equilibrium conditions is that models are schematized and simplified representations of reality. Model performance responds to the numerical parameterization of various processes that may introduce deviations from reality over the long-term. In other words, the model has its own equilibrium which may or may not be identical to reality. Such limitations and related uncertainties require consideration when assessing model performance, especially in comparison to data. For the application presented in this chapter, the primary uncertainty is in its performance over the short term and over small spatial scales. Model performance over the long-term and large spatial scales is comparable to data. Therefore, the morphodynamic model framework including the Morfac approach presented here is concluded to be suitable for assessing the long-term and large-scale morphodynamics in fine sediment settings where memory effects and sediment mobility have a strong influence on transport and morphological development.

4.7. CONCLUSIONS

MORPHODYNAMICS of fine sediment systems differ in several key respects from sandy systems. In addition to being dependent upon the external forcings (which is the case also in sandy systems), morphodynamics in fine sediment systems are also a consequence of non-equilibrium transport related to sediment mobility and memory effects induced by the time-history of morphological development. These processes were assessed empirically and used to develop a conceptual picture of sediment dynamics and transport regimes in the LPR and generally confirmed using the morphodynamic model framework and application presented in this chapter. Furthermore, morphological upscaling following the Morfac approach, and using formulations specifically adapted for fine sediment settings, is also shown to be an appropriate tool for computationally-efficient long-term morphodynamic modeling in such systems. The morphodynamic

model framework using Morfac presented here provides a tool for assessing the long-term morphodynamics in fine sediment systems for applications such as the design and impact of engineering interventions (e.g., dredging, river training works, etc.), impact of climate change, development of sediment management strategies, etc.

REFERENCES

[1] G. R. Lesser, J. A. Roelvink, J. A. T. M. van Kester, and G. S. Stelling, *Development and validation of a three-dimensional morphological model,* Coast Eng **51**, 883 (2004).

[2] J. A. Roelvink, *Coastal morphodynamic evolution techniques,* Coast Eng **53**, 277 (2006).

[3] H. J. Vested, C. Tessier, B. B. Christensen, and E. Goubert, *Numerical modelling of morphodynamics — Vilaine estuary,* Ocean Dynam **63**, 423 (2013).

[4] L. C. van Rijn, *Principles of Sediment Transport in Rivers, Estuaries, and Coastal Seas* (Aqua Publications, Emmeloord, The Netherlands, 1993).

[5] J. C. Winterwerp, T. van Kessel, D. S. van Maren, and B. C. van Prooijen, *Fine Sediment in Open Water — From Fundamentals to Modeling* (World Scientific, in press, 2021).

[6] E. Partheniades, *Erosion and deposition of cohesive soils,* J Hydraul Div-ASCE **91**, 105 (1965).

[7] A. J. Mehta, *Laboratory studies on cohesive sediment deposition and erosion,* in *Physical Processes in Estuaries*, edited by J. Dronker and W. van Leussen (Springer, Berlin, 1988) pp. 427–445.

[8] L. P. Sanford and J. P. Y. Maa, *A unified erosion formulation for fine sediments,* Mar Geol **179**, 9 (2001).

[9] R. Mathew and J. C. Winterwerp, *Surficial sediment erodibility from time-series measurements of suspended sediment concentrations: Development and validation,* Ocean Dynam **67**, 691 (2017).

[10] R. Mathew and J. C. Winterwerp, *Sediment dynamics and transport regimes in a narrow microtidal estuary,* Ocean Dynam **70**, 435 (2020).

[11] W. R. Geyer, J. D. Woodruff, and P. Traykovski, *Sediment transport and trapping in the Hudson River estuary,* Estuaries **24**, 670 (2001).

[12] J. M. McSweeney, R. J. Chant, and C. K. Sommerfield, *Lateral variability of sediment transport in the Delaware estuary,* J Geophys Res-Oceans **121**, 725 (2016).

[13] R. Ranasinghe, C. M. Swinkels, A. P. Luijendijk, J. A. Roelvink, J. Bosboom, M. J. F. Stive, and D. J. R. Walstra, *Morphodynamic upscaling with the morfac approach: Dependencies and sensitivities,* Coast Eng **58**, 806 (2011).

[14] G. R. Lesser, *An approach to medium-term coastal morphological modelling*, PhD dissertation, UNESCO-IHE and Technische Universiteit Delft (2009).

[15] M. van der Wegen and J. A. Roelvink, *Long-term morphodynamic evolution of a tidal embayment using a two-dimensional, process-based model,* J Geophys Res **113** (2008).

[16] G. Dam, M. van der Wegen, R. J. Labeur, and D. Roelvink, *Modeling centuries of estuarine morphodynamics in the Western Scheldt estuary,* Geophys Res Lett **43**, 3839 (2016).

[17] R. Styles, M. E. Brown, K. E. Brutsche, H. Li, T. M. Beck, and A. Sanchez, *Long-term morphological modeling of barrier island tidal inlets,* J Mar Sci Eng **4**, 65 (2016).

[18] N. K. Ganju, D. H. Schoellhamer, and B. E. Jaffe, *Hindcasting of decadal-timescale estuarine bathymetric change with a tidal-timescale model,* J Geophys Res **114**, F04019 (2009).

[19] D. A. George, G. Gelfenbaum, and A. W. Stevens, *Modeling the hydrodynamic and morphologic response of an estuary restoration,* Estuar Coast **35**, 1510 (2012).

[20] M. van der Wegen and B. E. Jaffe, *Processes governing decadal-scale depositional narrowing of the major tidal channel in San Pablo Bay, California, USA,* J Geophys Res Earth Surf **119**, 1136 (2014).

[21] U.S. Army Corps of Engineers, *Lower Passaic River Commercial Navigation Analysis* (New York, NY, USA, 2010).

[22] A. D'Alpaos, S. Lanzoni, M. Marani, and A. Rinaldo, *On the tidal prism-channel area relations,* J Geophys Res **115**, F01003 (2010).

[23] A. F. Blumberg and G. L. Mellor, *A coastal ocean numerical model,* in *Mathematical Modelling of Estuarine Physics*, edited by J. Sündermann and K. P. Holz (Springer-Verlag, New York).

[24] HydroQual, *Final Hydrodynamic Modeling Report: Lower Passaic River Restoration Project and Newark Bay Study* (Mahwah, NJ, 2008).

[25] Moffatt and Nichol and Deltares, *Appendix M: Sediment transport model of the Lower Passaic River, Lower Passaic River RI/FS* (Cooperating Parties Group, Newark, NJ, 2019).

[26] T. D. Borrowman, E. R. Smith, J. Z. Gailani, and L. Caviness, *Erodibility study of Passaic River sediments using USACE Sedflume* (ERDC TR-06-7, Kansas City, Missouri, 2006).

[27] J. C. Winterwerp and W. G. M. van Kesteren, *Introduction to the Physics of Cohesive Sediments in the Marine Environment, Vol. 56* (Elsevier, New York, 2004).

[28] L. P. Sanford, *Modeling a dynamically varying mixed sediment bed with erosion, deposition, bioturbation, consolidation, and armoring,* Comput Geosci **34**, 1263 (2008).

[29] J. Roberts, R. Jepsen, D. Gotthard, and W. Lick, *Effects of particle size and bulk density on erosion of quartz particles,* J Hydr Engrg **124**, 1261 (1998).

[30] Sea Engineering Inc., *Sedflume Analysis Data Report Newark Bay, New Jersey* (Santa Cruz, CA, 2013).

[31] N. A. Cheng, *Simplified settling velocity formula for sediment particles,* J Hydraul Eng **123**, 149 (1997).

[32] J. C. Winterwerp, *On the flocculation and settling velocity of estuarine mud,* Cont. Shelf Res **22**, 1339 (2002).

[33] D. Tran and K. Strom, *Floc sizes and resuspension rates from fresh deposits: Influences of suspended sediment concentration, turbulence, and deposition time,* (2019).

[34] J. Gessler, *The beginning of bedload movement of mixtures investigated as natural armoring in channels* (California Institute of Technology, Pasadena CA, 1967).

[35] L. C. van Rijn, D. J. R. Walstra, B. Grasmeijer, J. Sutherland, S. Pan, and J. P. Sierra, *The predictability of crossshore bed evolution of sandy beaches at the time scale of storms and seasons using process-based profile models,* Coast Eng **47**, 295 (2003).

[36] J. Sutherland, A. H. Peet, and R. L. Soulsby, *Evaluating the performance of morphological models,* Coast Eng **51**, 917 (2004).

[37] U.S. Army Corps of Engineers, *Geomorphological/Geophysical Characterization of The Nature and Dynamics of Sedimentation and Sediment Transport in Newark Bay focusing on the Effects related to Continued and Future Federal Navigation Channel Deepening and Maintenance* (New York, NY, USA, 2006).

[38] R. H. Meade, *Landward transport of bottom sediments of the Atlantic coastal plain,* J Sediment Petrol **39**, 222 (1969).

[39] J. Dronkers, *Convergence of estuarine channels,* Cont Shelf Res **144**, 120 (2017).

[40] R. E. Kopp, C. Andrews, A. Broccoli, A. Garner, D. Kreeger, R. Leichenko, N. Lin, C. Little, J. A. Miller, J. K. Miller, K. G. Miller, R. Moss, P. Orton, A. Parris, D. Robinson, W. Sweet, J. Walker, C. P. Weaver, K. White, M. Campo, M. Kaplan, J. Herb, and L. Auermuller, *New Jersey's Rising Seas and Changing Coastal Storms: Report of the 2019 Science and Technical Advisory Panel* (New Jersey Department of Environmental Protection, Trenton, NJ, USA, 2019).

[41] CDM Smith and Matrix New World, *Passaic River Basin Climate Resilience Planning Study* (North Jersey Transportation Planning Authority, Newark, NJ, USA, 2019).

[42] D. S. van Maren, T. van Kessel, K. Cronin, and L. Sittoni, *The impact of channel deepening and dredging on estuarine sediment concentration,* Cont Shelf Res **95**, 1 (2015).

[43] B. C. van Prooijen and J. C. Winterwerp, *A stochastic formulation for erosion of cohesive sediments,* J Geophys Res **115**, C01005 (2010).

5

SYNTHESIS, CONCLUSIONS, AND RECOMMENDATIONS

CONSISTENT with the general and specific research objectives presented in Chapter 1, this dissertation presents an analysis of transport and morphodynamics in a fine sediment system. The specific research objectives were addressed using a combination of data analyses, development of conceptual and theoretical formulations, application of analytical models, and the development and application of a numerical model. This chapter presents a synthesis of the key findings of this dissertation specifically with regard to the LPR as well as more broadly for such fine sediment systems. Key recommendations for future work in this subject area are also presented.

5.1. SYNTHESIS AND CONCLUSIONS

TRANSPORT in fine sediment systems is often a non-equilibrium process that is dependent on the availability of mobile sediment in the bed; this dissertation focuses on transport in such systems. Sediment mobility, i.e., the sediment inventory available for erosion under given shear stress, is related to the supply of sediments in the bed, sediment erodibility, and/or the settling velocity of fines, resulting in supply-limited, erosion-limited, and/or settling-limited conditions, respectively; these are also broadly referred to as starved-bed conditions. Such mobility considerations can control erosion locally, resulting in large-scale (spatial and temporal) non-linear system dynamics and dependencies with system forcings. Another phenomenon related to sediment mobility is the potential for hysteresis effects induced by the timing and sequencing of episodic erosional events — this induces a memory effect to transport, where erosion during past events limits mobility during future events and thus steers morphologic development. This implies a degree of uncertainty with regard to the predictability of transport and morphodynamics in starved-bed systems. Therefore, the major underlying theme of this dissertation concerns the predictability of the sediment dynamics and morphodynamics of this class of systems.

The attributes and phenomena characteristic of starved-bed transport have been observed in the Lower Passaic River (LPR). An extensive dataset of independent empirical measurements of various metrics has allowed an assessment of transport dynamics as well as the development of a numerical morphodynamic model of the LPR. The morphodynamic model is used to confirm the physical basis for the empirical observations, as well as to address various hypotheses.

The LPR is a short, narrow, microtidal estuary located on the east coast of the USA. The LPR stretches approximately 28 km from the head-of-tide (at Dundee Dam) to its mouth in Newark Bay, which is connected to the Atlantic Ocean via a pair of tidal inlets. The width of the LPR ranges from approximately 600 m at its mouth, declining to about 75 m at the head-of-tide. The hydrodynamic forcings within the LPR include the tides, estuarine circulation, and river flow. Semi-diurnal tides entering Newark Bay propagate to the LPR and the head-of-tide, with tidal range varying from 0.9 m to 2.1 m from neap to spring, and maximum currents typically occurring around mid-tide. The average river flow over Dundee Dam is about 34 m^3/s, although significant variations in flow rate can occur; during the periods analyzed in this dissertation, river flow rate ranged from a low of about 1 m^3/s to a high of about 700 m^3/s (representing an event with a return period of about 90 years). Salinity intrusion occurs during periods of low–average river flow (resulting in a partially-mixed water column), with the saline water flushed out of the LPR at high river flow (>200 m^3/s; return period of 2 years). The extent of salinity intrusion, as indicated by the location of the salt front, is a function of the tidal phase, river flow rate, spring–neap cycle, as well as offshore mean water level fluctuations; the salt front is also co-located with the ETM.

The LPR was extensively modified in several regards — wetland reclamation, deepening for navigation, shoreline armoring, construction of infrastructure such as bridges and railway crossings, etc. The last such major modification occurred several decades ago and involved the dredging of the navigation channel in the lower reaches of the estuary to depths of about 6 m to 10 m (with respect to MSL) — several meters below the original pre-industrial depths. Typical water depths along the thalweg in the LPR currently range between 5 m to 7 m (with respect to MSL), indicating significant infilling of the estuary. Navigation in the LPR has declined greatly over time and currently is limited to the lower 3 km (~2 miles) of the estuary. Nonetheless, navigation has a significant impact on the transport and fate of sediments and the morphodynamics in this reach of the estuary. In contrast, the reaches landward of the areas currently subject to navigation have experienced significant infilling and have more or less reattained their morphodynamic equilibrium profile. However, these reaches exist in a state of dynamic equilibrium with the river flow regime, generally experiencing infilling during low–moderate river flows and erosion during high river flows.

The sediment substrate within the LPR is composed of predominantly fine sediments. Although sands of size ranging up to 2000 μm are present locally in the lower 20 km of the estuary, clay content is in excess of about 10%. As a result, the majority of the bed in the LPR exhibits cohesive behavior. Significant fractions of sands (including gravel sized fractions of size >2000 μm) are found only in a short section towards the head-of-tide. Furthermore, the majority of the sediment loading to the LPR from the head-of-tide as well as from Newark Bay comprises of fine sediments. Because of depth-dependent

erodibility (as a consequence of consolidation) and armoring effects induced by the presence of sands in the bed, sediment transport in the LPR is below equilibrium capacity. In other words, the LPR exhibits the characteristics of a starved-bed system.

Starved-bed systems are characterized by a relatively easily-erodible surficial sediment stratum referred to as the fluff layer overlying less-erodible parent bed layers. Transport in such systems scales with tidal currents, with SSC variations that follow the periodic oscillation in tidal currents — reaching a maximum around mid-tide and a minimum around slack water. This implies that the fluff layer is depleted (by erosion) and replenished (by deposition) every tidal cycle. Various lines-of-evidence supporting the presence of the fluff layer, specifically in the LPR as well as more broadly in estuarine settings, are presented in Appendix A. The sediments within the fluff layer represents the sediment inventory responding to barotropic and baroclinic circulation, leading to phenomena such as the net up-estuary transport of sediments against the direction of residual flow, and the formation of ETMs. Appropriate representation of suspended sediment concentrations and fluxes in such systems therefore requires quantification of the erodibility of the fluff layer. Chapter 2 presents the development of an analytical approach, termed the entrainment flux method, for quantifying the erodibility of the fluff layer. The results of the entrainment flux method are also shown to be comparable to direct measurements of erodibility in sediment cores using a Gust Microcosm; this indicates that the entrainment flux method can be used to infer and quantify the erodibility of the fluff layer in such starved-bed systems.

In the LPR, fluff layer dynamics are responsible for sediment dynamics during low–moderate river flows. As river flow rate increases, ebb currents increase (and flood currents decrease), and the salt front is flushed out of the LPR. Simultaneously, the higher ebb currents cause erosion of the less-erodible layers underneath the fluff layer, and prevents deposition around slack water, i.e., prevents replenishment of the fluff layer. Thus, increasing river flow rate reduces or eliminates the impact of barotropic and baroclinic circulation on sediment dynamics. Consequently, sediment dynamics during high flow conditions scales with river flow rate, subject to limitations of supply- and erosion-limited transport. Such limitations are apparent in the LPR — erosion is estimated to be limited to the fluff layer during river flows up to about 200 m^3/s for the system as a whole. In other words, only the sediment inventory within the fluff layer is estimated to be flushed out of the river during rivers flows up to about 200 m^3/s. This implies that such events are not significant from a morphological perspective. Only when river flow exceeds 200 m^3/s for the system as a whole does the less-erodible parent bed erode, with erosion depths generally scaling with river flow rate (subject to limitations of supply- and erosion-limited transport). Thus, river flow rate acts to modulate the impact of barotropic and baroclinic circulation on sediment dynamics, the direction and magnitude of net sediment transport, and morphological evolution. Consequently, the morphodynamic status of the system at any given instant can fall into one of three river flow-dependent regimes — Regime I includes conditions when the system is importing sediments via barotropic and baroclinic pathways, Regime II includes conditions when the system is exporting sediments by flushing the fluff layer, and Regime III includes conditions when the system is exporting sediments by scouring more consolidated strata underneath the fluff layer. The thresholds between Regimes I and II are estimated as 20–

30 m^3/s and between Regimes II and III as 200 m^3/s for the system as a whole, although these thresholds decrease in the landward direction.

Such river flow-dependent transport regimes are typical of such fine sediment systems, having been empirically observed in estuaries such as the Hudson and Delaware Rivers in the USA, Huangmao-hai estuary in China, and Wairoa River in New Zealand (see Chapter 3 for further discussion). However, the morphological impact of such nonlinear transport and, in particular, the impact of episodic extreme events in such systems has been somewhat less studied. The morphological change measured in the LPR during Regime III events shows significant scour during such conditions. Furthermore, the application of the numerical model in Chapter 4 indicates that Regime III events play an active role in maintaining the dynamic morphological equilibrium in such systems by providing a mechanism that scours and exports sediment accumulating during Regimes I and II. These results confirm the hypothesis of other authors on the role of such extreme events (i.e., Regime III conditions).

In the LPR, sediments scoured from the landward reaches during Regime III events is typically deposited in the lower 2 miles of the estuary. As shown in Chapter 4, this reach is depositional during such conditions because it is not currently at morphodynamic equilibrium. Active navigation in this reach is responsible for maintaining a deeper cross-section than would be expected in the absence of navigation; propeller wash associated with transiting and maneuvering vessels provides a mechanism that scours sediment that accumulates during Regime III conditions. In the absence of navigation, this reach of the LPR is estimated to infill and follow morphodynamic trends apparent in more landward reaches. These results indicate the role of navigation in maintaining a morphodynamic equilibrium driven by anthropogenic forcings rather than natural forcings, and is of relevance for other systems experiencing navigation.

In order to address the question of the predictability of transport in starved-bed settings, various empirical measurements and quantitative analyses were used to develop and parameterize a process-based numerical morphodynamic model application of the LPR (see Chapter 4). The classic morphodynamic loop used extensively in sandy systems was modified to explicitly include sediment mobility considerations. Starved-bed conditions were represented using a multi-layer parent bed model that incorporates the effects of self-weight consolidation and swelling on sediment erodibility in time and over depth in the bed, and armoring effects on sediment erodibility were represented using a multi-class model including several sand-sized classes. The bed model also includes an easily-erodible fluff layer overlying less-erodible parent layers. The resulting model performance generally confirms the role of starved-bed conditions on sediment dynamics, and specifically the importance of the fluff layer for sediment dynamics during low–moderate river flows, the role of river flow in modulating sediment dynamics, the various time-scales of transport. Although the model does not capture the measured morphological response at local scales over the short-term, it predicts the large-scale spatial and temporal (river flow-dependent) short- and long-term morphological response of the system. Model performance is limited primarily by the availability of data on sediment stratigraphy, and spatial and temporal variations in erodibility of the parent bed. Nonetheless, the morphodynamic model framework is generally applicable to settings with starved-bed transport due to either decreasing erodibility with depth in the bed

(e.g., in a purely fine sediment system), or due to armoring in mixed sediment systems.

Further to the question of predictability of transport in starved-bed settings, the morphodynamic model framework was extended to include morphological upscaling using the Morfac technique which enables computationally efficient long-term morphodynamic modeling. The Morfac approach was originally developed and has been applied extensively for problems of sand transport in coastal settings over multi-year to millennial time-scales. However, it was not obvious that the Morfac approach can yield realistic results for fine sediment systems characterized by large memory effects and various time-scales of morphological response. Specific formulations and considerations were developed for appropriate representation of starved-bed transport within the context of the Morfac approach. The resulting morphodynamic model using Morfac reproduces the same performance as the more computationally-intensive approach over the short-term and the long-term measured morphological change in the LPR. The results support the use of the Morfac approach for studying the long-term morphological evolution of such starved-bed systems.

The application of the numerical morphodynamic model therefore supports the notion of predictability of morphodynamics in starved-bed systems. However, it should be noted that although large-scale spatial and temporal trends in transport and morphodynamics can be reliably predicted, predictions of small-scale spatial and temporal trends are more uncertain. Borrowing a terminology from climate science — the "morphological climate", i.e., the large-scale morphological response, may be predicted reasonably well but the "morphological weather", which reflects the small-scale variations around the large-scale response, is somewhat more uncertain. The latter suffers from uncertainties in initial conditions, availability of sufficient data, etc. Some uncertainty may also be related to the model framework — for instance, processes such as the role of bioturbation in increasing the erodibility of less-erodible layers exposed by erosion, and kinetics of flocculation and aggregation are not explicitly accounted for in the numerical framework presented here. Some uncertainty may be related to the availability of data for parameterizing the erodibility of the parent bed and fluff layers laterally and longitudinally in the estuary, the availability of sufficient grain size distribution measurements to enable the appropriate representation of armoring effects, the kinetics associated with consolidation and swelling, etc. These are potentially areas of further research and may serve to improve the performance of such morphodynamic models at small scales.

The data, analyses, and model application presented in this dissertation relate to the LPR. However, the underlying physics, the processes, the conceptual picture of sediment dynamics, and resulting numerical model framework are generally applicable to starved-bed fine sediment systems. For instance, fluff layer dynamics have been observed and its erodibility quantified in other estuaries as well. The entrainment flux method developed as part of this dissertation provides an alternate approach for quantifying fluff layer erodibility in such systems. Similarly, river flow-dependent transport dynamics (mainly the importing, i.e., Regime I, and exporting regimes during relatively low- and high-flow conditions, respectively) have been observed in other estuaries, indicating that this is a relatively generic process. However, the flow thresholds separating the importing and exporting regimes are specific to the particular system, although these may be estimated using shear stress maps under different river flows along with

estimated/measured thickness and erodibility of the fluff layer. The delineation of the exporting regime into exporting-flushing and exporting-scouring, Regimes II and III, respectively) allows for specific consideration of the morphological impact of episodic scouring events. Such Regime III events are important for maintaining the dynamic equilibrium morphology of such estuarine systems. This had previously only been speculated upon in the literature; the empirical evidence, as well as the application of the numerical model presented in this dissertation confirms the hypothesis on the role of Regime III events. Finally, the morphodynamic model framework and its extension to include the Morfac approach presented in this dissertation are based on common physical principles and formulations from the literature, and is therefore generally suitable for application in starved-bed systems. Furthermore, model performance, especially for large-scale spatial and temporal metrics, supports the notion of predictability in transport and its utility for morphodynamic studies in such starved-bed systems.

5.2. RECOMMENDATIONS

THIS dissertation examines a number of issues related to morphodynamics in fine sediment settings. Although the data used here are primarily from the LPR, the overall conceptual findings, and the analytical and numerical methods developed as part of this dissertation are generally applicable to similar estuaries. With some additional caveats and refinements, the findings and methods may also be applicable to additional types of estuaries such as ones with large inter-tidal areas. The analyses presented in this dissertation also provide an indication of areas of potential future research for additional understanding at a conceptual level as well as for application in engineering studies relying on numerical models. These are listed below in no particular order:

- **Spatial variations in fluff layer erodibility** — The numerical model presented in Chapter 4 relied on the definition of fluff layer erodibility. Although the erodibility of the fluff layer in the relatively deep areas along the thalweg was parameterized based on empirical data, erodibility in the sub-tidal shallows was parameterized as more erodible as a result of model calibration. Conceptually, this is a reasonable definition, with more erodible fluff layers likely related to the fact that the sub-tidal shallows are exchanging water and sediments with the upper portion of the water column in the relatively deeper areas along the thalweg. Given the expectation of a range of floc sizes and associated settling velocities in suspension along the thalweg, exchange of the upper portion of the water column with the sub-tidal shallows implies that the sub-tidal shallows receive preferentially higher proportion of smaller and slower-settling flocs. These relatively smaller flocs, in addition to settling to the bed at a slower rate, may also be more erodible than the faster-settling flocs in the thalweg. However, such variations in fluff layer erodibility remain to be verified empirically. Similarly, no information exists on longitudinal variations in fluff layer erodibility. Both lateral and longitudinal variations in fluff layer erodibility are an avenue for further research.

- **Spatial variation in parent bed erodibility** — The empirical data used to parameterize the erodibility of the parent bed in the numerical model presented in Chapter 4 were conducive to the development of only a single set of erodibility inputs

over the entire river. However, this is likely to be a simplification of the spatial heterogeneity in reality. For instance, conceptually, bed layers formed by sedimentation over recent decades in the formerly dredged navigation channel are expected to be more erodible than undisturbed bed layers in the sub-tidal shallows created over millennial time-scales. This issue can be addressed by a suitable empirical measurements of erodibility over the various geomorphic units and sediment substrate types expected at a given study area. Therefore, the development of morphodynamic models of fine sediment systems should take into consideration the need for adequate spatial characterization of parent bed erodibility.

- **Temporal trends in erodibility** — The self-weight consolidation or conversely, swelling of sediments, can impact sediment erodibility as a function of time. Although limited data was available to characterize the effect of consolidation on erodibility in sediments from the LPR, the impact of swelling has not been extensively studied. Similarly, bioturbation can also impact erodibility in a similar manner as swelling. Both processes deserve further study for morphodynamic relevance, perhaps more so for short- rather than long-term morphological evolution.

- **Sediment stratigraphy** — Similar to the temporal trends in erodibility, the impact of sediment stratigraphy via armoring effects on morphodynamics is expected to be more in the short term than over the long term. Therefore, morphodynamic studies assessing morphological impacts over the short term should take into consideration the need for adequate characterization of sediment stratigraphy.

It should be noted that although some incremental improvement may be achieved in the performance of such morphodynamic models by incorporation of the above recommendations, the practical feasibility of effectively addressing these recommendations is not clear. For instance, precise definition of sediment stratigraphy using current methods will involve collection of a large number of sediment cores followed by measurement of grain size distribution at fine depth intervals. Such a spatially comprehensive data collection is probably unlikely to be achieved using current analytical methods. Therefore, unless alternate data collection and measurement methods are developed and applied in order to appropriately address these recommendations, morphodynamic models are expected to be data-limited. This implies the potential for limitations in the performance of morphodynamic models. These limitations are perhaps more important for fine sediment systems because of the sensitivity of starved-bed transport to the constraints of sediment mobility. Therefore, morphodynamic models of such fine sediment systems should be applied with some caution. Specific recommendations for the use of such morphodynamic models for scientific as well as engineering studies are provided below:

- **Uncertainty analysis** — The application of morphodynamic models can benefit from a formal assessment of uncertainty. One way of assessing uncertainty in modeled outcomes is to perform a large number of simulations incorporating variations in the forcings/inputs of interest, for example, uncertainty in the sediment stratigraphy. For the model application presented in this dissertation, the approach included the specification of initial conditions based on the average

grain size distribution measured in sediment cores over relatively large reaches. An alternative approach would be to use the variability in grain size distribution measured in individual cores in any given reach to assign initial conditions probabilistically, perform a large number of simulations, and assess the modeled outcome in order to characterize uncertainty originating from data limitations for this parameter. A similar exercise could be conducted for other parameters of interest, either singly or in a covarying manner.

- **Multiple lines of evidence** — Another strategy for addressing uncertainty in modeled outcomes is to consider multiple lines of evidence in decision-making, with the model as one of many lines of evidence. Other lines of evidence may include analytical models, empirical data, conceptual models, physical models, pilot studies, etc.

- **Scale of model uncertainty relative to scale of interest** — Consideration of the scale of model uncertainty relative to the scale of relevance for the metric of interest from a management or engineering standpoint may provide justification for using modeled outcomes for decision-making despite model uncertainty. For instance, if time-scale is not an issue of concern for the management and engineering objectives, then short-term uncertainty in model performance is not relevant so long as long-term model performance is reliable.

A

LINES-OF-EVIDENCE FOR THE FLUFF LAYER

IN the analyses presented in Chapter 2, we introduce the behavior of a layer of easily erodible sediments (referred to as the fluff layer) on the river bed. There are several lines of evidence, some direct and others indirect, and some more definitive than others, to support the presence of such a fluff layer in the LPR. Two of these arguments, namely the intra-tidal fluctuations in SSC and the Gust Microcosm measurements, presented previously are also summarized here for completeness. The various lines of evidence include:

- SSC data (indirect evidence) — The intra-tidal variability in SSC presented in Figure 2.3 indicates erosion and deposition to the bed within the half-tide. This pattern of successive erosion and deposition at such time-scales implies a pool of surficial sediments, limited in consolidation by residence time in the bed (~6 h), and therefore easily erodible.

- Gust Microcosm measurements (direct evidence) — Measurements of the critical shear stress for erosion from the Gust Microcosm experiments presented in Figure 2.7 show erodible surficial sediments over the range of bed shear stresses in the LPR during low to moderate river flows and typical tidal conditions (the x-axis in panel b of Figure 2.9 provides an indication of the range of bed shear stresses in the LPR under such conditions). Furthermore, the cores tested in the Gust Microcosm experiments were collected around slack-water when the fluff layer is expected to be at its maximum thickness. Furthermore, the depth of erosion during the experiments is quite limited, and estimated to be only up to a few millimeters. The shallow depth of erosion in combination with the fact that the bed shear stresses imposed during the Gust Microcosm experiments are representative of the bed shear stresses in the LPR during low to moderate river flows and typical tidal conditions suggests that the sediments eroded during the Gust Microcosm experiments likely originated from the fluff layer.

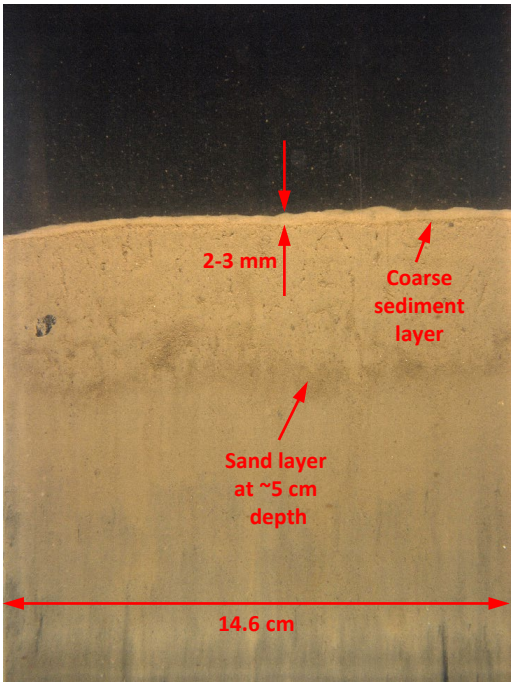

Figure A.1: Sediment depth-profile image (captured near Station 1 shown in Figure 2.1) during a SPI survey in the LPR.

- SPI data (indirect evidence) — High-resolution images of the in situ bed substrate and sediment-water interface were collected during a Sediment Profile Imaging (SPI) survey at several locations within the LPR (Germano and Associates, Inc. [1]). The SPI apparatus consists of a camera system housed within a wedge-shaped prism with a transparent faceplate. The faceplate is oriented vertically as the assembly is lowered into the sediment bed, thus allowing photographic imaging of the sediment-water interface and bed profile. The assembly is also held level through this process, allowing for an evaluation of sediment stratigraphy and bottom roughness amongst other properties relevant from biological and geochemical perspectives. Figure A.1 includes one of the images captured from the SPI survey, for a location at the mouth of the LPR (and in the vicinity of Station 1 shown in Figure 2.1). This image was taken at high-water when conceptually the fluff layer is expected to be at its maximum thickness. Distinct layers of different sediment types are apparent in this image, with a dark brown sand layer at (~5 cm depth and a thin dark brown layer with somewhat coarse sediment apparent about 2–3 mm below the sediment-water interface. The sediments above this coarse sediment layer, i.e., within the top 2–3 mm of the bed, appear to be somewhat finer in composition and lighter in color (likely well-oxygenated) than the sediments underneath. A similar surficial veneer of sediments were observed at a few other locations, most notably

at the locations sampled around high-water or low-water when the fluff layer is expected to be at its maximum thickness. Although the erodibility associated with this surficial veneer is unknown, its prevalence around slack water may be indicative of the fluff layer.

- Sedflume measurements (direct evidence) — Empirical observations of the erosion of surficial sediments during a Sedflume study in 2012 (Sea Engineering Inc. [2]) to measure the erosion properties of sub-surface sediments included visual observations of a thin surficial layer of easily-erodible sediment. The Sedflume experimental protocol consisted of running a sequence of increasing bed shear stresses (starting from 0.1 Pa) on undisturbed cores collected from various locations in Newark Bay and measuring the corresponding depth of erosion at each shear stress level. In several of the cores, a thin layer of loosely packed material was noted; this material typically eroded at the lowest shear stress run in the experiment (0.1 Pa). The bed thickness associated with this surficial layer was also smaller than the vertical resolution of the Sedflume device (0.5 cm). This provides another empirical line of evidence for the presence and easily-erodible nature of the fluff layer.

- Numerical modeling (indirect evidence) — The entrainment flux method presented herein was developed in the context of a numerical sediment transport model application of the LPR (unpublished work). This model, which includes a fluff layer parameterized using the entrainment flux method, has been calibrated and applied over various time-scales ranging from tidal to decadal, and covering the full range of river flows in the LPR. A sensitivity simulation with this model without including a fluff layer allows for an assessment of the importance of the fluff layer and also provides indirect support for the presence of the fluff layer — see also our next argument. The results of this sensitivity simulation showed that estuarine sediment dynamics such as tidal asymmetry in SSC, ETM formation, net up-estuary SS flux, net sedimentation, etc. during below-average flow conditions were not well reproduced. Only the inclusion of the fluff layer enabled the model to reproduce these SS dynamics. This comparison of model results, with and without considering a fluff layer, provides another line of evidence to support the existence of the fluff layer in the LPR.

- Estuary-scale processes (indirect evidence) — Theoretical arguments building on the findings of others also support the notion of an easily erodible fluff layer overlying less erodible strata. The net transport of fine sediments against the residual (river) flow during periods of low to moderate river flow and typical tidal conditions is governed by estuarine circulation and tidal asymmetry (in peak currents as well as slack-water duration). The latter process is also applicable up-estuary of the salt front (Friedrichs [3]; Dronkers [4]). In case of fine sediments limited by availability in the bed (starved-bed conditions), net sediment transport occurs due to scour lag and settling lag, induced around slack water (De Swart and Zimmerman [5]; van Straaten and Kuenen [6]). These lag effects implicitly assume the formation (via deposition) and erosion of an easily erodible layer of sediment over intra-tidal time-scales on an otherwise more or less stable bed. Thus, empirical

A

observations and the analytical formulations of net sediment transport in various tidal and estuarine systems reported upon by various authors also rely upon the notion of an easily erodible layer overlying less erodible strata.

In summary, several lines of evidence support the presence of a fluff layer in the LPR. The arguments range from direct measurements (such as Gust Microcosm, and Sedflume), indirect or inferred evidence (SSC data, SPI data, and numerical model application), and theoretical expectations. In addition, the results of numerical model sensitivity simulations with and without the fluff layer indicate the sediment fate and transport processes influenced by the presence of the fluff layer, and the relevance of the fluff layer to such fate and transport studies.

REFERENCES

[1] Germano and Associates, Inc., *Sediment Profile Imaging Survey of Sediment and Benthic Habitat Characteristics of the Lower Passaic River* (Bellevue, WA, 2005).

[2] Sea Engineering Inc., *Sedflume Analysis Data Report Newark Bay, New Jersey* (Santa Cruz, CA, 2013).

[3] C. T. Friedrichs, *Barotropic tides in channelized estuaries,* in *Contemporary Issues in Estuarine Physics*, edited by A. Valle-Levinson (Cambridge University Press, 2010) pp. 27–61.

[4] J. Dronkers, *Dynamics of coastal systems,* in *Advanced Series on Ocean Engineering*, Vol. 25 (World Scientific, 2005).

[5] H. E. De Swart and J. T. F. Zimmerman, *Morphodynamics of tidal inlet systems,* Annual Review of Fluid Mechanics **41**, 203 (2009).

[6] L. M. J. U. van Straaten and P. H. H. Kuenen, *Accumulation of fine grained sediments in the Dutch Wadden Sea,* Geologie en Mijnbouw **19** (1957).

B

VECTOR DECOMPOSITION — FLOW RATE

As part of the analyses presented in Chapter 3, several methods for flow decomposition were reviewed and tested. The method ultimately selected (referred to as the Analytical-Harmonic approach) is presented in Chapter 3. Two other methods are reviewed here; these derive from the literature and are referred to as the Averaging-Harmonic approach (Uncles and Jordan [1]; Winterwerp [2]; Costa [3]; Dyer [4]; Jay *et al.* [5]; Siegle *et al.* [6]), and the Signal Processing approach (Lerczak *et al.* [7]; Chant *et al.* [8]). The results of these methods differ primarily in the calculated estuarine circulation flow rate. Therefore, the results of these methods are compared against empirical evidence as well as the Analytical-Harmonic approach.

B.1. AVERAGING-HARMONIC APPROACH

The Averaging-Harmonic method is very similar to the Analytical-Harmonic approach. The primary difference is in the formulation used to calculate the flow rate associated with estuarine circulation. Given the time-series of instantaneous flow rates $q_{z,t}$ (Eq. 3.7), the flow rate associated with estuarine circulation is first calculated as:

$$q_{z,E} = \langle q_{z,t} - \bar{q}_t \rangle \tag{B.1}$$

As with the Analytical-Harmonic approach, tidal-period averaging is performed over two tidal cycles using a centered moving-window scheme. The advection term is subsequently calculated using Eq. 3.16 and decomposed to barotropic ($q_{z,T}$) and residual ($q_{z,R}$) terms using a 35 h low-pass filter as applied for the Analytical-Harmonic approach.

B.2. SIGNAL PROCESSING APPROACH

The Signal Processing method differs from the Analytical-Harmonic and Averaging-Harmonic approaches in the order of integration as well as the analytical techniques

B

used to decompose the measured flow rate time-series. First, the barotropic component is estimated by applying a low-pass filter on the measured time-series of flow rates $q_{z,t}$ (Eq. 3.7). The low-pass filter uses a Lanczos window with a filter cutoff of 35 h, resulting in low-pass flow term $q_{z,LP}$. The high-frequency barotropic term $q_{z,T}$ is estimated as:

$$q_{z,T} = q_{z,t} - q_{z,LP} \tag{B.2}$$

Subsequently, the residual (river) flow term $q_{z,R}$ is calculated as:

$$q_{z,R} = \bar{q}_{z,LP} \tag{B.3}$$

Finally, the estuarine term $q_{z,E}$ is estimated as

$$q_{z,E} = q_{z,LP} - q_{z,R} \tag{B.4}$$

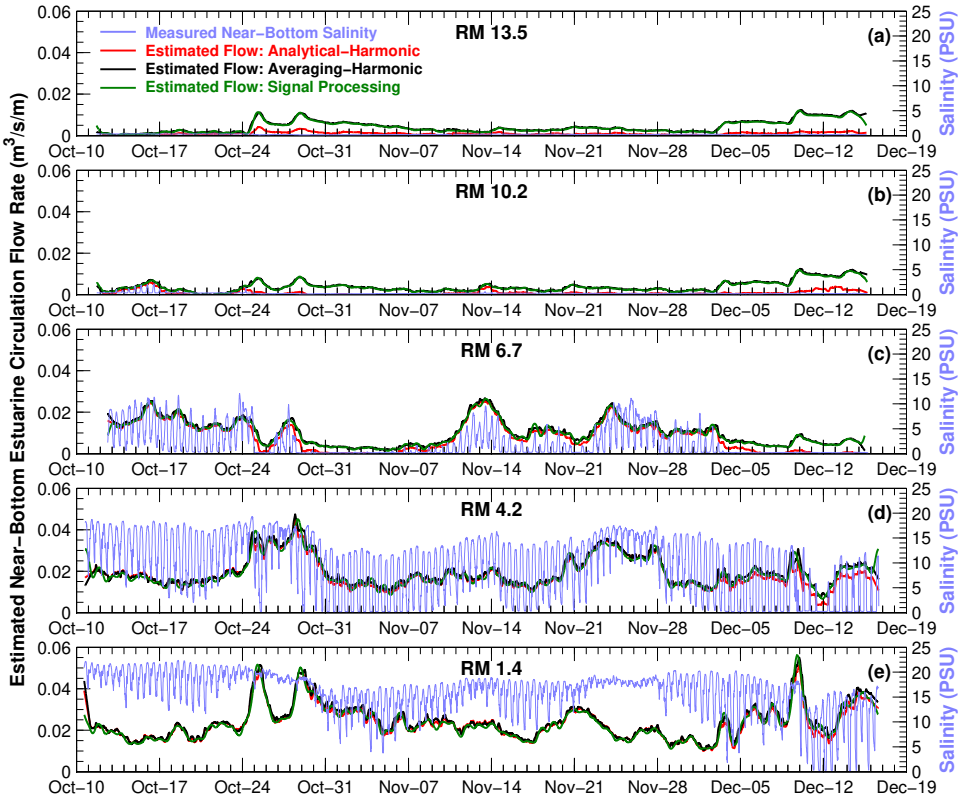

Figure B.1: Time-series comparison of measured near-bottom salinity and calculated near-bottom flow rate associated with estuarine circulation at the various mooring locations for the 2009 moored deployment. Flow rates were calculated using the various approaches described in Appendix B. Comparisons at (a) RM 13.5, (b) RM 10.2, (c) RM 6.7, (d) RM 4.2, and (e) RM 1.4.

B.3. RESULTS

FIGURE B.1 shows a comparison of the estimated near-bottom estuarine flow term using the three methods presented here in comparison to the measured near-bottom salinity at the various mooring locations. As seen in this comparison, the three methods give mostly similar results at all locations when the salt front is located at or landward of given location. The most significant difference between the three methods is at times/locations when/where the salt front is located seaward of given location, for instance, during October 29–November 7 and December 4 onwards at RM 6.7 and following October 17 at RMs 10.2 and 13.5. During such periods, the Averaging-Harmonic and the Signal Processing approaches calculate near-bottom estuarine flow, i.e., near-bottom flow directed up-estuary even in the absence of salinity, which runs counter to the definition of estuarine circulation, and the role of longitudinal density (salinity) gradients in inducing estuarine circulation. This artifact primarily derives from the fact that

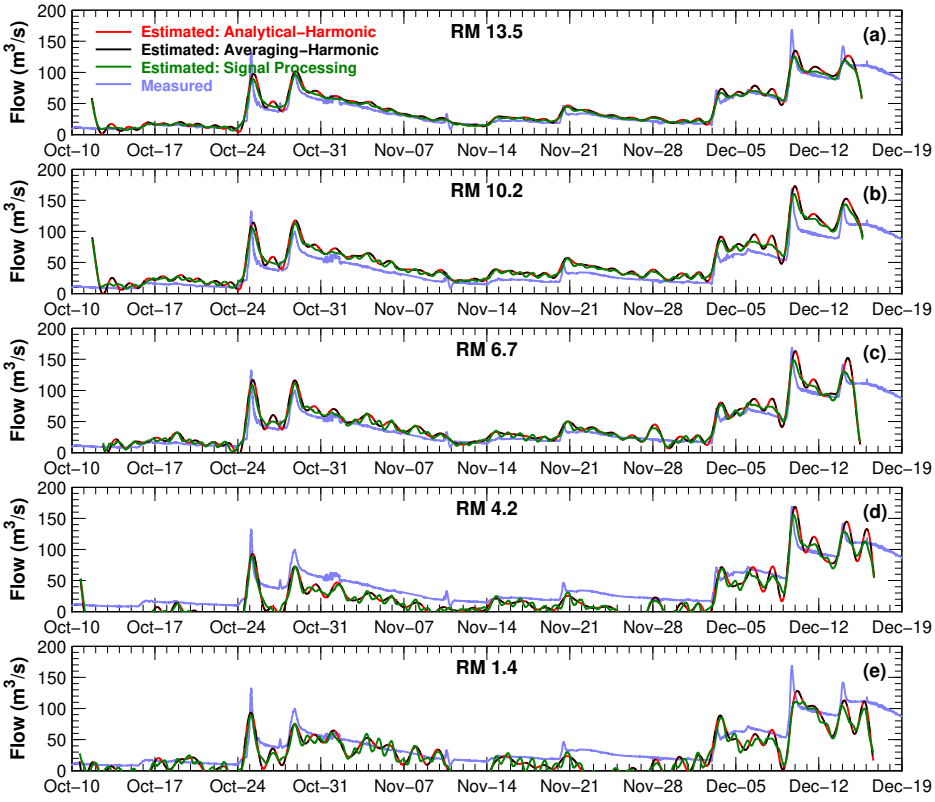

Figure B.2: Time-series comparison of measured river flow rate at the head-of-tide and calculated residual (river) flow rate at the various mooring locations for the 2009 moored deployment. Flow rates were calculated using the various approaches described in Appendix B. Comparisons at (a) RM 13.5, (b) RM 10.2, (c) RM 6.7, (d) RM 4.2, and (e) RM 1.4.

neither approach accounts for any deviation of the measured currents/flow rates due to the logarithmic velocity profile. In contrast, because the Analytical-Harmonic approach explicitly accounts for the logarithmic velocity profile as well as the pressure gradient induced by the longitudinal density gradient, the resulting estimates of near-bottom flow rate associated with estuarine circulation are consistent with the temporal trends in salinity at RM 6.7, 10.2, and 13.5.

Figure B.2 shows a comparison of the estimated residual (river) flow rates from the three methods in comparison to the measured freshwater flow from the head-of-tide. Results for the Analytical-Harmonic approach are identical to the Averaging-Harmonic approach at all locations. The results for the Signal Processing approach are mostly similar to the other two approaches in terms of the magnitudes and temporal trends. The main difference is a ringing artifact manifest in oscillatory river flow rates; such artifacts are typical of filters used in signal processing techniques such as applied here. Overall, the various methods give more or less similar results and tend to reproduce the magnitudes and temporal trends in measured freshwater flow rates, especially at RMs 6.7, 10.2, and 13.5. For reasons as described previously, the estimates at RMs 1.4 and 4.2 tend to be more comparable to measured flow rates during high river flow conditions than during low-average flow conditions.

The various approaches for flow decomposition reviewed and applied using the mooring data presented here tend to produce roughly similar results for the residual (river) flow rate, and the barotropic circulation terms (results not shown). The major difference is in the estuarine circulation term, with the Analytical-Harmonic approach producing results that are physically explainable and theoretically consistent with measured salinity. The Analytical-Harmonic approach therefore represents a refinement of the flow decomposition approach used in such studies in the literature, especially for dynamic systems where the prevalence of estuarine circulation may vary in time.

REFERENCES

[1] R. J. Uncles and M. B. Jordan, *Residual fluxes of water and salt at two stations in the Severn estuary,* Estuar Coast Mar Sci **9**, 287 (1979).

[2] J. C. Winterwerp, *Decomposition of the mass transport in narrow estuaries,* Estuar Coast Shelf S **16**, 627 (1982).

[3] R. G. Costa, *Flow-fine sediment hysteresis in sediment-stratified coastal waters,* (MS Thesis, University of Florida, Gainesville, 1989).

[4] K. R. Dyer, *Estuaries: A Physical Introduction*, 2nd ed. (John Wiley and Sons, New York, 1997).

[5] D. A. Jay, R. J. Uncles, J. Largier, W. R. Geyer, J. Vallino, and W. R. Boynton, *A review of recent developments in estuarine scalar flux estimation,* Estuaries **20**, 262 (1997).

[6] E. Siegle, C. A. F. Schettini, A. H. F. Klein, and E. E. Toldo, *Hydrodynamics and suspended sediment transport in the Camboriu estuary Brazil: Pre jetty conditions,* Braz J Oceanogr **57**, 123 (2009).

[7] J. A. Lerczak, W. R. Geyer, and R. J. Chant, *Mechanisms driving the time-dependent salt flux in a partially stratified estuary,* J Phys Oceanogr **36**, 2283 (2006).

[8] R. J. Chant, D. Fugate, and E. Garvey, *The shaping of an estuarine Superfund site: Roles of evolving dynamics and geomorphology,* Estuar Coast **34**, 90 (2011).

C

SCALAR DECOMPOSITION — SSC

THE SSC time-series data were not decomposed in a manner similar to the decomposition of flow rate in Chapter 3 for two reasons as elaborated below.

C.1. NEGATIVE CONCENTRATION COMPONENTS

THE application of decomposition techniques to SSC data such as summarized in Appendix A leads to the calculation of negative concentration components. Consider Eqs. C.1–C.4 which are generalized forms of the decomposition equations used in the Averaging-Harmonic Approach described in Appendix B. The Averaging-Harmonic Approach was chosen for this example because of the relatively simple equations involved.

$$\phi_{z,E} = \langle \phi_{z,t} - \bar{\phi}_t \rangle \tag{C.1}$$

$$\phi_{z,A} = \phi_{z,t} - \phi_{z,E} \tag{C.2}$$

$$\phi_{z,R} = \langle \phi_{z,A} \rangle \tag{C.3}$$

$$\phi_{z,T} = \phi_{z,A} - \phi_{z,R} \tag{C.4}$$

where, ϕ may refer to flow rate, SSC, or salinity. This discussion focuses only on the application of the above decomposition to a scalar such as salinity or SSC; the application to a vector quantity such as flow rate is described in Chapter 3. Consider a location in an estuary that exhibits a linear increase in salinity or SSC from surface to bottom that persists through the tidal cycle. Application of Eq. C.1 over depth results in a $c_{z,E}$ profile (i.e. salinity/SSC components attributable to estuarine exchange flow) with negative near-surface and positive near-bottom values. This is because Eq. C.1 expresses the tidally-averaged deviation from the vertical average for given quantity. Similarly, application of Eqs. C.2–C.4 results in positive and negative contributions attributable to the barotropic component; the residual component is always positive.

Application of these decomposition methods to a vector quantity such as the instantaneous flow rate (with the appropriate positive and negative sign to indicate directionality during the flood and ebb phases of the tide) decomposes the net flow rate to physically meaningful gross quantities such as tidal, estuarine circulation, and residual flow components. Furthermore, these gross quantities have a direction that is related to forcings such as the water level gradient, salinity gradient, and freshwater inflows from the head-of-tide. In contrast, application of these decomposition methods to a scalar quantity gives results that, although mathematically tractable, are physically meaningless (e.g., negative concentration components). In order to avoid analyses using negative concentration components, and because SSF at the scale of interest (depth- and tidally-integrated) are identical regardless of whether or not such decomposition of SSC is applied (see the following section), SSC decomposition was not implemented.

C.2. DEPTH- AND TIDALLY-INTEGRATED SSF

As shown next, SSF with and without SSC decomposition are identical. The instantaneous scalar flux f_t is written as:

$$f_t = q_{z,t} c_{z,t} \tag{C.5}$$

Substituting Eq. 3.8:

$$f_t = (q_{z,T} + q_{z,E} + q_{z,R}) c_{z,t} \tag{C.6}$$

The depth- and tidally-integrated net flux F is:

$$F = \int_0^T \int_0^{h_t} (q_{z,T} + q_{z,E} + q_{z,R}) c_{z,t} \, \mathrm{d}z\mathrm{d}t \tag{C.7}$$

The expansion of Eq. C.7 is the approach used in the analyses presented in Chapter 3 to calculate SSF associated with the individual transport processes:

$$F = \int_0^T \int_0^{h_t} q_{z,T} c_{z,t} \, \mathrm{d}z\mathrm{d}t + \int_0^T \int_0^{h_t} q_{z,E} c_{z,t} \, \mathrm{d}z\mathrm{d}t + \int_0^T \int_0^{h_t} q_{z,R} c_{z,t} \, \mathrm{d}z\mathrm{d}t \tag{C.8}$$

$$F = F_T + F_E + F_R \tag{C.9}$$

where, F_T, F_E, and F_R refer to the depth- and tidally-integrated flux components attributable to barotropic, estuarine exchange, and residual flow, respectively. Various authors (Lerczak *et al.* [1]; Chant *et al.* [2]; Jay *et al.* [3]; Siegle *et al.* [4]; etc.) have also decomposed scalar $c_{z,t}$ and have used the following expression to calculate the net depth- and tidally-integrated flux (for salinity as well as SSC):

$$F = \int_0^T \int_0^{h_t} q_{z,T} c_{z,T} \, \mathrm{d}z\mathrm{d}t + \int_0^T \int_0^{h_t} q_{z,E} c_{z,E} \, \mathrm{d}z\mathrm{d}t + \int_0^T \int_0^{h_t} q_{z,R} c_{z,R} \, \mathrm{d}z\mathrm{d}t \tag{C.10}$$

As explained previously, terms $c_{z,T}$ and $c_{z,E}$ include negative values, and because as shown next, the three terms on the RHS of Eq. C.8 are equivalent to the three terms on

the RHS of Eq. C.10, the SSC time-series data was not decomposed; Eq. C.8 was used to calculate the depth- and tidally-integrated SSF components presented in Chapter 3. Using the equations for the Averaging-Harmonic Approach as an example, the application of Eq. C.1–C.4 to the measured flow rate and SSC results in various flow rate and SSC components. These terms have the following properties and constraints that directly derive from Eq. C.1–C.4:

- $\phi_{z,t}$ is subject to the constraint $\phi_{z,t} = \phi_{z,T} + \phi_{z,E} + \phi_{z,R}$
- $\phi_{z,E}$ is a constant over the tidal period and is subject to the constraint $\int_0^{h_t} \phi_{z,E} \mathrm{d}z = 0$
- $\phi_{z,R}$ is a constant over the tidal period and is a constant over depth
- $\phi_{z,T}$ is variable over the tidal period, is a constant over depth, and is subject to the constraint $\int_0^T \phi_{z,T} \mathrm{d}t = 0$

Using the barotropic flux component (the first term on RHS of Eq. C.8) as an example, the depth- and tidally-integrated barotropic flux is:

$$F_T = \int_0^T \int_0^{h_t} q_{z,T} c_{z,t} \, \mathrm{d}z \mathrm{d}t \tag{C.11}$$

Using SSC components decomposed following Eqs. C.1–C.4, and substituting into Eq. C.11 gives:

$$F_T = \int_0^T \int_0^{h_t} q_{z,T} (c_{z,T} + c_{z,E} + c_{z,R}) \, \mathrm{d}z \mathrm{d}t \tag{C.12}$$

$$F_T = \int_0^T \int_0^{h_t} q_{z,T} c_{z,T} \, \mathrm{d}z \mathrm{d}t + \int_0^T \int_0^{h_t} q_{z,T} c_{z,E} \, \mathrm{d}z \mathrm{d}t + \int_0^T \int_0^{h_t} q_{z,T} c_{z,E} \, \mathrm{d}z \mathrm{d}t \tag{C.13}$$

Changing the order of integration, and considering that term $c_{z,E}$ is a constant over the tidal period, the second term on the RHS of Eq. C.13 becomes:

$$\int_0^{h_t} c_{z,E} \int_0^T q_{z,T} \, \mathrm{d}t \mathrm{d}z \tag{C.14}$$

Since $\int_0^T q_{z,T} \, \mathrm{d}t = 0$, Eq. C.14 evaluates to zero. Similarly, changing the order of integration, and considering that term $c_{z,R}$ is a constant over the tidal period and depth, the third term on the RHS of Eq. C.13 becomes:

$$c_{z,R} \int_0^{h_t} \int_0^T q_{z,T} \, \mathrm{d}t \mathrm{d}z \tag{C.15}$$

Equation C.15 also evaluates to zero for the same reason as Eq. C.14. Therefore, Eq. C.13 reduces to:

$$F_T = \int_0^T \int_0^{h_t} q_{z,T} c_{z,T} \, \mathrm{d}z \mathrm{d}t \tag{C.16}$$

In other words, Eq. C.16, which is the formulation used by others with SSC decomposition, is equivalent to Eq. C.11:

$$F_T = \int_0^T \int_0^{h_t} q_{z,T} c_{z,t} \, \mathrm{d}z\mathrm{d}t = \int_0^T \int_0^{h_t} q_{z,T} c_{z,T} \, \mathrm{d}z\mathrm{d}t \tag{C.17}$$

Similar analysis of the estuarine and residual flux components gives:

$$F_E = \int_0^T \int_0^{h_t} q_{z,E} c_{z,t} \, \mathrm{d}z\mathrm{d}t = \int_0^T \int_0^{h_t} q_{z,E} c_{z,E} \, \mathrm{d}z\mathrm{d}t \tag{C.18}$$

$$F_R = \int_0^T \int_0^{h_t} q_{z,R} c_{z,t} \, \mathrm{d}z\mathrm{d}t = \int_0^T \int_0^{h_t} q_{z,R} c_{z,R} \, \mathrm{d}z\mathrm{d}t \tag{C.19}$$

Therefore, integrated over depth and the tidal cycle, flux components calculated with and without SSC decomposition are identical. Another conclusion is that even though decomposition results in negative instantaneous concentration components, depth- and tidally-integrated fluxes are reliable. This proof also holds for the Signal Processing Approach included in Appendix B. The Analytical-Harmonic Approach for decomposing flow rates is not directly applicable to SSC since it accounts for hydrodynamic features such as the logarithmic velocity profile. Decomposition of SSC would need to be accomplished using an approach such as the Averaging-Harmonic Approach shown in Eqs. C.1–C.4. Nonetheless, because SSC decomposition is subject to the constraint $c_{z,t} = c_{z,T} + c_{z,E} + c_{z,R}$, integrated over depth and the tidal period, component fluxes calculated with and without SSC decomposition are identical.

REFERENCES

[1] J. A. Lerczak, W. R. Geyer, and R. J. Chant, *Mechanisms driving the time-dependent salt flux in a partially stratified estuary,* J Phys Oceanogr **36**, 2283 (2006).

[2] R. J. Chant, D. Fugate, and E. Garvey, *The shaping of an estuarine Superfund site: Roles of evolving dynamics and geomorphology,* Estuar Coast **34**, 90 (2011).

[3] D. A. Jay, R. J. Uncles, J. Largier, W. R. Geyer, J. Vallino, and W. R. Boynton, *A review of recent developments in estuarine scalar flux estimation,* Estuaries **20**, 262 (1997).

[4] E. Siegle, C. A. F. Schettini, A. H. F. Klein, and E. E. Toldo, *Hydrodynamics and suspended sediment transport in the Camboriu estuary Brazil: Pre jetty conditions,* Braz J Oceanogr **57**, 123 (2009).

D

MORPHOLOGICAL UPSCALING — BED LEVEL VERSUS BED MASS

THE classical approach to morphodynamic upscaling using the Morfac approach (Roelvink [1] and Ranasinghe *et al.* [2]) is shown in the left panel of Figure 4.4. Briefly, in this approach, bed level change calculated over the hydrodynamic timestep (Δh_{hyd}) is multiplied by f_{mor} to calculate the bed level change over the morphodynamic timestep (Δh_{mor}); see Eq. D.1.

$$\Delta h_{mor} = f_{mor} \Delta h_{hyd} \tag{D.1}$$

Application of Eq. D.1 to perform morphological upscaling in a numerical model implies that morphological change may not be consistent with sediment mass change in the bed. In contrast, Eq. 4.8 results in bed mass change that is consistent with morphological change and prevents certain model performance artifacts introduced by the classical approach in settings where transport is erosion-limited or affected by armoring. This is further illustrated with an application of the two morphodynamic upscaling methods to a synthesized hydrograph presented in Figure D.1.

The example application in Figure D.1 uses the same model application presented in Chapter 4 and includes a synthesized hydrograph starting at below-average river flow of 10 m^3/s and increasing to 450 m^3/s. The first 10 days of this simulation represent the hydrodynamic and sediment transport spin-up and is simulated using f_{mor} of 1. Subsequently, f_{mor} increases to 7 as flow increases to 50 m^3/s, at which point f_{mor} decreases to 1. The model was initialized with a bed comprised of the fluff and transition layers, and sub-surface layers comprised solely of the largest sand class included in the present application (which has τ_{Cr} = 3.1 Pa and is non-erodible under the shear stresses imposed in this example). Model performance is shown on the left panels using the classical approach to morphodynamic upscaling (Eq. D.1), and on the right panels using the approach used in Chapter 4 (Eq. 4.8). The results are presented for a grid cell located at RM 1.4 in the LPR.

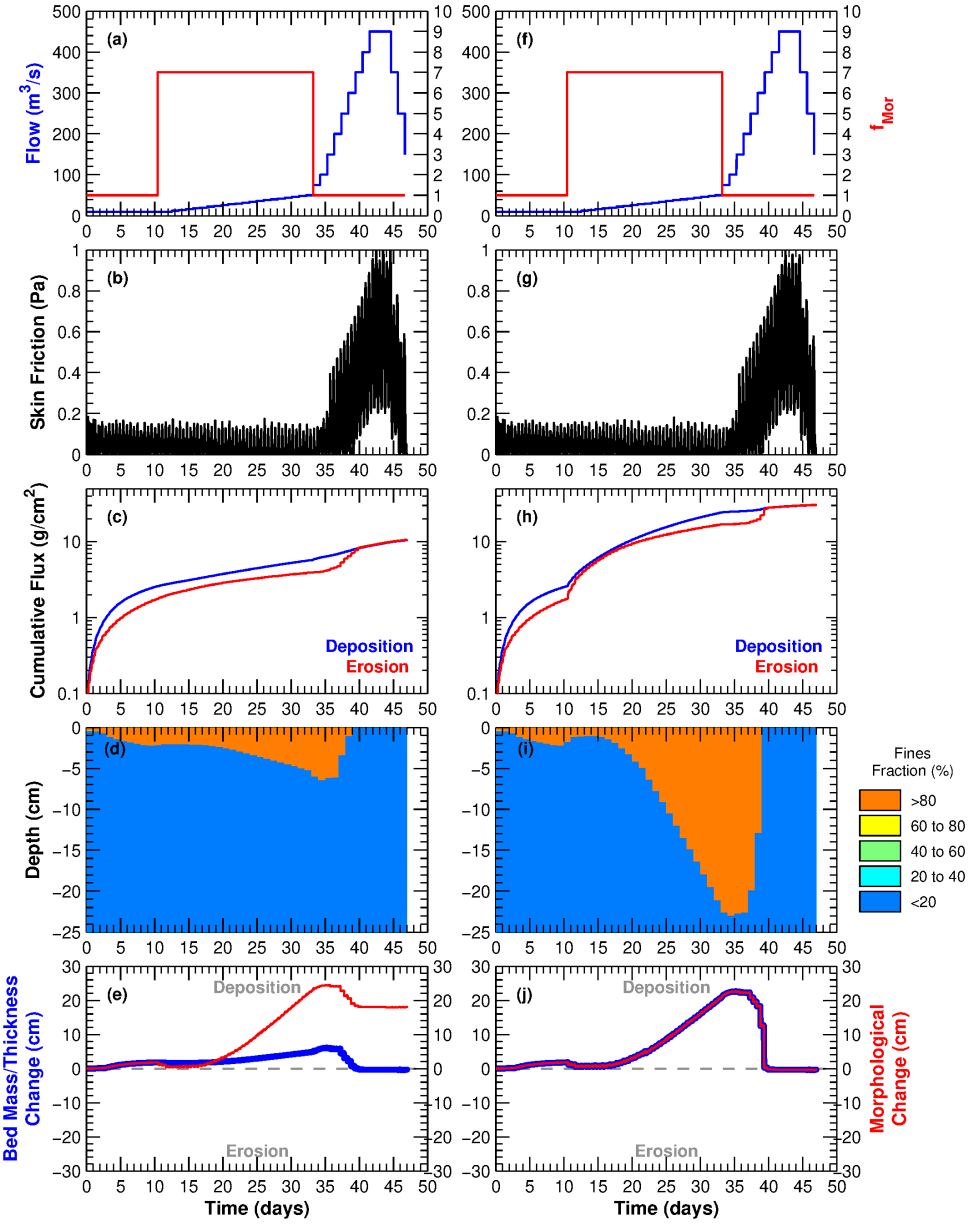

Figure D.1: Comparison of model performance over a synthesized hydrograph with morphological upscaling applied to bed level changes (panels a–e), and with morphological upscaling applied to bed mass changes (panels f–j).

Review of model performance for bed composition (panels d and i), and bed thickness (mass) and morphological change (panels e and j) shows the artifact associated with

the classical morphodynamic upscaling approach in a setting affected by bed armoring. The first 37 days of the simulation represent net depositional conditions, with both simulations showing net morphological change of approximately 24 cm. Since the classical approach does not preserve bed mass, the change in bed mass/thickness is only about 6 cm and much lower than morphological change during this period. This is also seen in the bed composition change over time, with the depositing fines creating about 6 cm of new layers on top of the initial bed layers. In contrast, the simulation with morphodynamic upscaling applied to bed mass preserves bed mass change and morphological change, with the depositing fines creating about 24 cm of new layers on top of the initial bed layers. During the high shear stress conditions over days 37–40, the entire depth of newly deposited sediment is eroded because skin friction during this period exceeds the critical shear stress of the deposited fine sediment layers. In the case of the simulation with morphodynamic upscaling applied to bed mass change, net erosion during this period is about 24 cm, with bathymetry reverting to the initial bathymetry following exposure of the armored bed layers. However, in the simulation with morphodynamic upscaling applied to bed level change, erosion of the 6 cm of deposited fines exposes the armored bed layer, and consequently, net morphological change over the 47-day simulation is calculated as net accretion (about 18 cm more deposition than the simulation with morphodynamic upscaling applied to bed mass change). This artifact in performance is a consequence of the fact that the classical approach does not conserve mass change in the bed. The same artifact is also introduced for a purely fine sediment setting, where depth-dependent variations in erodibility can have a similar effect as the armored layers used in this example. Therefore, in order to successfully apply morphodynamic upscaling in fine sediment settings, upscaling has to be applied to bed mass change rather than bed level change.

REFERENCES

[1] J. A. Roelvink, *Coastal morphodynamic evolution techniques,* Coast Eng **53**, 277 (2006).

[2] R. Ranasinghe, C. M. Swinkels, A. P. Luijendijk, J. A. Roelvink, J. Bosboom, M. J. F. Stive, and D. J. R. Walstra, *Morphodynamic upscaling with the morfac approach: Dependencies and sensitivities,* Coast Eng **58**, 806 (2011).

ACKNOWLEDGMENTS

This dissertation has been a journey of learning and a labor of love. It would not have been possible without the many individuals who are responsible for initiating me on this journey, and encouraging and supporting me along the way.

In looking back at my professional career, one of my regrets had been not being able to pursue a PhD in a subject I truly enjoy working on, that is, fate and transport studies in aquatic systems. Therefore, when this opportunity came about, I was grateful to have the opportunity to address this long-standing aspiration. At the same time, I was also excited to be able to continue working with Prof. Han Winterwerp, with whom I had already been working on for a few years on a consulting project.

Han, thank you for being my promoter, accepting me as your student and guiding me through this process the past several years. This experience has been one of the highlights of the past few years for me. I am grateful for your technical knowledge, thoughtful guidance, as well as the freedom you allowed in picking specific topics to pursue as part of this dissertation. I have learned a lot from you in this process — as a scientist, an engineer, and as a human being — and I hope we get to do some more work together.

I would also like to convey my gratitude to TU Delft for accepting me as a guest doctoral student. It has been an honor to have been part of an institution that is home to some of the foremost scientists in this field.

I would also like to thank my former colleagues at Moffatt and Nichol, specifically, John Headland and Rafael Cañizares, for their faith and confidence in me, and in initiating me on this path. I was fortunate to work on several interesting projects with them, and I was happy to be able to take what I learned as part of this dissertation and put to practical use. I am also grateful to them for exposing me to problems beyond environmental issues — to problems of coastal engineering, sediment management, flood protection, etc. I would also like to acknowledge the work of Dinesh Manian at Moffatt and Nichol — we worked together for several years on several projects, and he was instrumental in developing and implementing certain aspects of the work included in this dissertation.

I would also to thank my former colleagues at HydroQual, specifically, Ed Garland, Paul Paquin, Ben Wu, Pravi Shrestha, and Jim Hallden — some of my first experiences with modeling occurred under their guidance, and I have learned from them about the art, science, and tools of computational modeling.

I also wish to acknowledge that the majority of the data used in this dissertation was collected as part of the Remedial Investigation of the Lower Passaic River being conducted by the Cooperating Parties Group under supervision by the United States Environmental Protection Agency.

I would also like to thank my parents for encouraging me along the path of pursuing higher education. Lastly, and most importantly, I would also like to thank my wife,

Agnes, and son, Tommy. You have been extremely patient with me, as I've been preoccupied with this dissertation for several years now. I have spent far too many nights and weekends in front of the computer rather than spending time together with you. This dissertation would not have been possible without your support and patience.

Rooni Mathew
Hoboken, New Jersey, USA
April 2021

CURRICULUM VITÆ

Rooni Mathew was born on June 21, 1975 in the state of Kerala in South India. He studied studied Civil Engineering at the University of Pune, India, graduating with a Bachelors degree in 1996. Subsequently, he briefly worked at a construction firm and a software firm assessing vulnerabilities for the Y2K problem. Although he wasn't particularly successful at finding Y2K bugs, the experience did kindle an interest in the development and application of computational tools for addressing scientific and engineering problems.

In 1997, he started his studies at Duke University, USA, graduating in 1999 with a Masters degree in Civil and Environmental Engineering. His Masters thesis involved the development of a numerical model of the formation of porous beds by the deposition of cohesionless particles. Subsequently, from 1999–2008, he was employed at the consulting firm, HydroQual in New Jersey, USA. His experience working at HydroQual was formative and wide-ranging — he had the opportunity to work on problems of metal toxicity and inorganic chemical speciation in aquatic systems, bioaccumulation of hydrophobic organic chemicals, water quality, contaminant fate and transport, sediment transport, and hydrodynamics.

From 2008–2017, he was employed at the New York City office of Moffatt and Nichol, primarily focusing on problems of hydrodynamics, sediment transport, and contaminant fate and transport. During this time, he had the opportunity to work with Prof. Han Winterwerp and Leo Postma from Deltares on the environmental restoration project of the Lower Passaic River. The genesis for this dissertation as well as some of the material presented here grew from the collaboration with Prof. Winterwerp during those years. He has been a doctoral guest student at TU Delft from 2011 onwards. He is currently employed with CDM Smith in New York, USA as a surface water modeling expert.

Rooni Mathew has executed modeling projects all over the world using a variety of open source and commercial modeling packages such as EFDC, ECOM, Delft3D, and MIKE. He has worked on problems of hydrodynamics, sediment transport, and contaminant fate and transport in a variety of settings — coastal, estuarine, riverine, and lacustrine, for problems of sediment management, flood protection, impacts assessment, contaminated sediments, etc., typically at the planning and feasibility study stage as well as for engineering design. Over the years, he has worked on projects in the Housatonic River, Lower Passaic River, Newark Bay, Newtown Creek, San Francisco Bay, Coos Bay, Norfolk Harbor, Portland Harbor, USA; Canal del Dique, Magdalena River, and Buenaventura Bay, Colombia; and a country-wide lacustrine sedimentation assessment in Ireland.

Rooni Mathew married Agnes in 2008, and their son, Thomas, was born in 2008. In his free time, he enjoys watching his son's soccer (football) games, running, hiking, biking, and camping. His long-term goal is to hike all 46 high-peaks in the Adirondack Mountains in New York State, USA. Although he has managed only 3 peaks so far, he is optimistic about scaling more peaks after the completion of this dissertation.

LIST OF PUBLICATIONS

9. **R. Mathew**, and J. C. Winterwerp, *Morphodynamic modeling and morphological upscaling in a fine sediment system*, Advances in Water Resources [under review].

8. **R. Mathew**, and J. C. Winterwerp, *Sediment dynamics and transport regimes in a narrow microtidal estuary*, Ocean Dynamics **70**, 435–462 (2020).

7. **R. Mathew**, and J. C. Winterwerp, *Surficial sediment erodibility from time-series measurements of suspended sediment concentrations: development and validation*, Ocean Dynamics **67**, 691–712 (2017).

6. **R. Mathew**, J. A. McGrath, and D. M. DiToro, *Modeling polycyclic aromatic hydrocarbon bioaccumulation and metabolism in time-variable early life-stage exposures*, Environmental Toxicology and Chemistry **27**, 1515–1525 (2008).

5. **R. Mathew**, E. J. Garland, M. Velleux, P. R. Paquin, and S. Svirsky, *Summary of model simulation of PCB and solids fluxes in the Housatonic River, MA*, in *Proceedings of the Fourth International Conference on Remediation of Contaminated Sediments, Savannah, Georgia* (Battelle, 2007).

4. G. K. Bielmyer, M. Grosell, P. R. Paquin, **R. Mathew**, K. B. Wu, R. C. Santore, and K. V. Brix, *Validation study of the acute biotic ligand model for silver*, Environmental Toxicology and Chemistry **26**, 2241–2246 (2007).

3. D. M. DiToro, J. A. McGrath, D. J. Hansen, W. J. Berry, P. R. Paquin, **R. Mathew**, K. B. Wu, and R. C. Santore, *Predicting sediment metal toxicity using a sediment biotic ligand model: methodology and initial application*, Environmental Toxicology and Chemistry **24**, 2410–2427 (2005).

2. P. R. Paquin, V. Zoltay, R. P. Winfield, K. B. Wu, **R. Mathew**, R. C. Santore, and D. M. DiToro, *Extension of the biotic ligand model of acute toxicity to a physiologically-based model of the survival time of rainbow trout (Oncorhynchus mykiss) exposed to silver*, Comparative Biochemistry and Physiology Part C: Toxicology & Pharmacology **133**, 305–343 (2002).

1. R. C. Santore, **R. Mathew**, P. R. Paquin, and D. M. DiToro, *Application of the biotic ligand model to predicting zinc toxicity to rainbow trout, fathead minnow, and Daphnia magna*, Comparative Biochemistry and Physiology Part C: Toxicology & Pharmacology **133**, 271–285 (2002).